

University of Alberta

Twin G^ΛC-based Rosette Nanotubes: Structure and Chirality

by

Usha Devi Hemraz

A thesis submitted to the Faculty of Graduate Studies and Research
in partial fulfillment of the requirements for the degree of

Doctor of Philosophy

Department of Chemistry

©Usha Devi Hemraz

Fall 2010

Edmonton, Alberta

Permission is hereby granted to the University of Alberta Libraries to reproduce single copies of this thesis and to lend or sell such copies for private, scholarly or scientific research purposes only. Where the thesis is converted to, or otherwise made available in digital form, the University of Alberta will advise potential users of the thesis of these terms.

The author reserves all other publication and other rights in association with the copyright in the thesis and, except as herein before provided, neither the thesis nor any substantial portion thereof may be printed or otherwise reproduced in any material form whatsoever without the author's prior written permission.



Library and Archives
Canada

Published Heritage
Branch

395 Wellington Street
Ottawa ON K1A 0N4
Canada

Bibliothèque et
Archives Canada

Direction du
Patrimoine de l'édition

395, rue Wellington
Ottawa ON K1A 0N4
Canada

Your file *Votre référence*
ISBN: 978-0-494-81319-5
Our file *Notre référence*
ISBN: 978-0-494-81319-5

NOTICE:

The author has granted a non-exclusive license allowing Library and Archives Canada to reproduce, publish, archive, preserve, conserve, communicate to the public by telecommunication or on the Internet, loan, distribute and sell theses worldwide, for commercial or non-commercial purposes, in microform, paper, electronic and/or any other formats.

The author retains copyright ownership and moral rights in this thesis. Neither the thesis nor substantial extracts from it may be printed or otherwise reproduced without the author's permission.

AVIS:

L'auteur a accordé une licence non exclusive permettant à la Bibliothèque et Archives Canada de reproduire, publier, archiver, sauvegarder, conserver, transmettre au public par télécommunication ou par l'Internet, prêter, distribuer et vendre des thèses partout dans le monde, à des fins commerciales ou autres, sur support microforme, papier, électronique et/ou autres formats.

L'auteur conserve la propriété du droit d'auteur et des droits moraux qui protègent cette thèse. Ni la thèse ni des extraits substantiels de celle-ci ne doivent être imprimés ou autrement reproduits sans son autorisation.

In compliance with the Canadian Privacy Act some supporting forms may have been removed from this thesis.

While these forms may be included in the document page count, their removal does not represent any loss of content from the thesis.

Conformément à la loi canadienne sur la protection de la vie privée, quelques formulaires secondaires ont été enlevés de cette thèse.

Bien que ces formulaires aient inclus dans la pagination, il n'y aura aucun contenu manquant.


Canada

Examining Committee

Dr. Hicham Fenniri, Department of Chemistry

Dr. Derrick L. J. Clive, Department of Chemistry

Dr. David Bundle, Department of Chemistry

Dr. Glen Loppnow, Department of Chemistry

Dr. Frank Hegmann, Department of Physics

Dr. Alexander Adronov, Department of Chemistry, McMaster University

Abstract

Rosette Nanotubes (RNTs) are self-assembled architectures, generated from a self-complementary guanine-cytosine (G \wedge C) base. In solution, six G \wedge C motifs assemble to form hexameric rosettes, which stack to form the RNTs. Both single or twin G \wedge C-based (two G \wedge C units connected by a spacer) RNTs have built-in ability to self-assemble, however the latter have enhanced stability resulting from twice the number of intermolecular hydrogen-bonding interactions, greater preorganization and amphiphilic character as well as a lower charge density and steric repulsion on their outer surface. In order to fully exploit these organic materials for biomedical and other materials applications, an in-depth study of the physical properties of the twin RNTs was necessary. This thesis explores several newly synthesized G \wedge C motifs, with variations in functionalization, core structure and connectivity, which in addition to displaying novel self-assembly behaviour, also show unique physical properties.

The first chapter introduces relevant literature examples of self-assembled systems that exhibit supramolecular chirality. Notably, the sources of chirality and characterization techniques along with different factors leading to reversible supramolecular chirality inversions are presented. The second chapter describes how functionalization and core modification of newly synthesized twin G \wedge C compounds along with solvent and counterions, can influence the stability of RNTs, as indicated by their lengths at a given time. The third chapter examines

unique thermo-reversible circular dichroism activity shown by achiral twin G \wedge C-based RNTs. Evidence showing that real and reversible symmetry breaking could occur using a mechanical vortex in intrinsically achiral RNT systems is presented. Chapter four describes hypotheses behind the non-assembly of certain single G \wedge C-based modules and how higher pH and hydrogen-bond acceptor solvents promoted the formation of nanostructures. The fifth chapter describes a novel mode of self-assembly for a new analogue, having two twin G \wedge C moieties connected by an alkyl chain. Currently, this system shows comparable stability to RNTs having only one twin G \wedge C unit, but has the potential for increased stabilization if functionalized with solubilising groups. Chapter six describes the solid-phase synthesis and self-assembly characterization of two new twin G \wedge C motifs, bearing bioactive peptides for biological applications. Finally, an outlook of this thesis is presented.

Dedication

To my parents

*to whom I owe
my strong will to pursue my goals*

Acknowledgements

Foremost, I am thankful to my supervisor, Professor Hicham Fenniri for his support and guidance throughout graduate school. The stream of suggestions and discussions we had, ensured that I always had something to contemplate and thereby guaranteed my continued development. I am most grateful to Professor Fenniri for giving me the freedom to undertake a number research projects. I would also like to thank the faculty members for taking the time to serve on my committee.

I am thankful to all the present and past members of the Fenniri group whom I have been privileged to work with. You have created an enjoyable work environment and encouraged me a number of times. I am particularly thankful to Dr. Ross S. Johnson, Dr. Christophe Danumah, Dr. Takeshi Yamazaki and Dr. Rachel Beingssner with whom I worked closely and for all the stimulating discussions we had over the years. I am very grateful to Dr. Jae-Young Cho for obtaining TEM and AFM images presented in this thesis. Many thanks to Dr. Mounir El Bakkari, Dr. Juan-Pablo Bravo-Vasquez, Dr. Andrew Myles, Dr. Jesus Moralez, Dr. Azizul Haque, Dr. Ai Lin Chun, Alissa Cheung for their assistance throughout the years.

I am deeply indebted to the support services and research facilities at the National Institute for Nanotechnology and University of Alberta. I am thankful to Dr. Mike Xia, Dr. Marek Malac, Daniel Salamon, Julie Qian and Martin Cloutier from NINT and personnel from the NMR Lab, Spectral Services Lab, Mass Spectrometry Lab, machine shop, storeroom, glass shop and shipping from the Department of Chemistry.

I was very fortunate to have established successful collaborations with a number of researchers. I would like to thank Dr. Takeshi Yamazaki and Professor Andriy Kovalenko from NINT for the molecular modeling; Dr. Lijie Zhang, Yupeng

Chen and Professor Thomas Webster from Brown University; Oriol Arteaga and Professor Josep M. Ribo from University of Barcelona; Dr. Nathan Cowiesson from Monash University; Dr. Sarabjeet Singh and Professor Baljit Singh from University of Saskatchewan; and Professor Howard Young from University of Alberta (Department of Biochemistry).

I am deeply indebted to my family for their unconditional love and belief in the glory of God. You have been an invaluable source of strength and are my greatest joy. I am so grateful for your blessings, constant encouragement and sacrifices you made for me. To my parents – thank you for being there for me all the time. To my loving sisters, who are always so caring and supporting, and have been the fun elements during throughout my education. To my brother-in-law, who always encourages me. To my grandparents, late grandmother and late grandfather, whom I terribly miss. I would also like to express my gratitude to my best friend and husband for his love, support and valuable insight throughout my graduate studies. I would like to finish by thanking my friends for their moral support.

Table of contents

	Page
Chapter 1. Supramolecular Chirality	
1.1. Chirality and Supramolecular Chemistry	1
1.2. Supramolecular chirality	2
1.3. Common Tools for characterization of Supramolecular Chirality	2
1.4. Different cases of Supramolecular chirality	4
1.4.1. Supramolecular chirality due to chiral scaffolds	4
1.4.2. Supramolecular chirality based upon ‘Sergeants and Soldiers’ principle	6
1.4.3. Induced supramolecular chirality and ‘chiral memory’ concept	7
1.5. Supramolecular chirality in achiral systems	10
1.6. Reversible supramolecular chirality switch	13
1.6.1. Light	14
1.6.2. Solvent	17
1.6.3. Temperature	19
1.7. Conclusion	21
1.8. References	22
Chapter 2. Investigation of the structural and electrostatic factors affecting the self-assembly and stability of twin G\wedgeC-based rosette nanotubes	
2.1. Introduction	30
2.2. Design and synthesis of twin base monomers	32
2.3. Environmental and structural factors affecting self-assembly of twin G \wedge C-based RNTs	39
2.3.1. Effect of solvent and counterions	41
2.3.2. Effect of functional group variation	51
2.3.3. Modification to the core structure	64
2.3.3.1. Synthesis of the modified core structures	65

2.3.3.2. Microscopy characterization of the RNTs with modified core structures	68
2.4. Conclusion	71
2.5. Experimental section	72
2.5.1 General Procedures	72
2.5.2. Synthesis of target molecules	75
2.6. References	122

Chapter 3. Thermo-reversible supramolecular chirality from achiral self-assembling molecules

3.1. Introduction	126
3.2. Results	127
3.3. Solution phase characterization	129
3.4. Thermo-reversibility of the CD profiles	134
3.5. RNTs derived from single G ^A C base systems do not show CD activity	137
3.6. Effect of solvent, side-chain, functional group and counterions	138
3.6.1. Effect of solvent on CD activity	139
3.6.2. Effect of molecular structure on CD activity	143
3.6.3. Effect of counterions on CD activity	149
3.7. Cotton effects in acridine functionalized RNTs	151
3.8. Substitution on exocyclic nitrogen	153
3.9. Comparing the TBL system to previously reported systems	161
3.9.1. Effect of stirring on TBL's supramolecular chirality	161
3.9.2. Effect of temperature and stirring on the CD of the RNTs	163
3.9.3. Contamination of CD by LD	166
3.9.4. Effect of temperature and stirring while recording the CD spectra	172
3.10. Mueller matrix and standard commercial CD instrument	178
3.11. Convection and interaction with quartz surface	182
3.12. Effect of chiral substituents	190
3.14. Conclusion	197
3.15. Experimental section	199

3.16. References	201
------------------	-----

Chapter 4. Solvent effects on the self-assembly of RNTs

4.1. Introduction	208
4.2. Results	211
4.2.1. Synthesis of the monomers	212
4.2.2. Self-assembly	215
4.2.3. NMR experiments	227
4.3. Discussion	232
4.4. Conclusion	235
4.5. Experimental section	236
4.6. References	247

Chapter 5. Self-assembling system with four G \wedge C bicycles

5.1. Introduction	249
5.2. Characterization of the G \wedge C-4 module in solution	251
5.3. Molecular modeling of the G \wedge C-4 module	256
5.3.1. Model 1	256
5.3.2. Model 2	258
5.3.3. Model 3	259
5.3.4. Model 4	261
5.4. Conclusion	269
5.5. Experimental procedure	270
5.6. References	272

Chapter 6. Peptide modified rosette nanotubes for improved orthopedic applications

6.1. Introduction	273
6.2. General procedure for solid phase peptide synthesis of target molecules	276
6.3. Synthesis of TB-KRSR	277

6.4. Characterization and visualization of TB-KRSR	279
6.5. Synthesis of TB-KSDGR	282
6.6. Characterization and visualization of TB-KSDGR	284
6.7. Biological applications of TB-KRSR and TB-KSDGR	287
6.8. Conclusion	287
6.9. Experimental section	289
6.9.1 Synthesis of TB-KRSR	289
6.9.2. Synthesis of TB-KSDGR	292
6.10. References	296
Significance of this thesis work and outlook	298

List of figures

	Page
1.1 Disk-shaped molecule with chiral tails, which self-assembled hierarchically in chloroform to give long fibres.	5
1.2 Monofunctional oligo(<i>p</i> -phenylene vinylene) (MOPV) functionalized with a ureido- <i>s</i> -triazine unit, which dimerized with another MOPV through complementary hydrogen bonding.	6
1.3 Extended core disc-shaped molecules, which organized themselves in a columnar phase.	7
1.4 Helicity induced in achiral polymer poly((4-carboxyphenyl)acetylene) by chiral amines, was memorized after replacing the latter with an achiral amine.	8
1.5 Racemic mixture of <i>P</i> - and <i>M</i> - helical nanotubes favoured the <i>M</i> -handedness upon addition of chiral L-alanine.	10
1.6 Diprotonated meso-sulfonatophenyl substituted porphyrins, which give rise to <i>J</i> -aggregates upon self-assembly in water at dilute concentration.	11
1.7 Dendritic zinc porphyrin (top) formed <i>J</i> -aggregates through π -stacking and hydrogen-bonded interactions (bottom).	12
1.8 Structure of the oligo(<i>p</i> -phenylene vinylene) which can self-assemble in dodecane to produce fibers through dimerization and π -stacking.	13
1.9 X and Y are 2 stable forms of a system. Under conditions a, X can be converted to Y and the latter can be reverted back to X under conditions b.	13
1.10 Photochemical and thermal isomerization processes of (<i>P</i> , <i>P</i>)-trans form of a sterically hindered olefin.	15
1.11 Photochemical interconversion of right-handed (<i>P</i>) and left-handed (<i>M</i>) helices upon irradiation with <i>l</i> - or <i>r</i> -CPL.	16
1.12 Styryl-substituted, axially chiral bicyclo[3.2.1]octan-3-one compound which switched its chirality based on the sign of CPL.	17

1.13	Self-assembling guanine-cytosine motif, which formed RNTs of opposite helices in water and methanol.	18
1.14	The hexakis(phenylethynyl)benzene derivative bearing chiral alanine fragments which can stack to form helices.	19
1.15	Optically active helical polymer poly{(S)-3,7-dimethyloctyl-3-methylbutylsilylene}, which exhibited thermal chiroptical inversion.	19
1.16	Helical homopolymer or copolymer of propargylamides formed from polymerization of 1 and 2 .	20
2.1	Twin G \wedge C motif G0 (A), L-lysine functionalized single G \wedge C motif K1 (B), twin rosette formed from the association of 6 twin G \wedge C motifs (C) and RNT assembled from twin rosettes (D).	31
2.2	Functionalized twin G \wedge C motifs	32
2.3	Synthesis of G \wedge C aldehyde 2.13	33
2.4	General scheme for the synthesis of the self-assembling motifs TBL	34
2.5	Compounds isolated and their corresponding yields	35
2.6	Compounds isolated and their corresponding yields	36
2.7	Synthesis of K-TBL motif	37
2.8	Synthesis of the Di-Me-TBL module	38
2.9	Synthetic scheme for Acr-TBL	38
2.10	SEM images of But-TBL in methanol (left) and water (right) (0.0125 mg/mL, 0.017 mM).	39
2.11	TEM image (left) and AFM image (right) of But-TBL (0.0125 mg/mL, 0.017 μ M) in methanol.	40
2.12	Syn conformation of the two G \wedge C moieties, leading to the formation of twin rosettes, which then stack to give a rosette nanotube.	41
2.13	SEM images of But-TBL in MeOH-water mixtures: (A) 100% water (B) 25% MeOH (C) 50% MeOH (D) 75% MeOH (E) 95% MeOH (F) 99% MeOH after 1 day. Scale bar = 200 nm.	43
2.14	Percentage growth of RNTs with respect to 99% MeOH solution as a function of methanol/water ratio.	44

2.15	Histograms (A-F) of But-TBL self-assembled in increasing concentrations of MeOH.	45
2.16	SEM images of R-TBL, S-TBL, G0 and K-TBL as the TFA salts (A-D) and HCl salts (E-H) respectively, in MeOH after 1 day of aging.	46
2.17	SEM images of R-TBL (2.40) and S-TBL (2.44) as the TFA salts (A, C) and HCl salts (B, D) respectively, in water after 1 day of aging.	47
2.18	CD spectra for R-TBL, S-TBL, G0 and K-TBL as the TFA salts (A-D, respectively) in MeOH (dash) and water (solid).	48
2.19	SEM images of self-assembling modules Eth-TBL (A-C), But-TBL (D-F), S-TBL (G-I) and K-TBL (J-L) as HCl salts in MeOH.	50
2.20	SEM images of twin RNTs with the indicated side-chain in water, aged for 1 day. Scale bar 200 nm.	52
2.21	Histograms of But-TBL, OH-TBL, Me-TBL and Pent-TBL.	53
2.22	Histograms for the SEM images of NH-TBL (A), Eth-TBL (B), But-TBL (C) and Hex-TBL (D).	54
2.23	Conformational search for Eth-TBL (left), But-TBL (middle) and Hex-TBL (right). The lowest energy conformer for each RNT monomer is shown.	55
2.24	CD spectra of G0 (dash) and K-TBL (solid) as the TFA salts in MeOH after 14 days.	56
2.25	SEM images of Acr-TBL after 1 day of aging in MeOH (A) and water (D) and 14 days of aging in MeOH (B) and water (E).	57
2.26	TEM image of Acr-TBL in (A) MeOH and (B) water after 1 day of aging. Scale bar = 100 nm.	58
2.27	AFM image of Acr-TBL in MeOH (left) and water (right) cast on HOPG after 1 day of aging.	59
2.28	Conformations of Acr-TBL	59
2.29	Relative free energy as a function of the number of twin-rosette rings of Acr-TBL.	60
2.30	Most stable conformation of Acr-TBL #3 (A), Hexameric rosette (B) of A, RNTs (C and D) comprised of π - π stacked twin-rosettes B.	61

2.31	Association free energy of RNT #3.	61
2.32	Time-dependent UV-vis spectrum of Acr-TBL in water.	62
2.33	Time-dependent UV-vis spectrum of Acr-TBL in methanol.	63
2.34	Variants of the twin RNT monomers with the modifications indicated for the core structure.	64
2.35	Synthetic scheme for the synthesis of But-TBL-H	65
2.36	Synthetic scheme for the synthesis of ethyl modified G ^Λ C aldehyde 2.70 .	66
2.37	Synthetic scheme for the synthesis of But-TBL-E (2.72).	67
2.38	Synthetic scheme for the synthesis of But-TBL-M.	67
2.39	SEM (first column), TEM (second column) and AFM (third column) images of But-TBL (first row), But-TBL-H (second row), But-TBL-E (third row) and But-TBL-M (fourth row).	69
2.40	Summary of diameters of compounds with modified core structures using AFM and TEM imaging, along with their structures generated using molecular modeling.	70
3.1	Achiral twin RNT monomers that give a CD signal in methanol upon self-assembly.	127
3.2	CD at 10 °C (top left), SEM (top right), AFM (bottom left) and TEM (bottom right) of RNTs derived from monomer But-TBL (1) in methanol.	128
3.3	Time-dependent UV-vis spectra of But-TBL in methanol - (0.01 mg/mL, 20 °C).	130
3.4	Exciton band structure for J- and H-aggregates.	131
3.5	CD growth of But-TBL with time (CD recorded at 10 °C).	131
3.6	Growth of But-TBL RNTs after 30 min (left) and 7 days (right) monitored by SEM.	132
3.7	Time-dependent DLS spectrum of But-TBL in methanol.	133

3.8	CD spectra of But-TBL before and after (10 min) addition of 10 μ L of neat TFA in 2 mL of But-TBL RNT solution in methanol of a 0.017 mM concentration (A). The SEM images (B-F) show the RNT morphologies before (B) and after addition of TFA at 5 min (C), 15 min (D), 30 min (E) and 1 h (F) intervals. Scale bar = 200 nm.	134
3.9	VT-CD of K-TBL (TFA salt) in methanol.	135
3.10	VT-CD on But-TBL RNTs as the HCl salt in methanol.	136
3.11	Mirror image CD profiles at 10 and 40 $^{\circ}$ C (left) and graph showing the CD intensities at 231 mdeg while But-TBL was subjected to a series of 300 VT-CD cycles at 10 and 40 $^{\circ}$ C (right).	136
3.12	SEM images of But-TBL RNTs in methanol before (A) and after (B) 300 VT-CD cycles from 10 to 40 $^{\circ}$ C. Scale bar = 200 nm.	137
3.13	SEM images of K1 RNTs (left) and But-TBL RNTs (right) in methanol at a concentration of 0.017 mM in methanol, after 1 week of aging.	138
3.14	SEM images of But-TBL from a 100% DMSO (left) and 75% DMSO-MeOH stock solution	139
3.15	SEM images of But-TBL from a 50% DMSO (left) and 25% DMSO-MeOH stock solution	140
3.16	CD spectrum of DMSO-MeOH mixtures (left) and VT-CD spectrum for the 25% DMSO-MeOH solution (right) of But-TBL	141
3.17	CD profiles of But-TBL in neat MeOH at 10 $^{\circ}$ C after 1 day and 14 days of aging.	142
3.18	CD profiles of But-TBL recorded at 10 $^{\circ}$ C in binary mixtures of MeOH and water: 99% MeOH (A), 95% MeOH (B), 75% MeOH (C), 50% MeOH (D), 25% MeOH (E), 100% water (F) after 1 day and 14 days of aging.	142
3.19	SEM image of Hex-TBL at CD concentration (left) and its CD spectrum at 10 $^{\circ}$ C in methanol after aging for 15 days (right).	146
3.20	SEM image of Eth-TBL at CD concentration (left) and its CD spectrum at 10 $^{\circ}$ C in methanol after aging for 1 day (right).	146

3.21	SEM image of NH-TBL at CD concentration (left) and its CD spectrum at 10 °C from a 25% DMSO-MeOH stock solution for 7 days (right).	147
3.22	SEM image of OH-TBL at CD concentration (left) and its CD spectrum at 10 °C in methanol after aging for 3 days (right).	147
3.23	SEM image of Pent-TBL at CD concentration (left) and its CD spectrum at 10 °C in methanol for 7 days (right).	148
3.24	SEM image of Me-TBL at CD concentration (left) and its CD spectrum at 10 °C from a 25% DMSO-MeOH stock solution for 7 days (right).	148
3.25	SEM image of Di-Me-TBL at CD concentration (left) and its CD spectrum at 10 °C from a 25% DMSO-MeOH stock solution for 7 days (right).	149
3.26	SEM of RNTs derived from But-TBL monomer as HCl (A, B) and TFA (C, D) salts.	150
3.27	CD at 10 °C (left) and VT-CD (right) spectra of RNTs in MeOH derived from the But-TBL monomer isolated as HBr salt, aged for 5 days.	151
3.28	SEM of RNTs in MeOH derived from the But-TBL monomer isolated as the HBr salt, after 5 days of aging.	151
3.29	SEM image (left) after 3 days of aging and CD spectrum at 10 °C (right) after 17 days of aging of Acr-TBL at a concentration of 0.025 mg/mL in methanol.	152
3.30	Comparison of CD spectra of But-TBL and Acr-TBL in methanol (left) and VT-CD spectra for Acr-TBL in methanol (right).	153
3.31	Rotation of the G \wedge C discs in NH-TBL	153
3.32	Conformers of twin G \wedge C with NHCH ₃ (left) and NH ₂ (right) exocyclic substituent on the guanine face.	154
3.33	Potential barriers for rotation of most stable conformation of NH-TBL motif (with Me, no Me and no Me + no partial charges).	154

3.34	Conformational search to obtain the optimum values for the staggered angle (θ) and the stacking distance (D) between twin rosettes. The optimum values calculated for NH-TBL were: $\theta = 20^\circ$ and $D = 3.3 \text{ \AA}$.	155
3.35	One (left), two (centre), and three (right) twin-rosette discs constructed for NH-TBL using $\theta = 20^\circ$ and $D = 3.3 \text{ \AA}$	156
3.36	Potential barriers for rotation of NH-TBL for 1, 2 and 3 rosette rings at 10°C .	156
3.37	Potential barrier, internal energy and solvation free energy for NH-TBL for 1 rosette ring at 10°C (left) and 40°C (right).	157
3.38	Potential barrier, internal energy and solvation free energy for NH-TBL for 2 rosette rings at 10°C (left) and 40°C (right).	157
3.39	Potential barrier, internal energy and solvation free energy for NH-TBL for 3 rosette rings at 10°C (left) and 40°C (right).	158
3.40	Core modification of the G \wedge C motif of the twin RNTs monomers	158
3.41	SEM image (left) and CD (right) of the HCl salt of TBL-H in methanol after 4 days of aging.	159
3.42	SEM image of HCl salt of But-TBL-E in methanol after 2 weeks of aging.	160
3.43	SEM image (left) and CD spectrum (right) of HCl salt of But-TBL-M in methanol after 4 days of aging.	161
3.44	CD of But-TBL sample at 10°C (0.0125 mg/mL, 0.017 mM, aged for 5 days at room temperature) made by changing the direction of the vortex during synthesis.	162
3.45	CD growth of But-TBL sample A (stock solution aged at $21\text{-}23^\circ\text{C}$) with time (left) and SEM image of a 7-day diluted But-TBL sample (right).	164
3.46	CD growth of But-TBL sample B (stock solution aged at $2\text{-}8^\circ\text{C}$) with time (left) and SEM image of a 7-day diluted But-TBL sample (right).	164

3.47	CD growth of But-TBL sample C (stock solution aged at 33-38 °C) with time (left) and SEM image of a 7-day diluted But-TBL sample (right).	165
3.48	CD growth of But-TBL sample D (stock solution aged at 21-23 °C and stirred CW) with time (left) and SEM image of a 7-day diluted But-TBL sample (right).	166
3.49	CD growth of But-TBL sample (stock solution aged at 21-23 °C and stirred CCW) with time (left) and SEM image of a 7-day diluted But-TBL sample (right).	166
3.50	CD (left) and LD (right) of But-TBL methanolic solution at 10 °C.	167
3.51	CD (left) and LD (right) of But-TBL RNTs dip-coated film 1.	168
3.52	CD (left) and LD (right) of But-TBL RNTs dip-coated film 2.	169
3.53	LD spectra of RNTs dip-coated film 1 recorded when the substrate was at 0° and 90° relative to the beam of light.	170
3.54	Overlap of 2 films (cast with But-TBL RNTs) at different dihedral angles, φ .	171
3.55	LD spectra of But-TBL cast on films and upon overlap of two such films by varying the dihedral angle.	171
3.56	CD spectra of But-TBL cast on films and upon overlap of two such films by varying the dihedral angle.	172
3.57	CD signals of stirred and unstirred But-TBL solutions at 10 °C (left) and 40 °C (right).	173
3.58	CD signals of stirred and unstirred But-TBL samples at 23 °C.	174
3.59	CD signals of But-TBL at 10, 23 and 40 °C when stirred CW and CCW.	174
3.60	CD signals of But-TBL samples when stirred clockwise and counter-clockwise alternatively at 10 °C.	175
3.61	LD signals of But-TBL samples at 10 °C when unstirred, stirred in clockwise and stirred in counter-clockwise directions.	176

3.62	LD signals of But-TBL samples at 10 °C before and after TFA addition.	177
3.63	Edge mask (left): the edges of the cuvette were masked using 4 mm wide black tapes on both sides leaving a 2 mm central slit; and Central mask (right): the centre of the optical faces was masked by 6 mm wide black tape, leaving 2 mm margins on each side of the optical windows.	177
3.64	LD signals of But-TBL samples at 10 °C when the optical cell was unmasked, masked on the edges and in the centre.	178
3.65	Mueller matrix – a 4 x 4 matrix	179
3.66	The Mueller matrix for a general sample with mixed anisotropies	179
3.67	Mueller matrix obtained for But-TBL RNTs at room temperature (23°C).	181
3.68	Optical effects derived from the Mueller matrix obtained for But-TBL RNTs at 23 °C when stirred CW (solid), CCW (dash) and when unstirred (dot).	182
3.69	Top view of the sample holder used for CD and LD measurements in the solution phase.	183
3.70	Average preferential orientations of But-TBL at 10 and 40 °C	184
3.71	Optical effects – CD (left), LD (centre) and LD' (right) obtained from the analytical measurements using the 2-MGE at 10, 23 and 40 °C for the unstirred methanolic But-TBL sample and when stirring CW and CCW at 23 °C.	184
3.72	VT-CD signals of But-TBL in methanol in a cuvette having a volume of 0.45 mL and a pathlength of 0.3 cm.	185
3.73	CD profiles of But-TBL in methanol in the rectangular cuvette of 1-cm pathlength. The measurements were recorded with 2 mL and 3.5 mL (full) of solution.	186
3.74	CD spectra of But-TBL RNTs, recorded in cylindrical and rectangular cuvettes at 10 °C. Both cuvettes have pathlength of 1 cm.	187

3.75	CD profiles of But-TBL RNTs upon stirring (at 640 rpm) CW and CCW in cylindrical and rectangular cuvettes at 10 °C.	187
3.76	CD signals of But-TBL samples at 10 °C when stirred in clockwise direction at varying stirring speeds in the cylindrical cuvette.	188
3.77	CD signals of But-TBL in methanol at 10 °C in cuvette 1 (left) and cuvette 2 (right) having 1-cm pathlength	189
3.78	VT-CD signals of But-TBL in methanol in cuvette 3 (left) and cuvette 4 (right) having 1-cm pathlength. The measurements were carried out in Australia.	190
3.79	Functionalized chiral twin RNTs monomers	191
3.80	SEM image of the HCl salt of G0 (13) in methanol (left) and its CD spectrum at 10 °C (right) after 7 days of aging.	191
3.81	SEM image of the HCl salt of K-TBL (14) in methanol, aged for 1 day (left) and its CD spectrum at 10 °C (right) after 7 days of aging.	192
3.82	SEM image of the HCl salt of R-TBL (15) (left) and CD signal at 10 °C (right) after 1 day of aging in methanol.	193
3.83	SEM image of the HCl salt of S-TBL (16) (left) and CD signal at 10 °C (right) after 1 day of aging in methanol.	193
3.84	VT-CD spectra of the HCl salt of R-TBL in methanol for a 1-day aged solution (left) and for a 3-day aged solution (right).	194
3.85	VT-CD spectra of the HCl salt of R-TBL in methanol for a two-month aged solution.	194
3.86	SEM image of the TFA salt of G0 in methanol (left) aged for 2 days and its CD (right) 14 days of aging.	195
3.87	SEM images of the TFA salt of K-TBL in methanol (left) for 1 day, CD after 14 days of aging.	196
3.88	SEM images of the TFA salt of R-TBL in water (left) and in methanol (right).	196
3.89	SEM images of the TFA salt of S-TBL in water (left) and in methanol (right).	197

4.1	Water-soluble K1 module bearing a single G \wedge C unit (left) and G0 analogue with two G \wedge C units (right). Both motifs contain a L-lysine pendant.	208
4.2	Self-assembling modules K1 (A) and G0 (B). Single (C) and twin (D) rosettes obtained from the self-assembly of K1 and G0, respectively. RNTs obtained from K1 (E) and G0 (F).	209
4.3	Structure of 4.1 and intramolecular hydrogen bonding, which could prevent the cytosine face of the G \wedge C base from engaging in intermolecular hydrogen bonding.	210
4.4	Table showing the molecules studied in this chapter	211
4.5	Deprotection of precursor 2.50 ⁶ to give the G \wedge C analogue 4.2	212
4.6	Deprotection of molecule 2.21 ⁵ to give the G \wedge C analogue 4.3	212
4.7	Synthetic scheme for G \wedge C analogue 4.5	213
4.8	Synthetic scheme for G \wedge C analogue 4.7	213
4.9	Synthetic scheme for G \wedge C analogue 4.16	214
4.10	SEM images of 4.7 in water at a concentration of 0.33 mg/mL (left) and stained using 2% uranyl acetate solution in water (right, TE mode).	215
4.11	SEM images of 4.7 in water at a concentration of 0.1 mg/mL, stained with 2% uranyl acetate solution in water in SE mode (left) and in TE mode (right).	216
4.12	Initial conformations ($4 \times 3 \times 3 \times 3 = 108$) were generated by varying the dihedral angles around the four bonds indicated by arrows.	217
4.13	Association free energy (left) and solvation free energy (right) of the most stable RNT in water.	217
4.14	Formation of rosette and a nanotube from the assembly of the most stable conformer of molecule 4.7 in water.	218
4.15	SEM images of 4.5 at a concentration of 0.05 mg/mL in methanol in TE mode (left) and in SE mode (right).	219

4.16	AFM image of 4.5 at a concentration of 0.05 mg/mL in methanol, cast on a freshly cleaved mica substrate.	220
4.17	SEM images of compound 4.16 aged for 4 days in methanol and diluted to 0.2 mg/mL (left) and 0.1 mg/mL (right).	221
4.18	AFM images of compound 4.16 aged for 4 days in methanol and diluted to 0.2 mg/mL.	221
4.19	STM images of compound 4.8 aged for 4 days in methanol and diluted to 0.2 mg/mL.	222
4.20	SEM images of 4.5 (left), 4.7 (center) and 4.16 (right) at pH 11	223
4.21	SEM images of 4.2 at a concentration of 0.5 mg/mL in DMF upon aging for 1 day (left) and 3 days (right).	223
4.22	SEM images of 4.3 at a concentration of 0.5 mg/mL in DMF upon aging for 1 day and stained using uranyl acetate (left), and after 3 days of aging (right).	224
4.23	SEM images of 4.1 in DMF upon aging for 1 day at a concentration of 2.0 mg/mL (left) and diluting the 2.0 mg/mL solution into 0.5 mg/mL (right).	225
4.24	SEM images of 4.1 at a concentration of 0.5 mg/mL in DMA upon aging for 1 day, visualized at different locations on the same TEM grid.	225
4.25	SEM images of 4.2 at a concentration of 0.5 mg/mL in DMA upon aging for 1 day, showing agglomerates of short and long RNTs.	226
4.26	SEM images of 4.3 at a concentration of 0.5 mg/mL in DMA upon aging for 1 day, visualized at different locations on the same TEM grid.	226
4.27	TROESY spectrum for molecule 4.1 in deuterated DMSO.	228
4.28	TROESY spectrum for molecule 4.2 in deuterated DMSO	229
4.29	TROESY spectrum for molecule 4.3 in deuterated DMSO	230
4.30	TROESY spectrum for molecule 4.5 in deuterated DMSO	231
4.31	Table summarizing the net charge of the monobases and their self-assembly behaviour in methanol or in the aqueous media.	232

4.32	Table showing some of the physical properties of the solvents used.	234
5.1	Hydrogen bonding patterns in single (A), twin (B) and tetra (also named G \wedge C-4, C) G \wedge C systems.	250
5.2	Synthetic plan for the formation of the G \wedge C-4 module	251
5.3	SEM images of G \wedge C-4 module 5.3 in water	252
5.4	AFM images of the G \wedge C-4 module 5.3 in water	252
5.5	SEM images of the G \wedge C-4 (5.3) and But-TBL modules in water cast on the same grid.	253
5.6	SEM images of the G \wedge C-4 5.3 in DMSO (0.25 mg/mL)	254
5.7	SEM images of the G \wedge C-4 5.3 in DMSO (0.05 mg/mL)	254
5.8	SEM images of the G \wedge C-4 5.3 in methanol	255
5.9	TEM images of the G \wedge C-4 5.3 in water	256
5.10	Initial structure of the G \wedge C-4 module from model 1	257
5.11	Most stable conformation of the G \wedge C-4 module obtained from the above set parameters from model 1.	257
5.12	Rosette ring from the most stable conformation of the G \wedge C-4 module from model 1.	258
5.13	Most stable symmetrical conformation of the G \wedge C-4 module (from model 2), while maintaining only the G \wedge C base separation.	259
5.14	Helical tube of the G \wedge C-4 module from model 2	259
5.15	Most stable conformation of the G \wedge C-4 module in water from model 3	260
5.16	Different views of a rosette constructed from the self-assembly of six G \wedge C-4 modules in water from model 3.	260
5.17	Different views of a nanotube constructed from the stacking of the rosettes shown in water from model 3.	261
5.18	Side view of an all-syn quad-rosette from the G \wedge C-4 monomer, showing a stacking distance of 3.3 Å between the second and third G \wedge C moieties (model 4).	262

5.19	Top view, showing only the first rosette ring (A) and side view (B) of the unoptimized quad-rosette ring from G \wedge C-4 (model 4).	263
5.20	Top view (A) and side view (B) of the optimized quad-rosette ring with a syn-syn-syn conformation from G \wedge C-4 (model 4).	263
5.21	Top view (A) and side view (B) of the optimized quad-rosette ring with a syn-anti-syn conformation from G \wedge C-4 (model 4).	264
5.22	Nanotubes made up of 7 quad-rosettes from G \wedge C-4 module with SSS (A) and SAS (B) arrangements of the G \wedge C units. In both cases, the calculated diameters of the nanotubes were 3.1 nm.	265
5.23	Association free energies of nanotubes from G \wedge C-4 module with SSS and SAS arrangements of the G \wedge C units with increasing number of rosette stacks.	266
5.24	Molecular conformation adopted by SSS G \wedge C-4 (A), SAS G \wedge C-4 (B) and NH-TBL (C)	267
5.25	Nanotubes made up of 7 quad-rosettes from G \wedge C-4 module with SSS (A) and SAS (B) arrangements of the G \wedge C units, and nanotube derived from NH-TBL (C), generated by the stacking of 14 twin-rosettes.	267
5.26	Comparison of association free energies of nanotubes from G \wedge C-4 module with SSS and SAS arrangements of the G \wedge C units with increasing number of rosette stacks (up to 7 stacks), and association free energy of NH-TBL (up to 14 stacks).	268
6.1	Attachment of a bioactive peptide sequence with two G \wedge C units as compared to when functionalized with one G \wedge C unit.	275
6.2	Structures of TB-KRSR and TB-KSDGR	276
6.3	Synthetic scheme for the synthesis of TB-KRSR	278
6.4	Predicted mode of self-assembly of TB-KRSR modules to form the corresponding RNTs.	279
6.5	SEM images of TB-KRSR in water	280
6.6	TEM images of TB-KRSR in water	281
6.7	AFM images of TB-KRSR in water	282

6.8	Synthetic scheme for the synthesis of TB-KSDGR	283
6.9	Predicted mode of self-assembly of TB-KSDGR modules to form the corresponding RNTs.	284
6.10	SEM images of TB-KSDGR in water	285
6.11	TEM images of TB-KSDGR in water	286
6.12	AFM images of TB-KSDGR in water	287

List of Abbreviations

1D	One-dimensional
2-MGE	Two-modulator generalized ellipsometer
2D	Two-dimensional
3D-RISM	Three-dimensional molecular theory of solvation
A-OPV	Achiral oligo(<i>p</i> -phenylene vinylene)
Acr	Acridine
AFM	Atomic force microscopy
aq	Aqueous
Arg	Arginine
Asp	Aspartic acid
Bn	Benzyl
Boc ₂ O	Di- <i>tert</i> -butyldicarbonate
br	Broad
But	Butyl
C	Celsius
CAPS	<i>N</i> -cyclohexyl-3-aminopropanesulfonic acid
CB	Circular birefringence
CCW	Counter-clockwise
CD	Circular dichroism
CE	Cotton effect
CEs	Cotton effects
COSY	Correlation spectroscopy
CPL	circularly polarized light
CW	Clockwise
D	Dextrorotatory
d	Doublet
DCE	Dichloroethane
dH ₂ O	Deionized water
DIC	<i>N,N</i> -diisopropylcarbodiimide

DIEA	Diisopropylethylamine
DLS	Dynamic light scattering
DMA	<i>N,N</i> -dimethylacetamide
DMAP	4- <i>N,N</i> -Dimethylaminopyridine
DMF	<i>N, N</i> -dimethylformamide
DMSO	Dimethyl sulphoxide
DNA	Deoxyribonucleic acid
ee	Enantiomeric excess
Et ₂ O	Diethyl ether
Eth	Ethyl
EtOAc	Ethyl acetate
Fmoc	Fluorenylmethyloxycarbonyl
G ^Λ C	A self-assembling heterocyclic module with the donor-donor-acceptor face of guanine and the acceptor-acceptor-donor of cytosine
Gly	Glycine
h	hour
H-bond	Hydrogen bond
HBA	Hydrogen-bond acceptor
HBD	Hydrogen-bond donor
HBTU	O-Benzotriazole- <i>N,N,N',N'</i> -tetramethyl-uronium-hexafluoro-phosphate
Hex	Hexyl
HMBC	Heteronuclear multiple bond correlation
HMQC	Heteronuclear multiple quantum coherence
HOMO	Highest occupied molecular orbital
HOPG	Highly ordered pyrolytic graphite
HPLC	High performance liquid chromatography
HRMS	High resolution mass spectrometry
ICD	Induced circular dichroism
IR	Infrared

KRSR	Lysine-arginine-serine-arginine
KSDGR	Lysine-serine-aspartic acid-glycine-arginine
L	Levorotatory
<i>l</i> -CPL	Left circularly polarized light
LB	Linear birefringence
LD	Linear dichroism
LPL	Linearly polarized light
LUMO	Lowest occupied molecular orbital
m	Multiplet
MeOH	Methanol
min	minute
MOPV	Monofunctional oligo(<i>p</i> -phenylene vinylene)
mp	Melting point
Na(OAc) ₃ BH	Sodium triacetoxyborohydride
NMO	<i>N</i> -methyldmorpholine <i>N</i> -oxide
NMR	Nuclear magnetic resonance
NOESY	Nuclear Overhauser Enhancement spectroscopy
obs	Observed
Pbf	pentamethyldihydrobenzofurane-5-sulfonyl
Pent	Pentyl
ppm	Parts per million
pss	Photostationary state
q	Quartet
R	Rectus
<i>r</i> -CPL	Right circularly polarized light
R _f	Retention factor
RGD	Arginine-glycine-aspartic acid
RNT	Rosette nanotube
ROE	Rotating-frame Overhauser Enhancement
ROESY	Rotating-frame Overhauser Enhancement Spectroscopy
rpm	Revolutions per minute

s	Singlet
S	Sinister
SAS	Syn-anti-syn
SEM	Scanning electron microscopy
Ser	Serine
SiO ₂	Silica gel
SPPS	Solid-phase peptide synthesis
SSS	Syn-syn-syn
STM	Scanning tunneling microscopy
t	Triplet
<i>t</i> -BuOH	<i>tert</i> -Butanol
TB	Twin base
TBL	Twin base linker
^t Bu	<i>tert</i> -butyl
TEM	Transmission electron microscopy
TFA	Trifluoroacetic acid
THF	Tetrahydrofuran
TLC	Thin layer chromatography
TM-AFM	Tapping mode atomic force microscopy
TROESY	Transverse Rotating-frame Overhauser Enhancement Spectroscopy
UV	Ultraviolet
UV-Vis	Ultraviolet-Visible
VT	Variable temperature
VT-CD	Variable temperature circular dichroism

Chapter 1

Supramolecular Chirality

1.1. Chirality and supramolecular chemistry

The right- or left-handedness, scientifically termed as chirality,¹ has always fascinated scientists ever since the pioneering researches by Arago, Jean Baptiste Biot and Augustin Fresnel on optical rotation. The concept of chirality gained more attention and triggered more research when in 1848 Louis Pasteur established that sodium ammonium tartrate crystals came in two asymmetric forms that were mirror images of one another and solutions of one form rotated polarized light clockwise, while the other form rotated light counter-clockwise.²

In a different part of the world in 1890, Hermann Emil Fisher proposed the ‘lock and key’ model³ as the answer to the enzyme-substrate interactions. While at that time covalent synthesis of molecules was an established discipline, scientists were interested in the chemistry ‘beyond the molecule’.⁴ One of the major breakthroughs came when the structure of DNA was elucidated⁵ and it was realized that the two strands were connected through hydrogen bonds. Eventually chemists were inspired by these concepts, which were applied to the synthesis of macrocyclic molecules that could selectively bind to other molecules via non-covalent interactions⁶ such as hydrogen bonding, π - π stacking and van der Waals forces. The eminence of this field was recognized when Donald Cram, Jean-Marie Lehn and Charles Pedersen were awarded the Nobel Prize in 1987 for their pioneering work, and the field of “supramolecular chemistry” was officially born.⁷ With better understanding of how intra- and intermolecular interactions govern the molecular recognition process, supramolecular chemistry has been used for the generation of a plethora of intriguing functional structures on the nanoscale level, which are supported primarily by non-covalent interactions.

The importance of chirality in life⁸ is clear and having supramolecular chemistry as a tool for non-covalent synthesis, chemists ventured in the creation of some very challenging targets – artificial systems that would mimic nature. This introductory chapter will focus on the supramolecular chirality of artificial systems, and the common tools used for their detection. Since the amount of relevant literature is so large, this chapter will only illustrate systems that give rise to helical nanofibres formed in solution through self-assembly processes and are maintained by non-covalent forces. In addition, only the most recent examples relevant to this thesis will be discussed. Supramolecular chirality resulting from the association of chiral components as well as from the dissymmetric interactions of achiral components will be presented. Literature examples of supramolecular chirality induction by external stimuli will also be discussed. The last part of this chapter will be devoted mainly to reversible supramolecular chirality inversions, triggered by various factors.

1.2. Supramolecular chirality

The supramolecular chirality⁹ of a system has been described as the chirality resulting either from the association of chiral components or through the dissymmetric interaction of achiral building blocks. In most cases, supramolecular chirality is templated by the inherent chirality of the monomer (*R* or *S*) or by chiral additives in an achiral environment to induce supramolecular chirality in hydrogen-bonded assemblies, to give preferentially one of the two possible diastereomeric forms (*P* or *M*-helicity). Being non-mirror images allows these diastereomers to be present in unequal amounts due to their different free energies. In the more unconventional cases, supramolecular chirality has been reported in achiral systems, triggered by external stimuli. These factors allow the selection of either the left- or right-handed conformation, leading to the creation and amplification of optical activity.

1.3. Common tools for characterization of supramolecular chirality

The characterization of nanofibres is not an easy task. In addition to the techniques used to characterize simple organic molecules (namely, mass spectrometry, 1D- and 2D-NMR, elemental analysis), a number of other techniques are required to characterize the nanostructures formed both in solution phase as well as when cast on different substrates.¹⁰

The most prevalent technique used for determination of helicity in solution is circular dichroism¹¹ (CD). The latter is the difference in absorption of left- and right-circularly polarized light and has been an essential tool in monitoring the growth of supramolecular assemblies. When a chromophore, which is in a chiral and non-racemic environment, interacts with a neighbouring chromophore, absorption bands (also referred to as Cotton effects (CEs)) are obtained due to the coupling of the chromophores' transition dipoles. This spectroscopic method is very popular for the investigation of secondary structures of biopolymers such as DNA, peptides and nucleic acids.¹¹ Though the presence of CEs generally imply the existence or predominance of one helicity, it cannot be denied that the spectrum can be flawed with artifacts. One such artifact, which is due to alignment of the sample in solution, is linear dichroism¹² (LD) - a spectroscopic technique based on the difference in absorption of linearly polarized light parallel and perpendicular to an orientation axis. LD is a common phenomenon observed for intrinsically oriented systems such as liquid crystalline phases or those that are oriented in solution during the experiment. Some reports have subtracted the LD component from the signal obtained from the CD spectropolarimeter to reveal the real CD component using the equation below, however this is acceptable only in non-aligned and non-birefringent systems.

$$CD_{\text{true}} = CD_{\text{obs.}} - 0.02 (LD_{\text{obs.}})$$

It is also very crucial to obtain visual confirmation of the type of structures resulting from a system. The most common way to visualize those structures is

by deposition of the corresponding solution on a substrate. Common substrates used for this purpose are carbon coated copper grids, highly ordered pyrolytic graphite (HOPG), mica and silicon. The dried samples are then analyzed via various microscopy techniques. Though it is very common to observe the presence of the fibres by transmission electron (TEM), scanning electron (SEM) and atomic force (AFM) microscopies, the visualization and determination of the helicity within the fibres and the bundles can be a real challenge, especially for nanostructures below 5 nm in cross-section.

1.4. Different cases of supramolecular chirality

1.4.1. Supramolecular chirality due to chiral scaffolds

Nature is filled with various examples of supramolecular chiral architectures. It all started with the homochirality in living organisms.⁸ For instance, almost all active forms of amino acids are of the L-form and most biologically relevant sugars are of the D-form. These homochiral building blocks assemble to give biomolecules of one preferred handedness as a result of chiral amplification and transmission to the ensemble. In most of these cases, water is the medium, but not limited to this function, where these biological processes occur. The elegance and complexity of these natural homochiral architectures have inspired various research groups who have mimicked these natural systems to develop interesting artificial organic systems. In many cases a number of other solvents have been exploited. This section presents some examples of chiral supramolecular aggregates based on scaffolds possessing stereogenic centres. In most cases, CD is the method of choice for demonstrating the existence of chiral architectures and in these examples the CD signals result from inherently dissymmetric chromophores.

Engelkamp and co-workers designed a disk-shaped molecule with chiral tails (Figure 1.1), which self-assembled hierarchically in chloroform to give long fibres of right-handed helicity as a result of π - π stacking interactions of the phthalocyanine units.¹³ In order to maximize the van der Waals interactions, two

of these right-handed fibres twisted around each other to produce superhelices of left-handed helicity. The helicity in the self-assembled structures was due to transfer of chiral information from the remote chiral centres to the cores and it was possible to tune this resulting supramolecular chirality by the addition of potassium ions. The alkaline metal ions formed stable complexes with the crown ether fragments, thus preventing the transfer of chirality from the remote chiral centres to the core of the molecule. A number of techniques were used to characterize the nanostructures formed, but CD and the transmission electron micrographs, in particular, depicted the helical nature of the resulting nanostructures in solution.

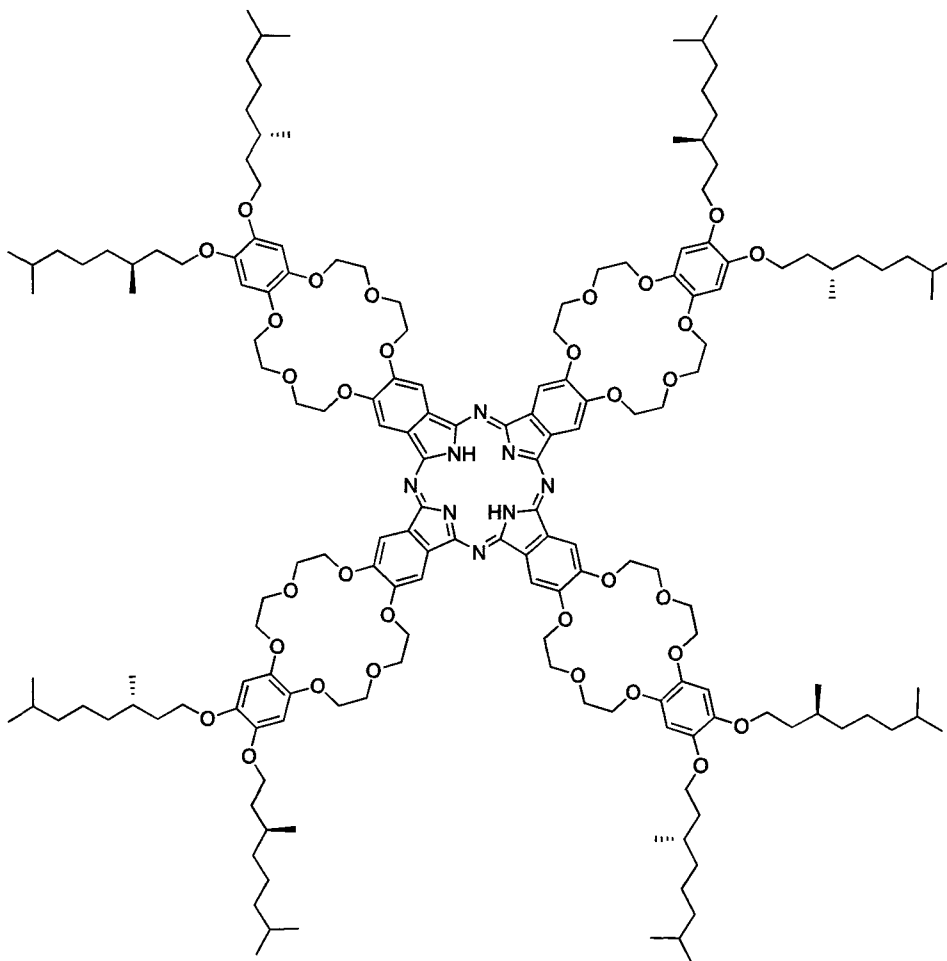


Figure 1.1: Disk-shaped molecule with chiral tails, which self-assembled hierarchically in chloroform to give long fibres.

Meijer and co-workers have reported a series of π -conjugated systems that undergo hierarchical self-assembly to produce helical aggregates towards the development of nanowires.¹⁴ The monofunctional oligo(*p*-phenylene vinylene) (MOPV) functionalized with a ureido-*s*-triazine unit dimerized with another MOPV through complementary quadruple hydrogen bonding, which then subsequently stacked into cylindrical chiral stacks via π - π interactions of the phenylenevinylene backbone. The presence of aggregates of one preferred handedness was reflected by an intense CD signal. MOPV in dodecane was molecularly dissolved at higher temperatures, while at lower temperatures it existed in the aggregated phase. Time-dependent CD experiments showed that the CD intensity decreased with increasing temperature, however, on cooling the CD signal was restored, suggesting the full reversibility of the system.

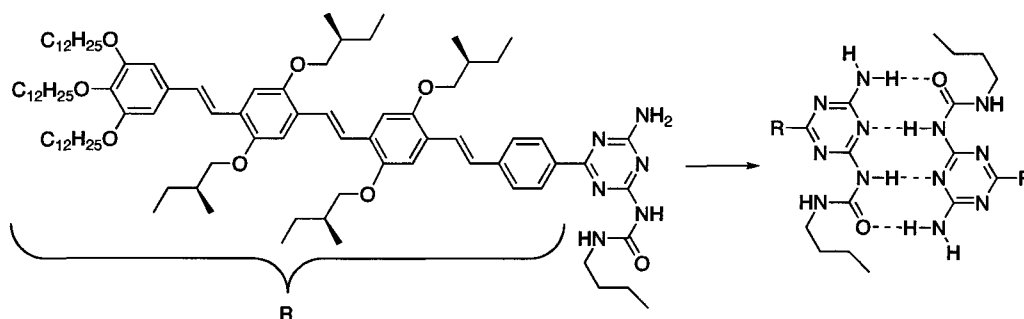


Figure 1.2: Monofunctional oligo(*p*-phenylene vinylene) (MOPV) functionalized with a ureido-*s*-triazine unit, which dimerized with another MOPV through complementary hydrogen bonding.

1.4.2. Supramolecular chirality based upon the ‘Sergeants and Soldiers’ principle

Green and co-workers reported the amplification of chirality in the synthesis of polyisocyanates.¹⁵ The latter are stiff helical polymers, which give rise to equal amounts of left- and right-handed structures. However, in the presence of even a small chiral bias, the achiral components follow the helicity induced by the chiral components. This phenomenon is termed as the ‘Sergeants and Soldiers’

principle where the chiral building blocks (Sergeants) direct the achiral units (Soldiers) to adopt a preferred helical sense. These types of chiral amplifications have also been observed in noncovalent macromolecular systems.

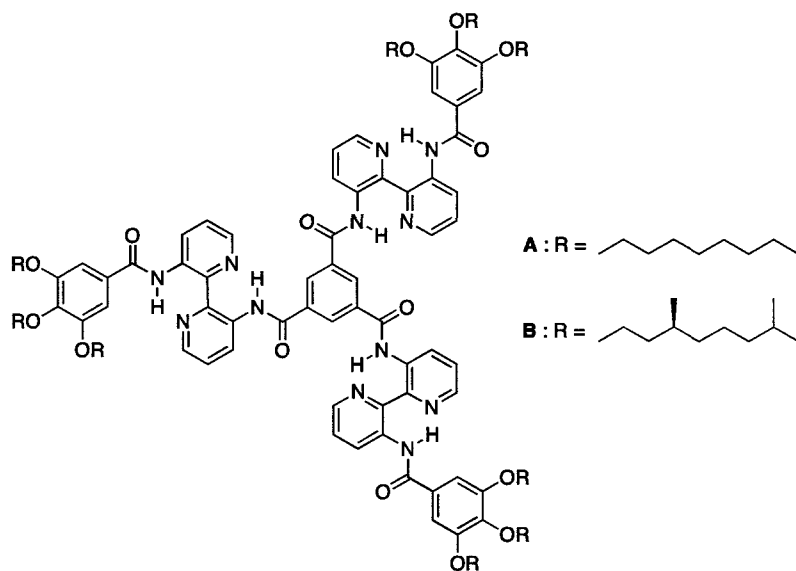


Figure 1.3: Extended core disc-shaped molecules, which organized themselves in a columnar phase.

Meijer and co-workers applied the ‘Sergeants and Soldiers’ principle to a number of self-assembling systems.¹⁶ For instance the extended core disc-shaped molecules **A** and **B** shown in Figure 1.3 organized themselves in a columnar phase with a 3.5 Å disc-disc distance within the columns.^{16a} The authors showed that the self-assembly of 100% of **A** result into equal amounts of the *P*- and *M*-helicities, which showed no optical activity. However addition of only 2.5% of chiral analogue **B** led to an extremely strong chiral amplification. By introducing the chiral components **B** (Sergeants) into the achiral stacks of **A** (Soldiers), the chiral components dictated the preferred helical sense of the entire stack. This was reflected by CEs associated with the π - π^* absorption band of the bipyridine moiety at $\lambda=387$ nm and $\lambda=369$ nm, which was similar in magnitude to that obtained for pure **B**.

1.4.3. Induced supramolecular chirality and ‘chiral memory’ concept

Chiral recognition is of great importance in living systems, which tend to have different pharmacological properties towards enantiomeric drugs.⁸ Similarly, extensive research has been done on host-guest systems,¹⁷ which are capable of opting for some molecules based on their chirality. In biological systems, often the host molecules are chiral and upon interaction with the chromophores possessing achiral guests, the host-guest complex will display an induced CD (ICD)¹⁸ since the host-guest now has a preferred handedness.

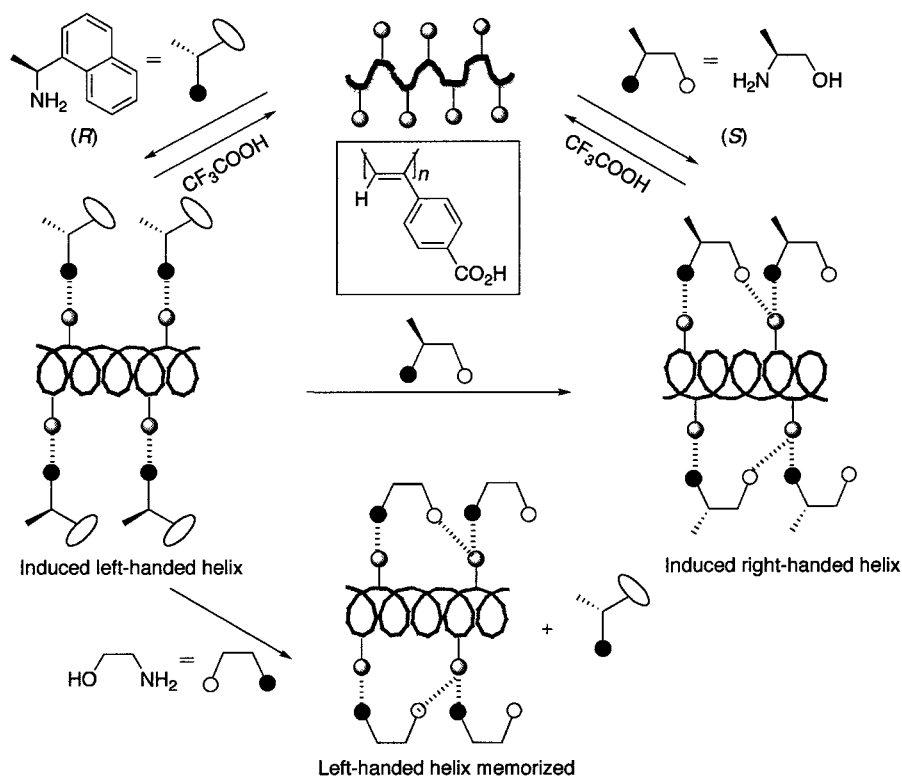


Figure 1.4: Helicity induced in achiral polymer poly((4-carboxyphenyl)acetylene) by chiral amines, was memorized after replacing the latter with an achiral amine.

Okamoto and co-workers showed how the optically inactive polymer poly((4-carboxyphenyl)acetylene) showed an ICD upon interaction with chiral amines.¹⁹ The achiral polymer gave rise to helical structures and the resulting supramolecular chirality was dictated by the molecular chirality of the chiral amines. The authors used this system as a probe to assign the chirality of the

amines based on the sign of the ICD. They went a step further when they later reported how this newly found helicity could be memorized when the chiral amine was replaced by an achiral amine as shown in Figure 1.4.

The strong CD signal due to the interaction of the polymer with the chiral amine, still persisted with almost the same intensity after being replaced with the achiral amine. This implied that not only handedness was memorized, but there was also no loss of macromolecular helicity.

The calixarene²⁰ skeleton has been used by various research groups for the demonstration of hydrogen-bonded assemblies and supramolecular chirality. Whitesides,²¹ Lehn,²² Reinhoudt²³ and others have studied the use of melamine moieties and barbituric or cyanuric acid derivatives for this purpose extensively. Reinhoudt and co-workers designed a strategy whereby they first employed chiral barbiturates (B) building blocks to induce supramolecular chirality in a hydrogen-bonded assembly, and then substituted them by achiral cyanurate units (A).^{23a} The resulting assembly (X) was chiral, though it did not have any chiral building blocks. Formation of such systems by use of only achiral units was not possible since their corresponding enantiomers for such molecules have the same energy, leading to a racemic mixture. The intensity of the CD signal did not increase when chiral assembly X was allowed to interact with B. In fact, the intensity of the CD signal was reduced to zero when a solution of X in benzene was heated in the presence of B, and the CD signal was not restored upon cooling.

Fenniri and co-workers observed an ICD signal for their dynamic system, which consisted of a self-assembling heterocyclic G \wedge C module with the donor-donor-acceptor face of guanine and the acceptor-acceptor-donor face of cytosine and an amino-benzo-18-crown-6-ether.²⁴ These heterocyclic building blocks spontaneously formed a hexameric rosette through the intermolecular hydrogen bonding, followed by stacking of these rosettes to produce a racemic mixture of *P*- and *M*- helical nanotubes via a dynamic self-assembly process. However,

upon addition of chiral amino acids such as L-alanine, only nanotubes of the *M*-helicity were formed, which was reflected by a characteristic ICD. The L-alanine was entrapped within the crown ether and created a chiral bias, which upon amplification resulted in the formation of one-handed nanotubes.

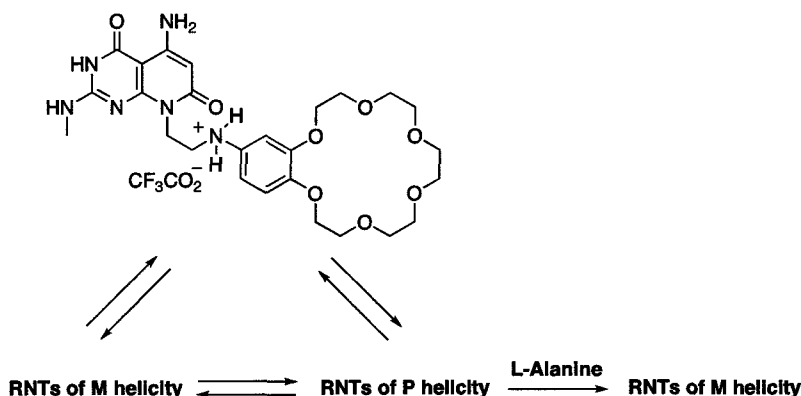


Figure 1.5: Racemic mixture of *P*- and *M*- helical nanotubes favoured the *M*-handedness upon addition of chiral L-alanine.

1.5. Supramolecular chirality in achiral systems

So far, all these supramolecularly chiral systems are either entirely or partly due to chiral building blocks. In other words, in absence of a chiral bias, only a racemic mixture will prevail, which is reflected by a CD silent spectrum. There have been cases of spontaneous symmetry breaking resulting in an excess of one of the enantiomers, however it is not possible to predict which enantiomer will form. These types of chiral symmetry breaking have been reported in crystallization²⁵ and liquid crystals.²⁶ Other cases whereby achiral systems have shown a preferred helical sense, have been due to the memorization of chirality, which was templated by some chiral components. However defying all these previous examples, Ribo and co-workers reported a system whose chirality could be selected upon interaction with a macroscopic chiral factor, namely, the vortex motion.²⁷ Their system consisted of homoassociates of diprotonated meso-sulfonatophenyl substituted porphyrins (Figure 1.6) formed in water, which existed as a liquid crystalline phase at higher concentrations and as ribbon-like aggregates at dilute concentrations. CD of these diluted solutions of these

aggregates showed CEs, which were not a result of LD. This was achieved by slow rotary evaporation (clockwise (CW) or counter-clockwise (CCW)) of very dilute solutions of the diprotonated porphyrins. The direction of the vortex motion dictated the chirality of the resulting aggregates. Since these samples did not racemize on standing, the authors concluded that this was a case of symmetry breaking.

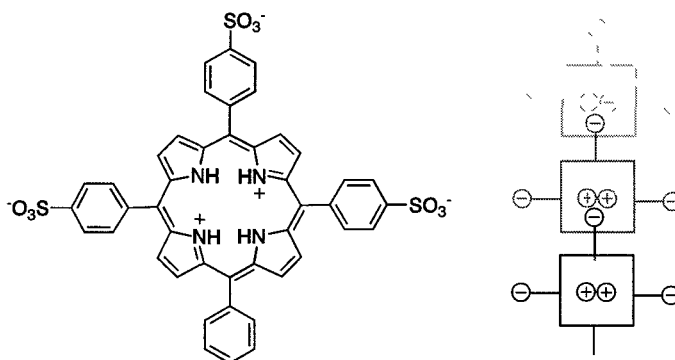


Figure 1.6: Diprotonated meso-sulfonatophenyl substituted porphyrins, which give rise to J-aggregates upon self-assembly in water at dilute concentration.

Along the same lines, Aida and co-workers reported a system that formed J-aggregates, which could temporarily align in a helical fashion in a vortex like mesogenic molecules in a liquid crystalline mesophase.²⁸ The achiral dendritic zinc porphyrin compound (Figure 1.7) formed nanofibres upon dissolution in benzene and as expected, CD measurement showed no optical activity. However stirring the sample during CD measurements gave rise to CD signals, whose spectral sign was dependent on the stirring direction.

The intensity of the CD signal was also governed by speed of the mechanical stirring of the solutions. Though a strong chiroptical activity was observed upon stirring, when stirring was stopped, the spectrum obtained, was CD-silent. Though the authors initially thought that the observed CD was due to helical twisting of the nanofibres in the vortex, they later found that it was due to macroscopic chiral alignment of the nanofibres. In fact, they showed that they

could create a similar effect by recording the CD from the overlapping of two oriented films.

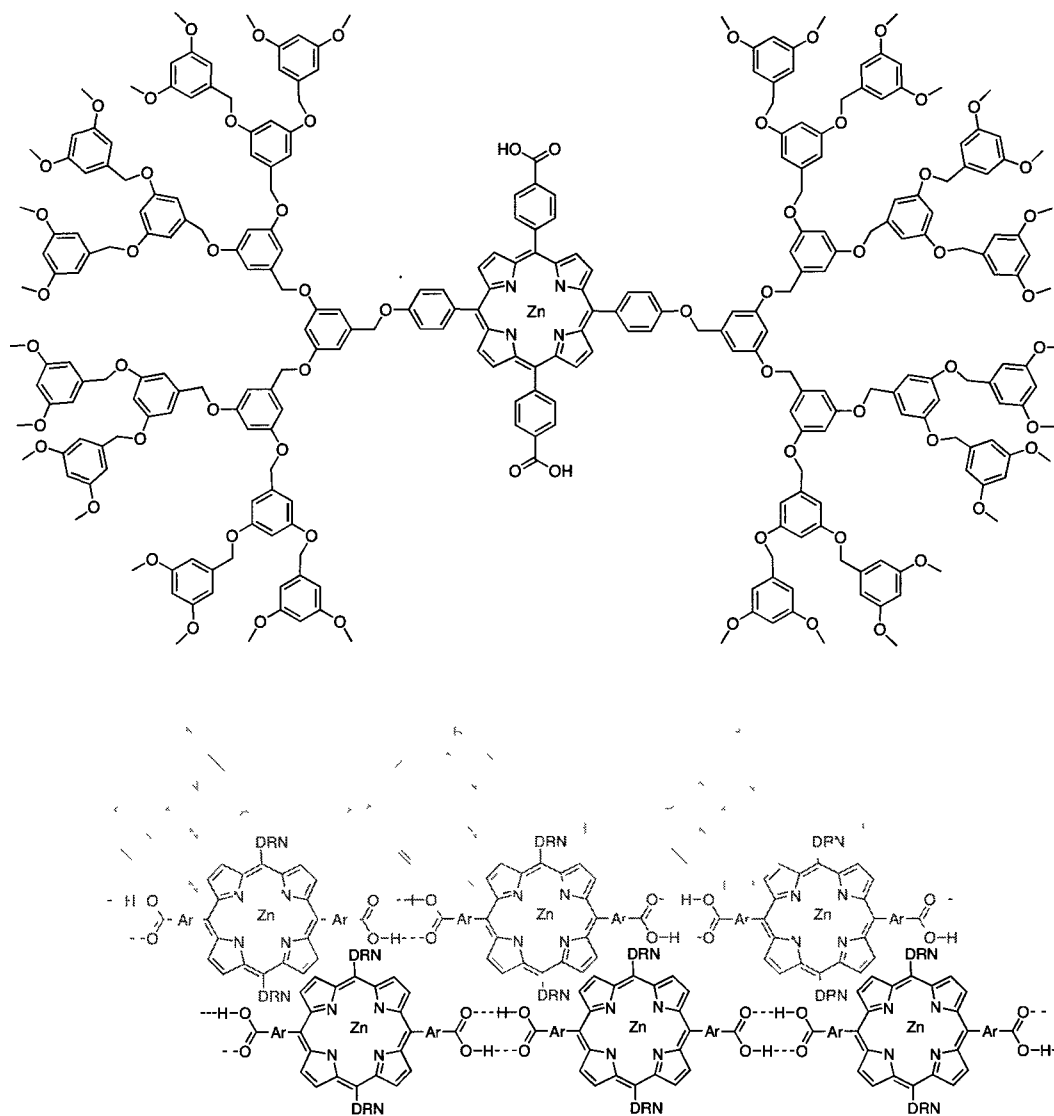


Figure 1.7: Dendritic zinc porphyrin (top) formed J-aggregates through π -stacking and hydrogen-bonded interactions (bottom).

Another system whereby an achiral derivative gave an unexpected CD signal in presence of a macroscopic effect, and not due to the molecular chirality, was the oligo(*p*-phenylene vinylene) molecule shown in Figure 1.8.²⁹ The oligo(*p*-phenylene vinylene) module formed bundles of long fibres in dodecane. A dilute, transparent and non-viscous solution of the molecule gave a monosignate CD response upon slow cooling from 363 K to 293 K at a rate of 60 K h⁻¹. The length

of the aggregates increased upon lowering of the temperature and at higher temperatures both CD and LD were absent, which suggested that fibres of a required length was needed to induce the LD and CD effects. The authors adopted the stirring experiments from Aida's laboratory (discussed previously), and on stirring, bisignate CD signals with sign inversion were obtained. Like Aida, Meijer too attributed the CD effects to the vortex flow created, which could also be reproduced using two aligned films. In this case, the CD effect was attributed to the convective flow resulting from the slow cooling of the solution. In addition, since a monosignate CD signal was obtained, the authors interpreted the CD effect as an artifact resulting from LD and linear birefringence (LB) and other possible optical imperfections of the CD instrument.³⁰

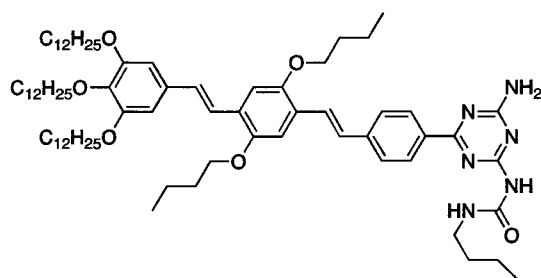


Figure 1.8: Structure of the oligo(*p*-phenylene vinylene) which can self-assemble in dodecane to produce fibres through dimerization and π -stacking.

1.6. Reversible supramolecular chirality switch

Manipulation of handedness is not an uncommon phenomenon. In fact, these studies have generated a lot of interest, in particular, in molecular electronics, where it is widely recognized that memory materials which can be reversibly written and read have powerful advantages over conventional magnetic materials.³¹ The fundamental requirement for a reversible switch is bistability³¹ - the existence of two forms of a molecule or system, which can be interconverted by external stimuli (Figure 1.9).

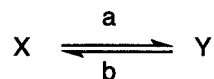


Figure 1.9: X and Y are two stable forms of a system. Under conditions a, X can be converted to Y and the latter can be reverted back to X under conditions b.

The following section deals with chirality inversions in supramolecular systems. Though such inversions can be triggered by a number of factors, only literature examples relevant to this thesis are presented.

1.6.1. Light

Photochromism³² is probably the most common form of chirality inversions. Controlling chemical processes by light has been utilized for years due to the ability of light to trigger a series of events, resulting in the amplification of a photochemical reaction. The most famous example is probably photography,³³ where free metallic silver is released when silver salts are exposed to light, giving rise to a stable form. As such, research towards the development of light-induced bistable molecules for various applications has attracted a lot of interest.

Firstly, a chiral molecular switch can be obtained from photobistable diastereomers of *P* and *M'* helicities, which can isomerize by irradiation of light of two different wavelengths. Feringa and co-workers have worked extensively on the generation of molecular switches based on the chemistry of sterically overcrowded alkenes.^{34, 31b, 31e} In 1999, the groups of Feringa and Harada came up with a helical alkene, which could undergo a repetitive, unidirectional rotation around the central carbon-carbon double bond to yield four discrete isomers.³⁵ These isomerizations were triggered by ultraviolet light or a temperature change of the system as illustrated in Figure 1.10. Irradiation of the (*P, P*)-trans isomer at $\lambda \geq 280$ nm and a temperature of -55 °C in hexane resulted in the formation of 95% of the less stable (*M, M*)-cis isomer. Similarly irradiation of the latter at $\lambda \geq 380$ nm gave the former predominantly. NMR and CD experiments were used to monitor this entire conversion, and the change in

helicity (from *P* to *M*) was detected by measuring the CD. The (*M, M*)-cis product was subsequently converted to the (*P, P*)-cis isomer irreversibly by raising the temperature to 20 °C. The resulting (*P, P*)-cis isomer was converted into (*M, M*)-trans isomer by irradiation of light of wavelength $\lambda \geq 380$ nm. The cycle of the unidirectional molecular rotor was finally completed when (*M, M*)-trans isomer was converted to the more favorable (*P, P*)-trans isomer by heating the solution to 60 °C.

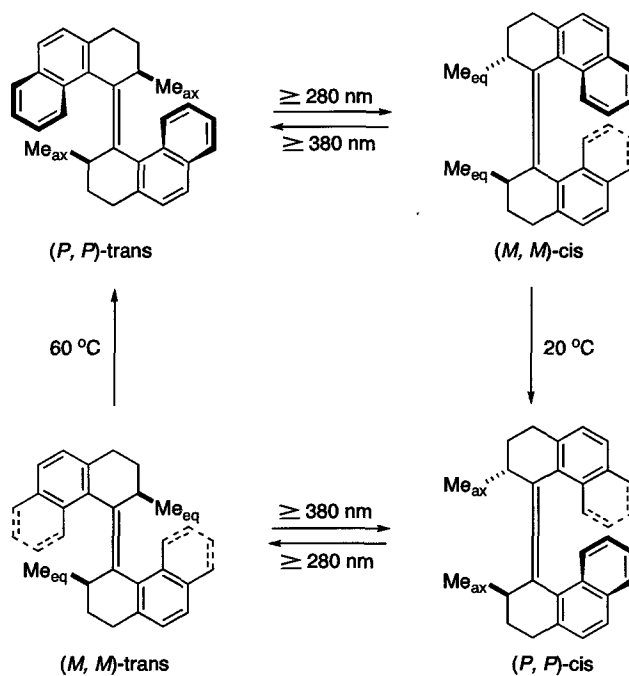


Figure 1.10: Photochemical and thermal isomerization processes of (*P, P*)-trans form of a sterically hindered olefin.

Secondly, bistable systems based on enantiomers can be achieved by irradiating a racemic mixture with circularly polarized light of one handedness at a single wavelength. The preferential absorption of either left- or right-circularly polarized light can lead to enantioselective switching in either direction. The enantiomeric excess at a photostationary state is given by:

$$ee_{\text{pss}} = g/2$$

where *g* is the anisotropy factor, which governs CPL based enantioselective switching.³⁶

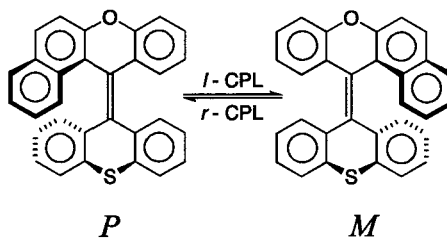


Figure 1.11: Photochemical interconversion of right-handed (*P*) and left-handed (*M*) helices upon irradiation with *l*- or *r*-CPL.

Huck *et al.* in 1996 reported the successful isomerization of the *P* into the *M* form of a sterically hindered alkene upon irradiation with *l*-CPL at 300 nm in hexanes.³⁷ Irradiation of a racemic mixture containing 50% of each handedness with *l*-CPL at 313 nm resulted into a CD signal comparable to the one obtained for a *M*-enriched sample. Consecutive irradiation of the samples with CPL was possible without loss in CD effects. The authors believed that this system could be applied as a potential data storage device. Not only was it possible to dictate the chirality of the system based on the handedness of CPL, it was also possible to erase the existing chirality by irradiating the sample with linearly polarized light (LPL). The authors also studied the photoisomerization of liquid crystals using the alkene shown in Figure 1.11 as a dopant. When 4'-(pentyloxy)-4-biphenylcarbonitrile and the racemic alkene were mixed, a stable nematic phase was formed. Irradiation of the nematic phase with *r*-CPL gave rise to cholesteric-textured structures.

Schuster and co-workers³⁸ used similar concepts as the above-mentioned example to generate a system that switched its helical sense upon irradiation with *l*- or *r*-CPL. The styryl-substituted, axially chiral bicyclo[3.2.1]octan-3-one derivative was attached as pendants to a polyisocyanate polymer. The resulting racemic polymer obtained was then irradiated with CPL, leading to the emergence of CD signals in the polymer backbone helix. The sign of the CD signal changed with a change in the handedness of the CPL.

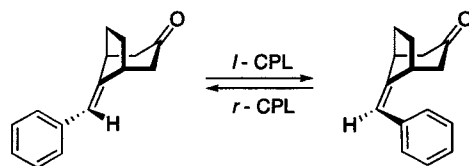


Figure 1.12: Styryl-substituted, axially chiral bicyclo[3.2.1]octan-3-one compound, which switched its chirality based on the sign of CPL.

1.6.2. Solvent

There are a number of literature examples for solvent-induced chirality inversions and most of these reports involved however deal with host-guests complexes, polymers or liquid crystals.³⁹⁻⁴¹ Novel research done within the Fenniri group led to the emergence of a system, which exhibited solvent-induced supramolecular inversion. The guanine-cytosine motif depicted in Figure 1.13 self-assembled in both water and methanol to give rise to RNTs of high aspect ratio as a result of stacking of the hexameric rosettes. Based on the solvent used for the self-assembly process, thermodynamically stable RNTs of opposite helices were obtained. Johnson *et al.* introduced a new term (*chiomer*), which was used to describe two conformational states that a molecule can adopt when it forms supramolecular structures.⁴² “A *chiomer* is a conformational supramolecular isomer that arises when the molecules of a supramolecular structure express multiple, thermodynamically stable, supramolecular chirality states under a given set of physical conditions.” It was found that mirror image CD signals were obtained for the water and methanol samples, implying that the RNTs adopted different helices in either solvent. The free energy pathways were found through molecular modeling and it was revealed that the water-chiomer was thermodynamically more favourable in both solvents, but due an initial energy barrier in methanol, in the latter solvent, formation of the water-chiomer was disfavored. It was, however, possible to switch the helicity of the left-handed RNTs in methanol by either heating the sample or adding catalytic amount of the right-handed RNTs formed in water.

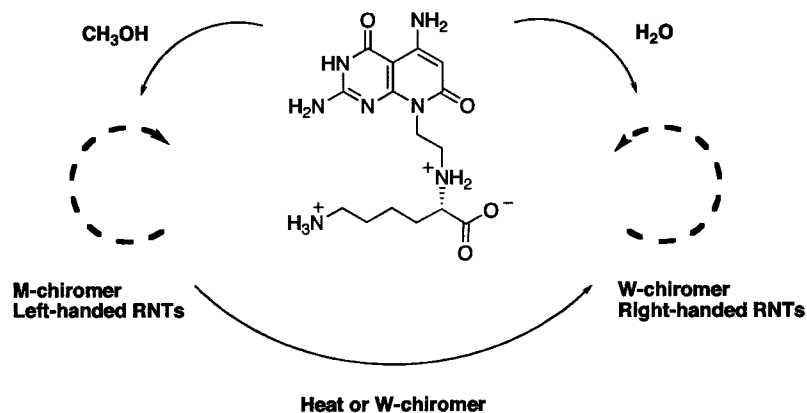


Figure 1.13: Self-assembling guanine-cytosine motif, which formed RNTs of opposite helices in water and methanol.

In 2009, Sakajiri and co-workers reported a solvent-induced chirality inversion for a C_6 -symmetric disk-like molecule.⁴³ The hexakis(phenylethynyl)benzene derivative bearing chiral alanine fragments formed a stable helical columnar assembly, fueled by various noncovalent interactions in hexanes. The resulting helix was formed from stacking of a nearly planar hexakis(phenylethynyl)benzene core. The authors predicted a disruption of this helical columnar assembly upon the addition of the polar solvent $CHCl_3$. However, it was experimentally observed that upon addition of 8-15 vol% of $CHCl_3$, an opposite handed helix was obtained. Addition of more $CHCl_3$ eventually led to the disruption of the supramolecular chirality as the monomers became molecularly dispersed. In $CHCl_3$, the hexakis(phenylethynyl)benzene core adopted a propeller-like conformation. It is interesting to note that the CD signals obtained had opposite signals, however the assemblies existing in the different solvent compositions were not even close to be mirror-image structures. In addition to CD, UV-vis, fluorescence measurements and molecular modeling were used to predict the type of structures present in the binary mixtures.

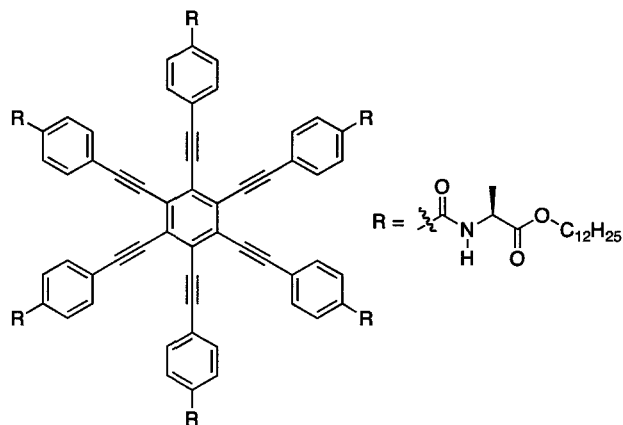


Figure 1.14: The hexakis(phenylethynyl)benzene derivative bearing chiral alanine fragments which can stack to form helices.

1.6.3. Temperature

The phenomenon of temperature-induced helix inversion has attracted a lot of attention since its discovery⁴⁴. Though most of the literature precedents dealt with liquid crystalline phases, a few cases involving isotropic liquids of supramolecular assemblies have also been reported. There have been some interesting reports of irreversible temperature-induced supramolecular chirality inversion⁴⁵, however reversible inversions remain more attractive.

In 2000, Fujiki reported a helical polymer comprising of flexible rodlike silicon main chain and enantiopure alkyl side chains, which exhibited thermally-driven helicity inversion -20 °C in isoctane.⁴⁶

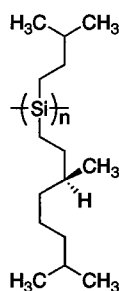


Figure 1.15: Optically active helical polymer poly{(S)-3,7-dimethyloctyl-3-methylbutylsilylene}, which exhibited thermal chiroptical inversion.

The polymer formed rodlike structures and had semiconducting properties. When it was subjected to CD measurements, a positive-signed CD spectrum with a Cotton effect at 320 nm was observed at a temperature of -40 °C in isoctane, which was due to the $\sigma\text{-}\sigma^*$ transition from silicon. Similarly another CD experiment at -5 °C in isoctane, revealed a negative-signed CD spectrum, which had an extremum of 322 nm. This observation pointed to the existence of helical structures, which were both energetically and spectroscopically inequivalent. Though the authors did not fully understand the origin of the helicity change, they predicted that this could be due to a shortening of Si-Si bond length due to decrease in temperature because there were no significant changes in the CD and UV absorption intensities.

In 2004, Masuda and co-workers reported the design of helical poly(*N*-propargylamides) that underwent a helical switch with thermal stimuli.⁴⁷ The poly(**1**) from Figure 1.16 had a positive monosignate CD signal with a pronounced CE at ca. 390 nm while the poly(**2**) had a similar but negative monosignate CD signal. Both homopolymers **1** and **2** showed only a slight decrease in the intensity of their respective CD signals when they were subjected to a variable temperature (VT) CD measurements from 0-55 °C. This prompted the authors to conclude that these two polymers, which had opposite helical sense to each other, were thermally stable and did not show any thermal helix inversion.

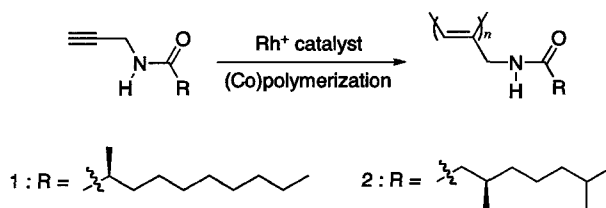


Figure 1.16: Helical homopolymer or copolymer of propargylamides formed from polymerization of **1** and **2**.

The authors then proceeded to conduct copolymerization of **1** and **2** at various compositions. They found that copolymer of 68/32% of **1/2** transformed from one

helical structure to another without going through a random coil conformation. The copolymer 68/32 was subjected to a VT-CD experiment from 0-55 °C and it was found that the copolymer adopted the helical sense similar to poly(1) at lower temperatures and that of poly(2) at temperatures higher than the compensation temperature.

1.7. Conclusion

Chirality is directly related to many aspects of life and it certainly remains one of the main interests in science. Therefore, research to rationalize the many puzzles involved in chirality and supramolecular chemistry remains a very important task. Great progress has been made in development of different kinds of artificial supramolecular chiral systems and on the way new and improved detection techniques have emerged. The extrapolation of some of these findings has allowed scientists to get insights on how nature functions, however, there still remains a lot to be done. With increased understanding of supramolecular chemistry, nanotechnology and the physical properties surrounding them, future systems will emerge and allow us to understand and hopefully mimic the various complex systems found in nature to a greater extent.

1.8. References

1. (a) Whyte, L. L. *Nature* **1958**, *182*, 198. (b) Cahn, R. S.; Ingold, C.; Prelog, V. *Angew. Chem. Int. Ed.* **1966**, *5*, 385-415.
2. Amabilino, D. B. *Chirality at the Nanoscale*, Wiley-VCH, Weinheim, **2009**.
3. Fischer, E. *Ber. Deutch Chem.* **1894**, *27*, 2984-2993.
4. Lehn, J. M. *Angew. Chem. Int. Ed.* **1990**, *29*, 1304-1319.
5. (a) Pauling, L.; Corey, R. B.; Branson, H. R. *Proc. Nat. Acad. Sci.* **1951**, *37*, 205-211. (b) Bragg, W. L.; Kendrew, J. C.; Perutz, M. F. *Proc. Roy. Soc. A* **1950**, *203*, 321-357. (c) Wilkins, M. H. F.; Gosling, R. G.; Seeds, W. E. *Nature* **1951**, *167*, 759-760. (d) Franklin, R. E.; Gosling, R. G. *Acta Cryst.* **1953**, *6*, 673-677. (e) Cochran, W.; Crick, F. H. C.; Vand, V. *Acta Cryst.* **1952**, *5*, 581-586. (f) Wilkins, M. H. F.; Randall, J. T. *Biochim. Biophys. Acta* **1953**, *10*, 192-193. (g) Watson, J. D.; Crick, F. H. C. *Nature* **1953**, *171*, 737-738. (h) Crick, F. H. C.; Watson, J. D. *Proc. Roy. Soc. A* **1954**, *223*, 80-96. (i) Wilkins, M. H. F.; Stokes, A. R.; Wilson, H. R. *Nature* **1953**, *171*, 738-740. (j) Franklin, R. E.; Gosling, R. G. *Nature* **1953**, *171*, 740-741. (k) Watson, J. D.; Crick, F. H. C. *Nature* **1953**, *171*, 737-738.
6. Fasman, G. D. *Circular dichroism and the conformational analysis of biomolecules*, Plenum Press, New York, **1996**.
7. Lehn, J-M. *Supramolecular chemistry*, VCH, New York, **1995**.
8. Lough, W. J.; Wainer, I. W. *Chirality in Natural and Applied Science*, CRC Press, Oxford, **2002**.
9. (a) Crego-Calama, M.; Reinhoudt, D. N. *Supramolecular Chirality, Top. Curr. Chem.*, **2006**. (b) Vazquez-Campos, S.; Crego-Calama, M.; Reinhoudt, D. N. *Supramolecular Chemistry* **2007**, *19*, 95-106.
10. Lee, C. C.; Grenier, C.; Meijer, E. W.; Schenning, A. P. H. J. *Chem. Soc. Rev.* **2009**, *38*, 671-683.
11. (a) Nakanishi, K.; Berova, N.; Woody, R. W. *Circular dichroism – Principles and applications*, Wiley-VCH, New York, **1994**. (b) Berova, N.; Di Bari, L.; Pescitelli, G. *Chem. Soc. Rev.* **2007**, *36*, 914-931.

12. (a) Rodger, A.; Norden, B. *Circular dichroism & linear dichroism*, Oxford University Press, **1997**. (b) Ohira, A.; Okoshi, K.; Fujiki, M.; Kunitake, M.; Naito, M.; Hagihara, T. *Adv. Mater.* **2004**, *16*, 1645-1650.
13. Engelkamp, H.; Middelbeek, S.; Nolte, R. J. M. *Science* **1999**, *284*, 785-788.
14. (a) Schenning, A. P. H. J.; Jonkheijm, P.; Peeters, E.; Meijer, E. W. *J. Am. Chem. Soc.* **2001**, *123*, 409-416. (b) Jeukens, C. R. L. P. N.; Jonkheijm, P.; Wijnen, F. J. P.; Gielen, J. C.; Christianen, P. C. M.; Schenning, A. P. H. J.; Meijer, E. W.; Maan, J. C. *J. Am. Chem. Soc.* **2005**, *127*, 8280-8281.
15. (a) Green, M. M.; Peterson, N. C.; Sato, T.; Teramoto, A.; Cook, R.; Lifson, S. *Science* **1995**, *268*, 1860-1866. (b) Green, M. M.; Rediy, M. P.; Johnson, R. J.; Darling, G.; O'leary, D. J.; Willson, G. *J. Am. Chem. Soc.* **1989**, *111*, 6452-6454.
16. (a) Palmans, A. R. A.; Vekemans, J. A. J. M.; Havinga, E. E.; Meijer, E. W. *Angew. Chem. Int. Ed. Engl.* **1997**, *36*, 2648-2651. (b) Brunsveld, L.; Meijer, E. W.; Prince, R. B.; Moore, J. S. *J. Am. Chem. Soc.* **2001**, *123*, 7978-7984. (c) Prince, R. B.; Moore, J. S.; Brunsveld, L.; Meijer, E. W.; *Chem. Eur. J.* **2001**, *7*, 4150-4154. (d) Brunsveld, L.; Lohmeijer, B. G. G.; Vekemans, J. A. J. M.; Meijer, E. W. *Chem Commun.* **2000**, 2305-2306. (e) Brunsveld, L.; Vekemans, J. A. J. M.; Hirschberg, J. H. K. K.; Sijbesma, R. P.; Meijer, E. W. *Proc. Natl. Acad. Sci.* **2002**, *99*, 4977-4982. (f) Schenning, A. P. H. J.; Kilbinger, A. F. M.; Biscarini, F.; Cavallini, M.; Cooper, H. J.; Derrick, P. J.; Feast, W. J.; Lazzaroni, R.; Leclere, Ph.; McDonell, L. A.; Meijer, E. W.; Meskers, S. C. J. *J. Am. Chem. Soc.* **2002**, *124*, 1269-1275. (g) El-ghayoury, A.; Schenning, A. P. H. J.; van Hal, P. A.; van Duren, J. K. J.; Janssen, R. A. J.; Meijer, E. W. *Angew. Chem. Int. Ed.* **2001**, *40*, 3660-3663. (h) Brunsveld, L.; Schenning, A. P. H. J.; Broeren, M. A. C.; Janssen, H. M.; Vekemans, J. A. J. M.; Meijer, E. W. *Chem. Lett.* **2000**, 292-293.
17. Cram, D. J. *Angew. Chem., Int. Ed.* **1988**, *27*, 1009-1020. (b) Lehn, J.-M. *Angew. Chem., Int. Ed.* **1988**, *27*, 89-112. (c) Schneider, H.-J.; Dürr, H.; Lehn, J.-M., Eds. *Frontiers in Supramolecular Organic Chemistry and Photochemistry*; VCH: Weinheim, **1988**. (d) Pirkle, W.; Pochapsky, T. C.

- Chem. Rev.* **1989**, *89*, 347-362. (e) Rebek, J. Jr. *Angew. Chem., Int. Ed. Engl.* **1990**, *29*, 245-255. (f) Seel, C.; Vögtle, F. *Angew. Chem., Int. Ed.* **1992**, *31*, 528-549. (g) Webb, T. H.; Wilcox, C. S. *Chem. Soc. Rev.* **1993**, 383-395. (h) Böhmer, V. *Angew. Chem. Int. Ed.* **1995**, *34*, 713-745. (i) Kirby, A. J. *Angew. Chem., Int. Ed.* **1996**, *35*, 706-724. (j) Bender, M. L.; Komiyama, M. *Cyclodextrin Chemistry*; Springer-Verlag: New York, **1977**. (k) Breslow, R. *Acc. Chem. Res.* **1980**, *13*, 170-177. (l) Tabushi, I. *Acc. Chem. Res.* **1982**, *15*, 66-72. (m) Li, S.; Purdy, W. C. *Chem. Rev.* **1992**, *92*, 1457-1470. (n) Wenz, G. *Angew. Chem., Int. Ed.* **1994**, *33*, 803-822. (o) Rekharsky, M. V.; Goldberg, R. N.; Schwarz, F. P.; Tewari, Y. B.; Ross, P. D.; Yamashoji, Y.; Inoue, Y. *J. Am. Chem. Soc.* **1995**, *117*, 8830-8840. (p) Diederich, F. *Angew. Chem., Int. Ed.* **1988**, *27*, 362-386.
18. (a) Harada, N.; Nakanishi, K. *Circular Dichroic Spectroscopy Exciton Coupling in Organic Stereochemistry*; University Science Book: Mill Valley, CA, **1983**. (b) Nakanishi, K.; Berova, N. In *Circular Dichroism Principles and Applications*; Nakanishi, K., Berova, N., Woody, R. W., Eds.; VCH: New York, **1994**. (c) Wiesler, W. T.; Nakanishi, K. *J. Am. Chem. Soc.* **1990**, *112*, 5574-5583. (d) Harada, N.; Saito, A.; Ono, H.; Gawronski, J.; Gawronska, K.; Sugioka, T.; Uda, H.; Kuriki, T. *J. Am. Chem. Soc.* **1991**, *113*, 3842-3850. (e) Berova, N.; Gargiulo, D.; Nakanishi, K.; Harada, N. *J. Am. Chem. Soc.* **1993**, *115*, 4769-4775. (f) Gargiulo, D.; Cai, G.; Ikemoto, N.; Bozhkova, N.; Odingo, J.; Berova, N.; Nakanishi, K. *Angew. Chem., Int. Ed.* **1993**, *32*, 888-891. (g) Gargiulo, D.; Ikemoto, N.; Odingo, J.; Bozhkova, N.; Iwashita, T.; Berova, N.; Nakanishi, K. *J. Am. Chem. Soc.* **1994**, *116*, 3760-3767. (h) Matile, S.; Berova, N.; Nakanishi, K.; Novkova, S.; Philipova, I.; Blagoev, B. *J. Am. Chem. Soc.* **1995**, *117*, 7021-7022. (i) Matile, S.; Berova, N.; Nakanishi, K.; Fleischhauer, J.; Woody, R. W. *J. Am. Chem. Soc.* **1996**, *118*, 5198-5206. (j) Rele, D.; Zhao, N.; Nakanishi, K.; Berova, N. *Tetrahedron* **1996**, *52*, 2759-2776.

19. (a) Yashima, E.; Matsushima, T.; Okamoto, Y.; *J. Am. Chem. Soc.* **1997**, *119*, 6345-6359. (B) Yashima, E.; Maeda, K.; Okamoto, Y. *Science* **1999**, *399*, 449-451.
20. (a) Gutsche, C. D. *Calixarenes*; Royal Society of Chemistry: Cambridge, UK, **1989**. (b) Gutsche, C. D.; Iqbal, M.; Nam, K. S.; See, K.; Alam, I. *Pure Appl. Chem.* **1989**, *60*, 483-488. (c) Diamond, D.; McKervey, M. A. *Chem. Soc. Rev.* **1996**, 15-24. (d) Takeshita, M.; Shinkai, S. *Bull. Chem. Soc. Jpn.* **1995**, *68*, 1088-1097.
21. (a) Whitesides, G. M.; Simanek, E. E.; Mathias, J. P.; Seto, C. T.; Chin, D. N.; Mammen, M.; Gordon, D. M. *Acc. Chem. Res.* **1995**, *28*, 37-44. (b) Seto, C. T.; Whitesides, G. M., *J. Am. Chem. Soc.* **1990**, *112*, 6409-6411. (c) Zerkowski, J. A.; Seto, C. T.; Wierda, D. A.; Whitesides, G. M. *J. Am. Chem. Soc.* **1990**, *112*, 9025-9026. (d) Seto, C. T.; Whitesides, G. M. *J. Am. Chem. Soc.* **1991**, *113*, 712-713. (e) Whitesides, G. M.; Mathias, J. P.; Seto, C. T. *Science* **1991**, *254*, 1312-1319. (f) Seto, C. T.; Whitesides, G. M. *J. Am. Chem. Soc.* **1993**, *115*, 1330-1340. (g) Seto, C. T., Mathias, J. P.; Whitesides, G. M. *J. Am. Chem. Soc.* **1993**, *115*, 1321-1329. (h) Mathias, J. P.; Simanek, E. E.; Seto, C. T.; Whitesides, G. M. *Angew. Chem. Int. Ed.* **1993**, *32*, 1766-1769. (i) Zerkowski, J. A.; Seto, C. T.; Wierda, D. A.; Whitesides, G. M.; *J. Am. Chem. Soc.* **1994**, *116*, 2382-2391. (j) Zerkowski, J. A., Mathias, J. P. and Whitesides, G. M., *J. Am. Chem. Soc.* **1994**, *116*, 4305-4315. (k) Mathias, J. P.; Seto, C. T.; Simanek, E. E.; Whitesides, G. M. *J. Am. Chem. Soc.* **1994**, *116*, 1725-1736.
22. Lehn, J. M. *Angew. Chem. Int. Ed.* **1988**, *27*, 89-112.
23. (a) Prins, L. J.; De Jong, F.; Timmerman, P.; Reinhoudt, D. N. *Nature* **2000**, *408*, 181-184. (b) Prins, L. J.; Jolliffe, K. A.; Hulst, R.; Timmerman, P.; Reinhoudt, D. N. *J. Am. Chem. Soc.* **2000**, *122*, 3617-3627. (c) Prins, L. J.; Huskens, J.; De Jong, F.; Timmerman, P.; Reinhoudt, D. N. *Nature* **1999**, *398*, 498-502. (d) Prins, L. J.; Timmerman, P.; Reinhoudt, D. N. *J. Am. Chem. Soc.* **2001**, *123*, 10153-10163. (e) Vreekamp, R. H.; Van Duynhoven, J. P. M.; Hubert, M.; Verboom, W.; Reinhoudt, D. N. *Angew. Chem. Int. Ed.* **1996**, *35*,

- 1215-1218. (f) Timmerman, P.; Vreekamp, R. H.; Hulst, R.; Verboom, W.; Reinhoudt, D. N.; Rissanen, K.; Udachin, K. A.; Ripmeester, J. *Chem. Eur. J.* **1997**, *3*, 1823-1832. (g) Crego Calama, M.; Fokkens, R.; Nibbering, N. M. M.; Timmerman, P.; Reinhoudt, D. N. *Chem. Commun.* **1998**, 1021-1022.
24. (a) Fenniri, H.; Deng, B. L.; Ribbe, A. E.; Hallenga, K.; Jacob, J.; Thiagarajan, P. *Proc. Natl. Acad. Sci.* **2002**, *99*, 6487-6492. (b) Fenniri, H.; Mathivanan, P.; Vidale, K. L.; Sherman, D. M.; Hallenga, K.; Wood, K. V.; Stowell, J. G. *J. Am. Chem. Soc.* **2001**, *123*, 3854-3855. (c) Fenniri, H.; Deng, B. L.; Ribbe, A. E. *J. Am. Chem. Soc.* **2002**, *124*, 11064-11072.
25. (a) Jacques, J.; Collet, A.; Wilen, S. H. *Enantiomers, Racemates, Resolutions* Wiley, New York, **1981**. (b) Kondepudi, D. K.; Kaufman, R. J.; Singh, N.; *Science* **1990**, *250*, 975-976. (c) Kondepudi, D. K.; Bullock, K. L.; Digits, J. A.; Hall, J. K.; Miller, J. M. *J. Am. Chem. Soc.* **1993**, *115*, 10211-10216. (d) Kondepudi, D. K.; Laudadio, J.; Asakura, K. *J. Am. Chem. Soc.* **1999**, *121*, 1448-1451.
26. (a) Schwartz, D. K.; Viswanathan, R.; Zasadzinski, J. A. N.; *Phys. Rev. Lett.* **1993**, *70*, 1267-1270. (b) Vanakaras, A. G.; Photinos, D. J. *J. Phys. Rev. E* **1998**, *57*, R4875-R4878. (c) Hough, L. E.; Jung, H. T.; Krueerke, D.; Heberling, M. S.; Nakata, M.; Jones, C. D.; Chen, D.; Link, D. R.; Zasadzinski, J.; Heppke, G.; Rabe, J. P.; Stocker, W.; Koerblova, E.; Walba, D. M.; Glaser, M. A.; Clark, N. A. *Science*, **2009**, *325*, 456-460.
27. Ribo, J.M.; Crusats, J.; Sagues, F.; Claret, J.; Rubires, R. *Science*, **2001**, *292*, 2063-2066.
28. Tsuda, A.; Alam M.A.; Harada, T.; Yamaguchi, T.; Ishii, N.; Aida, A. *Angew. Chem. Int. Ed.* **2007**, *46*, 8198-8202.
29. Wolffs, M.; George, S.J.; Tomovic, Z.; Meskers, S.C.J.; Shenning, A.; Meijer E.W. *Angew. Chem. Int. Ed.* **2007**, *46*, 8203-8205.
30. (a) Saeva, F. D.; Sharpe, P. E.; Olin, G. R.; *J. Am. Chem. Soc.* **1973**, *95*, 7656-7659. (b) Nordén, B. *J. Phys. Chem.* **1978**, *82*, 744-746. (c) Shindo, Y.; Nishio, M.; Maeda, S.; *Biopolymers* **1990**, *30*, 405-413. (d) Kuroda, R.; Harada, T.; Shindo, Y. *Rev. Sci. Instrum.* **2001**, *72*, 3802-3810. (e) Shindo,

- Y.; Ohmi, Y. *J. Am. Chem. Soc.* **1985**, *107*, 91-97. (f) Livolant, F.; Maestre, M. F.; *Biochemistry* **1988**, *27*, 3056.
31. (a) Ball, P.; Garwin, L. *Nature* **1992**, *355*, 761-766. (b) Feringa, B. L.; Jager, W. F.; de Lange, B. *Tetrahedron* **1993**, *49*, 8267-8310. (c) Kawai, S.; Gillat, L.; Lehn, J-M. *J. Chem. Soc. Chem. Commun.* **1994**, *8*, 1011-1013. (d) Emmelius, M.; Pawlowski, G.; Vollmann, H. W. *Angew. Chem. Int. Ed.* **1989**, *28*, 1445-1471. (e) Feringa, B. L.; van Delden, R. A.; Koumura, N.; Geertsema, E. M. *Chem. Rev.* **2000**, *100*, 1789-1816. (f) Feringa, B. L.; Huck, N. P. M.; Schoevaars, A. M.; *Adv. Mater.* **1996**, *8*, 681-684.
32. (a) Dürr, H., Bouas, H., Laurent, H. *Photochromism, Molecules and Systems in Studies in Organic Chemistry 40*. Elsevier, Amsterdam, **1990**. (b) El'tsov, A. V. *Organic Photochromes* Plenum Press, New York, **1990**. (c) Brown, G. H. *Photochromism in Techniques of Chemistry* Wiley-Interscience, New York, **1971**, 3. (d) Wasielewski, M. R. *Chem. Rev.* **1992**, *92*, 435-461. (e) Gostzola, D.; Niemczyk, M. P.; Wasielewski, M. R. *J. Am. Chem. Soc.* **1998**, *120*, 5118-5119. (f) Debreczeny, M. P.; Svec, W. A.; Wasielewski, M. R. *Science* **1996**, *274*, 584-587.
33. Rogers, D. *The Chemistry of Photography 2007*, The Royal Society of Chemistry, Cambridge, 1-232.
34. (a) Wynberg, H. *Acc. Chem. Res.* **1971**, *4*, 65-73. (b) Sandstrom, J. In *Topics in Stereochemistry* Wiley, New York, **1983**, *14*. (c) Feringa, B. L.; Wynberg, H. *J. Am. Chem. Soc.* **1977**, *99*, 602-603. (d) Laarhoven, W. H.; Prinsen, W. J. C. *Top. Curr. Chem.* **1984**, *125*, 63. (e) Martin, H. *Angew. Chem., Int. Ed.* **1974**, *13*, 649-660.
35. Koumura, N.; Zijlstra, R. W.; van Delden, R. A.; Harada, N.; Feringa, B. L.; *Nature* **1999**, *401*, 152-155.
36. Salvadori, P.; Bertucci, C.; Rosini, C. *Chirality* **1991**, *3*, 376-385.
37. Huck, N. P. M.; Jager, W. F.; de Lange, B.; Feringa, B. L.; *Science* **1996**, *273*, 1686-1688.
38. (a) Li, J.; Schuster, G. B.; Cheon, K-S.; Green, M. M.; Selinger, J. V. *J. Am. Chem. Soc.* **2000**, *122*, 2603-2612. (b) Suarez, M.; Schuster G.B. *J. Am.*

- Chem. Soc.* **1995**, *117*, 6732-6738. (c) Janicki, S. Z.; Schuster, G. B. *J. Am. Chem. Soc.* **1995**, *117*, 8524-8527. (d) Burnham, K. S.; Schuster G.B. *J. Am. Chem. Soc.* **1999**, *121*, 10245-10246.
39. a) Satrijo, A.; Meskers, S. C. J.; Swager, T. M. *J. Am. Chem. Soc.* **2006**, *128*, 9030-9031. (b) Goto, H.; Okamoto, Y.; Yashima, E. *Macromolecules* **2002**, *35*, 4590-4601. (c) Langeveld-Voss, B. M. W.; Christiaans, M. P. T.; Janssen, R. A. J.; Meijer, E. W. *Macromolecules* **1998**, *31*, 6702-6704. (d) Price, C. C.; Osgan, M. *J. Am. Chem. Soc.* **1956**, *78*, 4789-4790. (e) Furukawa, J. In *Optically Active Polymers*; Séléigny, E., Ed.; D. Reidel Publishing Co., Dordrecht, The Netherlands, **1979**, 317-330. (f) Pu, L. *Acta Polym.* **1997**, *8*, 116-141. (g) Bouman, M. M.; Meijer, E. W. *Adv. Mater.* **1995**, *7*, 385-387. (h) Bidan, G.; Guillerez, S.; Sorokin, V. *Adv. Mater.* **1996**, *8*, 157-160. (i) Kajitani, T.; Okoshi, K.; Sakurai, S.; Kumaki, J.; Yashima, E. *J. Am. Chem. Soc.* **2006**, *128*, 708-709. (j) Sakurai, S.; Okoshi, K.; Kumaki, J.; Yashima, E. *J. Am. Chem. Soc.* **2006**, *128*, 5650-5651. (k) Lam, J. W. Y.; Tang, B. Z. *Acc. Chem. Res.* **2005**, *38*, 745-754. (l) Fujiki, M.; Koe, J. R.; Motonaga, M.; Nakashima, H.; Terao, K.; Teramoto, A. *J. Am. Chem. Soc.* **2001**, *123*, 6253-6261. (m) Nakako, H.; Nomura, R.; Masuda, T. *Macromolecules* **2001**, *34*, 1496-1502. (n) Cheuk, K. K. L.; Lam, J. W. Y.; Chen, J.; Lai, L. M.; Tang, B. Z. *Macromolecules* **2003**, *36*, 9752-9762. (o) Maeda, K.; Mochizuki, H.; Watanabe, M.; Yashima, E. *J. Am. Chem. Soc.* **2006**, *128*, 7639-7650. (p) Okoshi, K.; Sakurai, S.; Ohsawa, S.; Kuwaki, J.; Yashima, E. *Angew. Chem. Int. Ed.* **2006**, *45*, 1-5. (q) Nakashima, H.; Fujiki, M.; Koe, J. R.; Motonaga, M. *J. Am. Chem. Soc.* **2001**, *123*, 1963-1969.
40. (a) Pohl, F. M.; Jovin, T. M. *J. Mol. Biol.* **1972**, *67*, 375-396. (b) Cosstick, R.; Eckstein, F. *Biochemistry* **1985**, *24*, 3630-3638. (c) Okamoto, Y.; Nakano, T.; Ono, E.; Hatada, K. *Chem. Lett.* **1991**, 525-528. (d) Steinberg, I. Z.; Harrington, W. F.; Berger, A.; Sela, M.; Katchalski, E. *J. Am. Chem. Soc.* **1960**, *82*, 5263-5279. (e) Blout, E. R.; Carver, J. P.; Gross, J. *J. Am. Chem. Soc.* **1963**, *85*, 644-646. (f) Gratzer, W. B.; Rhodes, W.; Fasman, G. D. *Biopolymers* **1963**, *1*, 319-330. (g) Letsinger, R. L. *Proc. Robert A. Welch*

- Found. Conf. Chem. Res.* **1985**, *29*, 459. (h) McIntosh, L. P.; Zielinski, W. S.; Kalish, B. W.; Pfeifer, G. P.; Sprinzl, M.; van de Sande, J. H.; Jovin, T. M. *Biochemistry* **1985**, *24*, 4806-4814. (i) Pu, Y.-M.; McDonagh, A. F.; Lightner, D. A. *J. Am. Chem. Soc.* **1993**, *115*, 377-380.
41. Celebre, G.; De Luca, G.; Maiorino, M.; Iemma, F.; Ferrarini, A.; Pieraccini, S.; Spada, G. P. *J. Am. Chem. Soc.* **2005**, *127*, 11736-11744. (b) Slaney, A. J.; Nishiyama, I.; Styring, P.; Goodby, J. W. *J. Mater. Chem.* **1992**, *2*, 805-810. (c) Loubser, C.; Wessels, P. L.; Styring, P.; Goodby, J. W. *J. Mater. Chem.* **1994**, *4*, 71-79. (d) Radley, K.; McLay, N. *J. Phys. Chem.* **1994**, *98*, 3071-3072.
42. Johnson, R. S.; Yamazaki, T.; Kovalenko, A.; Fenniri, H. *J. Am. Chem. Soc.* **2007**, *129*, 5735-5743.
43. Sakajiri, K.; Sugisaki, T.; Moriya, K.; Kutsumizu, S. *Org. Biomol. Chem.* **2009**, *7*, 3757-3762.
44. (a) Bradbury, E. M.; Carpenter, B. G.; Goldman, H. *Biopolymers* **1968**, *6*, 837-850. (b) Toriumi, H.; Saso, N.; Yasumoto, Y.; Sasaki, S.; Uematsu, I. *Polym. J.* **1979**, *11*, 977-981. (c) Watanabe, J.; Okamoto, S.; Satoh, K.; Sakajiri, K.; Furuya, H.; Abe, A. *Macromolecules* **1996**, *29*, 7084-7088. (d) Maeda, K.; Okamoto, Y. *Macromolecules* **1999**, *32*, 974-980
45. Sakai, N.; Matile, S. *Chirality*, **2004**, *16*, S28-S35.
46. Fujiki, M. *J. Am. Chem. Soc.* **2000**, *122*, 3336-3343.
47. Tabei, J.; Nomura, R.; Sanda, F.; Masuda, T. *Macromolecules* **2004**, *37*, 1175-1179.

Chapter 2

Investigation of the structural and electrostatic factors affecting the self-assembly and stability of twin G \wedge C-based rosette nanotubes

2.1. Introduction

Nature relies on a number of large and complex architectures to perform sophisticated processes, which demand the co-ordination of both non-directional and directional noncovalent interactions. In most cases, the existence of these superstructures originates from the hierarchical self-assembly of relatively simple monomeric building blocks like the DNA double helix¹ and the tobacco mosaic virus.² Using noncovalent interactions, a variety of artificial self-assembled structures such as capsules,³ vesicles⁴ and wires⁵ have emerged. However, achieving the complexity and molecular recognition ability of natural systems entail in-depth understanding of the forces and interactions that propel such organization. The majority of self-assembled supramolecular systems have been based on the built-in hydrogen bonding complementarity and directionality of the monomers, hydrophobic effects⁶ and aromatic stacking interactions.⁷ While the properties and stability of these and other supramolecular architectures largely depend on the structure of the monomers themselves, the formation and strength of the noncovalent bonds can be mediated by their surrounding environment. This gives the opportunity for not only internal control (e.g. structure of the monomer), but also external control (pH, solvent, temperature) of the self-assembly process.

About a decade earlier, our group reported a new class of organic materials, termed rosette nanotubes (RNTs).⁸ RNTs are obtained through self-assembly of the heterobicyclic G \wedge C motif - a self-complementary DNA base hybrid molecule, which features the hydrogen-bonding arrays of both guanine and cytosine. The versatility of the RNTs and ease of chemical modification have made them suitable for various tissue engineering and drug delivery applications.⁹ While both the single and the twin G \wedge C systems can self-assemble into RNTs, the twin G \wedge C variant is more robust, mainly due to its lower charge density, larger number

of hydrogen bonds per self-assembling motif and lower steric repulsion.¹⁰ The optimal utilization of the twin base RNT system relies on a better understanding of the factors that influence its stability, which include the solvent media, counterions and the structure of the self-assembling motifs. Towards this goal, we present a series of twin G \wedge C compounds functionalized with a range of substituents and variations in the core, along with their self-assembly behaviour in solution. Our objective was to compare the length of the resulting RNTs, by scanning electron microscopy (SEM) and atomic force microscopy (AFM), since this parameter is proportional to their relative stability. This approach was adopted because it was previously shown that increased hydrophobic stacking interactions led to an increased stabilization in some systems.¹¹

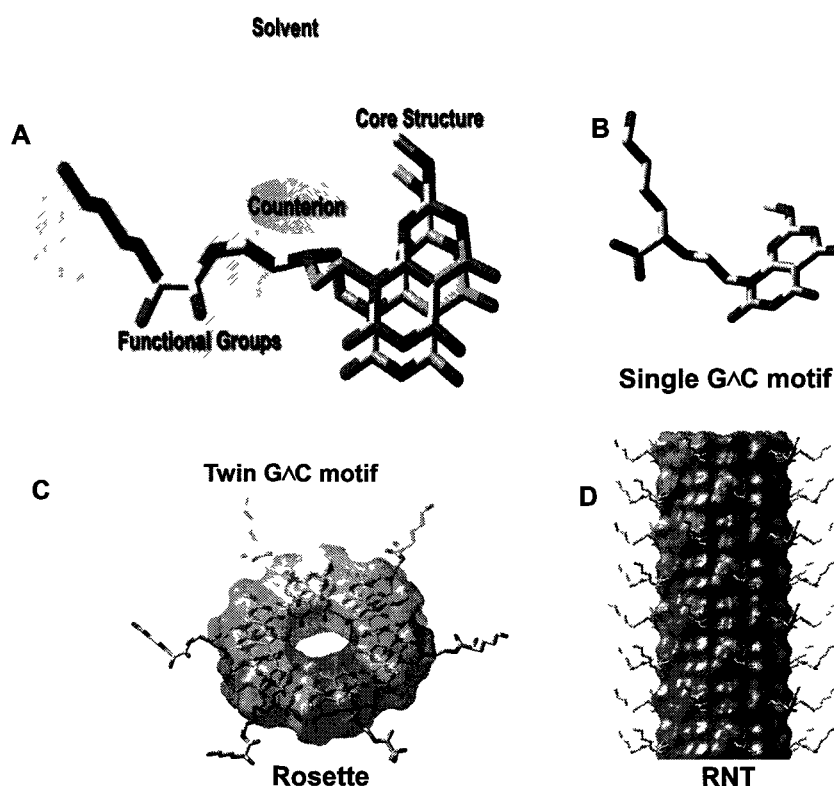
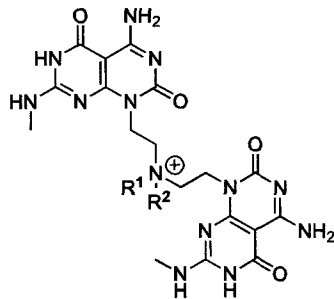


Figure 2.1. Twin G \wedge C motif G0¹⁰ (A), L-lysine functionalized single G \wedge C motif K1^{8a-b} (B), twin rosette formed from the association of 6 twin G \wedge C motifs (C) and RNT assembled from twin rosettes (D).

2.2. Design and synthesis of twin base monomers



Entry*	Nomenclature	R ¹	Entry*	Nomenclature	R ¹
1	NH-TBL	H	8	R-TBL	
2	Eth-TBL		9	S-TBL	
3	But-TBL		10	G0	
4	Hex-TBL		11	K-TBL	
5	OH-TBL		12	Di-Me-TBL	
6	Me-TBL		13	Acr-TBL	
7	Pent-TBL				

* R² = H except for 12, where R² = Me

Figure 2.2: Functionalized twin G \wedge C motifs.

Thirteen twin G \wedge C motifs were synthesized (Figure 2.2) that were both unfunctionalized (entry 1) and functionalized with primary amines (entries 2-4), alcohols (entry 5), aliphatic (entries 6-7, 12), chiral (entries 8-11) and aromatic groups (entry 13). The key role of the amines was to connect the two G \wedge C units. However, the choice of the functional groups to be expressed on the surface of the RNTs would allow investigation of structural and electrostatic effects on self-assembly and predict the stability of the RNTs. For instance, entries 1-4 investigate the effect of hydrophobic tail size; entries 3, 5 and 7 probe the

electrostatic nature of terminal atom; entries 6-9 and 12 examine the influence of hydrophobic effect; entries 8-11 explore the effect of proximity of the chiral centre to the G \wedge C bases on the supramolecular chirality of the system; and finally entry 13 examines the effect of additional stacking interactions on the RNT surface. As a general nomenclature, the self-assembling motifs are referred to as TBL, which stands for twin base linker.

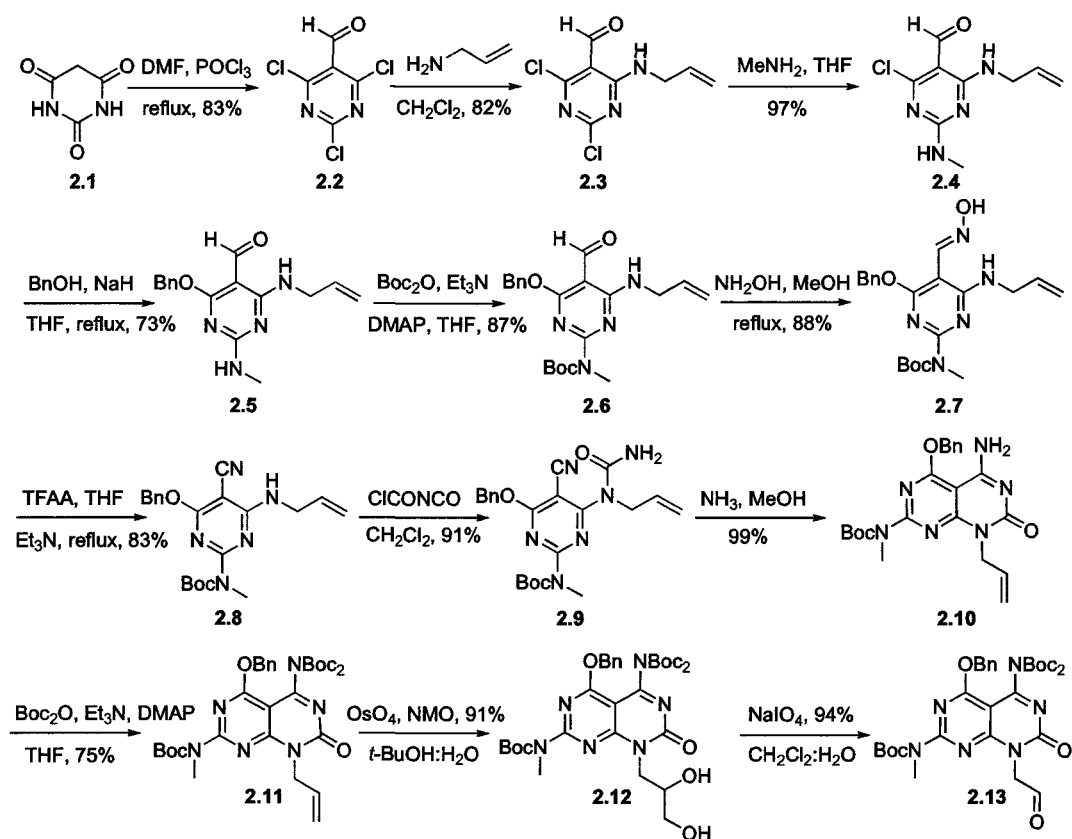


Figure 2.3: Synthesis of G \wedge C aldehyde **2.13**.

The main precursor for the synthesis of these twin G \wedge C molecules is the heterobicyclic G \wedge C aldehyde **2.13**, which was obtained in 12 steps with an average stepwise yield of 87% (Figure 2.3), according to a previously reported procedure.^{8a-b} Barbituric acid (**2.1**) was first converted to 2,4,6-trichloropyrimidine-5-carbaldehyde (**2.2**) under standard Vilsmeier-Haack formylation conditions. Compound **2.2** was then reacted with allylamine to give compound **2.3** in 82% yield. The latter was then subjected to two consecutive nucleophilic

aromatic substitution reactions (2.3 → 2.4 → 2.5) to afford the diamine derivative 2.5. Selective Boc protection of the methylamine fragment followed by oxime synthesis gave rise to compound 2.7. Dehydration of compound 2.7 in the presence of trifluoroacetic anhydride yielded nitrile 2.8. Subsequent reaction with *N*-chlorocarbonyl isocyanate followed by cyclization in a methanolic solution of ammonia produced compound 2.10. Standard Boc protection of the primary amine of compound 2.10 afforded derivative 2.11, which was subjected to Lemieux-Johnson conditions (2.11 → 2.12 → 2.13) to give the desired aldehyde 2.13 in excellent yield.

The general scheme for synthesis of the self-assembling motifs and their intermediates is shown in Figure 2.4. The final compounds were obtained in three to four steps starting from the amines and GAC aldehyde 2.13. A reductive amination reaction between the amine and 2.13 produced the protected monobase, which was then coupled with a second equivalent of 2.13 to yield the protected twin-base derivative. In some cases, the protected monobase intermediates were not isolated. The desired products were obtained as hydrochloride salts, after deprotection in 95% TFA/thioanisole and anion exchange.

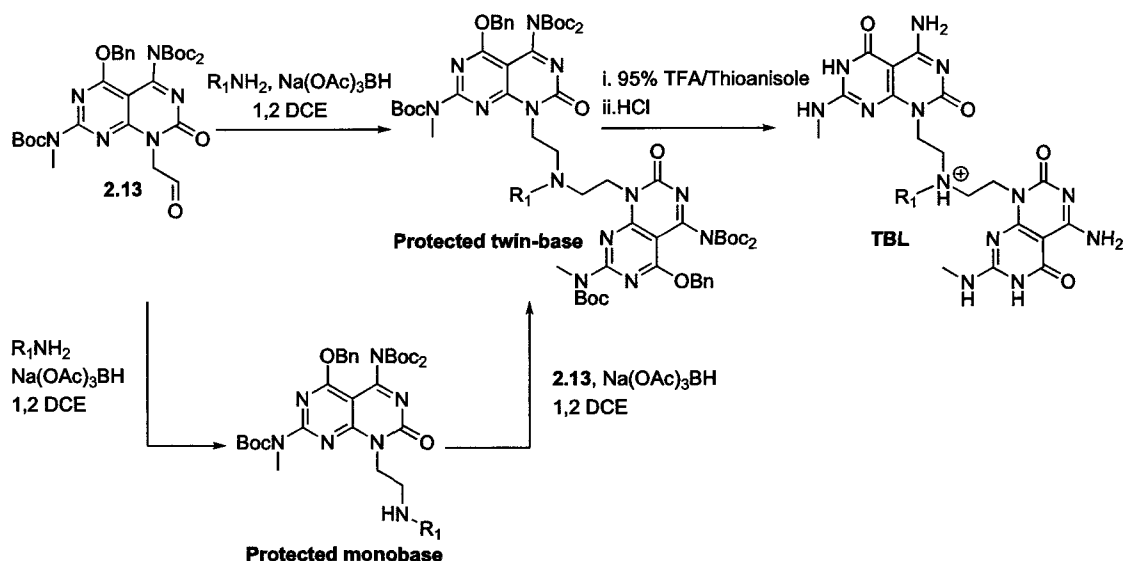


Figure 2.4: General scheme for the synthesis of the self-assembling motifs TBL

Amine	Protected monobase	Protected twin-base	TBL
$\text{H}_2\text{N}-$ 2.31	Not isolated	 2.32 Yield = 46%	 2.33 Yield = 97%
$\text{H}_2\text{N}-$ 2.34	Not isolated	 2.35 Yield = 40%	 2.36 Yield = 98%
 2.37	 2.38 Yield = 40%	 2.39 Yield = 33%	 2.40 Yield = 89%
 2.41	 2.42 Yield = 45%	 2.43 Yield = 31%	 2.44 Yield = 93%

Figure 2.6: Compounds isolated and their corresponding yields

The chiral analogue G0 (**2.45**) was synthesized by another group member according to a previously reported procedure.¹⁰ Both the TFA (**2.45A**) and the HCl (**2.45B**) salts were used for the experiments.

Another chiral analogue K-TBL (**2.52**), bearing L-lysine was synthesized (Figure 2.7). This molecule has the same chirality as G0 and two extra carbon atoms in the linker connecting the amino acid and the GAC bicycles. Coupling of (9H-fluoren-9-yl)methyl 4-aminobutylcarbamate (**2.46**) and the di-Boc protected lysine (**2.47**) gave rise to amide **2.48**. Removal of Fmoc protecting group under basic condition furnished the free amine **2.49**, which was coupled to aldehyde

2.13 to produce the lysine derivative **2.50**. The latter was coupled with another equivalent of **2.13** to yield the protected dimer **2.51**. Subsequent deprotection of **2.51** in 95% TFA/thioanisole gave the TFA salt **2.52A**, which was then converted to the hydrochloride salt **2.52B** in quantitative yield.

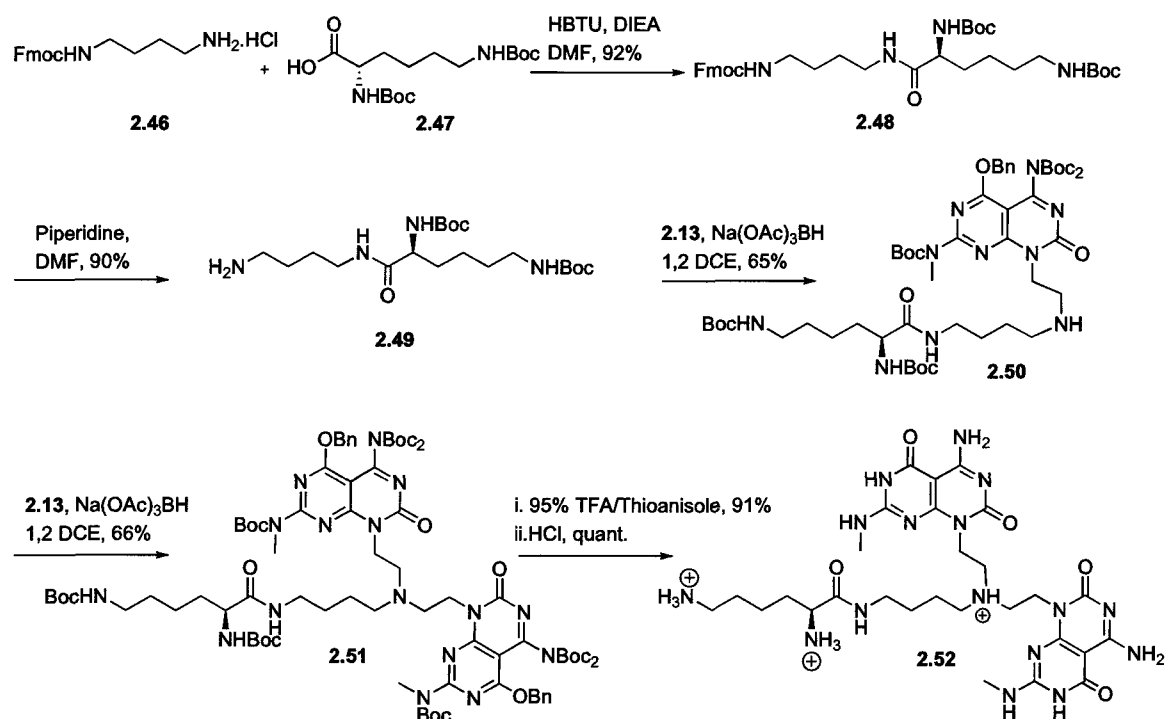


Figure 2.7: Synthesis of K-TBL motif

The Di-Me-TBL (**2.54**) variant was synthesized in two steps starting from dimer **2.32** (Figure 2.8). Methylation of the latter in the presence of a large excess of methyl iodide under anhydrous conditions gave the dimethylated product **2.53** in 74% yield. Deprotection of **2.53**, followed by anion exchange gave Di-Me-TBL (**2.54**) as the hydrochloride salt in 90% yield.

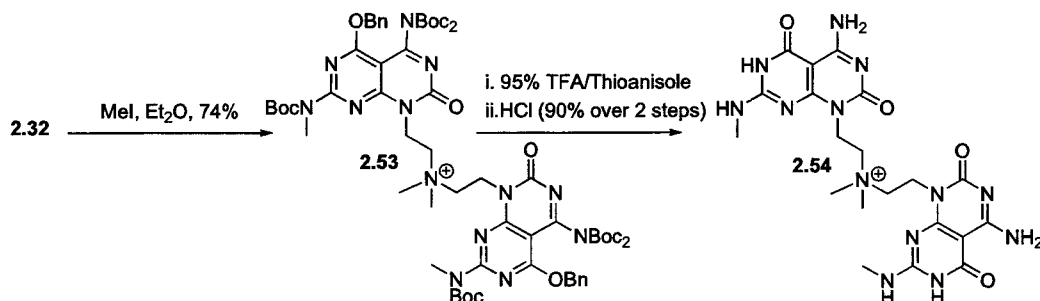


Figure 2.8: Synthesis of the Di-Me-TBL module

The acridine-functionalized motif **2.58** was synthesized as illustrated in Figure 2.10. Acridine-9-carboxylic acid (**2.55**) was coupled to (9*H*-fluoren-9-yl)methyl-4-aminobutylcarbamate hydrochloride to give the Fmoc protected amide **2.56** in 59% yield. Removal of the Fmoc group, followed by reductive coupling to aldehyde **2.13** furnished dimer **2.57**. Deprotection and anion exchange produced the acridine derivative **2.58** as a hydrochloride salt in excellent yield.

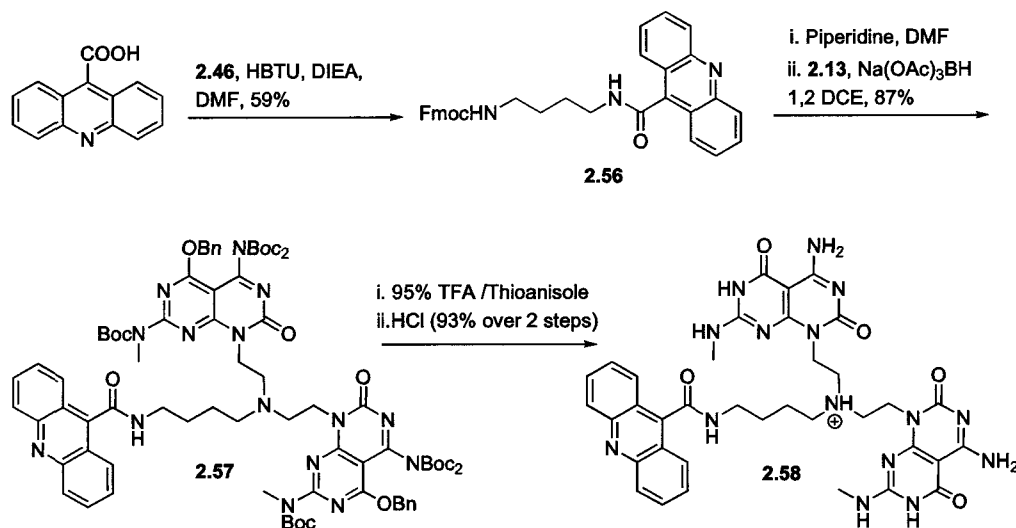


Figure 2.9: Synthetic scheme for Acr-TBL.

2.3. Environmental and structural factors affecting self-assembly of twin GAC-based RNTs

With compounds 1-13 in hand, we then investigated how the corresponding twin RNT stability could be optimized. Along with analytical instrumentation, SEM and AFM were used to obtain the length of the RNTs at a given time.

- Environmental factors:
 - Solvent system
 - Counterions
- Structural aspects:
 - Nature of functional group attached to the twin GAC motifs
 - Core structure of the self-assembling twin GAC motifs

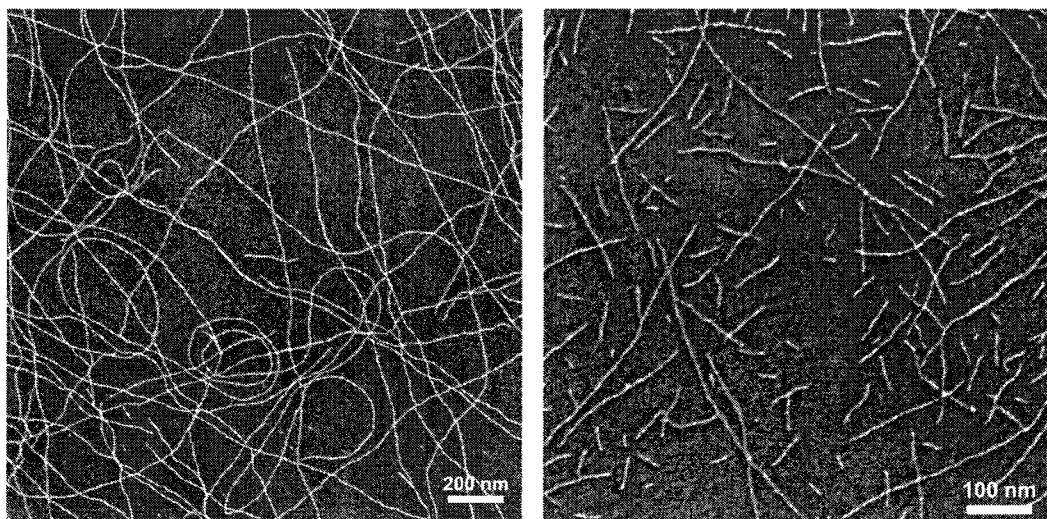


Figure 2.10: SEM images of But-TBL in methanol (left) and water (right) (0.0125 mg/mL, 0.017 mM).

But-TBL (**2.23**) was used as the model compound to investigate the general mode of self-assembly in most cases. Stock solutions of But-TBL (isolated as the HCl salt) in methanol and water were prepared at a concentration of 0.5 mg/mL (0.685 mM) and 1.0 mg/mL (1.37 mM), and were aged for 1 day. The SEM samples were prepared by diluting aliquots of the stock solution prior to depositing 2.0 μL of the diluted solution on TEM grids. The sample was stained using 2% uranyl

acetate solution for TEM visualization. For AFM, the sample was cast on a mica substrate.

The SEM images revealed rosette nanotubes of high aspect ratio present in both solvents, which could grow several micrometres in length. However, a difference in morphology was observed, with shorter tubes in water.

TEM was used to obtain the diameter of these nanotubes and diameter measurements showed no detectable differences in either solvent ($3.5 \text{ nm} \pm 0.2 \text{ nm}$).

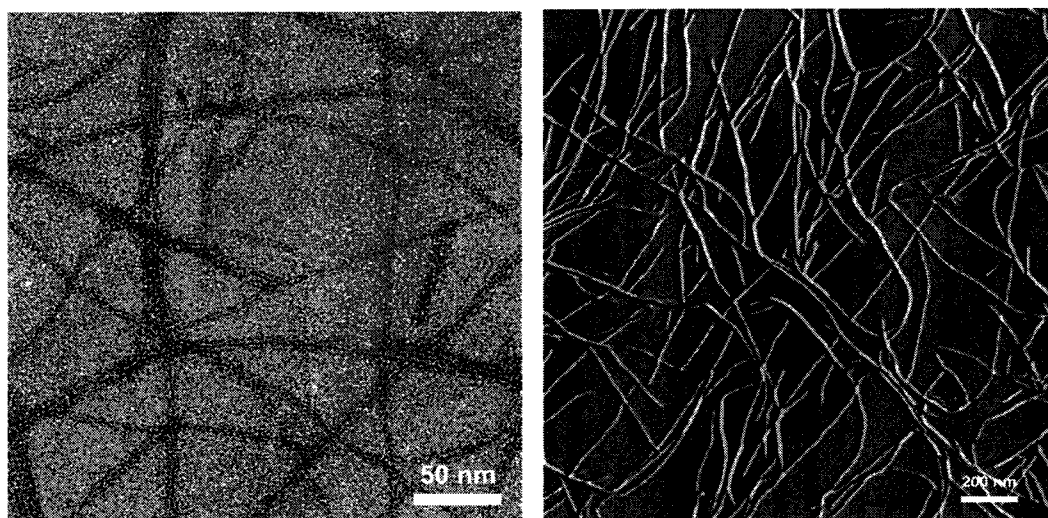


Figure 2.11: TEM image (left) and AFM image (right) of But-TBL (0.0125 mg/mL , $0.017 \text{ } \mu\text{M}$) in methanol.

The AFM images obtained in tapping mode (TM-AFM) showed structures of high aspect ratio (Figure 2.11) with heights $2.5 \text{ nm} \pm 0.2 \text{ nm}$. This value is lower than the average value obtained from TEM measurements and is most likely due to the flattening of the soft organic RNTs under the AFM tip in tapping mode, thus leading to a smaller measured height value.¹²

Previous work from our group predicted that self-assembly proceeded with stacking of rosettes, formed from complementary hydrogen bonding of six twin G \wedge C motifs. These hexameric twin rosettes are maintained by 36 H-bonds. Based on this work, we assume that the self-assembling modules discussed in this chapter adopt a similar mode of aggregation.

The models generated for But-TBL was based on the most stable structure obtained for the G0 motif.¹⁰ The most stable conformation for a single But-TBL motif had an eclipsed syn arrangement with a distance of 3.9 Å between two G \wedge C bases. This conformer was used to build a six-fold symmetry twin rosette maintained by 36 H-bonds, and further, a RNT with 7 double rosettes with an inter-twin rosette distance of 3.3 Å and a rotation angle of 30° per twin rosette. The average outer diameter of the resulting rosette nanotube was 3.8 nm.

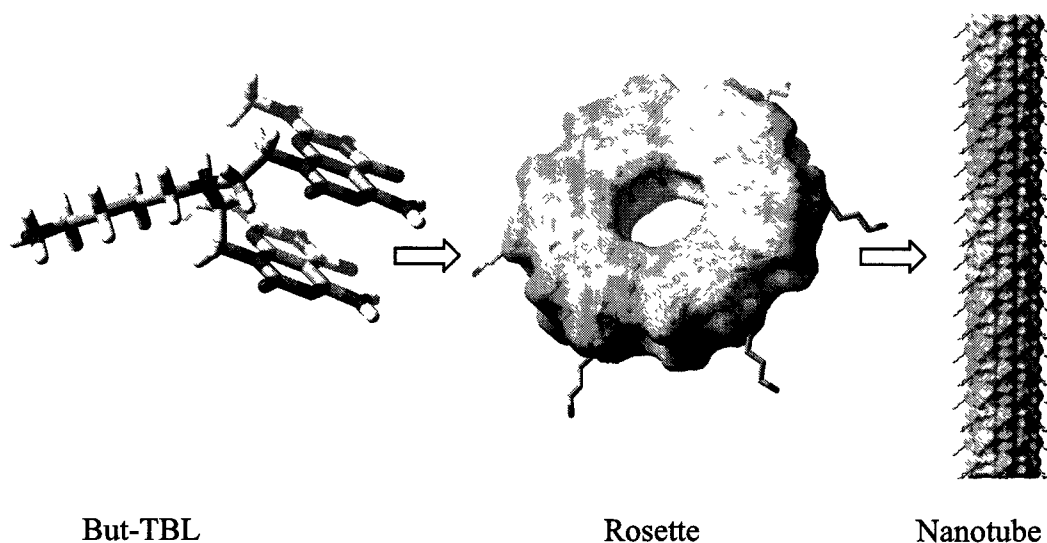


Figure 2.12: Syn conformation of a twin G \wedge C, leading to the formation of twin rosettes, which then stack to give a rosette nanotube.

2.3.1. Effect of solvent and counterions

As with any self-assembled systems, the surrounding medium is critical to the formation and stability of RNTs, thus allowing for adjustments to be made to tune the properties of these materials as required. In previously reported studies of G0

(**2.45A**), the self-assembly was linked to the protonation sites of the L-lysine side chain.¹⁰ Three different aggregation states corresponding to short well-dispersed RNTs, ribbons and superhelices were observed under acidic (pH 4), neutral (pH 7) and basic (pH 11) conditions respectively. Temperature dependent CD studies of G0 as the TFA salt (**2.45A**) also showed that the RNTs are very stable even at 95 °C.¹⁰

Along with pH and temperature, the solvent properties¹³ are equally crucial to the self-assembly and stability of the RNTs. While these supramolecular structures can be formed in both polar and non-polar solvents,^{8c} for biomaterials applications self-assembly under physiological conditions is desired. In this environment, the aggregation is driven by entropy, whereby water molecules are released into the bulk solvent as rosettes stack to form RNTs.^{8a} The difference in morphology observed for the model compound But-TBL (**2.23**) from the SEM images in water and methanol (Figure 2.10) was further investigated with the intent to optimize the twin-RNT formation in the polar environment. As such, self-assembly of the But-TBL was studied in neat and binary mixtures of MeOH (0%, 25%, 50%, 75%, 95% 99%) and water.

Stock solutions of But-TBL in methanol-water mixtures were prepared at 0.5 mg/mL (0.685 mM) and aged for 1 day. The SEM samples were prepared by diluting aliquots of the stock solution to a concentration of 0.0125 mg/mL (0.017 mM) (using the respective solvent systems) prior to depositing 2.0 μ L of the diluted solutions on carbon grids.

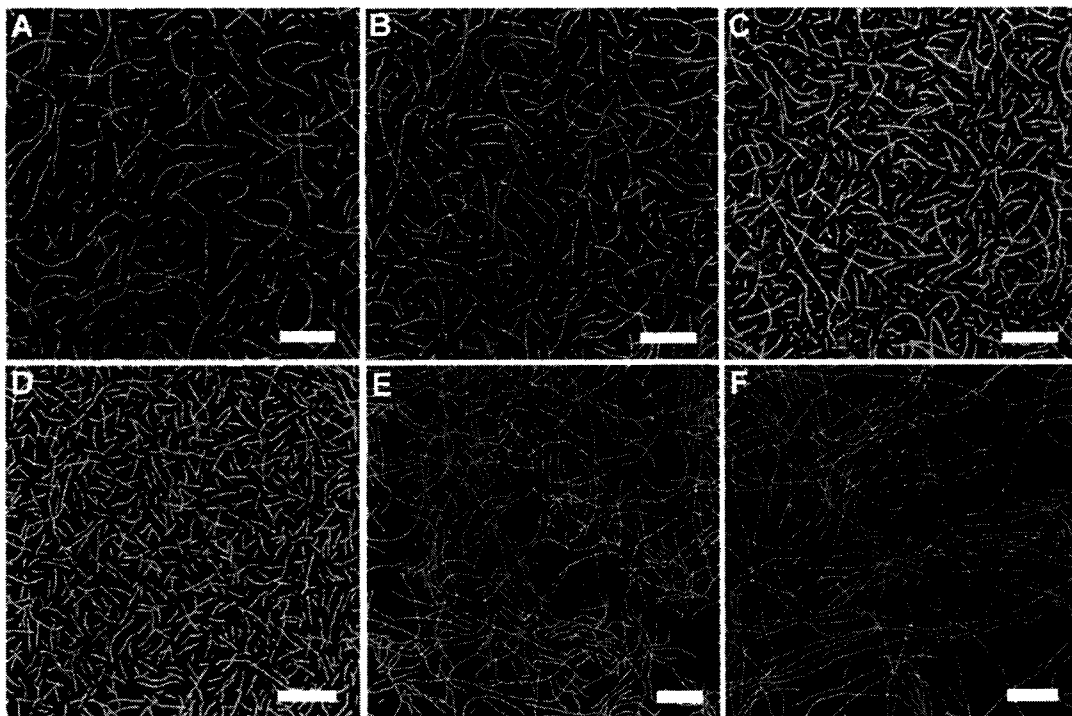


Figure 2.13: SEM images of But-TBL in MeOH-water mixtures: (A) 100% water (B) 25% MeOH (C) 50% MeOH (D) 75% MeOH (E) 95% MeOH (F) 99% MeOH after 1 day. Scale bar = 200 nm.

The graph (sigmoid fit) in Figure 2.14 depicts the percentage growth in total RNT length (with respect to the 99% MeOH solution F) that is measured in each of the SEM images A-E after 1 day of aging in the respective solvent systems. The RNTs that are quantified in each image are only those, which have π - π stacked into RNTs of detectable length. The growth kinetics of the RNTs varies with the solvent system and from the SEM images A-F, it is apparent that the growth is faster with higher concentrations of MeOH. We propose that because of decreased cation and anion solvation of the chloride and the ammonium ions in MeOH, and the resulting tighter ion pairs, the charge density on the RNTs is lower, leading to longer, faster forming and more stable RNTs.

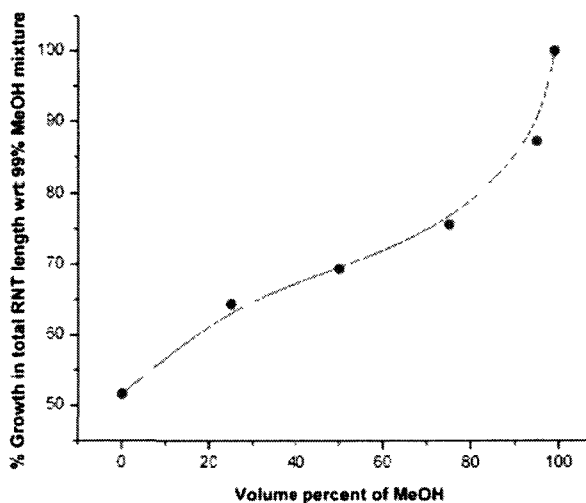


Figure 2.14: Percentage growth of RNTs with respect to 99% MeOH solution as a function of methanol-water ratio after 1 day.

In addition to more abundant RNT density, the solvent system also affects the length distribution of the RNTs. The RNT's length was categorized into three groups: 10-100 nm (short tubes), 101-300 nm (medium sized tubes) and 301-2000 nm (long tubes). It was found that the length of the RNT increased with increasing amount of MeOH. The RNT length distribution is shown in the histograms in Figure 2.15 (See experimental section for method of generating histograms). About 90% of RNTs consist of short to medium-sized nanotubes that are less than 300 nm for the 0-75% MeOH solution samples (A-D). In contrast, 40.3% and 80% of the total visible RNTs range between 300-2000 nm for E and F, which have a 95% and 99% MeOH ratio, respectively.

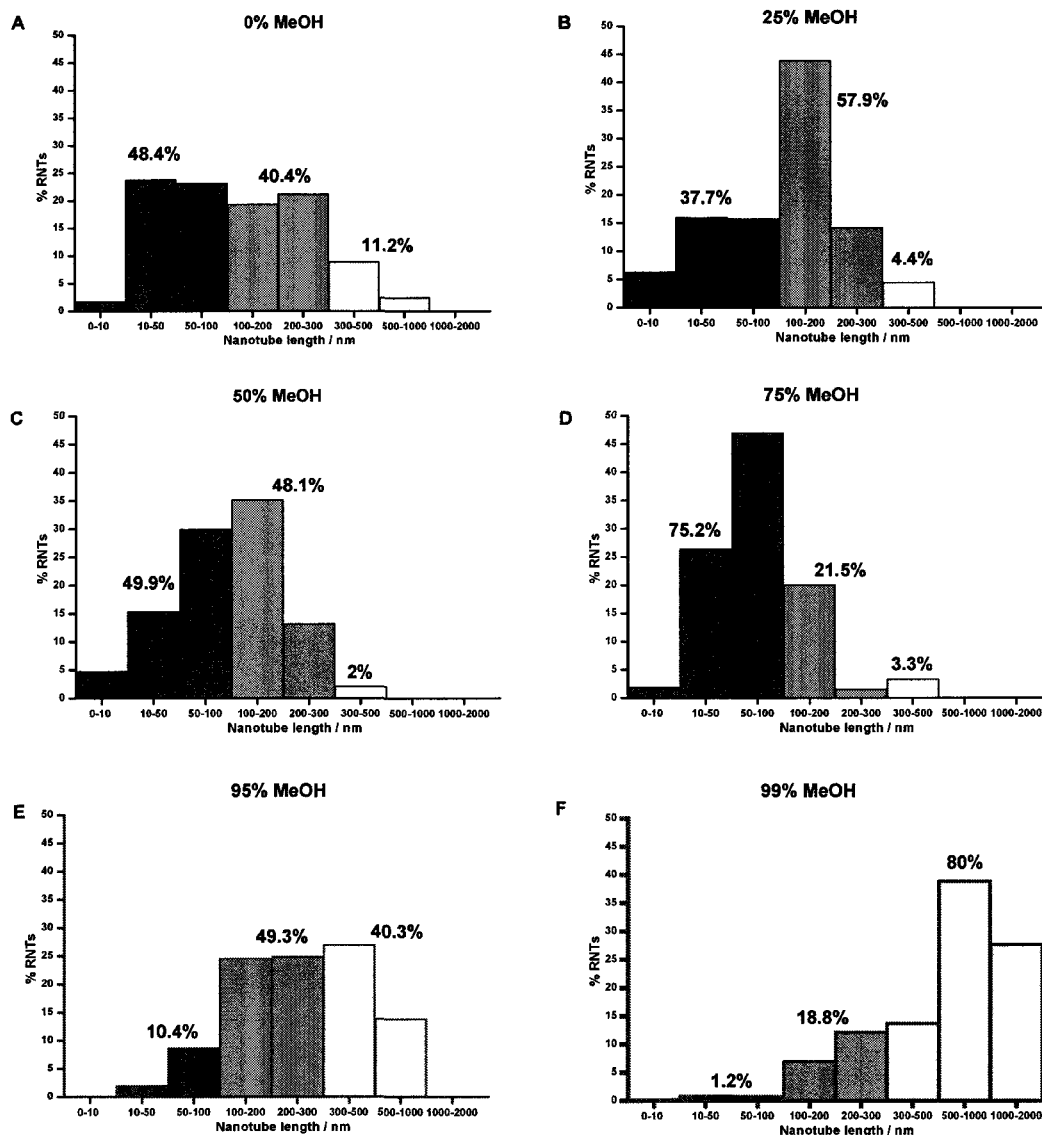


Figure 2.15: Histograms (A-F) of But-TBL self-assembled in increasing concentrations of MeOH.

The importance of ion solvation on RNT stability is further highlighted from the self-assembly of the chiral G \wedge C bases from Figure 2.2 (Entries 8-11, namely molecules R-TBL (2.40), S-TBL (2.44), G0 (2.45), K-TBL (2.52)) in MeOH. Anion exchange from TFA to chloride ions leads to a drastic change in the RNT lengths. RNTs self-assembled with CF₃COO⁻ ions (Figure 2.16, A-D) were noticeably shorter in all cases compared to those with Cl⁻ ions (Figure 2.16, E-H).

This was not surprising since the electrostatic interaction between Cl^- and the ammonium group on the G \wedge C base should be greater than with the more polarizable CF_3COO^- . This observation is in contrast to the self-assembly of R-TBL (or S-TBL) in water, which formed RNTs that were similar in length regardless of the counterion. Compared to self-assembly in MeOH, there is negligible difference in the RNT's lengths between the chloride and TFA salts in water, as seen in the SEM images in Figure 2.17. In this case, the electrostatic interaction between the water molecules, which have a high dielectric constant, and the individual ions of the G \wedge C base salt are greater than the attraction between the ion pairs regardless if CF_3COO^- or Cl^- ions are present.

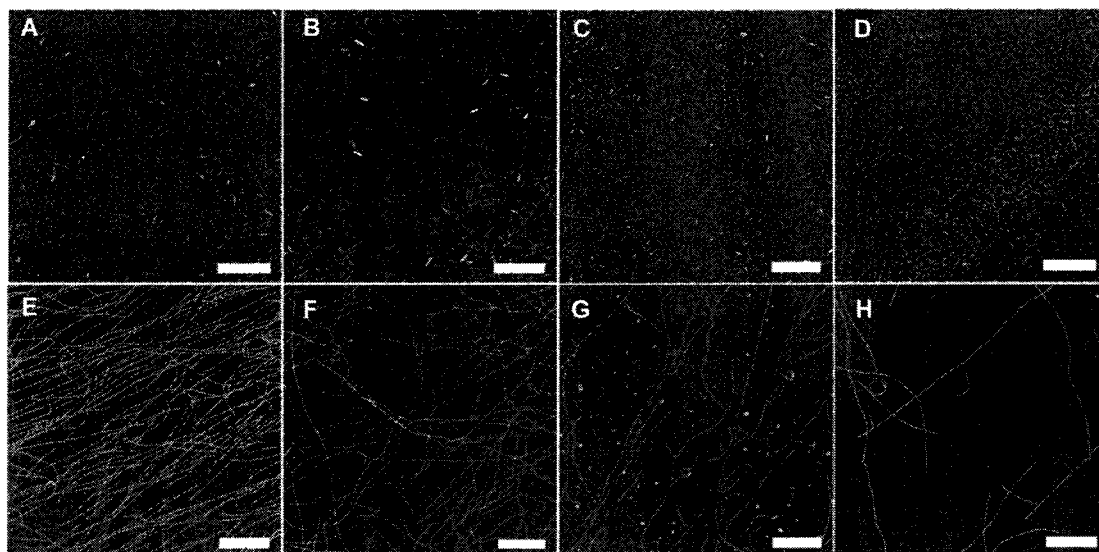


Figure 2.16: SEM images of R-TBL, S-TBL, G0 and K-TBL as the TFA salts (A-D) and HCl salts (E-H) respectively, in MeOH after 1 day of aging. Scale bar 300 nm.

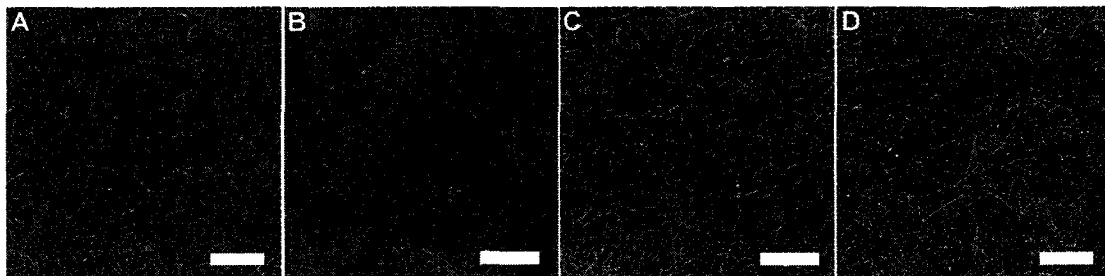


Figure 2.17: SEM images of R-TBL (**2.40**) and S-TBL (**2.44**) as the TFA salts (A, C) and HCl salts (B, D) respectively, in water after 1 day of aging. Scale bar 300 nm.

Along with solvent playing an important role in the RNT stability, it can also dictate the supramolecular chirality of these self-assembled structures. We have previously shown that a motif bearing a single G \wedge C base functionalized with L-lysine and self-assembled in water and MeOH gave RNTs with opposite supramolecular chiralities.^{8d} Theoretical modeling revealed that the solvent molecules located in the pockets of the RNT surface can trigger a molecular switching, which result in conformers of opposite chiralities.

To verify whether a similar effect would occur with chiral twin-G \wedge C motifs R-TBL (**2.40A**), S-TBL (**2.44A**), G0 (**2.45A**) and K-TBL (**2.52A**), CD spectroscopy was used to study their self-assembly in water and MeOH (Figure 2.18). The profiles and sign of the CD spectra of enantiomers R-TBL (**2.40A**) and S-TBL (**2.44A**) were not altered by the solvent, when compared to each other and the resulting RNTs had opposite helicities (reflected by the mirror-image CD signals) as expected per the basic supramolecular chirality principles.¹⁴ In a similar manner, the CD of G0 (**2.45A**) was not changed by the solvent environment.

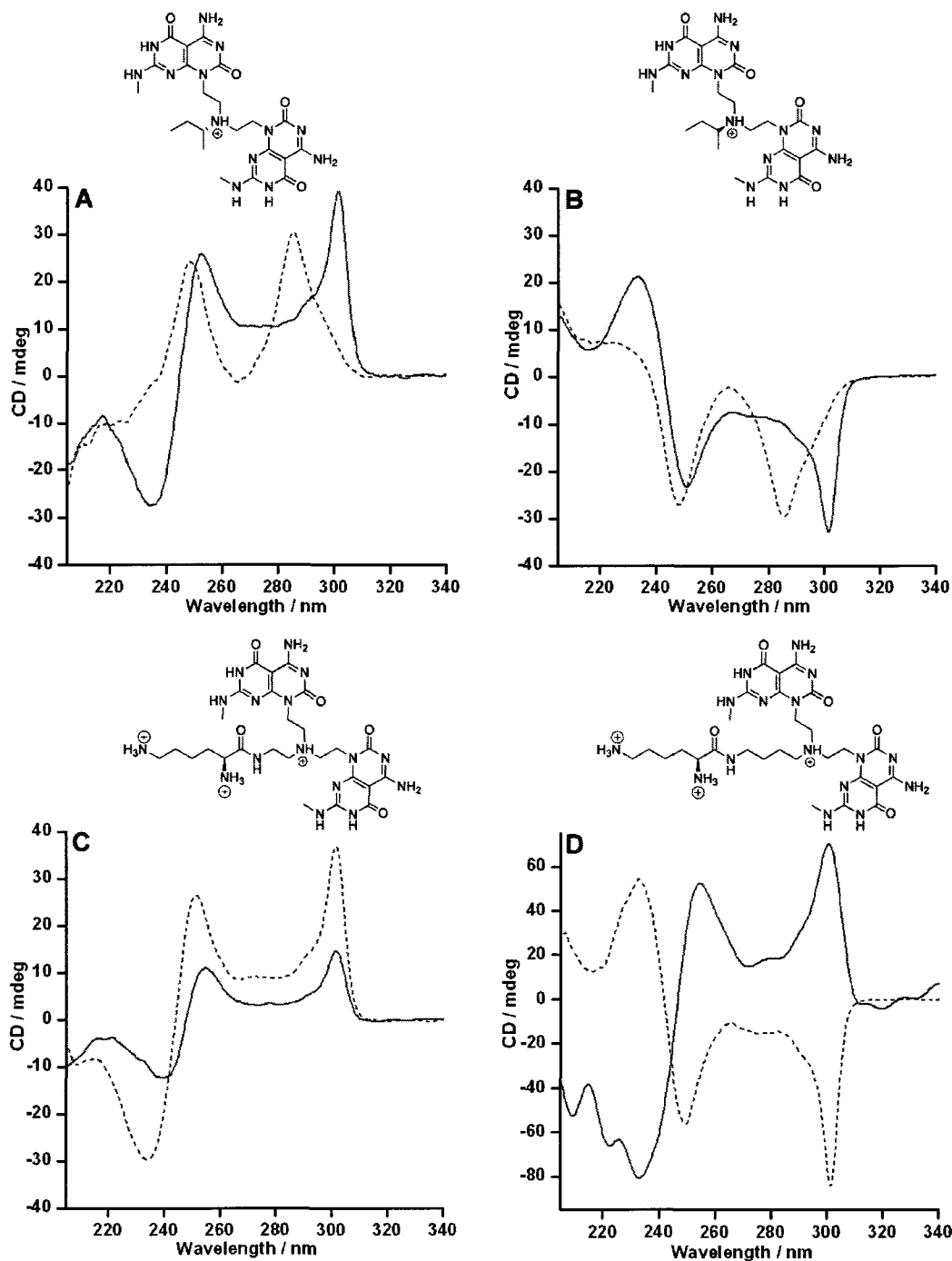


Figure 2.18: CD spectra for R-TBL, S-TBL, G0 and K-TBL as the TFA salts (A-D, respectively) in MeOH (dash) and water (solid). Spectra of R-TBL and S-TBL were obtained after 1 day of self-assembly and G0 and K-TBL after 14 days. For better visualization, the spectrum of K-TBL (D) in water was multiplied by a factor of 20.

However, this was not the case for K-TBL (2.52A), which exhibited CD signals of opposite signs in MeOH and water. This suggests that each of the two different solvent molecules have a unique arrangement around the RNTs and that their intermolecular interactions with the twin GAC motif dictate the RNT supramolecular chirality.^{8d} The CD spectra of K-TBL were always mirror image of the spectra in MeOH, thus establishing that the supramolecular chirality recorded is not a random process. This is the first reported example of a twin-GAC motif that undergoes a similar solvent-induced chirality switching by an achiral solvent. We presume that in this case too the orientation of the side-chain dictates the supramolecular chirality, which are mirror-image conformers (also termed as chiomers^{8d}) in water and MeOH.

While it was evident from the previously discussed sections, that the nature of the solvent can affect the output, size distribution and supramolecular chirality of RNTs, the presence of trace amount of certain solvents can also affect the formation and dispersion of the RNTs. Research done within our group has demonstrated how the solvent molecules (as little as 1%) located in the pockets of the RNT surface can switch the RNT supramolecular chirality.^{8d} In this context, we were interested in investigating if residual water present (accounting for less than 1%) in the methanolic RNT solution could impact the self-assembly behaviour. For this purpose, RNT monomers (Eth-TBL, But-TBL, S-TBL and K-TBL as the HCl salts) were prepared in 99.8% HPLC grade methanol at a concentration of 0.5 mg/mL. These stock solutions were then aged for 1 day and aliquots were diluted to give 2 mL of 0.0125 mg/mL diluted RNT solutions. Dried molecular sieves (3 Å, 10 beads per sample) were added to the methanolic solutions for removal of residual water. Drops of these samples were cast onto TEM grids at 1 h and 1 day after the addition of molecular sieves. While prior to addition of the drying agent, long and well-dispersed RNTs were observed throughout the grid, after 1 h of the molecular sieves addition, the RNTs merged into thick bundles. Upon standing for 1 day, almost no nanotubes were observed by SEM imaging (Figure 2.25).

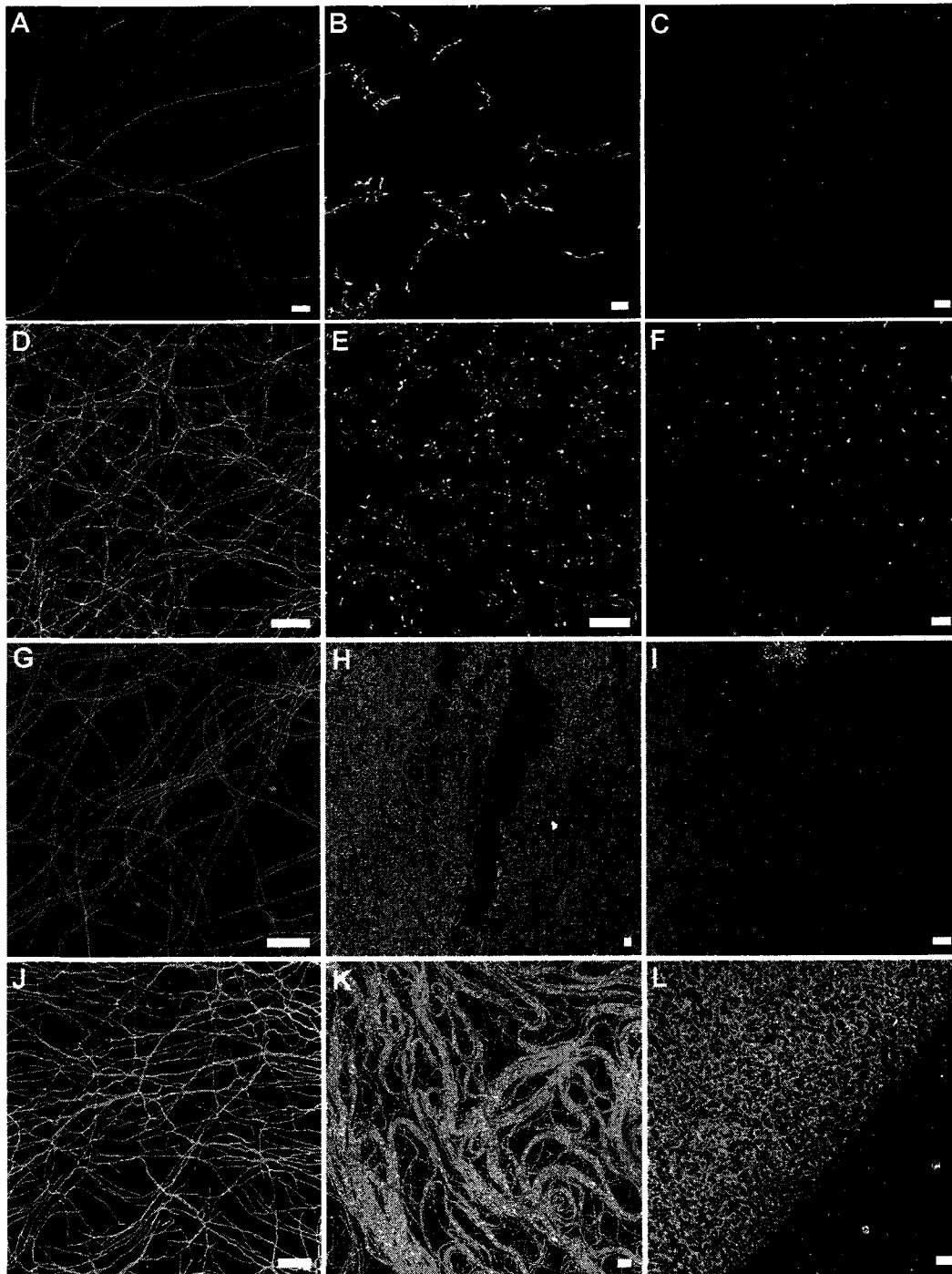


Figure 2.19: SEM images of self-assembling modules Eth-TBL (A-C), But-TBL (D-F), S-TBL (G-I) and K-TBL (J-L) as HCl salts in MeOH. The first column of images (A, D, G and J) corresponds to the samples prior to the addition of molecular sieves. The second column of images (B, E, H and K) corresponds to the samples 1 h after the addition of molecular sieves. The third column of images

(C, F, I and L) corresponds to the samples 1 day after the addition of molecular sieves, showing the collapse of the RNT structure. Scale bar = 200 nm.

In some cases, the RNTs precipitated out of the methanolic solution and this was visible to the naked eye. These results compelled us to believe that trace amount of water is crucial for the self-assembly and dispersion process, since taking out these water molecules from the pre-made RNTs led to its aggregation and subsequent precipitation. It is postulated that trace water molecules present in an ocean of methanol molecules are the ones that provide the first layer of solvation in the pockets and around the RNT surface. The nanotubes are preferentially solvated by water since the latter is a better solvent for ions than methanol. Removal of this hydrophilic solvation shell leads to a less charged RNT species since in methanol tighter ion pairs are formed. The dispersion, which resulted from repulsion between the charged species, decreases as the amount of water in the medium are greatly reduced, thus leading to thicker bundles. As the remaining water molecules are sequestered by the drying agent, larger aggregates are formed, which eventually precipitate out of solution.

2.3.2. Effect of functional group variation

Indeed the presence and nature of the solvent system dictates whether self-assembly would occur, since in its absence, supramolecular architectures cannot prevail. However the structure of the monomeric building blocks that makes up a supramolecule is equally important. The functional groups expressed on the periphery of the nanotubes, their hydrophobicity and charge strongly influence the self-assembly process, particularly in highly polar solvents such as water and MeOH. Self-assembly of the RNTs is usually faster in MeOH than in water. As such, it was easier to distinguish the effect of different functional groups in water, where the RNT growth rate was slower.

Stock solutions of the monomers (entries 1-7, 12, Figure 2.2) were prepared at 1.0 mg/mL in water and were aged for 1 day. The SEM samples were prepared by

diluting aliquots of the stock solution to 0.05 mg/mL prior to depositing 2.0 μL of the diluted solution on carbon grids (Figure 2.20).

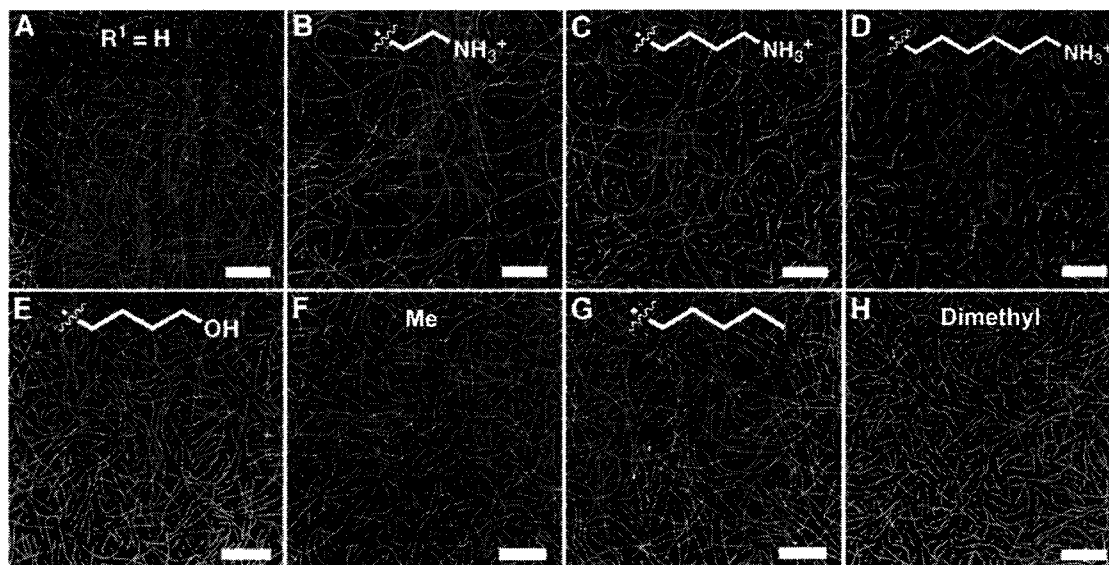


Figure 2.20: SEM images of twin RNTs with the indicated side-chain in water, aged for 1 day. Scale bar 200 nm.

In an attempt to quantify the self-assembly process, the RNT length distribution was obtained and compared by making histograms for each sample. In the first case, But-TBL (C) OH-TBL (E), Me-TBL (F) and Pent-TBL (G) were compared. From the histograms (Figure 2.21), for Pent-TBL more than 53% of the RNTs were greater than 300 nm in length, whereas for But-TBL and OH-TBL, this corresponded to only 37% and 16% of the RNT population. All three monomers have functional groups with the same alkyl chain length of 4 atoms, but have either charged (But-TBL, NH_3^+), polar (OH-TBL, OH) or neutral (Pent-TBL, Me) terminal ends. We presume that the hydrophobic nature of the pentyl group on the self-assembly of Pent-TBL contributes to the enhanced association and growth of the longer RNTs in the aqueous solvent. Such favourable interaction is missing for the charged and polar side-chains of But-TBL and OH-TBL respectively. The importance of the hydrophobic effect was further demonstrated with RNTs Me-TBL and Pent-TBL. Both display non-polar alkyl groups (Me and pentyl respectively) but differ by 4 carbon atoms. While Me-TBL has 16% percent of

RNTs greater than 300 nm in length and none larger than 1000 nm, the more hydrophobic Pent-TBL has over three times the number of RNTs within this range and quite notably, 5% which were significantly longer (1000 -2000 nm).

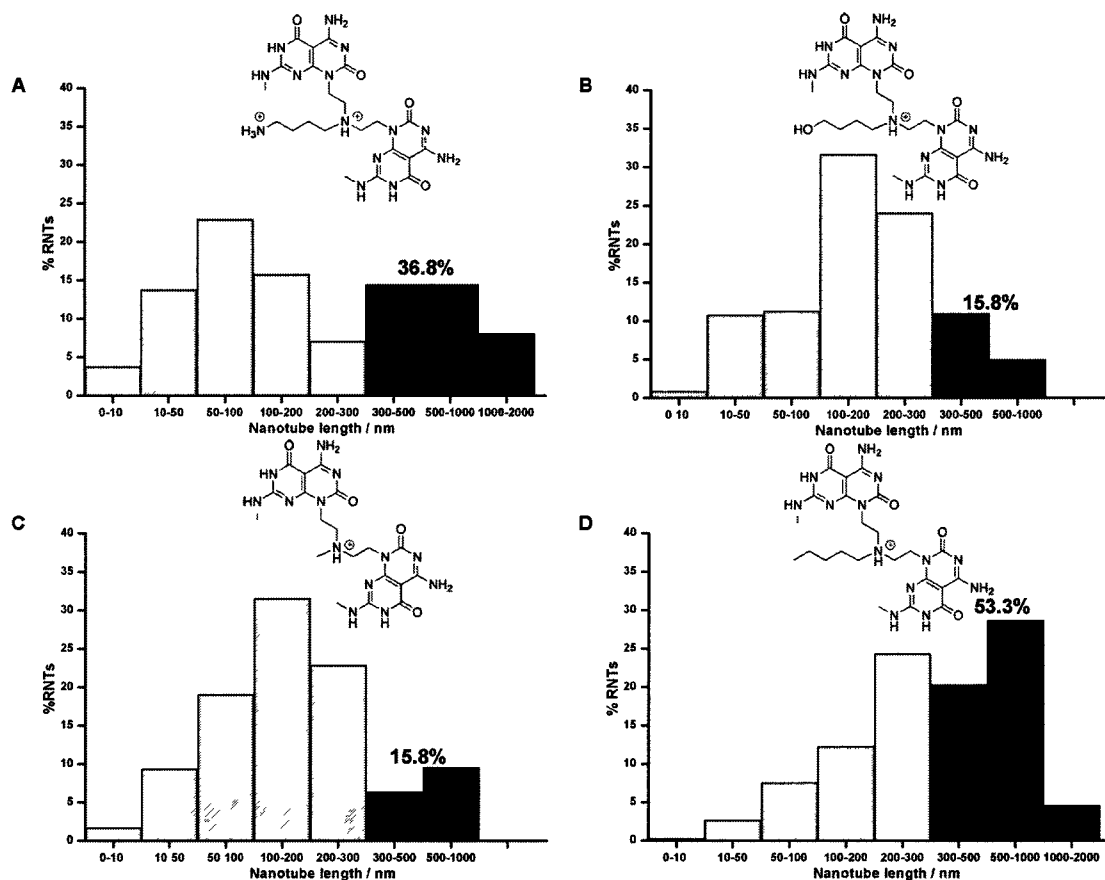


Figure 2.21: Histograms of But-TBL (A), OH-TBL (B), Me-TBL (C) and Pent-TBL (D). These histograms reveal that the percentage of RNTs greater than 300 nm is significantly greater for Pent-TBL with the neutral pentyl functional group than for But-TBL and OH-TBL, which have charged (NH_3^+) or polar side chains (OH) of the same length.

Subtle changes in the charge density of the functional groups also have dramatic effect on the self-assembly process as illustrated with Eth-TBL, But-TBL and Hex-TBL (Figure 2.22). Although these monomers differ from each other by the sequential addition of two methylene groups, the population of RNTs below 200 nm increased dramatically in water from 21% to 92% between Eth-TBL and Hex-

TBL respectively. Most importantly in the case of Hex-TBL, there were no RNTs greater than 300 nm in length. It was postulated that the difference in self-assembly might arise from the ability of longer side-chains to form intramolecular H-bonds with the GAC base, thereby hindering RNT formation.

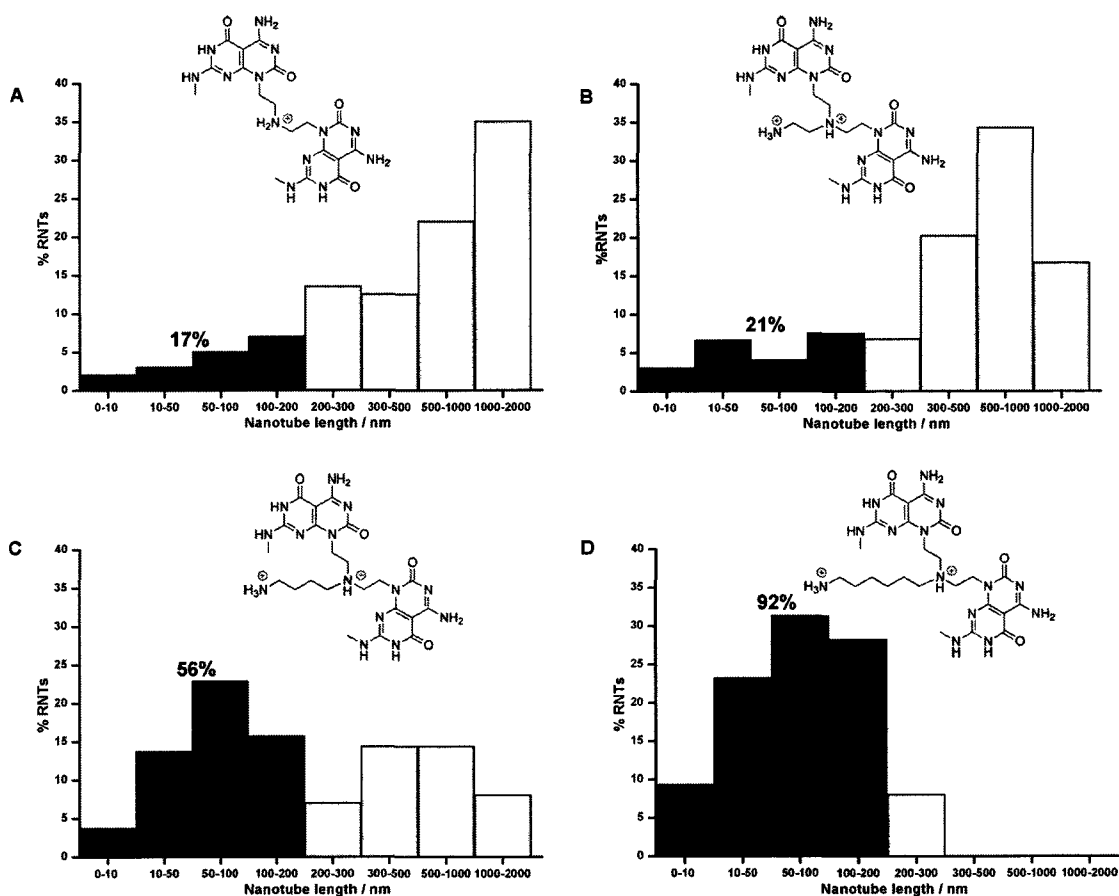


Figure 2.22: Histograms for the SEM images of NH-TBL (A), Eth-TBL (B), But-TBL (C) and Hex-TBL (D). These histograms reveal that the percentage of RNTs less than 200 nm in length increases from 21% to 56% and to 92 % for Eth-TBL (B), But-TBL (C) and Hex-TBL (D) respectively.

A conformational search using molecular modeling resulted in the sampling of 8, 38 and 499 conformations for Eth-TBL, But-TBL and Hex-TBL respectively (Figure 2.23). These conformations were subjected to 3D-RISM¹⁵ calculations to obtain the solvation free energies in water with chloride counterions. The most

stable conformations obtained had the side-chains in the extended form, which implies that intramolecular H-bonding may not be the cause for a difference in RNT formation. At the same time, this also means that analogues with the longer chains lack the diversity of the side-chain conformation. This conformational entropic loss disfavours the self-assembly process for Hex-TBL. Interestingly, the NH-TBL RNTs which lacks the side-chain, has approximately 17% of RNTs below 200 nm, which is nearly identical to that observed with Eth-TBL after 1 day. Thus, there is very little difference in the RNT stability between the unfunctionalized version (NH-TBL) with +1 net charge and the functionalized derivative (Eth-TBL) with +2 net charge.

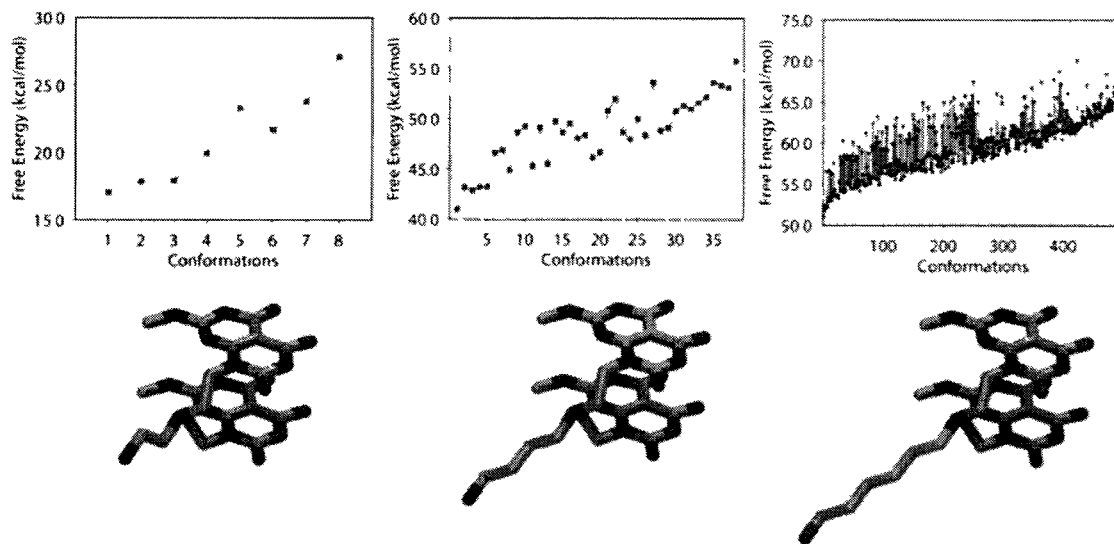


Figure 2.23: Conformational search for Eth-TBL (left), But-TBL (middle) and Hex-TBL (right). The lowest energy conformer for each RNT monomer is shown.

It is known that the structure of a molecule dictates its molecular chirality and quite often this difference in molecular chirality is also expressed at the macromolecular level. Such an example is illustrated by the mirror-image CD signals, which is due to the RNTs of opposite helicities, for the analogues TBL-R and TBL-S in either water or methanol (Figure 2.18 - A, B). Another such example is the opposite Cotton effects seen for G0 and K-TBL modules in MeOH

(Figure 2.24). Though these two monomers have the same point chirality, it is the orientation of the side-chain that dictates the RNT's supramolecular chirality in solution.

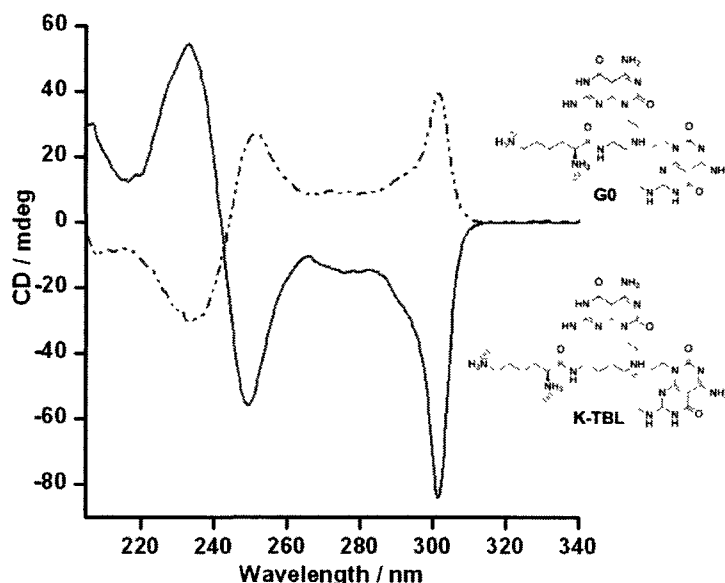


Figure 2.24: CD spectra of G0 (dash) and K-TBL (solid) as the TFA salts in MeOH after 14 days of aging.

While studies up to this point focused on twin-motifs that featured one functional group, bis-alkylated adducts such as Di-Me-TBL (**2.54**) which is dimethylated is also an interesting candidate for self-assembly. With an interplanar separation between the rosettes around 4.0 \AA ,^{10,16} in theory, this pocket should be able to accommodate functional groups with a diameter less than 4.0 \AA in order to maintain the required π - π stacking interactions between the two GAC units during rosette and nanotube formation. In the present case, which is the most simple, SEM images of RNTs Di-Me-TBL (Figure 2.20, H) were very similar in length compared to Me-TBL (Figure 2.20, F) which has only one methyl group but has the same net charge. Similar RNT stabilities were expected since the diameter of this methyl group in **2.54** is within the 4.0 \AA limit.¹⁷ However, if bisalkylated adducts such as Di-Me-TBL have functional groups greater than 4.0

Å in diameter, we would expect a decrease in the stability of the RNTs, due to disruption of the stacking interactions between the GAC units.

In order to further investigate the scope of these functional group studies, the twin-motif Acr-TBL (**2.58**) coupled to acridine was explored. These aromatic acridine molecules are significant for their antimicrobial and anticancer properties.¹⁸ More pertinent to these studies however, is their known ability to intercalate nucleic acids¹⁹ and exhibit several polymorphic structures in the solid state due to strong electrostatic and π - π interactions.²⁰

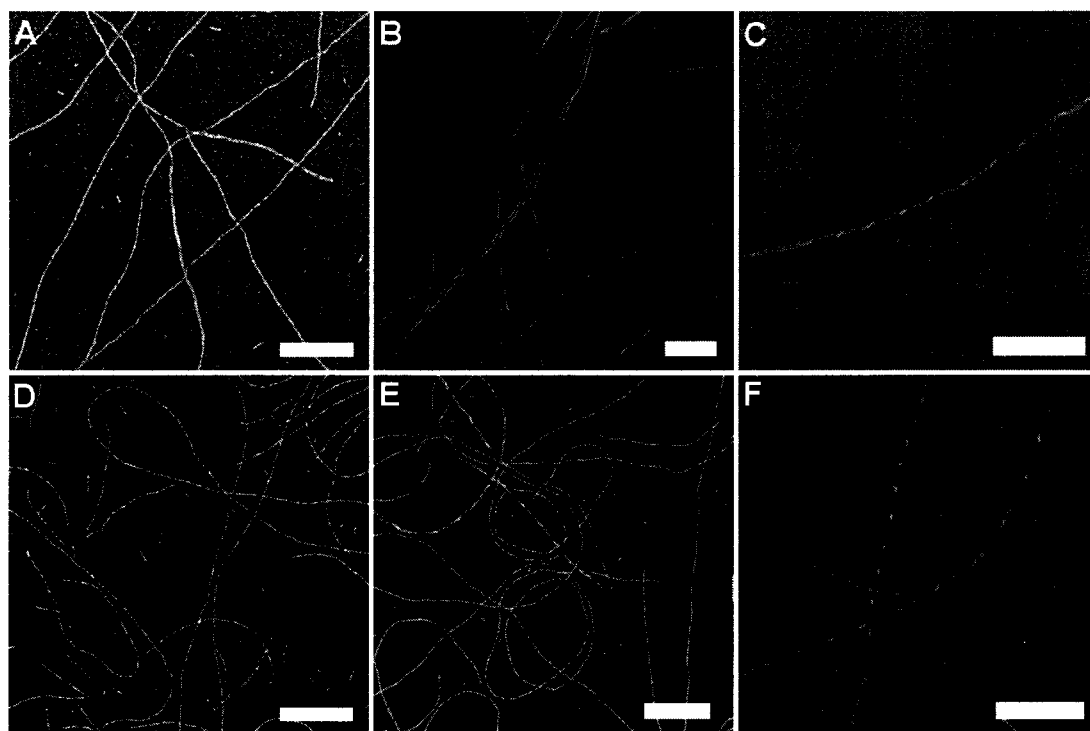


Figure 2.25: SEM images of Acr-TBL after 1 day of aging in MeOH (A) and water (D) and 14 days of aging in MeOH (B) and water (E). Helical bundles are observed in MeOH (C) and water (F) after 3 days and 14 days of aging, respectively. Scale bar = 200 nm.

Self-assembly of Acr-TBL into single RNTs would demonstrate the selectivity and stability of these architectures in the presence of the aromatic fragment, which was expected to alter the self-assembly pathway and supramolecular structure

formed. As shown in Figure 2.25, long and well-dispersed RNTs were observed in both MeOH and water solvents after 1 day of aging, thereby confirming the robust nature of the twin G \wedge C design. As the stock solutions were aged over longer time periods, thicker bundles emerged. Helical nanofibres were also observed in both solvents. TEM images of Acr-TBL established that the outer diameter of the RNTs was 5.2 ± 0.2 nm, which is in agreement with the theoretical value of 5.1 nm, whereby the acridine units are extended out from the periphery of the RNT.

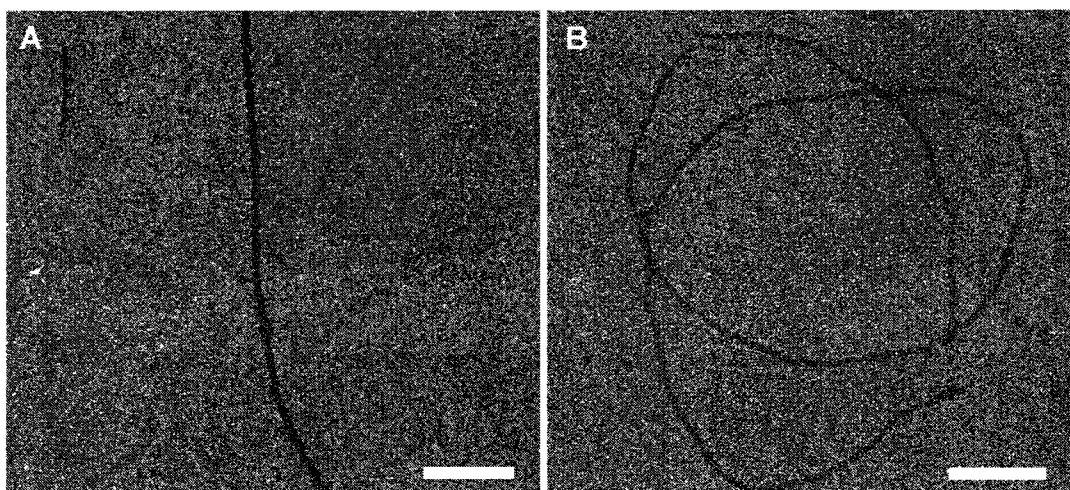


Figure 2.26: TEM image of Acr-TBL in (A) MeOH and (B) water after 1 day of aging. Scale bar = 100 nm.

Morphologies similar to the ones observed during SEM and TEM imaging were also found for the AFM images in both water and methanol.

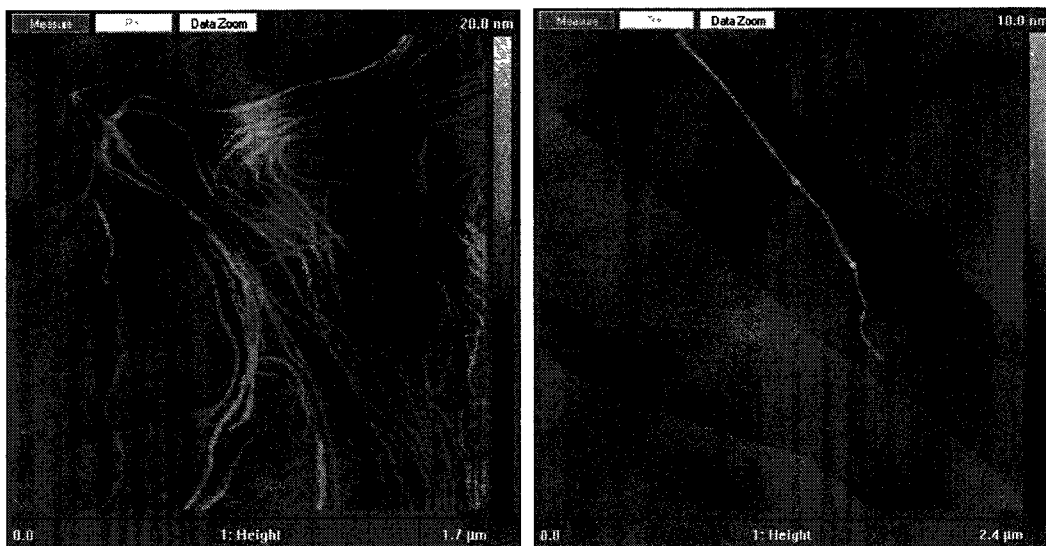


Figure 2.27: AFM image of Acr-TBL in MeOH (left) and water (right) cast on HOPG after 1 day of aging.

The conformation adopted by Acr-TBL in solution was elucidated using molecular modeling. By varying the dihedral angle indicated in Figure 2.28 (by 0° , 90° , 180° , and 270°), the four initial conformations of the motif were generated.

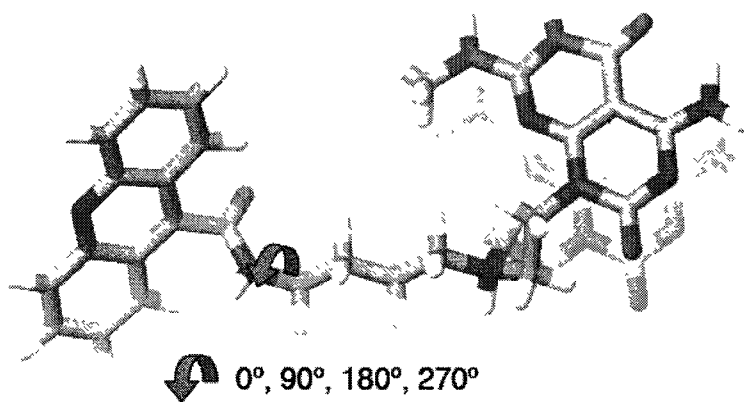


Figure 2.28: Conformations of Acr-TBL

Using these four motifs, the four RNTs each consisting of 9 twin-rosette rings were generated. The side-chain conformation was optimized with the top two and bottom two twin-rosette rings as well as all G \wedge C bases fixed to reduce the end effect. After the minimization, the central twin-rosette in each four RNTs were

taken to finally construct RNTs composed of N=1-9 twin-rosettes. A stacking distance of 4 Å and staggering angle of 30° between the twin-rosette rings was applied.^{10,16} By applying Macromodel and 3D-RISM theory¹⁵ (in water + Cl⁻), the free energies of each RNTs were obtained. The graph in Figure 2.29 shows the relative free energy as a function of the number of twin-rosette rings, N, with respect to the free energy of #2 RNT.

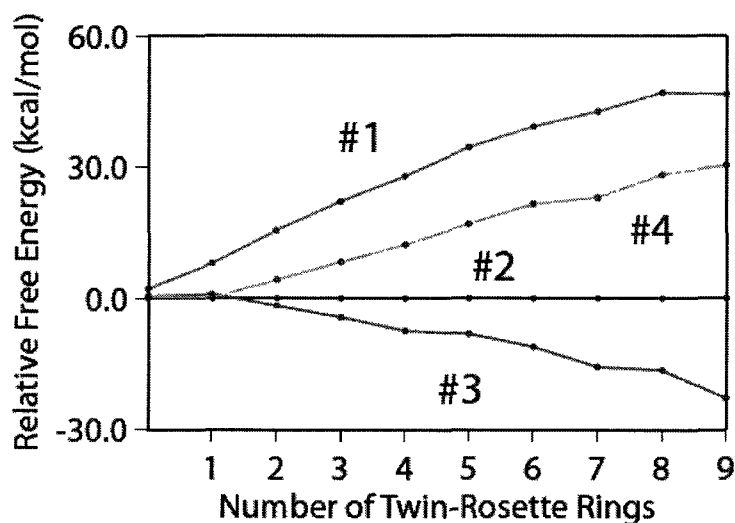


Figure 2.29: Relative free energy as a function of the number of twin-rosette rings of Acr-TBL.

The most stable RNT was #3, and the conformation of the single motif, single twin-rosette ring, and RNT are as follows.

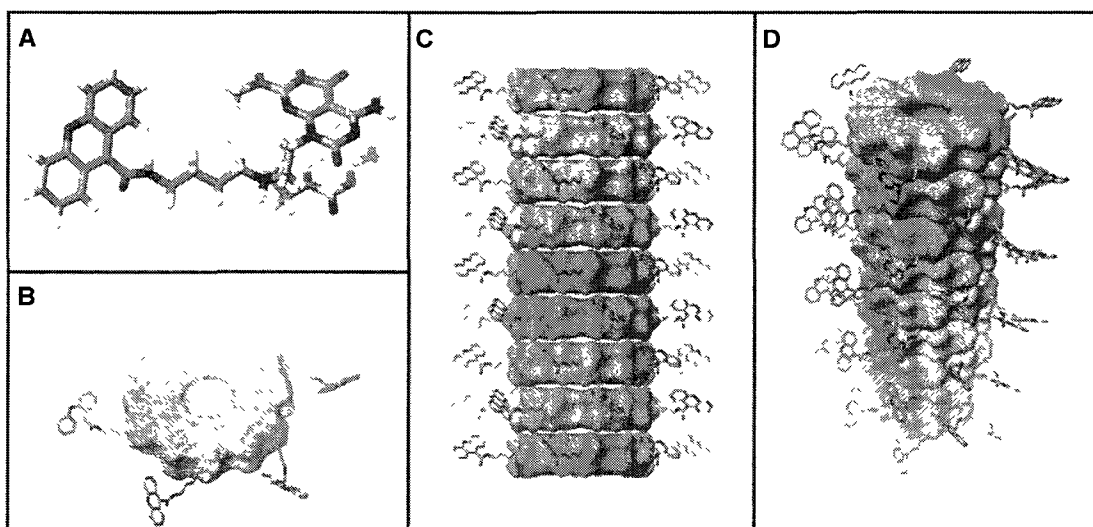


Figure 2.30: Most stable conformation of Acr-TBL #3 (A), Hexameric rosette (B) of A, RNTs (C and D) comprised of π - π stacked twin-rosettes B.

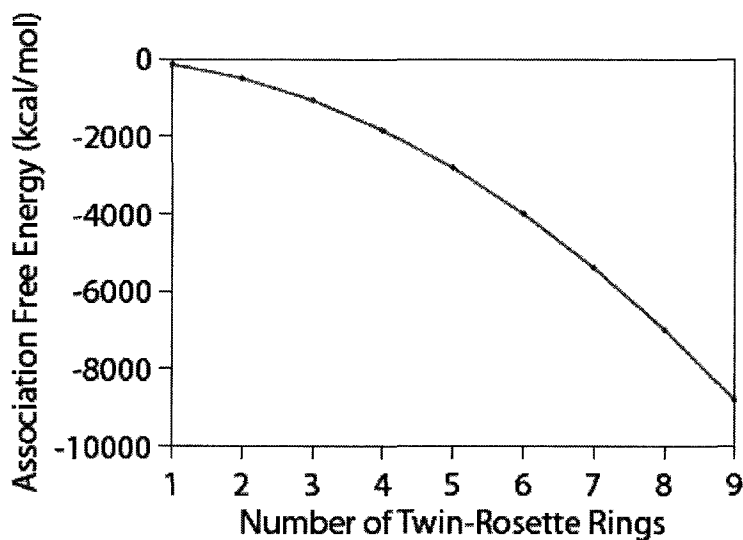


Figure 2.31: Association free energy of RNT #3.

The association free energy of this RNT shows that it can form RNT without any potential barriers (Figure 2.31). The outer diameter of RNT #3 was calculated to be 5.1 nm, which is in agreement with the diameter obtained from TEM measurements. The calculated distance between the acridines is more than 10 Å, which indicates that interaction with neighbouring or adjacent acridine units is

unlikely.

TEM measurement and the modeling method used were inadequate for predicting that the acridine units were not intercalating between the G_AC motifs within its own RNT or with neighbouring RNTs as the bundles form over time. Thus the self-assembly was monitored by UV-Vis spectroscopy.

Time dependent UV-vis spectroscopy was carried out in both water and MeOH over a month to investigate the dynamics of the RNTs' solutions. Stock solutions at 0.5 mg/mL were prepared by dissolving the compound in water and MeOH. The solutions were sonicated and aged at room temperature. Aliquots of the solutions were taken at different time intervals (1 h, 1, 2, 4, 7, 14, 21 and 28 days) and diluted to 0.0125 mg/mL with the respective solvent and the UV-vis spectra were recorded. For the purpose of clarity, only data obtained at 1 h, 1, 4, 14 and 28 days have been plotted.

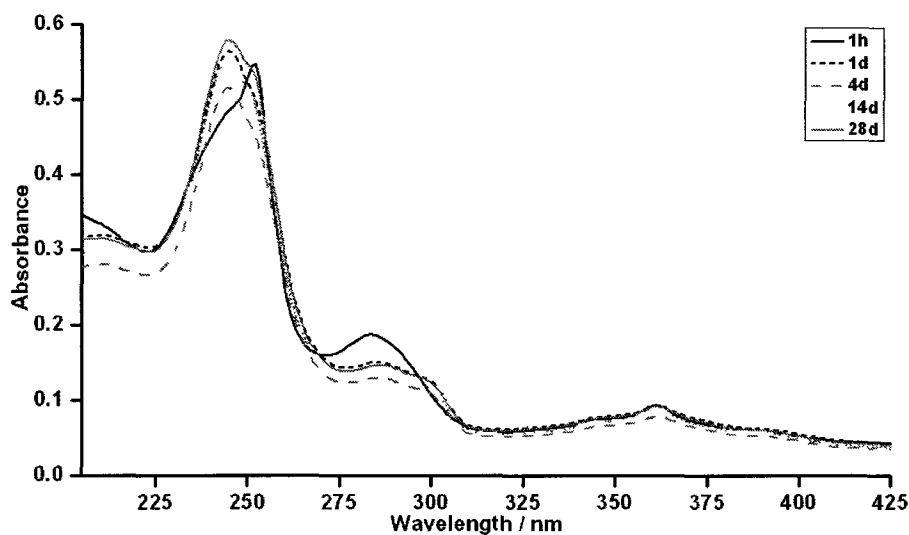


Figure 2.32: Time-dependent UV-vis spectrum of Acr-TBL in water.

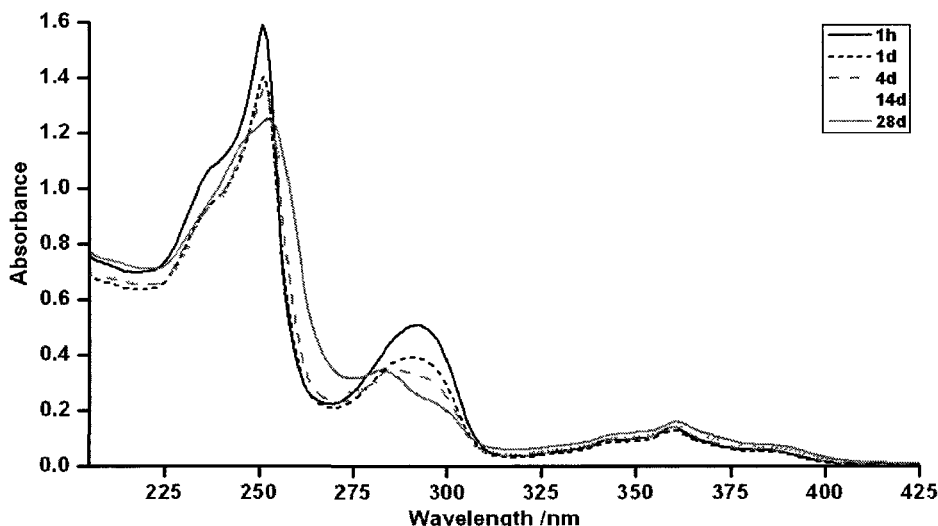


Figure 2.33: Time-dependent UV-vis spectrum of Acr-TBL in methanol.

As shown in Figures 2.32 and 2.33, there were some spectral differences for Acr-TBL when self-assembled in water and MeOH, which arise due to solvent polarity.²¹ In the case of water, the absorbance bands arising from $n \rightarrow \pi^*$ transitions within the twin RNTs were shifted to shorter wavelengths ($\lambda_{\text{max}} = 252 \text{ nm} \rightarrow \lambda_{\text{max}} = 246 \text{ nm}$, *hypsochromic shift*) as a result of increased solvation of the carbonyl lone pair of electrons. For the $\pi \rightarrow \pi^*$ transitions, a bathochromic shift ($\lambda_{\text{max}} = 283 \text{ nm} \rightarrow \lambda_{\text{max}} = 286 \text{ nm}$) was observed due to attractive polarization forces between the solvent molecules and the absorber, which lowers the energy levels of both the excited and unexcited states. As such, the wavelength difference between the $n \rightarrow \pi^*$ and $\pi \rightarrow \pi^*$ transitions increased in water as the RNTs grew over time ($\lambda_{\text{max}} = 252, 283 \text{ nm}$ for 1 h $\rightarrow \lambda_{\text{max}} = 246, 286 \text{ nm}$ for 28 days). The reverse trend was observed for the RNTs in MeOH with $n \rightarrow \pi^*$ ($\lambda_{\text{max}} = 251 \text{ nm}$, 1 h $\rightarrow \lambda_{\text{max}} = 253 \text{ nm}$, 28 days, and $\pi \rightarrow \pi^*$ ($\lambda_{\text{max}} = 292 \text{ nm}$, 1 h $\rightarrow \lambda_{\text{max}} = 283 \text{ nm}$, 28 days) transitions. In the UV region from 200-300 nm, both acridine and the bases have intense absorption bands, due to which this region was not suitable to follow any acridine-base interaction. The acridine fragment also has weak bands between 325 to 400 nm - a region free of GAC base residue absorptions. Thus, it was chosen to monitor potential changes on the acridine portion. It was speculated that if the acridine moiety inserted between two twin

rosettes, a significant hypochromic effect would be observed due to stacking interactions. The absence of hypochromism in this region for both water and MeOH samples ruled out the possibility of intercalation. This also indicates that stacking interactions between the G \wedge C rosettes and acridine units of neighbouring RNTs or between acridine units within the same RNT were not occurring during RNT growth.

2.3.3. Modification to the core structure

So far we studied the effect of the side-chain on the central nitrogen atom connecting the two G \wedge C units and established that the nature of the side-chain greatly influenced the self-assembly, aggregation and supramolecular chirality of the RNTs. By molecular modeling, it was found that the twin G \wedge C system self-organizes into a syn conformer.¹⁰ Though this syn conformer has favourable π - π stacking interactions, substitution on the exocyclic nitrogen can greatly affect the self-assembly process. Thus we designed RNTs with different substituents on the exocyclic nitrogen as compared to But-TBL. It was envisaged that a bulkier group would increase the steric repulsion between the G \wedge C moieties, thus disfavoring RNT formation. We therefore embarked on making analogues of the self-assembling building block But-TBL by varying the functionality on the exocyclic nitrogen of the G \wedge C heterocycles as shown below.

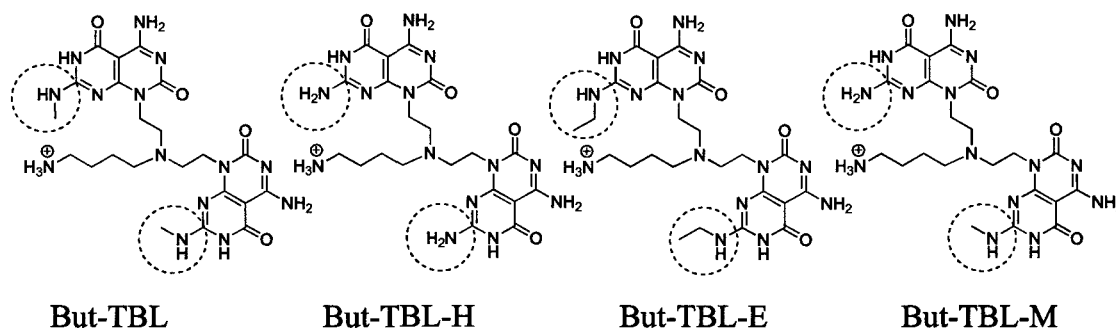


Figure 2.34: Variants of the twin RNT monomers with the modifications indicated for the core structure.

2.3.3.1. Synthesis of the modified core structures

The But-TBL-H analogue was synthesized as follows:

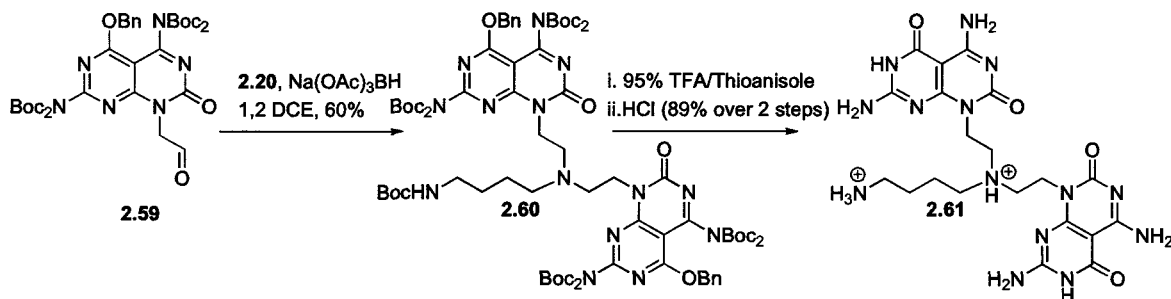


Figure 2.35: Synthetic scheme for the synthesis of But-TBL-H

Coupling of the aldehyde^{8d} **2.59** with *tert*-butyl 4-aminobutylcarbamate through a reductive amination reaction gave the protected dimer **2.60** in 60% yield. Removal of all the protecting groups using TFA, followed by anion exchange gave rise to the hydrochloride salt **2.61** in 89% yield. Compared to But-TBL, in this molecule the secondary methylamine group was replaced by a primary amino group, hence it was sterically less hindered.

The main precursor to the synthesis of But-TBL-E was the aldehyde **2.70**, which was synthesized according to the synthetic plan illustrated in Figure 2.36. A nucleophilic substitution reaction on 4-(allylamino)-2,6-dichloropyrimidine-5-carbaldehyde using ethylamine produced 4-(allylamino)-6-chloro-2-(ethylamino)pyrimidine-5-carbaldehyde (**2.62**) in 74% yield. The product was subjected to another nucleophilic substitution reaction using benzyl alcohol to afford 4-(allylamino)-6-(benzyloxy)-2-(ethylamino)pyrimidine-5-carbaldehyde (**2.63**) in 75% yield. The selective Boc protection of the exocyclic ethylamine gave *tert*-butyl 4-(allylamino)-6-(benzyloxy)-5-formylpyrimidin-2-ylethylcarbamate (**2.64**) in 90% yield. Subsequent reaction of the aldehyde functionality with hydroxylamine hydrochloride gave rise to compound **2.65** in 90%, which was then subjected to a dehydration reaction using trifluoroacetic anhydride to produce *tert*-butyl 4-(allylamino)-6-(benzyloxy)-5-cyanopyrimidin-

2-ylethylcarbamate (**2.66**) in 93% yield. Reaction of **2.66** with *N*-chlorocarbonylisocyanate followed by cyclization in a concentrated methanolic solution of ammonia gave rise to *tert*-butyl 1-allyl-4-amino-5-(benzyloxy)-1,2-dihydro-2-oxopyrimido[4,5-*d*]pyrimidin-7-ylethylcarbamate (**2.68**) in 74% yield over two steps. The primary amino group of the cyclized product **2.68** was protected using Boc_2O to give the desired compound **2.69** in 90% yield. Finally, the allyl group was subjected to a Lemieux-Johnson transformation to furnish the corresponding aldehyde **2.70** in 57% yield over two steps.

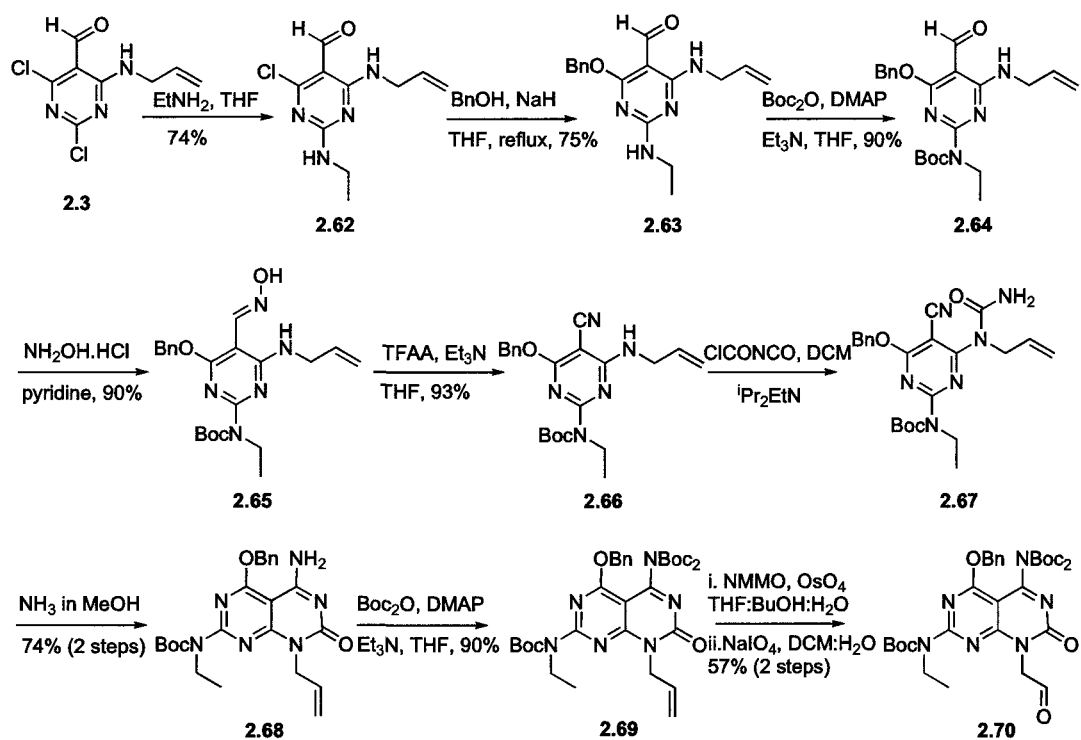


Figure 2.36: Synthetic scheme for the synthesis of ethyl modified GAC aldehyde **2.70**.

The aldehyde **2.70** was coupled to *tert*-butyl 4-aminobutylcarbamate through a reductive amination reaction to produce the protected dimer **2.71** in 73% yield. Deprotection using TFA in the presence of thioanisole, followed by anion exchange gave rise to the hydrochloride salt **2.72** in 87% yield. While this new

variant (But-TBL-E) possessed all the requirements for RNTs formation, it also had a bigger steric bulk on the exocyclic nitrogen as compared to But-TBL.

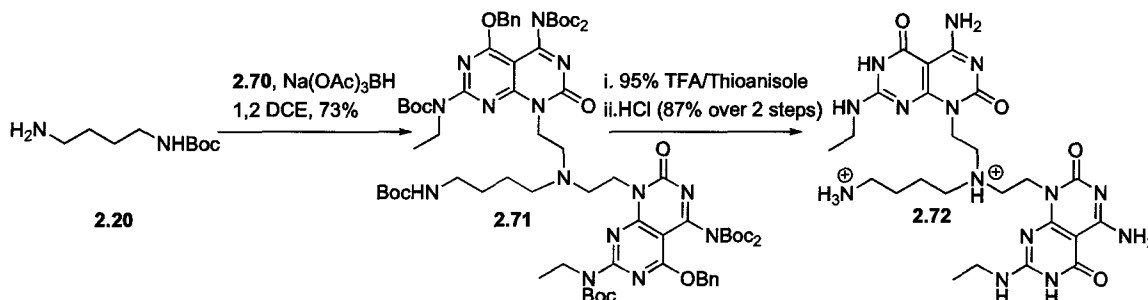


Figure 2.37: Synthetic scheme for the synthesis of But-TBL-E (2.72).

The heterogeneous variant of But-TBL was synthesized using the aldehydes 2.59 and 2.13, whereby the molecule consisted of two different GAC moieties, with one having a primary amino group and the other one possessing a secondary methyl amino group. The aldehyde 2.59 was coupled to *tert*-butyl 4-aminobutylcarbamate through a reductive amination reaction. Once the first coupling was completed, the crude product was reacted with aldehyde 2.13 to produce the heterogeneous dimer 2.73 in 40% yield. Cleavage of the acid-labile protecting groups under the acidic conditions, followed by anion exchange gave rise to the hydrochloride salt 2.74 in good yield.

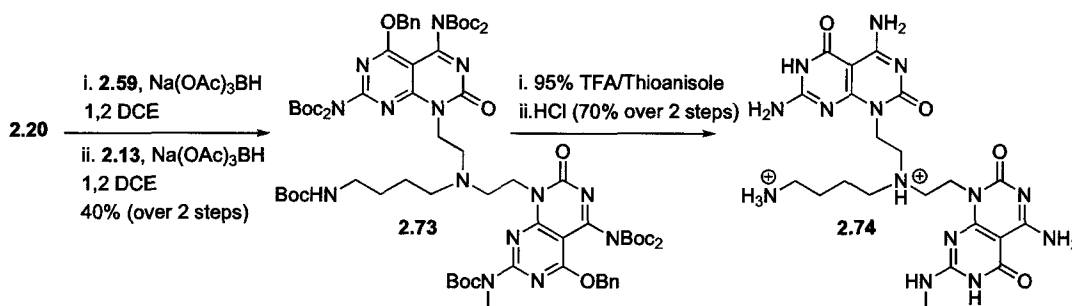


Figure 2.38: Synthetic scheme for the synthesis of But-TBL-M.

2.3.3.2. Microscopy characterization of the RNTs with modified core structures

Stock solutions of the monomers (But-TBL, But-TBL-H, But-TBL-E, But-TBL-M), isolated as HCl salts were prepared at a concentration of 0.5 mg/mL in methanol. The samples were aged and aliquots of the solutions were diluted to 0.0125 mg/mL and cast on TEM grids and freshly cleaved mica surfaces for the morphology visualization. The SEM, TEM and AFM images (Figure 2.45) are for samples aged for 3 days except for But-TBL-E module, which was aged for 14 days. Results from these characterization techniques and molecular modeling are summarized in Figure 2.46.

The values obtained from AFM are lower than those obtained by TEM due to compression arising from the interaction with the tip.¹¹ Although TEM measurements revealed that the diameters of But-TBL (B), But-TBL-H (E), But-TBL-E (H) and But-TBL-M (K) were of negligible difference, the lengths of But-TBL-E RNTs, which feature the two ethyl groups, were shorter than the other three as seen by the SEM and AFM images. This demonstrates that functional groups on the exocyclic nitrogen larger than methyl do in fact destabilize the RNTs as the rosettes π - π stack and thereby provides yet another alternative means of tailoring the stability and length distribution of the RNTs.

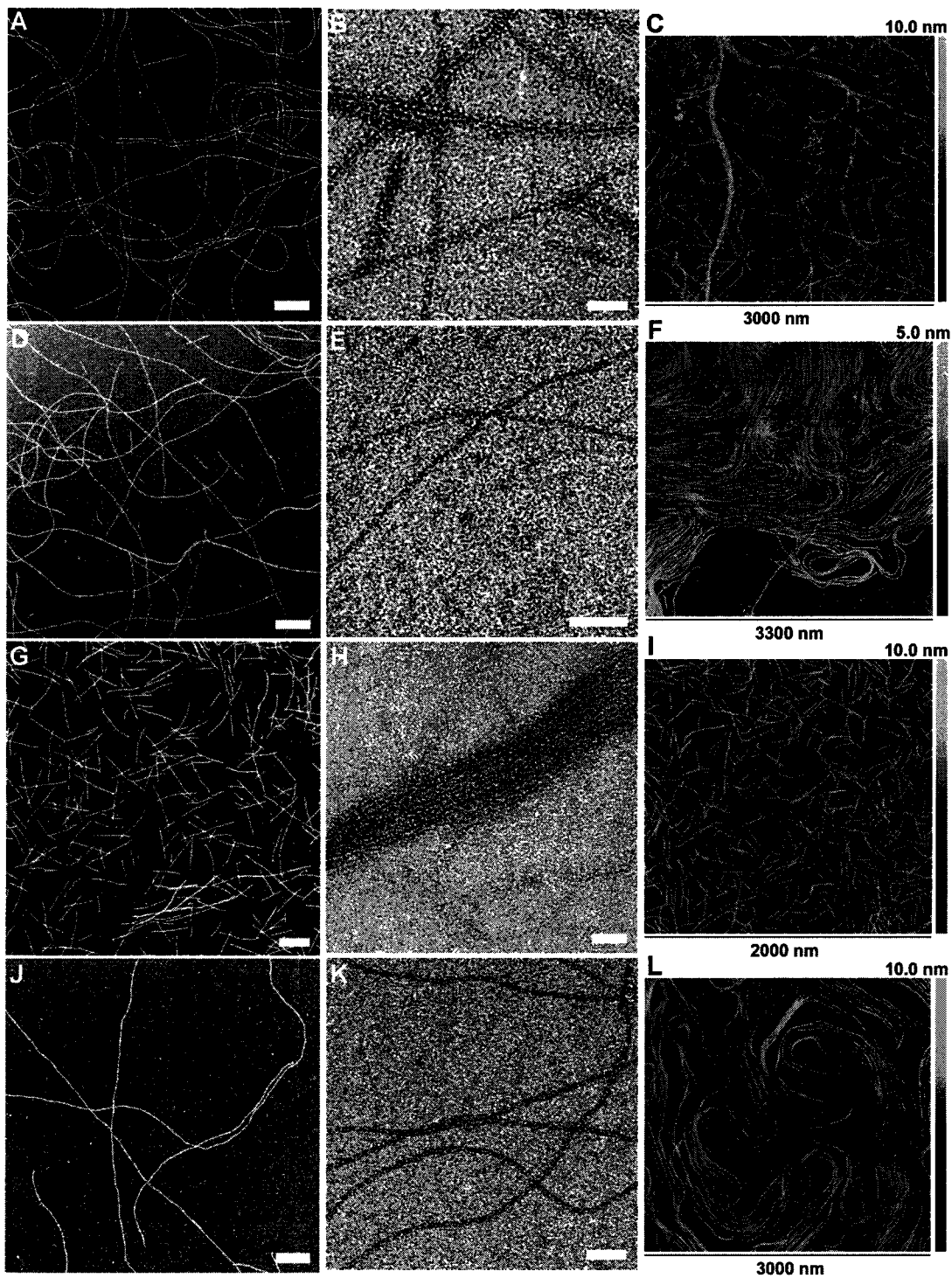


Figure 2.39: SEM (first column), TEM (second column) and AFM (third column) images of But-TBL (first row), But-TBL-H (second row), But-TBL-E (third row) and But-TBL-M (fourth row). The scale bars for the SEM images are 200 nm and for the TEM images are 20 nm.

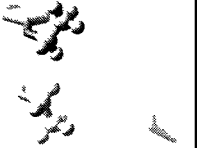
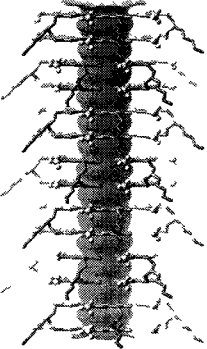
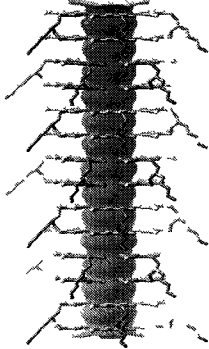
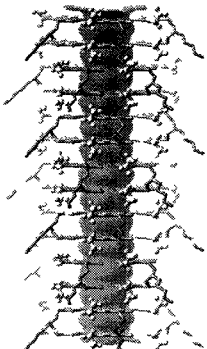
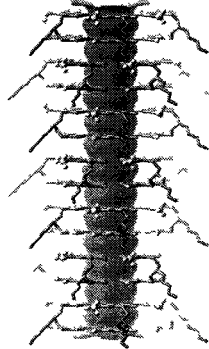
Monomers	But-TBL	But-TBL-H	But-TBL-E	But-TBL-M
Structure of motif				
RNT structure				
Diameter by AFM / nm	2.9 ± 0.2	3.0 ± 0.1	3.0 ± 0.2	3.0 ± 0.1
Diameter by TEM / nm	3.5 ± 0.2	3.5 ± 0.2	3.6 ± 0.2 nm	3.6 ± 0.2 nm
Calculated diameter / nm	3.8	3.8	3.8	3.8

Figure 2.40: Summary of diameters of compounds with modified core structures using AFM and TEM imaging, along with their structures generated using molecular modeling.

2.4. Conclusion

The self-assembly of twin G \wedge C motif-based RNTs with controlled stability demands a delicate balance of both environmental factors and structural elements. This chapter has introduced several newly synthesized twin G \wedge C compounds with different functional groups, core modification and steric bulk. The RNT forming ability of these compounds were investigated under different conditions, including solvent systems, charge density and counterions. The relative stability of the RNTs was investigated by comparison of their abundance and length distribution in solution. Solvent choice is one key component in the self-assembly process, as it determines the extent of solvation of positively charged twin-motif and negatively charged counterions present. In general, it was found that longer and more abundant RNTs were formed in methanol than in water due to decreased cation and anion solvation and tighter ion pairs. Less polarizable counterions, such as chloride, led to the formation of longer RNTs. It was found that the solvent system and counterions affected the supramolecular chirality of RNTs derived from chiral twin G \wedge C building blocks. The molecular structure of the RNT forming motif also had a big impact on the length, abundance, dispersion and supramolecular chirality of the higher order aggregates. Through UV-vis study, it was found that the acridine moieties from the acridine functionalized RNTs was not intercalating between the rosettes. Although the aromatic acridine unit does not appear to affect the π - π stacking of rosettes, bisalkylated adducts (such as Di-Me-TBL) which have groups greater than 4.0 Å in diameter, will likely decrease the stability of the RNTs by disrupting these stacking interactions. In a similar manner, changing the core structure of the motif from expressing a methylamine to an ethylamine group undoubtedly destabilizes the RNTs through a similar mechanism. Finally, using results from this chapter, the polarity, hydrophobicity and charge density could be tuned to generate longer RNTs.

2.5. Experimental Section

2.5.1. General procedures

2.5.1.1. Self-assembly

Stock solutions of 0.5 mg/mL (average concentration of 6.68×10^{-4} M for samples, except 4.92×10^{-4} M for G0, K-TBL and Acr-TBL) of RNTs or as indicated in the results were prepared by dissolving the RNT-forming motifs either in deionized water (dH₂O) or HPLC grade methanol. The solutions were then sonicated for 5 min, heated for 10 s using a heat gun and then filtered through a 0.25 μ m Whatmann filter membrane. The stock solutions were then allowed to age at room temperature. Aliquots from these RNT stock solutions were diluted and used for CD and UV-vis experiments as well as imaging by AFM, SEM and TEM.

2.5.1.2. SEM imaging

Stock solutions of the twin bases (0.5 mg/mL, average concentration of 6.68×10^{-4} M for samples, except 4.92×10^{-4} M for G0, K-TBL and Acr-TBL) of RNTs were prepared by dissolving the RNT-forming motifs either in dH₂O or MeOH. The solutions were diluted to 0.025 or 0.0125 mg/mL with dH₂O or MeOH (as indicated) prior to imaging. The SEM samples were prepared by floating a carbon-coated 400-mesh copper grid (Electron Microscopy Sciences) on a droplet of the diluted RNT solution for 10 s. The grid was blotted using filter paper. The RNT-coated grid was then air-dried and heated on a hotplate (100 °C) for 15 min before imaging to remove any residual solvents. All SEM images were obtained without negative staining (unless indicated otherwise), at 5 kV accelerating voltage and a working distance of 5.0 mm or at 30 kV accelerating voltage and a working distance of 7.0 mm on a high resolution Hitachi S-4800 cold field emission SEM.

2.5.1.3. Histograms

The histograms correspond to the rosette nanotube length distributions for the depicted SEM images. Though quantifying all the monomers involved in rosettes

at all stages of self-assembly would be the ideal representation of self-assembly, it is a challenging process due to the instrument limitations. As such, visible nanotubes ranging from 10 - 2000 nm on the SEM images were measured. The rosette nanotube formation is the consequence of stacking interactions between the rosettes, which is fueled by a number of favourable interactions, and is a fair approximation depicting the degree of self-assembly. The sum of the length of all visible nanotubes by SEM imaging, was obtained. The percentage of each length range was calculated and histograms representing the length distribution for the images were obtained using OriginPro software.

2.5.1.4. AFM imaging

For AFM imaging, one drop of the diluted RNT solution was deposited onto a freshly cleaved mica substrate (1 cm²) for 10 s and excess solution was blotted using filter paper. The sample surface was imaged using a Digital Instruments/ Veeco Instruments MultiMode Nanoscope IV AFM equipped with an E scanner in tapping mode. Silicon cantilevers (MikroMasch USA, Inc.) with low spring constants of 4.5 N/m, a scan rate of 0.5-1 Hz and amplitude setpoint of 1 V were used. The diameter values obtained by AFM are lower than the average value obtained from TEM measurements. This is most likely due to the flattening of the soft organic RNTs upon the tapping of the AFM tip, thus leading to a smaller measured diameter value.

2.5.1.5. TEM imaging

TEM imaging was performed on a Hitachi HF3300 microscope operating at 200 kV. Compounds were prepared as described in the self-assembly section and aged for 2 weeks (unless indicated otherwise). An aliquot (0.02 mL) of each of the solutions was deposited on a 400-mesh carbon coated grid (Electron Microscopy Sciences), then blotted after 10 s using filter paper. The samples were negatively stained with either 2% uranyl acetate. Uranyl acetate solutions were prepared by dissolving uranyl acetate crystals in MeOH or in dH₂O by sonicating for 10 min. The stains were then filtered through a 0.25 µm Whatmann filter

membrane and stored in the dark at room temperature for subsequent uses. All samples were air-dried before imaging and heated on a hotplate (100 °C) for 15 min prior to imaging to remove any residual solvents. The average diameters of the nanotubes were determined by randomly measuring individual assemblies using Digital Micrograph software (version 3.9.3 by Gatan).

2.5.1.6. CD spectroscopy

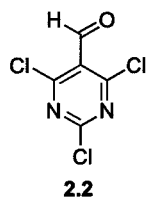
All circular dichroism spectra were recorded on a JASCO J-810 spectropolarimeter. Samples were scanned from 350-200 nm at a rate of 100 nm/min. Stock solutions (0.5 mg/mL) of the chiral samples were prepared in dH₂O or MeOH aged for different time intervals at room temperature. Their CD spectra were recorded by taking aliquots of the stock solutions and diluting them to (0.025 mg/mL, 3.34×10^{-5} M for R-TBL, S-TBL and 2.46×10^{-5} M for G0, K-TBL) at 10°C in dH₂O or MeOH.

2.5.1.7. General methods

Unless otherwise noted, all reactions were performed under an atmosphere of N₂ using oven-dried glassware equipped with a magnetic stirrer and rubber septum. Reagent grade solvents CH₂Cl₂, THF, Et₂O and CH₃OH were purified on an MBraun solvent purification system prior to use. All other commercial reagents were used without purification unless otherwise stated. Reactions were monitored by TLC analysis using silica-coated TLC plates and visualized under UV light. ¹H and ¹³C NMR spectra were recorded in the specified deuterated solvent. The NMR data is presented as follows: chemical shift, peak assignment, multiplicity, coupling constant, integration. Residual ¹H shifts in CDCl₃ (7.24 ppm) and d₆-DMSO (2.5 ppm) were used as the internal references where stated for ¹H NMR. The following abbreviations were used to explain the multiplicities: s = singlet, d = doublet, t = triplet, m = multiplet, bs = broad singlet. CDCl₃ (77.0 ppm), d₆-DMSO (39.5 ppm) were used as the internal references for ¹³C NMR as stated.

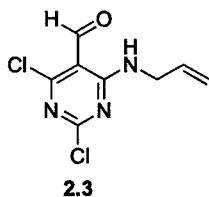
2.5.2 Synthesis of target molecules

2, 4, 6-trichloropyrimidine-5-carbaldehyde (2.3)^{8a}



POCl₃ (300 mL, 3210 mmol), barbituric acid (60 g, 469 mmol) and *N, N*-dimethylformamide (27.2 mL, 469 mmol) were added at room temperature and stirred under N₂. The mixture was allowed to reflux for 20 h and was then cooled down to room temperature. Excess POCl₃ was then removed by simple distillation, and the resulting brown viscous liquid was gently added to crush ice (~1000 g) with continuous stirring. The resulting pale brown precipitate was then filtered, washed with dH₂O (2 L) and dried under high vacuum. Recrystallization from EtOAc and hexanes gave the desired compound C₅HCl₃N₂O (**2.2**) as pale yellow crystals in 85% yield. R_f = 0.37 (10% EtOAc in hexanes); ¹H NMR (400 MHz, CDCl₃): δ = 10.42 (s, 1H).

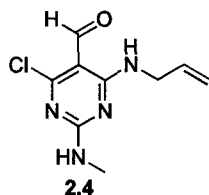
4-(allylamino)-2, 6-dichloropyrimidine-5-carbaldehyde (2.3)^{8a}



To a stirred solution of **2.2** (84 g, 397 mmol) in CH₂Cl₂ at -78°C, allylamine (60 mL, 801 mmol) was added gradually under nitrogen. The resulting mixture was stirred at -78 °C for 2 h and then allowed to -20 °C warm up for 3 h. The reaction was then quenched with dH₂O and extracted with CH₂Cl₂. The organic layers were combined and washed with dH₂O (60 mL), brine (30 mL), and then dried over anhydrous Na₂SO₄ to yield a crude yellow solid. Recrystallization using CH₂Cl₂ and hexanes gave rise to the desired product C₈H₇Cl₂N₃O (**2.3**) as a pale yellow solid in 82% yield. R_f = 0.34 (10% EtOAc in hexanes); ¹H NMR (300 MHz,

CDCl₃): δ = 10.34 (s, 1H), 9.39 (bs, 1H), 5.97-5.86 (m, 1H), 5.32-5.22 (m, 2H), 4.26-4.21 (m, 2H).

4-(allylamino)-6-chloro-2-(methylamino)pyrimidine-5-carbaldehyde (2.4)^{8a}



Methylamine (2.0 M solution in THF, 15.6 mL, 432 mmol) was added to solution of **2.3** (50.0g, 216 mmol) in THF 0 °C under N₂. The reaction mixture was stirred at 0 °C for 2 h. Removal of solvent under reduced pressure afforded the crude product as off-white solid. Recrystallization using CH₂Cl₂ and hexanes gave rise to the desired product C₉H₁₁N₄O **2.4** as a white crystalline solid in 97% yield. R_f = 0.21 (10% EtOAc in hexanes); ¹H NMR (300 MHz, CDCl₃): δ = 10.05 (s, 1H), 9.39 (bs, 1H), 6.00-5.90 (m, 1H), 5.74 (bs, 1H), 5.25 (d, *J* = 17.1 Hz, 2H), 5.17 (d, *J* = 10.2 Hz, 2H), 4.19 (t, *J* = 5.6 Hz, 2H), 3.01 (d, *J* = 4.8 Hz, 3H).

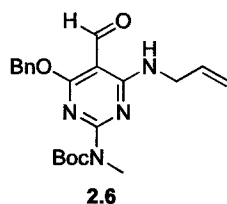
4-(allylamino)-6-(benzyloxy)-2-(methylamino)pyrimidine-5-carbaldehyde (2.5)^{8a}



Benzyl alcohol was added (27.3 mL, 264 mmol) to a solution of NaH (7.80 g, 325 mmol) in THF at room temperature under N₂ and stirred for 15 min. The solution was cooled to 0 °C and then added gradually to a solution of **2.4** (30.0 g, 132 mmol) in THF. The mixture was warmed to room temperature and then refluxed for 22 h, after which it was then cooled to 0°C and quenched with saturated NH₄Cl. Removal of solvent under reduced pressure gave a brown paste. The latter was dissolved in DCM, washed with dH₂O (100 mL), brine (50 mL) and dried over anhydrous Na₂SO₄. Evaporation followed by flash column

chromatography (0-5% EtOAc in hexanes) yielded the desired compound $C_{16}H_{18}N_4O_2$ as a pale yellow solid (**2.5**) in 77% yield. $R_f = 0.45$ (30% EtOAc in hexanes); 1H NMR (400 MHz, $CDCl_3$): $\delta = 9.98$ (s, 1H), 9.34 (bs, 1H), 9.17 (bs, 1H), 7.37-7.28 (m, 5H), 5.96-5.90 (m, 1H), 5.50 - 5.10 (m, 4H), 4.17 (m, 2H), 3.07 (d, $J = 5.2$ Hz, 3H).

***tert*-butyl 4-(allylamino)-6-(benzyloxy)-5-formylpyrimidin-2-yl(methyl)-carbamate (**2.6**)^{8a}**



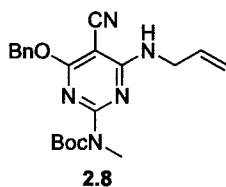
4-*N,N*-dimethylaminopyridine (8.07 g, 66.0 mmol) and triethylamine (56 mL, 288 mmol) were added to a solution of **2.5** (39.5 g, 132 mmol) in THF at room temperature under N_2 . After 5 min of stirring, Boc_2O (57.6 g, 264 mmol) was added and the reaction mixture was stirred for 24 h. The reaction was quenched with dH_2O (50 mL) and solvent was removed under reduced pressure. The crude product was washed with dH_2O (100 mL), 5% aqueous $NaHCO_3$ (100 mL) and brine (100 mL), along with extraction using EtOAc. Drying over anhydrous Na_2SO_4 , followed by solvent removal under reduced pressure afforded a yellow solid, which was purified by flash column chromatography (0-5% EtOAc in hexanes). The desired compound $C_{21}H_{26}N_4O_4$ was obtained as pale yellow solid (**2.6**) in 88 % yield. $R_f = 0.34$ (10% EtOAc in hexanes); 1H NMR (400 MHz, $CDCl_3$): $\delta = 10.15$ (s, 1H), 9.20 (t, $J = 5.7$ Hz, 1H), 7.42 - 7.30 (m, 5H), 5.94-5.87 (m, 1H), 5.49 (s, 2H), 5.25-5.12 (m, 2H), 4.19 (t, $J = 5.6$ Hz, 2H), 3.38 (s, 3H), 1.55 (s, 9H).

(E)-tert-butyl-4-(allylamino)-6-(benzyloxy)-5-((hydroxyimino)methyl)-pyrimidin-2-yl(methyl)carbamate (2.7)^{8a}



KHCO₃ (46.5 g, 465 mmol) and hydroxylamine hydrochloride (16.3 g, 232 mmol) were added to a stirred solution of **2.6** (46.5 g, 117 mmol) in anhydrous methanol (50 mL) at room temperature under N₂. The resulting slurry was refluxed for 3 h and then cooled to room temperature and the solvent was removed under reduced pressure. The residual solid was dissolved in EtOAc (500 mL), washed with dH₂O (50 mL) and brine (10 mL), and the organic layer was dried over anhydrous Na₂SO₄. Evaporation of the solvent gave rise to the desired compound C₂₁H₂₇NO₄ as a white solid (**2.7**) in 88% yield. This material was used in the next step without further purification. *R*_f = 0.51 (30% EtOAc in hexanes); ¹H NMR (300 MHz, CDCl₃): δ = 8.56 (s, 1H), 8.03 (t, *J* = 5.3 Hz, 1H), 7.44-7.29 (m, 5H), 5.99-5.89 (m, 1H), 5.42 (s, 2H), 5.23-5.10 (m, 3H), 4.22-4.12 (m, 2H), 3.36 (s, 3H), 1.54 (s, 9H).

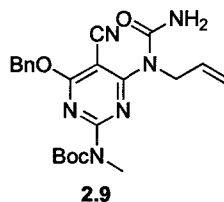
tert-butyl 4-(allylamino)-6-(benzyloxy)-5-cyanopyrimidin-2-yl(methyl)carbamate (2.8)



Compound **2.7** (42.6 g, 103 mmol), Et₃N (50.0 mL, 364 mmol), and THF (700 mL) were cooled to 0°C, then trifluoroacetic anhydride (28.0 mL, 201 mmol) was slowly added over 2 h. The reaction mixture was allowed to warm to room temperature and was refluxed for 3 h. After cooling down to room temperature, the reaction was quenched with dH₂O and the solvent was removed under reduced pressure. The residual solid was dissolved in EtOAc (300 mL), washed with dH₂O

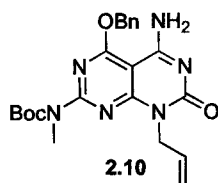
(50 mL), 5% aqueous NaHCO₃ (20 mL), and brine (20 mL). The organic layer was dried over anhydrous Na₂SO₄, filtered, and evaporated to yield a brown solid, which was purified by flash chromatography (0-30% EtOAc in hexanes). Purification of the orange crystals by recrystallizing from EtOAc and hexanes gave the desired product C₂₁H₂₅N₅O₃ as pale yellow crystals (**2.8**) in 83% yield. *R_f* = 0.63 (30% EtOAc in hexanes); ¹H NMR (400 MHz, CDCl₃): δ = 7.43-7.30 (m, 5H), 5.89-5.83 (m, 1H), 5.45 (s, 2H), 5.41 (t, *J* = 7.2 Hz, 1H), 5.25-5.15 (m, 2H), 4.15-4.12 (m, 2H), 3.38 (s, 3H), 1.52 (s, 9H).

***tert*-butyl-4-(1-allylureido)-6-(benzyloxy)-5-cyanopyrimidin-2-yl(methyl)-carbamate (**2.9**)^{8a}**



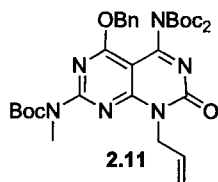
Freshly distilled *N*-chlorocarbonylisocyanate (13.8 mL, 172.0 mmol) was added dropwise to a solution of compound **2.8** (34.0 g, 86.0 mmol) in CH₂Cl₂ (120 mL) at 0°C over a period of 30 min under N₂. The reaction mixture was allowed to stir for another 2h at room temperature. The reaction mixture was cooled to 0°C and carefully quenched with dH₂O (50 mL, exothermic reaction). The product was extracted with CH₂Cl₂ (500 mL) and the resulting organic layer was washed with dH₂O (2 x 50 mL) and brine (50 mL) and dried over anhydrous Na₂SO₄. Filtration and evaporation of the organic solvents under reduced pressure yielded **2.9** C₂₂H₂₆N₆O₄ in 91% as a viscous liquid, which was used in the next step without further purification. *R_f* = 0.16 (30% EtOAc in hexanes); ¹H NMR (300 MHz, CDCl₃): δ = 7.46-7.32 (m, 5H), 5.93-5.88 (m, 1H), 5.61 (s, 2H), 5.18 (m, 2H), 4.92 (m, 2H), 3.45 (s, 3H), 1.55 (s, 9H).

***tert*-butyl-8-allyl-5-amino-4-(benzyloxy)-7-oxo-7,8-dihydropyrimido[4,5-*d*]-pyrimidin-2-yl(methyl)carbamate (2.10)^{8a}**



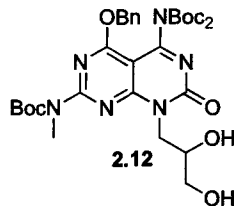
Compound **2.9** (19.89 g, 45.4 mmol) was stirred in 7 M NH₃ in CH₃OH (35 mL) under N₂ at room temperature for 3 h. Excess NH₃ in CH₃OH was removed under reduced pressure and the desired compound **2.10** C₂₂H₂₆N₆O₄ was obtained as a white solid in 99% yield. This crude material was used for the next step without further purification. R_f = 0.26 (EtOAc); ¹HNMR (300 MHz, CDCl₃): δ = 7.45-7.31 (m, 5H), 5.91-5.80 (m, 1H), 5.52 (s, 2H), 5.30-5.15 (m, 2H), 5.15-4.92 (m, 2H), 3.40 (s, 3H), 1.52 (s, 9H).

Compound 2.11^{8a}



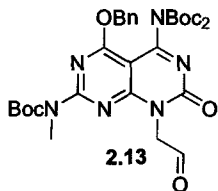
4-*N,N*-dimethylaminopyridine (10.0 g, 82.0 mmol), Et₃N (65.0 mL, 467 mmol) and Boc₂O (74.0 g, 308 mmol) were added to a stirred solution **2.10** (34.0 g, 77.5 mmol) in THF (100 mL), under N₂. After stirring for 24 h at room temperature, the reaction was quenched with dH₂O (30 mL) and the solvent was removed under reduced pressure. The residual solid was dissolved in EtOAc (300 mL), washed with dH₂O (25 mL), 5% aqueous NaHCO₃ (50 mL), brine (50 mL) and dried over anhydrous Na₂SO₄. Removal of solvent afforded the crude product, which was purified through column chromatography (0-50% EtOAc in hexanes) to give the desired product **2.11** C₃₂H₄₂N₆O₈ as a white foam in 75% yield. R_f = 0.65 (50% EtOAc in hexanes); ¹H NMR (400 MHz, CDCl₃): δ = 7.43-7.29 (m, 5H), 5.97-5.89 (m, 1H), 5.54 (s, 2H), 5.17 (m, 2H), 4.92 (m, 2H), 3.43 (s, 3H), 1.56 (s, 9H), 1.30 (s, 18H).

Compound 2.12^{8a}



50% aqueous *N*-methylmorpholine *N*-oxide (28.0, 59.0 mmol) was added to a stirred solution of compound 2.11 (37.0 g, 57.9 mmol) in *t*-BuOH / dH₂O (8:1, 1080 mL) at room temperature and stirred for 5 min. OsO₄ (0.031 M solution in *t*-BuOH, 30 mL, 0.932 mmol) was slowly added and the resulting brown solution was stirred for 24 h. The reaction mixture was quenched with aqueous sodium sulfite until all the excess OsO₄ was destroyed (brown solution turns colorless). Diol 2.12 was extracted in CHCl₃ (300 mL) and washed with dH₂O (50 mL) and brine (50 mL). The organic layer was dried over anhydrous Na₂SO₄, filtered, and evaporated under reduced pressure to yield the compound 2.12 C₃₂H₄₄N₆O₁₀ as a white foam in 91%. The crude product was used in the next step without further purification. *R*_f = 0.15 (60% EtOAc in hexanes); ¹H NMR (400 MHz, CDCl₃): δ = 7.43-7.34 (m, 5H), 5.56 (s, 2H), 4.59 (dd, *J* = 4.0, 4.0 Hz, 2H), 4.14 (q, *J* = 4.8 Hz, 1H), 4.08 (d, *J* = 5.2 Hz, 1H), 3.56 (q, *J* = 5.0 Hz, 2H), 3.47 (s, 3H), 3.28 (t, *J* = 7.0 Hz, 1H), 1.58 (s, 9H), 1.35 (s, 9H), 1.34 (s, 9H).

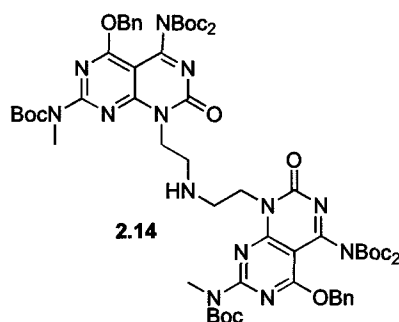
Compound 2.13^{8a}



Sodium periodate (22.3 g, 104.4 mmol) was added to a stirred solution of compound 2.12 (35.1 g, 52.2 mmol) in CH₂Cl₂ / dH₂O (4:1, 925 mL) and stirred at room temperature for 24 h. The mixture was then filtered through a pad of celite and washed with CH₂Cl₂ (200 mL). Separation and evaporation of the organic layer under reduced pressure followed column chromatography (0-30% EtOAc in hexanes) yielded compound 2.13 C₃₁H₄₀N₆O₉ as a white foam in 94% yield. *R*_f =

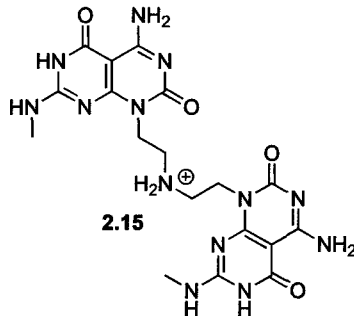
0.45 (30% EtOAc in hexanes); ^1H NMR (400 MHz, CDCl_3): δ = 9.62 (s, 1H), 7.43-7.32 (m, 5H), 5.56 (s, 2H), 5.12 (s, 2H), 3.37 (s, 3H), 1.55 (s, 9H), 1.32 (s, 18H).

Compound 2.14



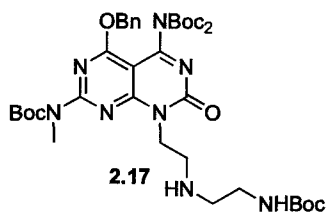
Compound **2.13** (0.100 g, 0.155 mmol) was added to a solution of 7 M NH_3 in MeOH (0.022 mL, 0.155 mmol) in 1,2 DCE (20 mL) at room temperature under N_2 and stirred for 30 min. Sodium triacetoxy borohydride (0.039 g, 0.186 mmol) was added and the resulting mixture was stirred for an additional 2 h. Another equivalent of **2.13** (0.100 g, 0.155 mmol) was added to the reaction mixture and upon stirring for 30 min, sodium triacetoxy borohydride (0.039 g, 0.186 mmol) was added. Stirring was maintained for an additional 15 h. The reaction mixture was diluted with CH_2Cl_2 (50 mL) and washed with water (10 mL), brine (15 mL), dried over Na_2SO_4 and concentrated. Flash chromatography of the residue over silica gel (0-5% MeOH in CH_2Cl_2) gave **2.14** (0.150, 76%) as a white foam. R_f = 0.56 (5% MeOH in CH_2Cl_2); ^1H NMR (500 MHz, CDCl_3): δ = 7.47-7.31 (m, 10H), 5.58 (s, 4H), 4.37 (t, J = 7.0 Hz, 4H), 3.50 (s, 6H), 2.90 (t, J = 6.9 Hz, 4H), 1.75 (bs, 1H), 1.56 (s, 18H), 1.30 (s, 36H); ^{13}C NMR (125 MHz, CDCl_3): δ = 165.6, 161.1, 161.0, 160.3, 155.8, 152.5, 149.2, 134.9, 128.6, 128.5, 128.4, 92.9, 83.6, 83.0, 70.0, 46.7, 43.1, 34.9, 28.1, 27.8 ppm; HRMS: calcd for $\text{C}_{62}\text{H}_{84}\text{N}_{13}\text{O}_{16}\text{N} [\text{M}+\text{H}]^+$: 1266.6154; found: 1266.6159.

Compound 2.15



Compound **2.14** (0.042 g, 0.033 mmol) was stirred in a 95% TFA in thioanisole (10 mL) for 72 h. Et₂O (60 mL) was then added to the reaction mixture and the precipitate formed, was centrifuged down. The residual solid was resuspended in Et₂O, sonicated and centrifuged down. This process was repeated until the spotting of the Et₂O produced no UV active spot. The solid was dried and then dissolved in 1 M hydrochloric acid (10 mL), followed by removal of water under reduced pressure. This process was repeated two more times before the solid was dried under vacuo for 72 h to give **2.15** (0.022 g, 97%) as an off-white powder; ¹H NMR (600 MHz, d₆-DMSO + 2 drops of TFA): δ = 12.28 (bs, 2H), 9.20 (s, 2H), 8.87 (bs, 4H), 8.57 (app. q, 2H, *J* = 4.2 Hz), 4.32 (t, 4H, *J* = 5.1 Hz), 3.29 (m, 4H), 2.91 (d, 6H, *J* = 4.8 Hz); ¹³C NMR (150 MHz, d₆-DMSO): δ = 161.4, 160.5, 156.4, 156.0, 148.8, 83.0, 46.1, 39.0, 28.5 ppm; HRMS: calcd for C₁₈H₂₄N₁₃O₄ [M+H]⁺: 486.2069; found: 486.2065; elemental analysis calcd (%) for C₁₈H₂₃N₁₃O₄(HCl)₄(H₂O)_{1.33}(Et₂O)_{0.33}: C 34.15, H 4.89, N 26.78; found: C 34.36, H 4.49, N 26.40.

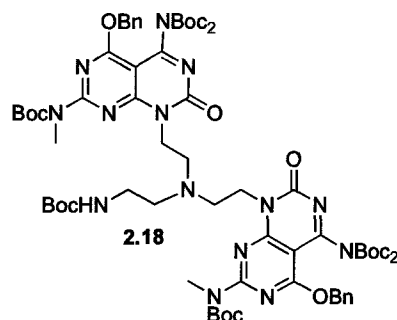
Compound 2.17



Compound **2.13** (0.150 g, 0.234 mmol) was added to a solution of *tert*-butyl 4-aminoethylcarbamate (0.43 mL, 0.263 mmol) in 1,2 DCE (20 mL) at room temperature under N₂ and stirred for 30 min. Sodium triacetoxy borohydride

(0.060 g, 0.286 mmol) was added and the resulting mixture was stirred for an additional 15 h. The reaction mixture was diluted with CH₂Cl₂ (50 mL) and then washed with water (10 mL), brine (15 mL), dried over Na₂SO₄ and concentrated. Flash chromatography of the residue over silica gel using (0-10% MeOH in EtOAc) gave **2.17** (0.126 g, 69%) as a white foam. R_f = 0.42 (10% MeOH in EtOAc); ¹H NMR (500 MHz, CDCl₃): δ = 7.45-7.31 (m, 5H), 5.56 (s, 2H), 4.94 (bs, 1H), 4.44 (t, *J* = 8.3 Hz, 2H), 3.46 (s, 3H), 3.17 (app. q, *J* = 7.0 Hz, 2H), 3.00 (t, *J* = 8.3 Hz, 2H), 2.75 (t, *J* = 7.3 Hz, 2H), 1.58 (s, 9H), 1.42 (s, 9H), 1.33 (s, 18H); ¹³C NMR (125 MHz, CDCl₃): δ = 165.8, 161.2, 161.0, 160.4, 160.5, 156.1, 155.9, 152.6, 149.3, 134.9, 128.6, 128.5, 128.4, 93.0, 83.8, 83.1, 70.1, 48.8, 46.8, 43.2, 40.4, 34.9, 28.5, 28.2, 28.1, 27.8 ppm; HRMS: calcd for C₃₈H₅₇N₈O₁₀ [M+H]⁺ : 785.4192; found: 785.4195.

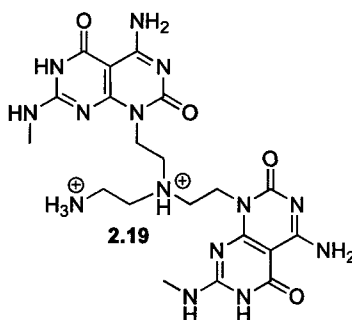
Compound 2.18



Compound **2.13** (0.041 g, 0.064 mmol) was added to a solution of **2.17** (0.050 g, 0.064 mmol) in 1,2 DCE (10 mL) at room temperature under N₂ and stirred for 30 min. Sodium triacetoxy borohydride (0.016 g, 0.076 mmol) was added and the resulting mixture was stirred for an additional 15 h. The reaction mixture was diluted with CH₂Cl₂ (50 mL) and washed with water (10 mL), brine (15 mL), dried over Na₂SO₄ and concentrated. Flash chromatography of the residue over silica gel (0-70% EtOAc in hexanes) gave **2.18** (0.036 g, 40%) as a white foam. R_f = 0.30 (60% EtOAc in hexanes); ¹H NMR (500 MHz, CDCl₃): δ = 7.45-7.30 (m, 10H), 5.56 (s, 4H), 5.08 (bs, 1H), 4.39 (dd, *J* = 7.5 Hz, 7.5 Hz, 4H), 3.48 (s, 6H), 3.19 (m, 2H), 2.93 (dd, *J* = 7.5 Hz, 7.5 Hz, 4H), 2.83 (t, *J* = 6.3 Hz, 2H), 2.67 (m, 2H), 1.55 (s, 18H), 1.41 (s, 9H), 1.30 (s, 36H); ¹³C NMR (125 MHz,

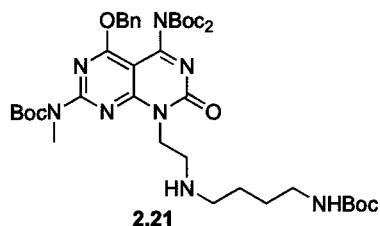
CDCl₃): δ = 165.9, 161.5, 161.2, 160.9, 155.8, 152.7, 149.4, 135.2, 128.8, 93.1, 83.9, 83.1, 70.3, 51.4, 41.7, 35.3, 28.7, 28.3, 28.1 ppm; HRMS: calcd for C₆₉H₉₇N₁₄O₁₈ [M]⁺: 1409.7100; found: 1409.7102.

Compound 2.19



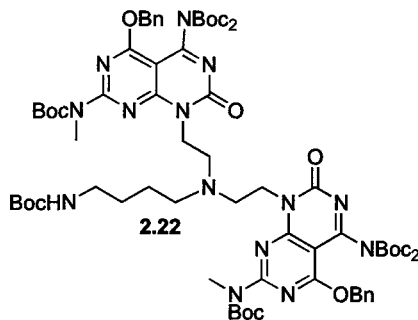
Compound **2.18** (0.036 g, 0.026 mmol) was stirred in a 95% TFA in thioanisole (10 mL) for 72 h. Et₂O (60 mL) was then added to the reaction mixture and the precipitate formed, was centrifuged down. The residual solid was resuspended in Et₂O, sonicated and centrifuged down. This process was repeated until the spotting of the Et₂O produced no UV active spot. The solid was dried and then dissolved in 1 M hydrochloric acid (10 mL), followed by removal of water under reduced pressure. This process was repeated two more times before the solid was dried under vacuo for 72 h to give **2.19** (0.036 g, 100%) as an off-white powder; ¹H NMR (500 MHz, d₆-DMSO): δ = 12.31 (s, 2H), 11.98 (bs, 1H) 9.19 (s, 2H), 8.80 (s, 2H), 8.38 (s, 2H), 8.05 (bs, 3H), 4.50-4.20 (m, 6H), 4.10-3.50 (m, 6H), 2.91 (d, *J* = 4.7 Hz, 6H); ¹³C NMR (150 MHz, d₆-DMSO): δ = 161.4, 160.3, 156.5, 156.2, 148.4, 82.9, 50.6, 38.10, 30.9, 28.6, 28.4 ppm; HRMS: calcd for C₂₀H₂₉N₁₄O₄ [M-H]⁺ :529.2491; found: 529.2489; elemental analysis calcd (%) for C₂₀H₂₈N₁₄O₄(HCl)₅(H₂O)(Et₂O)_{0.25}: C, 33.75, H, 5.06, N, 26.24; found: C 33.46, H 4.85, N 26.49.

Compound 2.21



Compound **2.13** (1.00 g, 1.57 mmol) was added to a solution of *tert*-butyl 4-aminobutylcarbamate (0.30 mL, 2.95 mmol) in 1,2 DCE (30 mL) at room temperature under N₂ and stirred for 30 min. Sodium triacetoxy borohydride (0.395 g, 1.88 mmol) was added and the resulting mixture was stirred for an additional 15 h. The reaction mixture was diluted with CH₂Cl₂ (50 mL) and then washed with water (10 mL), brine (15 mL), dried over Na₂SO₄ and concentrated. Flash chromatography of the residue over silica gel using (0-10% MeOH in EtOAc) gave **2.21** (1.36 g, 93%) as a white foam. R_f = 0.25 (10% MeOH in EtOAc); ¹H NMR (500 MHz, CDCl₃): δ = 7.44-7.32 (m, 5H), 5.56 (s, 2H), 4.75 (bs, 1H), 4.50 (t, *J* = 6.3 Hz, 2H), 3.46 (s, 3H), 3.07 (app. t, *J* = 6.0 Hz, 4H), 2.73 (t, *J* = 6.9 Hz, 2H), 1.58 (s, 9H), 1.54-1.44 (m, 4H), 1.42 (s, 9H), 1.33 (s, 18H); ¹³C NMR (125 MHz, CDCl₃): δ = 165.8, 161.2, 160.9, 160.5, 156.0, 155.9, 152.6, 149.3, 134.9, 128.6, 128.5, 128.3, 93.1, 83.8, 83.3, 70.1, 49.0, 47.0, 42.6, 40.2, 34.9, 28.4, 28.1, 27.8, 27.6, 26.3 ppm; HRMS: calcd for C₄₀H₆₁N₈O₁₀ [M+H]⁺: 813.4505; found: 813.4507.

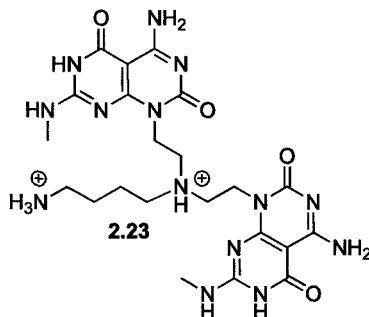
Compound 2.22



Compound **2.13** (0.100 g, 0.155 mmol) was added to a solution of **2.21** (0.126 g, 0.155 mmol) in 1,2 DCE (10 mL) at room temperature under N₂ and stirred for 30

min. Sodium triacetoxy borohydride (0.039 g, 0.186 mmol) was added and the resulting mixture was stirred for an additional 15 h. The reaction mixture was diluted with CH₂Cl₂ (50 mL) and washed with water (10 mL), brine (15 mL), dried over Na₂SO₄ and concentrated. Flash chromatography of the residue over silica gel (0-50% EtOAc in hexanes) gave **2.22** (204 mg, 91%) as a white foam. R_f = 0.26 (50% EtOAc in hexanes); ¹H NMR (500 MHz, CDCl₃): δ = 7.46-7.33 (m, 10H), 5.57 (s, 4H), 4.87 (bs, 1H), 4.39 (t, *J* = 7.2 Hz, 4H), 3.48 (s, 6H), 3.06 (m, 2H), 2.90 (t, *J* = 7.3 Hz, 4H), 2.67 (m, 2H), 1.56 (s, 18H), 1.41 (s, 13H), 1.31 (s, 36H); ¹³C NMR (125 MHz, CDCl₃): δ = 165.7, 161.2, 161.1, 160.3, 156.1, 155.6, 152.6, 149.3, 135.0, 128.6, 128.5, 127.8, 114.0, 92.9, 83.7, 82.9, 78.8, 70.1, 53.9, 50.9, 41.3, 40.5, 35.0, 29.7, 28.5, 28.1, 27.9, 25.1 ppm; HRMS: calcd for C₇₁H₁₀₀N₁₄O₁₈Na [M+Na]⁺: 1459.7238; found: 1459.7238.

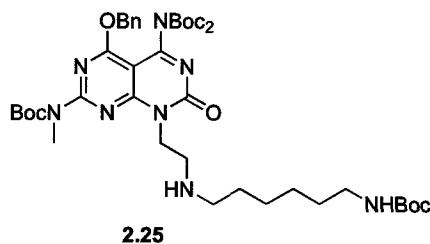
Compound 2.23



Compound **2.22** (0.106 g, 0.0737 mmol) was stirred in a 95% TFA in thioanisole (10 mL) for 72 h. Et₂O (60 mL) was then added to the reaction mixture and the precipitate formed, was centrifuged down. The residual solid was resuspended in Et₂O, sonicated and centrifuged down. This process was repeated until the spotting of the Et₂O produced no UV active spot. The solid was dried and then dissolved in 1 M hydrochloric acid (10 mL), followed by removal of water under reduced pressure. This process was repeated two more times before the solid was dried under vacuo for 72 h to give **2.23** (0.051 g, 94%) as an off-white powder. Decomposition = 296-301 °C; ¹H NMR (600 MHz, d₆-DMSO): δ = 12.32 (s, 2H), 11.63 (bs, 1H) 9.15 (s, 2H), 8.90 (s, 2H), 8.57 (app. q, *J* = 4.8 Hz, 2H), 8.11 (bs, 3H), 4.45 (bs, 2H), 3.46 (bs, 3H), 3.30 (bs, 4H), 2.95 (d, *J* = 4.7 Hz, 6H), 2.81-

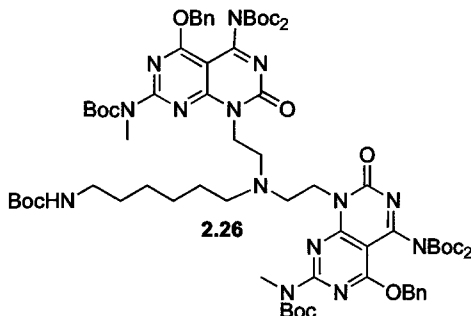
2.75 (m, 2H), 1.85-1.75 (m, 2H), 1.70-1.58 (m, 2H); ^{13}C NMR (100 MHz, d_6 -DMSO): δ = 160.3, 159.6, 155.9, 155.6, 147.6, 82.4, 51.2, 48.3, 37.8, 36.0, 27.7, 23.8, 19.7; HRMS: calcd for $\text{C}_{22}\text{H}_{33}\text{N}_{14}\text{O}_4$ $[\text{M}-\text{H}]^+$: 557.2804; found: 557.2803; elemental analysis calcd (%) for $\text{C}_{22}\text{H}_{32}\text{N}_{14}\text{O}_4(\text{HCl})_4(\text{H}_2\text{O})_{1.5}$: C 36.00, H 5.42, N 26.72; found: C 36.31, H 5.35, N 26.44.

Compound 2.25



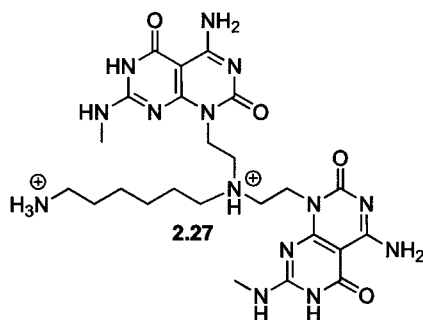
Compound **2.13** (0.260 g, 0.406 mmol) was added to a solution of *tert*-butyl 6-aminoethylcarbamate (0.092 g, 0.425 mmol) in 1,2 DCE (10 mL) at room temperature under N_2 and stirred for 30 min. Sodium triacetoxy borohydride (0.102 g, 0.486 mmol) was added and the resulting mixture was stirred for an additional 24 h. The reaction mixture was diluted with CH_2Cl_2 (50 mL) and then washed with water (10 mL), brine (10 mL), dried over Na_2SO_4 and concentrated. Flash chromatography of the residue over silica gel using (0-5% MeOH in CH_2Cl_2) gave **2.25** (0.226 g, 66%) as a pale yellow oil. R_f = 0.40 (5% MeOH in CH_2Cl_2); ^1H NMR (400 MHz, CDCl_3): δ = 7.46-7.31 (m, 5H), 5.57 (s, 2H), 4.52 (bs, 1H), 4.45 (t, J = 6.8 Hz, 2H), 3.46 (s, 3H), 3.08 (app. q, J = 4.3 Hz, 2H), 2.99 (t, J = 6.6 Hz, 2H), 2.63 (t, J = 7.2 Hz, 2H), 1.59 (s, 9H), 1.44 (s, 13H), 1.33 (s, 18H), 1.31-1.24 (m, 4H); ^{13}C NMR (125 MHz, CDCl_3): δ = 165.7, 161.1, 161.0, 160.3, 156.0, 155.9, 152.6, 149.3, 134.9, 128.6, 128.5, 128.4, 93.0, 83.7, 83.0, 70.0, 49.6, 47.1, 43.1, 40.5, 34.9, 30.0, 29.9, 28.4, 28.1, 27.8, 26.9, 26.7 ppm; HRMS: calcd for $\text{C}_{42}\text{H}_{65}\text{N}_8\text{O}_{10}$ $[\text{M}+\text{H}]^+$: 841.4818; found 841.4815.

Compound 2.26



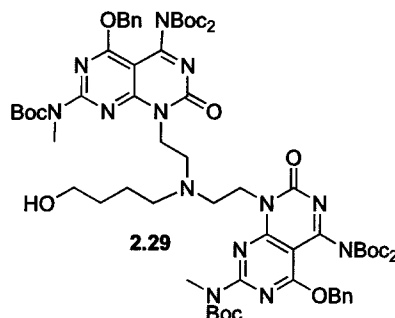
Compound **2.25** (0.080 g, 0.095 mmol) was added to a solution of **2.13** (0.061 g, 0.095 mmol) in 1,2 DCE (10 mL) at room temperature under N₂ and stirred for 30 min. Sodium triacetoxy borohydride (0.024 g, 0.114 mmol) was added and the resulting mixture was stirred for an additional 30 h. The reaction mixture was diluted with CH₂Cl₂ (50 mL) and washed with water (10 mL), brine (15 mL), dried over Na₂SO₄ and concentrated. Flash chromatography of the residue over silica gel (0-50% EtOAc in hexanes) gave **2.26** (0.060 g, 43%) as a pale yellow oil. R_f = 0.54 (50% EtOAc in hexanes); ¹H NMR (500 MHz, CDCl₃): δ = 7.46-7.31 (m, 10H), 5.57 (s, 4H), 4.63 (bs, 1H), 4.38 (t, *J* = 7.2 Hz, 4H), 3.49 (s, 6H), 3.08 (app. q, *J* = 6.5 Hz, 2H), 2.89 (t, *J* = 7.5 Hz, 4H), 2.65 (t, *J* = 7.5 Hz, 2H), 1.57 (s, 18H), 1.43 (s, 13H), 1.31 (s, 36H), 1.29-1.20 (m, 4H); ¹³C NMR (125 MHz, CDCl₃): δ = 165.6, 161.2, 161.0, 160.2, 155.6, 152.5, 149.2, 135.0, 128.5, 92.8, 83.6, 82.9, 70.0, 54.2, 51.0, 41.4, 40.7, 35.0, 29.7, 29.6, 28.4, 28.1, 27.8, 27.0, 26.8 ppm; HRMS: calcd for C₇₃H₁₀₄N₁₄O₁₈ [M]⁺: 1465.7726; found: 1465.7727.

Compound 2.27



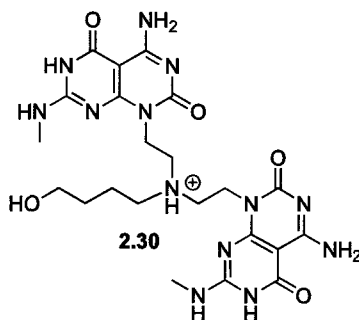
Compound **2.26** (0.060 g, 0.041 mmol) was stirred in a 95% TFA in thioanisole (10 mL) for 72 h. Et₂O (60 mL) was then added to the reaction mixture and the precipitate formed, was centrifuged down. The residual solid was resuspended in Et₂O, sonicated and centrifuged down. This process was repeated until the spotting of the Et₂O produced no UV active spot. The solid was dried and then dissolved in 1 M hydrochloric acid (10 mL), followed by removal of water under reduced pressure. This process was repeated two more times before the solid was dried under vacuo for 72 h to give **2.27** (0.019 g, 59%) as an off-white powder; ¹H NMR (400 MHz, d₆-DMSO): δ = 12.29 (bs, 2H), 11.56 (bs, 1H) 9.15 (s, 2H), 8.82 (s, 2H), 8.46 (s, 2H), 7.96 (bs, 3H), 4.45 (bs, 4H), 3.36 (bs, 6H, merged with H₂O peak), 2.95 (d, *J* = 4.7 Hz, 6H), 2.80 (m, 2H), 1.71 (m, 2H), 1.54 (m, 2H), 1.30 (m, 4H); ¹³C NMR (100 MHz, d₆-DMSO): δ = 160.7, 159.8, 156.3, 155.8, 148.0, 82.6, 52.0, 48.5, 40.3, 38.5, 36.0, 27.9, 26.6, 25.5, 25.3 ppm; HRMS: calcd for C₂₄H₃₇N₁₄O₄ [M-H]⁺: 585.3117; found: 585.3115; elemental analysis calcd (%) for C₂₄H₃₆N₁₄O₄(HCl)₅(H₂O)₂: C 35.90, H 5.65, N 24.42; found: C 36.18, H 5.29, N 23.99.

Compound 2.29



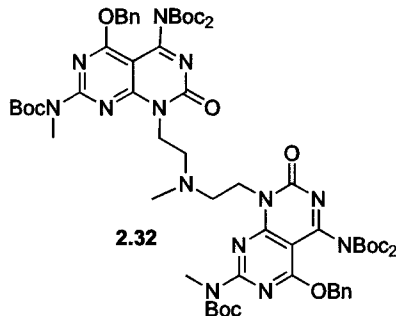
4-Aminobutan-1-ol (0.016 g, 0.180 mmol) was added to a solution of **2.13** (0.100 g, 0.156 mmol) in 1,2 DCE (20 mL) at room temperature under N₂ and stirred for 30 min. Sodium triacetoxy borohydride (0.079 g, 0.376 mmol) was added and the resulting mixture was stirred for 24h. **2.13** (0.100 g, 0.156 mmol) was again added to the reaction mixture and stirred for 30 min, prior to the addition of sodium triacetoxy borohydride (0.079 g, 0.376 mmol). The resulting solution was then stirred for another 72 h. The reaction mixture was diluted with CH₂Cl₂ (50 mL), washed with water (10 mL), NaHCO₃ (10 mL), brine (20 mL), dried over Na₂SO₄ and concentrated. Flash chromatography of the residue over silica gel (0-7% MeOH in CH₂Cl₂) gave **2.29** (0.134 g, 64%) as a white foam. R_f = 0.24 (7% MeOH in CH₂Cl₂); ¹H NMR (500 MHz, CDCl₃): δ = 7.45-7.31 (m, 10H), 5.56 (s, 4H), 4.43 (t, *J* = 7.3 Hz, 4H), 3.54 (t, *J* = 5.8 Hz, 2H), 3.49 (s, 6H), 2.94 (t, *J* = 7.3 Hz, 4H), 2.69 (t, 2H, *J* = 6.0 Hz), 1.55 (s, 18H), 1.53-1.47 (m, 4H), 1.30 (s, 36H); ¹³C NMR (125 MHz, CDCl₃): δ = 165.6, 161.2, 161.0, 160.3, 155.6, 152.5, 149.3, 134.9, 128.5, 92.9, 83.7, 82.9, 70.0, 62.6, 53.6, 50.7, 35.0, 28.1, 27.8, 26.1, 25.2 ppm; HRMS: calcd for C₆₆H₉₂N₁₃O₁₇ [M+H]⁺: 1338.6725; found: 1338.6729.

Compound 2.30



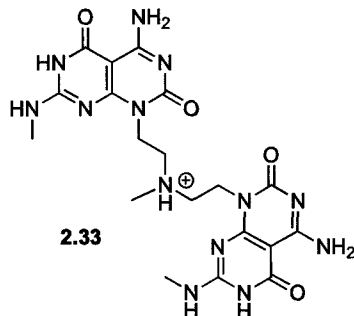
Compound **2.29** (0.126 g, 0.094 mmol) was stirred in a 95% TFA in thioanisole (10 mL) for 72 h. Et₂O (60 mL) was then added to the reaction mixture and the precipitate formed, was centrifuged down. The residual solid was resuspended in Et₂O, sonicated and centrifuged down. This process was repeated until the spotting of the Et₂O produced no UV active spot. The solid was dried and then dissolved in 1 M hydrochloric acid (10 mL), followed by removal of water under reduced pressure. This process was repeated two more times before the solid was dried under vacuo for 72 h to give **2.30** (0.062 g, 86%) as an off-white powder; ¹H NMR (600 MHz, d₆-DMSO): δ = 12.33 (bs, 2H), 11.40 (bs, 1H), 9.17 (s, 2H), 8.86 (bs, 2H), 8.49 (bs, 2H), 4.46 (bs, 4H), 3.44-3.28 (m, 8H), 2.95 (d, *J* = 4.6 Hz, 6H), 1.85-1.73 (m, 2H), 1.46-1.41 (m, 2H); ¹³C NMR (100 MHz, d₆-DMSO): δ = 161.1, 160.3, 156.6, 156.3, 148.4, 83.1, 60.4, 52.6, 48.9, 36.6, 29.8, 28.4, 20.2 ppm; HRMS: calcd for C₂₂H₃₂N₁₃O₅ [M]⁺: 558.2644; found: 558.2641; elemental analysis calcd (%) for C₂₂H₃₁N₁₃O₅(HCl)_{4.5}(H₂O)_{1.5}(Et₂O)_{0.25}: C 36.01, H 5.39, N 23.73; found: C 36.17, H 5.02, N 23.88.

Compound 2.32



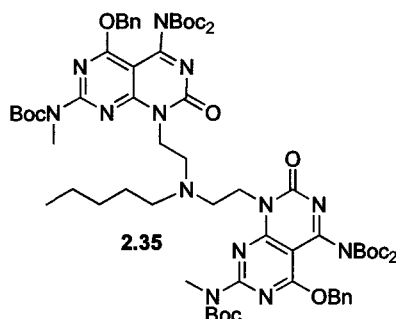
Methylamine (2M in THF, 86.0 μ L, 0.172 mmol) was added to a stirred solution of **2.13** (0.100 g, 0.156 mmol) in 1,2 DCE (20 mL) at room temperature under N₂ and stirred for 30 min. Sodium triacetoxy borohydride (0.079 g, 0.376 mmol) was added and the resulting mixture was stirred for 2h. **2.13** (0.100 g, 0.156 mmol) was again added to the reaction mixture and stirred for 30 min, prior to the addition of sodium triacetoxy borohydride (0.079 g, 0.376 mmol). The resulting solution was then stirred for another 24 h. The reaction mixture was diluted with CH₂Cl₂ (50 mL), washed with water (10 mL), NaHCO₃ (10 mL), brine (20 mL), dried over Na₂SO₄ and concentrated. Flash chromatography (0-100% EtOAc in hexanes) gave **2.32** as a white foam in 46% yield, R_f = 0.23 (40% EtOAc in hexanes) as well as the desired product minus Boc in 18% yield, R_f = 0.39 (5% MeOH in CH₂Cl₂); ¹H NMR (500 MHz, CDCl₃): δ = 7.45-7.29 (m, 10H), 5.56 (s, 4H), 4.39 (t, *J* = 7.3 Hz, 4H), 3.49 (s, 6H), 2.82 (t, *J* = 7.5 Hz, 4H), 2.49 (s, 3H), 1.57 (s, 18H), 1.30 (s, 36H); ¹³C NMR (125 MHz, CDCl₃): δ = 165.6, 161.1, 161.0, 160.2, 155.6, 152.5, 149.1, 134.9, 128.5, 92.9, 83.6, 82.9, 70.0, 54.2, 42.5, 41.1, 35.0, 28.1, 27.9 ppm; HRMS: calcd for C₆₃H₈₆N₁₃O₁₆ [M+H]⁺: 1280.6310; found: 1280.6309.

Compound 2.33



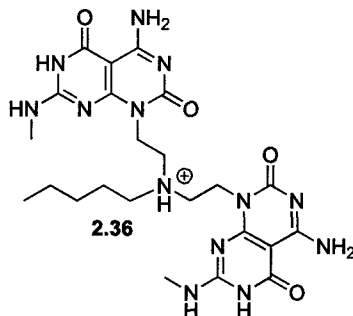
Compound **2.32** (0.100 g, 0.078 mmol) was stirred in 95% TFA in thioanisole (10 mL) for 72 h. Et₂O (60 mL) was then added to the reaction mixture and the precipitate formed, was centrifuged down. The residual solid was resuspended in Et₂O, sonicated and centrifuged down. This process was repeated until the spotting of the Et₂O produces no UV active spot. The white solid was dried and was then dissolved in 1 M hydrochloric acid (10 mL), followed by removal of water under reduced pressure. This process was repeated two more times before the solid was dried under vacuo for 72 h to yield **2.33** (0.055 g, 97%) as an off-white powder; ¹H NMR (500 MHz, d₆-DMSO + 2 drops of TFA): δ = 12.23 (bs, 2H), 11.08 (bs, 1H), 9.12 (s, 2H), 8.84 (s, 2H), 8.53 (s, 2H), 4.42 (bs, 2H), 4.34 (bs, 2H), 3.51 (bs, 2H), 3.38 (bs, 2H), 2.92 (s, 3H), 2.91 (d, *J* = 2.1 Hz, 6H); ¹³C NMR (125 MHz, d₆-DMSO): δ = 160.7, 159.8, 156.2, 155.7, 148.0, 82.6, 52.2, 39.6, 36.5, 27.9 ppm; HRMS: calcd for C₁₉H₂₆N₁₃O₄ [M]⁺: 500.2225; found: 500.2230; elemental analysis calcd (%) C₁₉H₂₅N₁₃O₄(HCl)₅(H₂O)_{1.5}(Et₂O)_{0.25}: C 33.03, H 4.92, N 25.03; found; C 33.45, H 4.65, N 24.29.

Compound 2.35



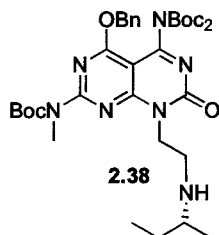
Pentylamine (18 μ L, 0.156 mmol) was added to a solution of **2.13** (0.100 g, 0.156 mmol) in 1,2 DCE (20 mL) at room temperature under N₂ and stirred for 30 min. Sodium triacetoxy borohydride (0.039 g, 0.186 mmol) was added and the resulting mixture was stirred for an additional 12 h. The reaction mixture was diluted with CH₂Cl₂ (50 mL) and then washed with water (10 mL), brine (15 mL), dried over Na₂SO₄ and concentrated. Fresh 1,2 DCE (20 mL) and additional **2.13** (0.100 g, 0.156 mmol) was added to the residue and stirred for 30 min, prior to the addition of sodium triacetoxy borohydride (0.039 g, 0.186 mmol), and stirring was continued for another 15 h. The reaction mixture was diluted with CH₂Cl₂ (50 mL) and washed with water (10 mL), NaHCO₃ (10 mL), brine (15 mL), dried over Na₂SO₄ and concentrated. Flash chromatography of the residue over silica gel (0-100% EtOAc in hexanes) gave **2.35** as a white foam in 46% yield, R_f = 0.61 (50% EtOAc in hexanes) as well as the desired product minus Boc in 30% yield, R_f = 0.64 (EtOAc); ¹H NMR (500 MHz, CDCl₃): δ = 7.46-7.33 (m, 10H), 5.57 (s, 4H), 4.39 (t, *J* = 7.3 Hz, 4H), 3.50 (s, 6H), 2.90 (t, *J* = 7.5 Hz, 4H), 2.65 (t, *J* = 7.5 Hz, 2H), 1.56 (s, 18H), 1.44-1.32 (m, 2H), 1.31 (s, 36H), 1.29-1.18 (m, 4H), 0.86 (t, *J* = 7.3 Hz, 3H); ¹³C NMR (125 MHz, CDCl₃): δ = 165.6, 161.2, 161.1, 160.2, 155.6, 152.6, 149.2, 135.0, 128.5, 92.8, 83.6, 82.8, 70.0, 54.3, 51.0, 41.4, 35.0, 29.5, 28.1, 27.8, 27.5, 22.7, 14.1 ppm; HRMS: calcd for C₆₇H₉₄N₁₃O₁₆ [M+H]⁺: 1336.6936; found: 1336.6933.

Compound 2.36



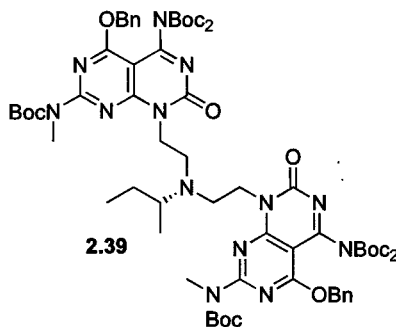
Compound **2.35** (0.096 g, 0.072 mmol) was stirred in a 95% TFA in thioanisole (10 mL) for 72 h. Et₂O (60 mL) was then added to the reaction mixture and the precipitate formed was stirred for another 30 min, after which it was centrifuged down. The residual solid was resuspended in Et₂O, sonicated and centrifuged down. This process was repeated until the spotting of the Et₂O produces no UV active spot. The white solid was dried and then dissolved in 1 M hydrochloric acid (10 mL), followed by removal of water under reduced pressure. This process was repeated two more times before the solid was dried under vacuo for 72 h to yield **2.36** (0.051 g, 98%) as an off-white powder; ¹H NMR (500 MHz, d₆-DMSO): δ = 12.26 (bs, 2H), 11.05 (bs, 1H), 9.17 (s, 2H), 8.70 (bs, 2H), 8.22 (bs, 2H), 4.44 (m, 4H), 3.46 (bs, 4H, merged with H₂O peak) 3.25 (m, 2H), 2.94 (d, *J* = 4.4 Hz, 6H), 1.69 (m, 2H), 1.27 (m, 4H), 0.85 (t, *J* = 6.6 Hz, 3H); ¹³C NMR (100 MHz, d₆-DMSO): δ = 161.4, 160.5, 156.8, 156.5, 148.6, 83.3, 52.7, 49.2, 36.8, 28.8, 28.6, 22.9, 22.3, 14.4; HRMS: calcd for C₂₃H₃₄N₁₃O₄ [M+H]⁺: 556.2851; found: 556.2853; elemental analysis calcd (%) for C₂₃H₃₃N₁₃O₄ (HCl)₃(H₂O)₃: C 38.42, H 5.89, N 25.32; found: C 38.78, H 5.53, N 25.08.

Compound 2.38



(R)-butan-2-amine (26 μ L, 0.352 mmol) was added to a solution of **2.13** (0.150 g, 0.234 mmol) in 1,2 DCE (20 mL) at room temperature under N₂ and stirred for 30 min. Sodium triacetoxy borohydride (0.078 g, 0.371 mmol) was added and the resulting mixture was stirred for an additional 24 h. The reaction mixture was diluted with CH₂Cl₂ (50 mL), washed with water (20 mL), brine (20 mL), dried over Na₂SO₄ and concentrated. Flash chromatography of the residue over silica gel (0-5% MeOH in CH₂Cl₂) gave **2.38** (0.066 g, 40%) as a white foam. R_f = 0.39 (5% MeOH in CH₂Cl₂); $[\alpha]_D^{25}$ -2.4 (*c* 1.5, CHCl₃); ¹H NMR (400 MHz, CDCl₃): δ = 7.45-7.33 (m, 5H), 5.56 (s, 2H), 4.47 (t, *J* = 6.6 Hz, 2H), 3.46 (s, 3H), 3.07 (m, 2H), 2.70 (m, 2H), 1.58 (s, 9H), 1.48-1.39 (m, 2H), 1.34 (s, 18H), 1.05 (d, *J* = 6.3 Hz, 3H), 0.85 (t, *J* = 7.5 Hz, 3H); ¹³C NMR (100 MHz, CDCl₃): δ = 165.7, 161.1, 160.9, 160.4, 155.8, 152.6, 149.2, 134.9, 128.6, 128.5, 128.3, 93.1, 83.8, 83.2, 70.1, 54.5, 44.2, 43.1, 34.9, 28.2, 27.8, 19.0, 10.2 ppm; HRMS: calcd for C₃₅H₅₂N₇O₈ [M+H]⁺: 698.3872; found: 698.3873.

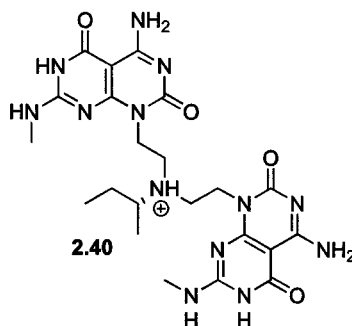
Compound 2.39



Compound **2.38** (0.150 g, 0.215 mmol) was added to a solution of **2.13** (0.138 g, 0.216 mmol) in 1,2 DCE (20 mL) at room temperature under N₂ and stirred for 30 min. Sodium triacetoxy borohydride (0.051 g, 0.243 mmol) was added and the

resulting mixture was stirred for an additional 30 h. The reaction mixture was diluted with CH₂Cl₂ (50 mL) and then washed with water (2 x 10 mL), brine (15 mL), dried over Na₂SO₄ and concentrated. Flash chromatography of the residue over silica gel (0-30% EtOAc in hexanes) gave **2.39** (0.103 g, 36%) as a white foam. $R_f = 0.44$ (30% EtOAc in hexanes); $[\alpha]_D^{25} +10.6$ (*c* 0.7, CHCl₃); ¹H NMR (600 MHz, CDCl₃): $\delta = 7.44$ -7.31 (m, 10H), 5.56 (s, 4H), 4.34 (m, 4H), 3.48 (s, 6H), 2.90 (m, 2H), 2.81 (q, *J* = 6.4 Hz, 1H), 2.73 (m, 2H), 1.55 (s, 18H), 1.48-1.39 (m, 2H), 1.30 (s, 36H), 0.90 (d, *J* = 6.0 Hz, 3H), 0.86 (t, *J* = 7.2 Hz, 3H); ¹³C NMR (125 MHz, CDCl₃): $\delta = 165.7, 161.3, 161.1, 160.3, 155.6, 152.6, 149.3, 149.2, 135.1, 128.7, 128.6, 92.9, 84.0, 82.8, 70.3, 54.0, 47.3, 43.0, 35.0, 29.5, 28.1, 27.9, 14.7, 11.7$ ppm; HRMS: calcd for C₆₆H₉₂N₁₃O₁₆ [M+H]⁺: 1322.6780; found: 1322.6783.

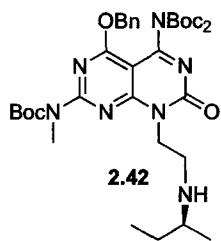
Compound 2.40



Compound **2.39** (0.066 g, 0.050 mmol) was stirred in a 95% TFA in thioanisole (10 mL) for 72 h. Et₂O (60 mL) was then added to the reaction mixture and the precipitate formed, was centrifuged down. The residual solid was resuspended in Et₂O, sonicated and centrifuged down. This process was repeated until the spotting of the Et₂O produced no UV active spot. The solid was dried and then dissolved in 1 M hydrochloric acid (10 mL), followed by removal of water under reduced pressure. This process was repeated two more times before the solid was dried under vacuo for 72 h to give **2.40** (0.033 g, 89%) as an off-white powder; ¹H NMR (600 MHz, d₆-DMSO): $\delta = 12.30$ (s, 2H), 11.50 (bs, 1H) 9.17 (s, 2H), 8.84 (bs, 2H), 8.43 (bs, 2H), 4.53 (m, 4H), 3.42 (m, 5H, merged with H₂O peak), 2.95 (d, *J* = 4.8 Hz, 6H), 2.03 (m, 1H), 1.42 (m, 1H), 1.29 (s, 3H), 0.91 (s, 3H); ¹³C

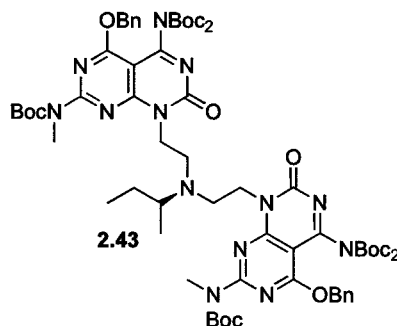
NMR (150 MHz, d_6 -DMSO): δ = 161.3, 160.3, 156.6, 156.2, 148.3, 83.0, 60.6, 47.0, 46.8, 37.2, 28.4, 12.6, 10.8 ppm; HRMS: calcd for $C_{22}H_{33}N_{13}O_4$ $[M+H]^+$: 543.2768; found: 271.6381; elemental analysis calcd (%) for $C_{22}H_{31}N_{13}O_4(HCl)_4(H_2O)_2(Et_2O)_{0.25}$: C 37.23, H 5.64, N 24.54; found: C 37.74, H 5.22, N 24.13.

Compound 2.42



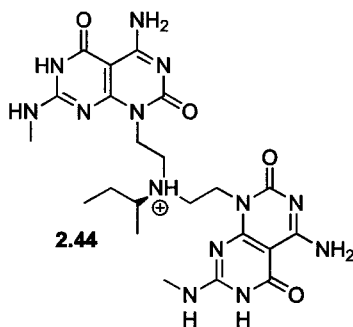
(S)-butan-2-amine (26 μ L, 0.352 mmol) was added to a solution of **2.13** (0.150 g, 0.234 mmol) in 1,2 DCE (20 mL) at room temperature under N_2 and stirred for 30 min. Sodium triacetoxo borohydride (0.078 g, 0.371 mmol) was added and the resulting mixture was stirred for an additional 24 h. The reaction mixture was diluted with CH_2Cl_2 (50 mL), washed with water (20 mL), brine (20 mL), dried over Na_2SO_4 and concentrated. Flash chromatography of the residue over silica gel (0-5% MeOH in CH_2Cl_2) gave **2.42** (0.074 g, 45%) as a white foam. R_f = 0.39 (5% MeOH in CH_2Cl_2); $[\alpha]_D^{25}$ +2.0 (c 2.4, $CHCl_3$); 1H NMR (400 MHz, $CDCl_3$): δ = 7.44-7.32 (m, 5H), 5.56 (s, 2H), 4.47 (t, J = 6.7 Hz, 2H), 3.46 (s, 3H), 3.04 (m, 2H), 2.70 (m, 2H), 1.58 (s, 9H), 1.48-1.41 (m, 2H), 1.33 (s, 18H), 1.05 (d, J = 6.3 Hz, 3H), 0.85 (t, J = 7.5 Hz, 3H); ^{13}C NMR (100 MHz, $CDCl_3$): δ = 165.7, 161.1, 160.9, 160.4, 155.8, 152.6, 149.2, 134.9, 128.6, 128.5, 128.3, 93.0, 83.8, 83.1, 70.1, 54.5, 44.2, 43.2, 34.9, 28.1, 27.8, 19.0, 10.1 ppm; HRMS: calcd for $C_{35}H_{52}N_7O_8$ $[M+H]^+$: 698.3872; found: 698.3876.

Compound 2.43



Compound **2.42** (0.150 g, 0.215 mmol) was added to a solution of **2.13** (0.138 g, 0.216 mmol) in 1,2 DCE (20 mL) at room temperature under N₂ and stirred for 30 min. Sodium triacetoxy borohydride (0.051 g, 0.243 mmol) was added and the resulting mixture was stirred for an additional 30 h. The reaction mixture was diluted with CH₂Cl₂ (50 mL) and then washed with water (2 x 10 mL), brine (15 mL), dried over Na₂SO₄ and concentrated. Flash chromatography of the residue over silica gel (0-30% EtOAc in hexanes) gave **2.43** (0.096 g, 34%) as a white foam. R_f = 0.44 (30% EtOAc in hexanes); [α]_D²⁵ -11.1 (c 0.7, CHCl₃); ¹H NMR (600 MHz, CDCl₃): δ = 7.45-7.31 (m, 10H), 5.56 (s, 4H), 4.36 (bs, 4H), 3.48 (s, 6H), 2.91 (bs, 2H), 2.83 (bs, 1H), 2.75 (bs, 2H), 1.55 (s, 18H), 1.47-1.38 (m, 2H), 1.30 (s, 36H), 0.92 (bs, 3H), 0.87 (t, *J* = 6.9 Hz, 3H); ¹³C NMR (150 MHz, CDCl₃): δ = 165.6, 161.2, 161.0, 160.2, 155.6, 152.5, 149.2, 149.1, 135.0, 128.5, 128.5, 92.8, 83.6, 82.8, 70.0, 53.4, 47.2, 35.0, 28.1, 27.8, 14.6, 11.6 ppm; HRMS: calcd for C₆₆H₉₂N₁₃O₁₆ [M+H]⁺: 1322.6780; found: 1322.6779.

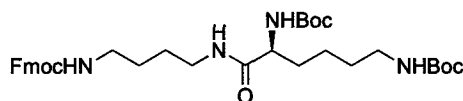
Compound 2.44



Compound **2.43** (0.063 g, 0.048 mmol) was stirred in a 95% TFA in thioanisole (10 mL) for 72 h. Et₂O (60 mL) was then added to the reaction mixture and the

precipitate formed, was centrifuged down. The residual solid was resuspended in Et₂O, sonicated and centrifuged down. This process was repeated until the spotting of the Et₂O produced no UV active spot. The solid was dried and then dissolved in 1 M hydrochloric acid (10 mL), followed by removal of water under reduced pressure. This process was repeated two more times before the solid was dried under vacuo for 72 h to give **2.44** (0.032 g, 93%) as an off-white powder; ¹H NMR (600 MHz, d₆-DMSO): δ = 12.30 (s, 2H), 11.42 (bs, 1H), 9.17 (s, 2H), 8.84 (bs, 2H), 8.41 (bs, 2H), 4.53 (m, 4H), 3.38 (m, 5H, merged with H₂O peak), 2.94 (d, *J* = 4.8 Hz, 6H), 2.00 (m, 1H), 1.45 (m, 1H), 1.29 (s, 3H), 0.91 (s, 3H); ¹³C NMR (150 MHz, d₆-DMSO): δ = 161.2, 160.3, 156.6, 156.3, 148.2, 83.0, 60.5, 47.0, 46.4, 37.2, 28.4, 12.6, 10.8 ppm; HRMS: calcd for C₂₂H₃₃N₁₃O₄ [M+H]⁺: 543.2768; found: 271.6382; elemental analysis calcd (%) for C₂₂H₃₁N₁₃O₄(HCl)_{3.5}(H₂O)₂(Et₂O)_{0.25}: C 38.17, H 5.71, N 25.16, found C 38.01, H 5.39, N 25.24.

Compound 2.48

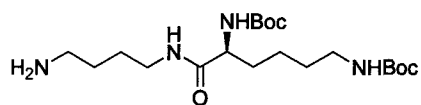


2.48

To a stirred solution of (9*H*-fluoren-9-yl)methyl 4-aminobutylcarbamate hydrochloride (1.00 g, 2.89 mmol) in DMF (10 mL), DIEA (0.51 mL, 2.85 mmol) was added and the mixture was stirred for 20 min at room temperature under N₂. The lysine derivative **2.47** (1.00 g, 2.89 mmol) and HBTU (1.64 g, 4.33 mmol) were then added and the resulting mixture was stirred for another 7 h. The reaction mixture was diluted with Et₂O (50 mL) and then washed with water (2 x 10 mL), citric acid (10 mL), NaHCO₃ (10 mL), brine (15 mL), dried over Na₂SO₄ and concentrated. Flash chromatography of the residue over silica gel (10-100% EtOAc in hexanes) gave **2.48** as an off-white foam in 92% yield. R_f 0.33 (50% EtOAc in hexanes); ¹H NMR (400 MHz, CDCl₃): δ = 7.74 (d, *J* = 7.6 Hz, 2H), 7.58 (d, *J* = 7.6 Hz, 2H), 7.38 (t, *J* = 7.6 Hz, 2H), 7.29 (t, *J* = 7.0 Hz, 2H), 6.31 (bs, 1H), 5.12 (bs, 1H), 5.01 (bs, 1H), 4.61 (bs, 1H), 4.38 (d, *J* = 6.4 Hz, 2H), 4.19

(t, $J = 6.8$ Hz, 1H), 3.99 (m, 1H), 3.26 (m, 2H), 3.19 (m, 2H), 3.08 (t, $J = 6.4$ Hz, 2H), 1.80-1.46 (m, 8H), 1.42 (s, 18H), 1.38-1.33 (m, 2H); ^{13}C NMR (125 MHz, CDCl_3): $\delta = 158.8, 158.0, 144.0, 141.4, 127.6, 127.0, 125.1, 119.9, 80.1, 79.2, 66.6, 47.3, 40.6, 39.9, 38.6, 31.9, 29.7, 28.4, 28.3, 27.3, 26.6, 22.7$ ppm; HRMS: calcd for $\text{C}_{35}\text{H}_{50}\text{N}_4\text{O}_7$ $[\text{M}+\text{Na}]^+$: 661.3572; found: 661.3571.

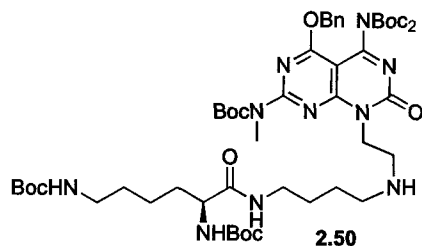
(S)-tert-butyl 6-(4-aminobutylamino)-6-oxohexane-1,5-diylidicarbamate (2.49)



2.49

To a stirred solution of **2.48** (1.19 g, 1.87 mmol) in DMF (10 mL), piperidine (1.6 mL) was added and the mixture was stirred for 2 h at room temperature under N_2 . The reaction mixture was concentrated. Purification of the residue by flash chromatography over silica gel (100-90% EtOAc in MeOH) gave **2.49** as a colourless oil in 90% yield. $R_f = 0.21$ (75% EtOAc in MeOH); ^1H NMR (300 MHz, CDCl_3): $\delta = 6.89$ (bs, 1H), 5.21 (bs, 1H), 4.72 (bs, 1H), 4.01 (q, $J = 6.3$ Hz, 2H), 3.26 (q, $J = 5.7$ Hz, 2H), 3.10 (q, $J = 6.6$ Hz, 2H), 2.75 (t, $J = 6.2$ Hz, 2H), 1.86-1.75 (m, 2H), 1.67 (s, 9H), 1.63-1.48 (m, 6H), 1.44 (s, 9H), 1.39-1.23 (m, 2H); ^{13}C NMR (100 MHz, CDCl_3): $\delta = 172.0, 156.2, 155.2, 79.9, 79.0, 50.6, 41.2, 39.6, 39.1, 32.1, 29.9, 29.5, 28.3, 28.2, 26.7, 22.5$ ppm; HRMS: calcd for $\text{C}_{20}\text{H}_{40}\text{N}_4\text{O}_5$ $[\text{M}+\text{H}]^+$: 417.3076; found: 417.3072.

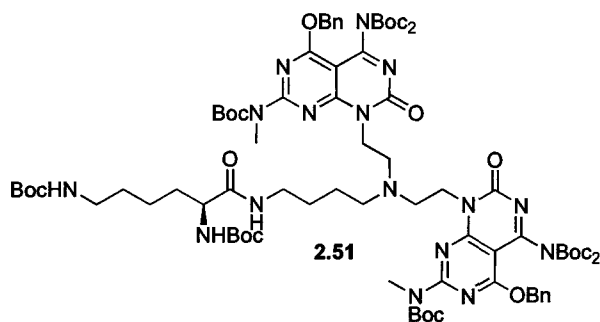
Compound 2.50



To a stirred solution of **2.49** (0.288 g, 0.692 mmol) in 1,2 dichloroethane (20 mL), **2.13** (0.443 g, 0.692 mmol) was added at room temperature under N_2 . The mixture was stirred for 30 min before addition of sodium triacetoxyborohydride

(0.176 g, 0.800 mmol) and the resulting mixture was stirred for an additional 15 h. The reaction mixture was diluted with CH₂Cl₂ (50 mL) and then washed with water (2 x 10 mL), brine (15 mL), dried over Na₂SO₄ and concentrated. Flash chromatography of the residue over silica gel (0-3% MeOH in CH₂Cl₂) gave **2.50** as a white foam in 65% yield. R_f = 0.37 (5% MeOH in CH₂Cl₂); ¹H NMR (500 MHz, CDCl₃): δ = 7.43-7.32 (m, 5H), 6.75 (bs, 1H), 5.56 (s, 2H), 5.31 (d, *J* = 8.0 Hz, 2H), 4.75 (bs, 1H), 4.50 (m, 2H), 4.03 (bs, 1H), 3.46 (s, 3H), 3.22 (m, 2H), 3.12-3.03 (m, 4H), 2.74 (m, 2H), 1.85-1.59 (m, 4H), 1.57 (s, 9H), 1.54-1.46 (m, 2H), 1.41 (s, 18H), 1.39-1.33 (m, 2H), 1.32 (s, 18H), 1.28-1.19 (m, 2H); ¹³C NMR (125 MHz, CDCl₃): δ = 172.5, 165.6, 161.0, 160.8, 156.1, 155.8, 155.7, 152.4, 149.3, 134.6, 128.5, 128.0, 127.6, 113.8, 93.3, 84.0, 83.5, 79.5, 78.8, 70.2, 54.3, 48.0, 46.3, 40.8, 40.0, 38.3, 35.0, 32.3, 29.3, 28.3, 28.2, 28.0, 27.7, 26.2, 23.8, 22.5 ppm; HRMS: calcd for C₅₁H₈₁N₁₀O₁₃ [M+H]⁺: 1041.5979; found: 1041.5983.

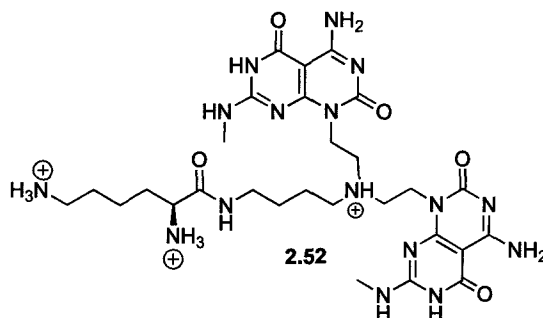
Compound 2.51



Compound **2.13** (0.192 g, 0.298 mmol) was added to a solution of **2.50** (0.311 g, 0.299 mmol) in 1,2 DCE (20 mL) at room temperature under N₂ and stirred for 30 min. Sodium triacetoxy borohydride (0.074 g, 0.352 mmol) was added and the resulting mixture was stirred for an additional 15 h. The reaction mixture was diluted with CH₂Cl₂ (50 mL) and then washed with water (2 x 10 mL), brine (20 mL), dried over Na₂SO₄ and concentrated. Flash chromatography of the residue over silica gel (10-80% EtOAc in hexanes) gave **2.51** (0.326 g, 66%) as a white foam. R_f = 0.42 (70% EtOAc in hexanes); ¹H NMR (500 MHz, CDCl₃): δ = 7.45-7.28 (m, 10H), 6.64 (bs, 1H), 5.57 (s, 4H), 4.77 (bs, 1H), 4.37 (m, 4H), 4.11 (m, 2H), 3.48 (s, 6H), 3.33 (m, 1H), 3.18 (m, 1H), 3.08 (m, 2H), 2.90 (t, *J* = 6.5 Hz,

4H), 2.67 (app. q, $J = 7.5$ Hz, 2H), 1.62-1.58 (m, 2H), 1.56 (s, 18H), 1.54-1.43 (m, 6H), 1.42 (s, 9H), 1.41 (s, 9H), 1.32 (s, 18H), 1.31 (s, 18H); ^{13}C NMR (100 MHz, CDCl_3): $\delta = 172.2, 171.0, 165.5, 161.2, 160.9, 160.2, 156.2, 156.0, 155.6, 152.4, 149.2, 149.1, 134.8, 128.4, 128.3, 127.7, 113.8, 92.8, 83.6, 82.8, 70.0, 60.3, 54.4, 50.8, 41.1, 40.1, 38.9, 34.9, 32.4, 29.4, 28.3, 28.2, 28.0, 27.7, 26.7, 24.6, 22.7$ ppm; HRMS calcd for $\text{C}_{82}\text{H}_{120}\text{N}_{16}\text{O}_{21}\text{Na}$ $[\text{M}+\text{Na}]^+$: 1687.8706; found: 1687.8700.

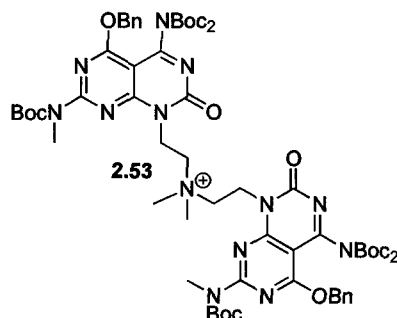
Compound 2.52



Compound **2.51** (0.093 g, 0.0558 mmol) was stirred in 95% TFA in thioanisole (10 mL) for 72 h. Et_2O (60 mL) was then added to the reaction mixture and the precipitate formed was stirred for another 30 min, after which it was centrifuged down. The residual solid was resuspended in Et_2O , sonicated and centrifuged down. This process was repeated until the spotting of the Et_2O produced no UV active spot. The white solid obtained (0.069 g, 91%) was dried (K-TBL-TFA, **2.52A**) and part of the sample was then dissolved in 1 M hydrochloric acid (10 mL), followed by removal of water under reduced pressure. This process was repeated two more times before the solid was dried under vacuo for 72 h to yield the desired compound **2.52B** as an off-white powder in quantitative yield; ^1H NMR (600 MHz, $\text{d}_6\text{-DMSO}$): $\delta = 12.32$ (s, 2H), 11.50 (s, 1H), 9.20 (s, 2H), 9.83 (bs, 3H), 8.46 (bs, 2H), 8.31 (bs, 3H), 8.03 (bs, 3H), 4.50 (bs, 4H), 3.77 (m, 1H), 3.52-3.40 (m, 6H, merged with water peak), 3.19-3.09 (m, 2H), 2.92 (d, $J = 4.8$ Hz, 6H), 2.79-2.74 (m, 2H), 1.82-1.65 (m, 4H), 1.61-1.43 (m, 4H), 1.41-1.32 (m, 2H); ^{13}C NMR (125 MHz, $\text{d}_6\text{-DMSO}$): $\delta = 168.2, 160.7, 159.7, 156.2, 155.7, 148.0, 82.6, 51.8, 48.5, 38.1, 37.8, 30.2, 28.9, 28.5, 27.8, 26.1, 25.8, 21.1$ ppm; HRMS calcd for $\text{C}_{28}\text{H}_{45}\text{N}_{16}\text{O}_5$ $[\text{M}-2\text{H}]^+$: 685.3753; found: 685.3759; elemental

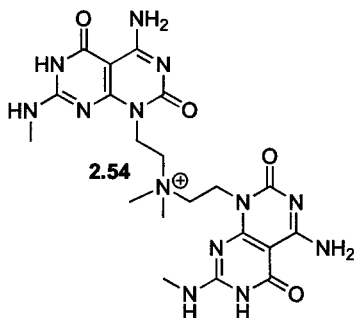
analysis calcd (%) for $C_{28}H_{44}N_{16}O_5(TFA)_{5.5}(H_2O)_2$: C 34.75, H 4.00, N 16.63; found C 35.15, H 4.40, N 16.40; elemental analysis calcd (%) for $C_{28}H_{44}N_{16}O_5(HCl)_8(H_2O)_3(Et_2O)_{0.25}$: C 33.20, H 5.81, N 21.36; found C 33.12, H 5.93, N 21.42.

Compound 2.53



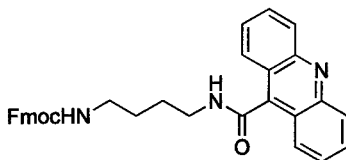
Methyl iodide (0.15 mL, large excess) was added to a solution of **2.32** (0.110 g, 0.086 mmol) in anhydrous Et_2O (5 mL) at room temperature under argon and stirred for 72 h. The reaction mixture then concentrated and flash chromatography (0-5% MeOH in CH_2Cl_2) gave **2.53** (0.083 g, 74%) as a pale yellow foam. $R_f = 0.29$ (7% MeOH in CH_2Cl_2); 1H NMR (500 MHz, $CDCl_3$): $\delta = 7.42-7.32$ (m, 10H), 5.57 (s, 4H), 4.85 (t, $J = 7.0$ Hz, 4H), 4.11 (t, $J = 7.0$ Hz, 4H), 3.68 (s, 6H), 3.51 (s, 6H), 1.53 (s, 18H), 1.33 (s, 36H); ^{13}C NMR (125 MHz, $CDCl_3$): $\delta = 165.7, 161.3, 161.1, 160.5, 155.2, 151.8, 149.2, 134.6, 128.6, 128.1, 93.3, 84.2, 83.4, 70.4, 61.2, 52.3, 37.4, 35.3, 28.1, 27.9, 27.8$ ppm; HRMS: calcd for $C_{64}H_{88}N_{13}O_{16}^+$ [M]: 1294.6467; found; 1294.6466.

Compound 2.54



Compound **2.53** (0.041 g, 0.032 mmol) was stirred in 95% TFA in thioanisole (10 mL) for 72 h. Et₂O (60 mL) was then added to the reaction mixture and the precipitate formed, was centrifuged down. The residual solid was resuspended in Et₂O, sonicated and centrifuged down. This process was repeated until the spotting of the Et₂O produced no UV active spot. The white solid was dried and was dissolved in 1 M hydrochloric acid (10 mL), followed by removal of water under reduced pressure. This process was repeated two more times before the solid was dried under vacuo for 72 h to yield **2.54** (0.020 g, 90%) as an off-white powder; ¹H NMR (500 MHz, d₆-DMSO): δ = 12.36 (bs, 2H), 9.23 (s, 2H), 8.88 (bs, 2H), 8.47 (q, *J* = 4.6 Hz, 2H), 4.51 (t, *J* = 7.2 Hz, 4H), 3.64 (t, *J* = 7.3 Hz, 4H), 3.30 (s, 6H), 2.95 (d, *J* = 4.7 Hz, 6H); ¹³C NMR (125 MHz, d₆-DMSO): δ = 160.7, 159.5, 156.2, 155.8, 140.3, 129.5, 82.6, 50.8, 40.2, 39.6, 27.9 ppm; HRMS: calcd for C₂₀H₂₈N₁₃O₄⁺ [M]: 514.2382; found: 514.2382; elemental analysis calcd (%) for C₂₀H₂₈N₁₃O₄⁺(HCl)₄(H₂O)_{2.5}: C 34.05, H 5.29, N 25.81, found C 34.55, H 4.68, N 25.46.

(9*H*-fluoren-9-yl)methyl 4-(acridine-9-carboxamido)butylcarbamate (**2.56**)

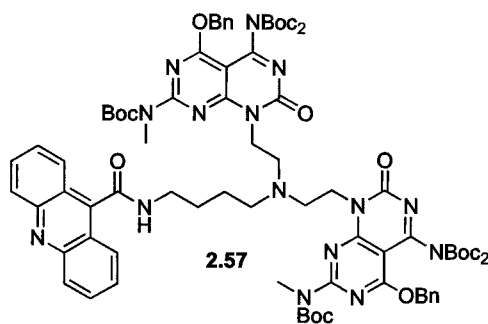


2.56

DIEA (0.36 mL, 2.09 mmol) was added to a solution of (9*H*-fluoren-9-yl)methyl 4-aminobutylcarbamate hydrochloride (0.726 g, 2.09 mmol) in DMF (10 mL) and was stirred for 10 min at room temperature under argon. Acridine-9-carboxylic

acid (0.467 g, 2.09 mmol) and HBTU (1.19 g, 3.14 mmol) were then added and the resulting mixture was stirred for another 5 h. The reaction mixture was diluted with CH₂Cl₂ (50 mL) and then washed with water (10 mL), NaHCO₃ (10 mL), brine (15 mL), dried over Na₂SO₄ and concentrated. Flash chromatography of the residue over silica gel (100% CH₂Cl₂ to 5% MeOH in CH₂Cl₂ to 5% DMF in CH₂Cl₂) gave a yellow paste. The latter was dissolved in CH₂Cl₂ (50 mL) and washed with water (10 mL) to remove DMF and concentrated. Et₂O was added to the viscous oil to crash out **2.56** (0.640 g, 59%) as a yellow solid. R_f 0.42 (7% MeOH in CH₂Cl₂); mp 173-174 °C; ¹H NMR (500 MHz, CDCl₃): δ = 8.03 (d, *J* = 9.0 Hz, 2H), 7.95 (d, *J* = 7.5 Hz, 2H), 7.70 (d, *J* = 7.5 Hz, 2H), 7.65 (t, *J* = 7.5 Hz, 2H), 7.53 (d, *J* = 7.5 Hz, 2H), 7.46 (t, *J* = 7.5 Hz, 2H), 7.33 (t, *J* = 7.3 Hz, 2H), 7.24 (t, *J* = 7.3 Hz, 2H), 5.29 (bs, 1H), 4.32 (d, *J* = 7.0 Hz, 2H), 4.14 (t, *J* = 6.8 Hz, 1H), 3.67 (q, *J* = 6.0 Hz, 2H), 3.25 (q, *J* = 6.0 Hz, 2H), 1.83-1.76 (m, 2H), 1.72-1.63 (m, 2H); ¹³C NMR (125 MHz, CDCl₃): δ = 180.5, 156.6, 143.9, 141.2, 127.6, 127.1, 127.0, 125.8, 125.0, 122.2, 119.9, 66.5, 47.2, 40.5, 39.8, 27.6, 26.7 ppm; HRMS: calcd for C₃₃H₃₀N₃O₃ [M+H]⁺: 516.2282; found: 516.2279.

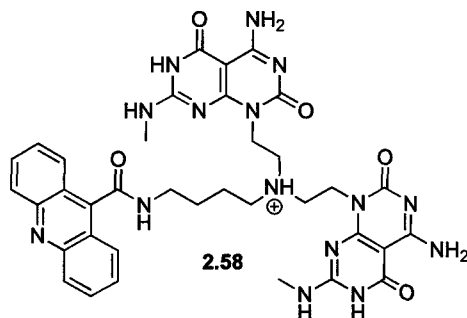
Compound 2.57



20% piperidine in DMF (5 mL) was added to **2.56** (0.030 g, 0.058 mmol) and the solution was stirred for 1 h at room temperature under N₂. The reaction mixture was concentrated, then diluted with CH₂Cl₂ (20 mL) and washed with NaHCO₃ (10 mL), brine (15 mL), dried over Na₂SO₄ and evaporated to yield a yellow oil. 1,2 DCE (20 mL) and **2.13** (0.037 g, 0.058 mmol) were then added to the yellow oil, which was stirred for 30 min, prior to the addition of sodium triacetoxy borohydride (0.013 g, 0.062 mmol) and stirring was continued for another 3 h

(until all **2.13** was consumed). The reaction mixture was diluted with CH₂Cl₂ (20 mL) and then washed with NaHCO₃ (10 mL), brine (15 mL), dried over Na₂SO₄ and concentrated. Fresh 1,2 DCE (20 mL) and **2.13** (0.037 g, 0.058 mmol) were then added to the yellow oil formed, which was stirred for 30 min, prior to the addition of sodium triacetoxo borohydride (0.037 g, 0.058 mmol) and stirring was continued for another 30 h. The reaction mixture was diluted with CH₂Cl₂ (50 mL) and then washed with water (10 mL), NaHCO₃ (10 mL), brine (15 mL), dried over Na₂SO₄ and concentrated. Flash chromatography of the residue over silica gel (0-70% EtOAc in hexanes) gave **2.57** (0.078 g, 87%) a yellow foam. R_f = 0.29 (70% EtOAc in hexanes); ¹H NMR (500 MHz, CDCl₃): δ = 8.13 (d, *J* = 9.0 Hz, 2H), 8.01 (d, *J* = 9.0 Hz, 2H), 7.73-7.69 (ddd, *J* = 9.0 Hz, 6.5 Hz, 1.5 Hz, 2H), 7.51-7.47 (ddd, *J* = 8.5 Hz, 6.5 Hz, 1.0 Hz, 2H), 7.42-7.38 (m, 4H), 7.35-7.30 (m, 6H), 7.15 (t, *J* = 5.8 Hz, 1H), 5.52 (s, 4H), 4.35 (t, *J* = 7.3 Hz, 4H), 4.64 (q, *J* = 6.5 Hz, 2H), 3.43 (s, 6H), 2.93 (t, *J* = 7.3 Hz, 4H), 2.77 (t, *J* = 6.8 Hz, 2H), 1.77-1.74 (dddd, *J* = 7.5 Hz, 7.5 Hz, 7.0 Hz, 7.0 Hz, 2H), 1.61-1.56 (m, 2H), 1.53 (s, 18H), 1.25 (s, 36H); ¹³C NMR (125 MHz, CDCl₃): δ = 167.0, 165.6, 161.1, 161.0, 160.2, 155.6, 152.4, 149.4, 148.6, 141.5, 134.9, 130.3, 129.6, 128.5, 128.5, 128.4, 126.6, 125.4, 122.3, 92.8, 83.7, 82.9, 70.0, 53.8, 50.8, 41.2, 40.2, 34.9, 28.1, 27.9, 27.8, 27.2, 25.5 ppm; HRMS: calcd for C₈₀H₁₀₀N₁₅O₁₇ [M+H]⁺: 1542.7416; found: 1542.7407.

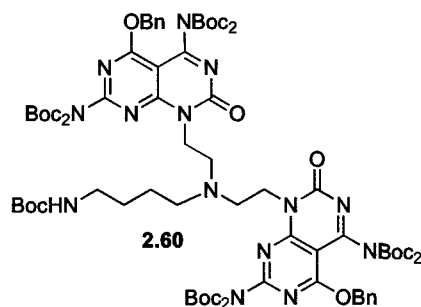
Compound 2.58



Compound **2.57** (0.075 g, 0.049 mmol) was stirred in 95% TFA in thioanisole (10 mL) for 48 h. Et₂O (60 mL) was then added to the reaction mixture to give a yellow precipitate, which was centrifuged down. The residual solid was

resuspended in Et₂O, sonicated and centrifuged down. This process was repeated until the spotting of the Et₂O produced no UV active spot. The yellow solid was dried, then dissolved in 1 M hydrochloric acid (10 mL) and evaporated. This process was repeated two more times before the solid was dried under vacuo for 72 h to yield **2.58** (0.045 g, 93%) as a yellow powder; ¹H NMR (600 MHz, d₆-DMSO): δ = 12.30 (bs, 2H), 11.69 (bs, 1H), 9.27 (t, *J* = 4.8 Hz, 1H), 9.19 (bs, 2H), 8.83 (bs, 2H), 8.42-8.30 (m, 4H), 8.12-7.98 (m, 4H), 7.80 (bs, 2H), 4.51 (bs, 4H), 3.58-3.35 (m, 8H), 2.92 (d, *J* = 4.8 Hz, 6H), 1.92-1.84 (m, 2H), 1.79-1.73 (m, 2H); ¹³C NMR (150 MHz, d₆-DMSO): δ = 165.5, 162.4, 161.2, 160.3, 159.5, 156.6, 156.2, 148.4, 128.1, 126.6, 122.3, 83.1, 52.4, 49.5, 49.0, 36.6, 28.4, 26.8, 21.0 ppm; HRMS: calcd for C₃₆H₄₀N₁₅O₅ [M]⁺: 762.3331; found: 762.3327; elemental analysis calcd (%) for (C₃₆H₃₉N₁₅O₅)(HCl)₅(H₂O)₂(Et₂O)_{0.25}: C 44.50, H 5.10, N 21.04; found: C 44.59, H 5.11, N 21.03.

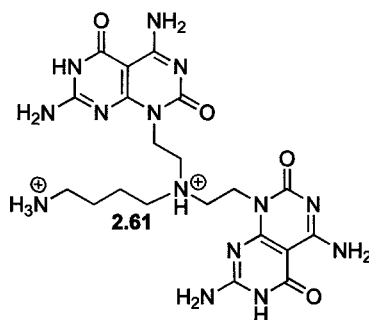
Compound 2.60



Compound **2.59** (0.075 g, 0.103 mmol) was added to a solution of *tert*-butyl 4-aminobutylcarbamate (0.020 mL, 0.103 mmol) in 1,2 DCE (20 mL) at room temperature under N₂ and stirred for 30 min. Sodium triacetoxy borohydride (0.023 g, 0.110 mmol) was added and the resulting mixture was stirred for 1.5 h. The reaction mixture was diluted with CH₂Cl₂ (50 mL) and then washed with water (10 mL), brine (15 mL), dried over Na₂SO₄ and concentrated. Fresh 1,2 DCE (20 mL) and **2.59** (0.075 g, 0.103 mmol) was added to the residue and stirred for 30 min, prior to the addition of sodium triacetoxy borohydride (0.023 g, 0.110 mmol) and stirring was continued for another 36 h. The reaction mixture was diluted with CH₂Cl₂ (50 mL) and washed with water (10 mL), NaHCO₃ (10

mL), brine (15 mL), dried over Na₂SO₄ and concentrated. Flash chromatography of the residue over silica gel using (0-3% MeOH in CH₂Cl₂) gave **2.60** (0.100 g, 60%) as a colourless oil. R_f = 0.33 (5% MeOH in CH₂Cl₂); ¹H NMR (600 MHz, CDCl₃): δ = 7.41-7.30 (m, 10H), 5.51 (s, 4H), 4.92 (m, 1H), 4.38 (t, *J* = 6.9 Hz, 4H), 2.91 (m, 2H), 2.90 (t, *J* = 6.9 Hz, 4H), 2.60 (m, 2H), 1.52 (s, 36H), 1.38 (s, 18H), 1.36-1.31 (m, 4H), 1.27 (s, 27H); ¹³C NMR (150 MHz, CDCl₃): δ = 167.7, 166.3, 161.3, 161.1, 160.0, 158.7, 158.6, 156.0, 155.1, 149.4, 149.2, 149.0, 134.4, 128.7, 128.6, 128.5, 94.1, 93.7, 84.5, 84.4, 83.9, 83.8, 70.4, 55.7, 53.4, 50.5, 41.3, 40.5, 30.7, 28.4, 27.8, 27.8, 27.7, 25.1 ppm; HRMS: calcd for C₇₉H₁₁₂N₁₄O₂₂Na [M+Na]⁺: 1631.7968; found: 1631.8005.

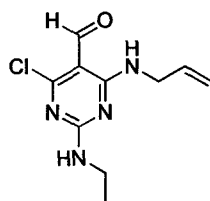
Compound 2.61



Compound **2.60** (0.090 g, 0.056 mmol) was stirred in 95% TFA in thioanisole (10 mL) for 48 h. Et₂O (60 mL) was then added to the reaction mixture to give a white precipitate, which was centrifuged down. The residual solid was resuspended in Et₂O, sonicated and centrifuged down. This process was repeated until the spotting of the Et₂O produced no UV active spot. The yellow solid was dried, then dissolved in 1 M hydrochloric acid (10 mL) and evaporated. This process was repeated two more times before the solid was dried under vacuo for 72 h to yield **2.61** (0.039 g, 89%) as an off-white powder; ¹H NMR (600 MHz, d₆-DMSO): δ = 12.20 (bs, 2H), 11.08 (bs, 1H), 9.14 (bs, 2H), 8.77 (bs, 2H), 8.67 (bs, 2H), 8.01 (bs, 3H), 7.84 (bs, 2H), 4.34 (m, 4H), 3.48 (m, 4H), 3.01 (m, 2H), 2.81 (m, 2H), 1.79 (m, 2H), 1.64 (m, 2H); ¹³C NMR (150 MHz, d₆-DMSO): δ = 165.5, 162.4, 161.2, 160.3, 159.5, 156.6, 156.2, 148.4, 128.1, 126.6, 122.3, 83.1, 52.4, 49.5, 49.0, 36.6, 28.4, 26.8, 21.0 ppm; HRMS: calcd for C₂₀H₂₉N₁₄O₄ [M-H]⁺:

529.2491; found: 529.2491; elemental analysis calcd (%) for $(C_{20}H_{28}N_{14}O_4)(HCl)_6(H_2O)(Et_2O)_{0.25}$: C 32.18, H 4.95, N 25.02; found: C 32.19, H 4.95, N 24.99.

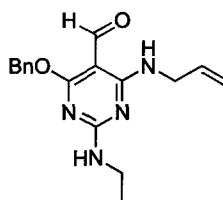
4-(allylamino)-6-chloro-2-(ethylamino)pyrimidine-5-carbaldehyde (**2.62**)



2.62

Ethylamine (70% in H_2O , 4.22 mL, 52.2 mmol) was added to a solution of **2.3** (6.06 g, 26.1 mmol) in THF (100 mL) at 0 °C under N_2 and the reaction mixture was stirred at room temperature for 1 h. Upon removal of solvent, the residue was washed with ice-cold Et_2O to give **2.62** (6.02 g, 74%) as a white solid. $R_f = 0.61$ (10% EtOAc in hexanes); mp = 144-145 °C; 1H NMR (600 MHz, $CDCl_3$): $\delta = 10.02$ (s, 1H), 9.36 (bs, 1H), 6.22 (bs, 1H), 5.94-5.87 (m, 1H), 5.22 (d, $J = 18.0$ Hz, 1H), 5.15 (d, $J = 10.2$ Hz, 1H), 4.15 (dd, $J = 5.4$ Hz, 5.4 Hz, 2H), 3.46 (m, 2H), 1.20 (t, $J = 7.5$ Hz, 3H); ^{13}C NMR (150 MHz, $CDCl_3$): $\delta = 188.4, 165.5, 162.3, 160.8, 133.7, 166.4, 101.7, 42.9, 36.4, 14.5$ ppm; HRMS: calcd for $C_{10}H_{13}N_4ClO [M]^+$: 241.0851; found: 241.0852.

4-(allylamino)-6-(benzyloxy)-2-(ethylamino)pyrimidine-5-carbaldehyde (**2.63**)

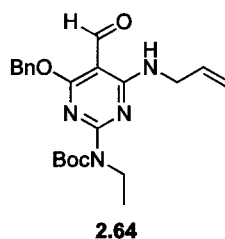


2.63

Benzyl alcohol was added (2.50 mL, 24.2 mmol) to NaH (1.27 g, 52.9 mmol) in THF (20 mL) at room temperature under N_2 and stirred for 15 min. The solution was cooled to 0 °C and added gradually to a stirred solution of **2.62** (5.42 g, 22.5 mmol) in THF (100 mL). The mixture was warmed to room temperature and

refluxed for 6 h, after which it was cooled to room temperature and quenched with dH₂O. Upon evaporation, the residue was dissolved in CH₂Cl₂, washed with dH₂O (20 mL), brine (20 mL) and dried over Na₂SO₄. Evaporation, followed by flash chromatography over silica gel (0-5% EtOAc in hexanes) gave **2.63** (5.26 g, 75%) as a pale yellow oil. $R_f = 0.78$ (10% EtOAc in hexanes); ¹H NMR (600 MHz, d₆-DMSO): $\delta =$ (because of hydrogen bonding between the oxygen atom of the aldehyde and the hydrogen atom of the allylic nitrogen, this compound displays two sets of peaks) 9.85 (s, 1H, minor isomer), 9.82 (s, 1H, major isomer), 9.22 (t, $J = 5.7$ Hz, 1H, major isomer), 9.07 (t, $J = 5.7$ Hz, 1H, minor isomer), 7.77 (t, $J = 5.7$ Hz, 1H, major isomer), 7.74 (t, $J = 6.0$ Hz, 1H, minor isomer), 7.44-7.30 (m, 10H, major and minor isomers merged), 5.95-5.86 (m, 2H, major and minor isomers merged), 5.44 (s, 2H, minor isomer), 5.38 (s, 2H, major isomer), 5.17-5.12 (m, 2H, minor isomer), 5.10-5.07 (m, 2H, major isomer), 4.09 (t, $J = 5.7$ Hz, 2H, major isomer), 4.04 (t, $J = 5.7$ Hz, 2H, minor isomer), 3.37-3.28 (m, 4H, major and minor isomers merged), 1.10 (t, $J = 7.2$ Hz, 3H, major isomer), 1.06 (t, $J = 7.5$ Hz, 3H, major isomer); ¹³C NMR (150 MHz, d₆-DMSO): $\delta =$ (this compound displays two sets of peaks for some carbons) 184.7, 184.6, 171.6, 171.0, 163.2, 163.0, 162.4, 162.0, 137.3, 137.1, 135.6, 128.9, 128.8, 128.3, 128.2, 128.1, 115.9, 115.8, 92.4, 92.2, 67.4, 67.2, 42.5, 42.2, 36.0, 15.3, 14.9 ppm; HRMS: calcd for C₁₇H₂₁N₄O₂ [M+H]⁺: 313.1659; found: 313.1656.

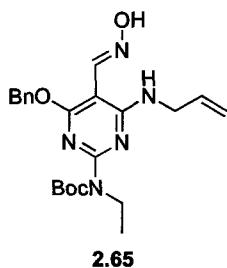
***tert*-butyl-4-(allylamino)-6-(benzyloxy)-5-formylpyrimidin-2-yl(ethyl)-carbamate (2.64)**



4-*N*, *N*-dimethylaminopyridine (0.32 g, 0.039 mmol), triethylamine (16.2 mL, 83.3 mmol) and Boc₂O (6.33 g, 29.0 mmol) were added to **2.63** (39.5 g, 132 mmol) in THF (100 mL) at room temperature under N₂ and stirred for 12 h. The

reaction mixture was quenched with dH₂O (20 mL) and evaporated. The residue was washed with dH₂O (20 mL), 5% aqueous NaHCO₃ (20 mL) and brine (20 mL), along with extraction using EtOAc. Drying over Na₂SO₄, filtration and evaporation, followed by flash chromatography of the residue over silica gel (0-10% EtOAc in hexanes) gave **2.64** (5.72 g, 90%) as pale yellow oil. *R_f* = 0.50 (5% EtOAc in hexanes); ¹H NMR (600 MHz, CDCl₃): δ = 10.13 (s, 1H), 9.22 (t, *J* = 5.4 Hz, 1H), 7.42-7.29 (m, 5H), 5.94-5.87 (m, 1H), 5.46 (s, 2H), 5.24-5.08 (m, 2H), 4.18-4.15 (m, 2H), 3.94 (q, *J* = 7.2 Hz, 2H), 1.54 (s, 9H), 1.23 (t, *J* = 6.6 Hz, 3H); ¹³C NMR (150 MHz, CDCl₃): δ = 187.5, 171.4 162.8, 161.4, 153.4, 136.4, 134.1, 128.5, 128.3, 128.2, 128.1, 128.0, 116.1, 94.3, 81.7, 68.2, 43.0, 42.7, 28.2, 27.9, 27.8, 14.0 ppm; HRMS: calcd for C₂₂H₂₉N₄O₄ [M+H]⁺: 413.2183; found: 413.2182.

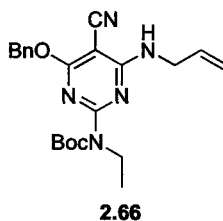
(*E*)-tert-butyl-4-(allylamino)-6-(benzyloxy)-5-((hydroxyimino)methyl)-pyrimidin-2-yl(ethyl)carbamate (2.65)



Hydroxylamine hydrochloride (1.84 g, 26.2 mmol) and KHCO₃ (5.26 g, 52.6 mmol) were added to a stirred solution of **2.64** (5.26 g, 12.3 mmol) in anhydrous methanol (50 mL) at room temperature under N₂. The resulting slurry was refluxed for 3 h and cooled to room temperature. The residual solid obtained upon evaporation, was dissolved in EtOAc (100 mL), washed with dH₂O (20 mL) and brine (20 mL), and dried over anhydrous Na₂SO₄. Evaporation of the solvent gave rise to **2.65** (5.07 g, 90%) as a white paste, which was used in the next step without further purification. *R_f* = 0.39 (20% EtOAc in hexanes); ¹H NMR (600 MHz, CDCl₃): δ = 8.56 (s, 1H), 8.35 (bs, 1H), 8.07 (t, *J* = 5.4 Hz, 1H), 7.42-7.29 (m, 5H), 5.96-5.89 (m, 1H), 5.41 (s, 2H), 5.21-5.08 (m, 2H), 4.18 (t, *J* = 5.7 Hz, 2H), 3.91 (q, *J* = 6.8 Hz, 2H), 1.53 (s, 9H), 1.23 (t, *J* = 6.9 Hz, 3H); ¹³C NMR

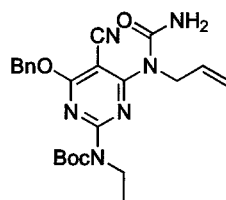
(150 MHz, CDCl₃): δ = 167.3, 153.8, 146.5, 136.8, 134.9, 128.4, 128.0, 115.6, 87.4, 70.5, 68.0, 43.4, 42.7, 29.7, 29.3, 28.3, 14.1 ppm; HRMS: calcd for C₂₂H₃₀N₅O₄ [M+H]⁺: 428.2292; found: 428.2295.

***tert*-butyl-4-(allylamino)-6-(benzyloxy)-5-cyanopyrimidin-2-yl(ethyl)-
carbamate (2.66)**



Trifluoroacetic anhydride (3.9 mL, 28.0 mmol) was slowly added to a stirred solution of **2.65** (5.07 g, 11.8 mmol) and Et₃N (8.2 mL, 59.7 mmol) in THF (100 mL) at 0°C over 30 min. The reaction mixture was warmed to room temperature and refluxed for 3 h. Upon cooling to room temperature, the reaction mixture was quenched with dH₂O and evaporated. The residue was dissolved in EtOAc (100 mL), washed with dH₂O (20 mL), 5% aqueous NaHCO₃ (20 mL), and brine (20 mL). The organic layer was dried over Na₂SO₄ and evaporated to yield an orange solid, which was purified by flash chromatography (0-20% EtOAc in hexanes). The orange crystals obtained were further purified by recrystallization from EtOAc and hexanes to give **2.66** (4.51 g, 93%) as pale yellow crystals. mp = 93-94 °C; *R_f* = 0.58 (20% EtOAc in hexanes); ¹H NMR (600 MHz, CDCl₃): δ = 7.44-7.30 (m, 5H), 5.93-5.85 (m, 1H), 5.45 (s, 2H), 5.43 (bs, 1H), 5.24 (dd, *J* = 16.8 Hz, 1.2 Hz, 1H), 5.18 (dd, *J* = 10.2 Hz, 1.2 Hz, 1H), 4.14 (t, *J* = 5.7 Hz, 2H), 3.91 (q, *J* = 6.8 Hz, 2H), 1.53 (s, 9H), 1.20 (t, *J* = 7.2 Hz, 3H); ¹³C NMR (150 MHz, CDCl₃): δ = 170.3, 164.0, 160.4, 153.1, 136.0, 133.7, 128.5, 128.1, 127.9, 117.1, 114.8, 81.9, 69.0, 68.6, 43.7, 42.8, 28.2, 13.9 ppm; HRMS: calcd for C₂₂H₂₈N₅O₃ [M+H]⁺: 410.2187; found: 410.2186.

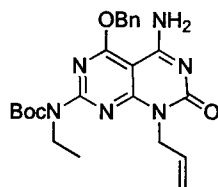
***tert*-butyl-4-(1-allylureido)-6-(benzyloxy)-5-cyanopyrimidin-2-yl(ethyl)-
carbamate (2.67)**



2.67

Freshly distilled *N*-chlorocarbonylisocyanate (0.440 mL, 5.49 mmol) was added dropwise to a stirred solution of compound **2.66** (0.750 g, 1.83 mmol) in CH₂Cl₂ (50 mL) at 0 °C over 30 min under argon. The reaction mixture was stirred for 2 h at room temperature, then cooled to 0°C and carefully quenched with dH₂O (10 mL, exothermic reaction). The product was extracted with CH₂Cl₂ (100 mL) and the organic layer was washed with dH₂O (20 mL), brine (20 mL) and dried over Na₂SO₄. Evaporation of solvent gave **2.67** as a white paste, which was used in the next step without further purification. *R*_f = 0.58 (50% EtOAc in hexanes); ¹H NMR (600 MHz, CDCl₃): δ = 7.43-7.32 (m, 5H), 5.89-5.82 (m, 1H), 5.50 (s, 2H), 5.26 (dd, *J* = 17.4 Hz, 1.2 Hz, 1H), 5.17 (dd, *J* = 12.0 Hz, 1.2 Hz, 1H), 4.92 (d, *J* = 4.8 Hz, 2H), 3.95 (q, *J* = 7.2 Hz, 2H), 1.54 (s, 9H), 1.22 (t, *J* = 7.2 Hz, 3H); ¹³C NMR (150 MHz, CDCl₃): δ = 172.2, 163.1, 158.2, 155.3, 152.2, 135.3, 133.3, 128.7, 128.4, 127.4, 116.9, 113.9, 83.2, 70.6, 69.6, 48.1, 42.6, 29.7, 28.0, 13.9 ppm; HRMS: calcd for C₂₃H₂₉N₆O₄ [M+H]⁺: 453.2245; found: 453.2245.

***tert*-butyl-8-allyl-5-amino-4-(benzyloxy)-7-oxo-7,8-dihydropyrimido[4,5-*d*]-
pyrimidin-2-yl(ethyl)carbamate (2.68)**

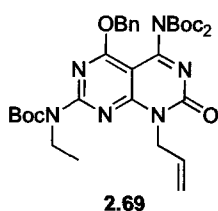


2.68

Crude material **2.67** from the previous step was stirred in 7 M NH₃ in CH₃OH (15 mL) under N₂ at room temperature for 3 h. Excess NH₃ in CH₃OH was removed under reduced pressure and **2.68** (0.620 g, 75%) was obtained as a white paste

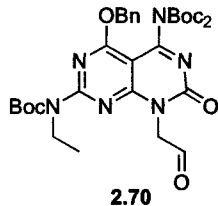
over 2 steps, which was used for the next step without further purification. $R_f = 0.22$ (7% MeOH in CH_2Cl_2); $^1\text{H NMR}$ (600 MHz, CDCl_3): $\delta = 7.47\text{-}7.37$ (m, 5H), 7.12 (bs, 2H), 5.96-5.90 (m, 1H), 5.60 (s, 2H), 5.23 (d, $J = 18.0$ Hz, 1H), 5.15 (d, $J = 10.2$ Hz, 1H), 4.83 (d, $J = 4.2$ Hz, 2H), 4.01 (q, $J = 6.8$ Hz, 2H), 1.57 (s, 9H), 1.27 (t, $J = 6.6$ Hz, 3H); $^{13}\text{C NMR}$ (150 MHz, CDCl_3): $\delta = 166.5, 160.5, 160.4, 160.3, 155.3, 152.6, 134.8, 132.4, 129.0, 128.9, 128.7, 117.5, 82.5, 70.6, 70.2, 44.7, 43.0, 29.7, 28.1, 13.9$ ppm; HRMS: calcd for $\text{C}_{23}\text{H}_{29}\text{N}_6\text{O}_4$ $[\text{M}+\text{H}]^+$: 453.2245; found: 453.2245.

Compound 2.69



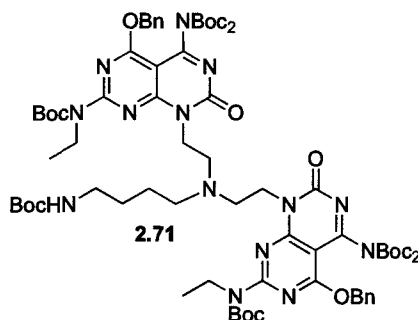
4-*N*, *N*-dimethylaminopyridine (0.180 g, 1.50 mmol), Et_3N (0.761 mL, 5.48 mmol) and Boc_2O (1.32 g, 5.48 mmol) were added to **2.68** (0.620 g, 1.37 mmol) in THF (50 mL) at room temperature under N_2 and stirred for 24 h. The reaction was then quenched with dH_2O (20 mL) and the solvent was removed under reduced pressure. The residual solid was dissolved in EtOAc (100 mL), washed with dH_2O (20 mL), 5% aqueous NaHCO_3 (20 mL), brine (20 mL), dried over Na_2SO_4 and evaporated. The residue was purified through flash chromatography (0-40% EtOAc in hexanes) to give **2.69** (0.726 g, 78%) as a white foam. $R_f = 0.68$ (50% EtOAc in hexanes); $^1\text{H NMR}$ (600 MHz, CDCl_3): $\delta = 7.41\text{-}7.29$ (m, 5H), 5.96-5.89 (m, 1H), 5.53 (s, 2H), 5.18-5.13 (m, 2H), 4.89 (d, $J = 5.4$ Hz, 2H), 3.98 (q, $J = 6.8$ Hz, 2H), 1.55 (s, 9H), 1.30 (s, 18H), 1.24 (t, $J = 7.2$ Hz, 3H); $^{13}\text{C NMR}$ (150 MHz, CDCl_3): $\delta = 165.7, 160.9, 160.7, 160.3, 155.4, 152.4, 149.2, 134.9, 131.2, 128.5, 128.3, 117.9, 92.9, 83.6, 82.8, 70.0, 45.2, 43.0, 28.0, 27.9, 27.8, 13.8$ ppm; HRMS: calcd for $\text{C}_{33}\text{H}_{45}\text{N}_6\text{O}_8$ $[\text{M}+\text{H}]^+$: 653.3293; found: 653.3291.

Compound 2.70



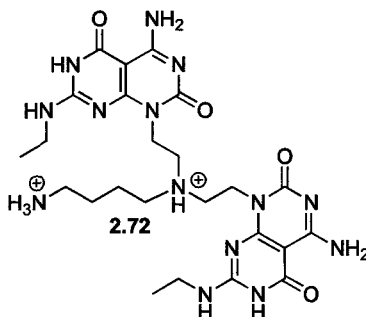
50% aqueous *N*-methylmorpholine *N*-oxide (0.420 mL, 2.15 mmol) was added to **2.69** (0.700 g, 1.07 mmol) in *t*-BuOH / dH₂O / THF (10:1:2, 13 mL) at room temperature and stirred for 5 min. OsO₄ (0.049 M solution in *t*-BuOH, 1.08 mL, 0.053 mmol) was slowly added and the resulting brown solution was stirred for 6 h. The reaction mixture was quenched with aqueous sodium sulfite until all the excess OsO₄ was destroyed (brown solution turns colorless). The resulting diol was extracted using CH₂Cl₂ (100 mL) and washed with dH₂O (20 mL), brine (20 mL), dried over anhydrous Na₂SO₄ and evaporated to yield a pale yellow oil. To the latter, sodium periodate (0.457 g, 2.14 mmol) in CH₂Cl₂ / dH₂O (4:1, 10 mL) was added and stirred at room temperature for 18 h. The crude product was washed with dH₂O (20 mL), 5% aqueous NaHCO₃ (20 mL), and brine (20 mL) and extracted using CH₂Cl₂ (100 mL), then dried over anhydrous Na₂SO₄. Removal of solvent and purification through column chromatography (0 - 50% EtOAc in hexanes) gave the desired product **2.70** (0.400 g, 57%) as a white solid. *R_f* = 0.58 (50% EtOAc in hexanes); ¹H NMR (600 MHz, CDCl₃): δ = 9.64 (s, 1H), 7.44-7.33 (m, 5H), 5.56 (s, 2H), 5.12 (s, 2H), 3.93 (q, *J* = 7.0 Hz, 2H), 1.56 (s, 9H), 1.35 (s, 18H), 1.22 (t, *J* = 7.2 Hz, 3H); ¹³C NMR (125 MHz, CDCl₃): δ = 193.7, 165.7, 161.1, 160.8, 160.6, 155.4, 152.1, 149.1, 134.8, 128.6, 128.2, 92.9, 83.9, 83.1, 70.2, 51.9, 43.0, 28.0, 27.8, 13.7 ppm; HRMS: calcd for C₃₂H₄₃N₆O₉ [M+H]⁺: 655.3086; found: 655.3088.

Compound 2.71



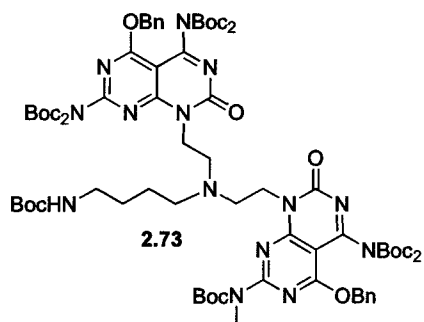
Compound **2.70** (0.080 g, 0.122 mmol) was added to a solution of *tert*-butyl 4-aminobutylcarbamate (0.023 mL, 0.122 mmol) in 1,2 DCE (20 mL) at room temperature under N₂ and stirred for 30 min. Sodium triacetoxy borohydride (0.027 g, 0.129 mmol) was added and the resulting mixture was stirred for 3 h. The reaction mixture was diluted with CH₂Cl₂ (50 mL) and then washed with water (10 mL), brine (15 mL), dried over Na₂SO₄ and concentrated. Fresh 1,2 DCE (20 mL) and **2.70** (0.080 g, 0.122 mmol) was added to the residue and stirred for 30 min, prior to the addition of sodium triacetoxy borohydride (0.027 g, 0.129 mmol), and stirring was continued for another 24 h. The reaction mixture was diluted with CH₂Cl₂ (50 mL) and washed with water (10 mL), NaHCO₃ (10 mL), brine (15 mL), dried over Na₂SO₄ and concentrated. Flash chromatography of the residue over silica gel using (0-65% EtOAc in hexanes) gave **2.71** (0.131 g, 73%) as a colourless oil. R_f = 0.29 (50% EtOAc in hexanes); ¹H NMR (600 MHz, CDCl₃): δ = 7.44-7.32 (m, 10H), 5.55 (s, 4H), 4.89 (m, 1H), 4.39 (t, *J* = 7.5 Hz, 4H), 4.04 (q, *J* = 7.0 Hz, 4H), 3.06 (m, 2H), 2.90 (t, *J* = 7.5 Hz, 4H), 2.68 (m, 2H), 1.56 (s, 18H), 1.45-1.42 (m, 4H), 1.41 (s, 9H), 1.32 (s, 36H), 1.26 (t, *J* = 6.9 Hz, 6H); ¹³C NMR (150 MHz, CDCl₃): δ = 165.7, 161.1, 160.8, 156.0, 155.6, 152.2, 149.3, 135.0, 128.5, 128.5, 128.3, 17.7, 92.9, 83.6, 82.7, 70.0, 53.8, 50.9, 43.0, 41.3, 40.5, 28.4, 28.0, 27.8, 25.1, 14.0 ppm; HRMS: calcd for C₇₃H₁₀₅N₁₄O₁₈ [M+H]⁺: 1465.7726; found: 1465.7690.

Compound 2.72



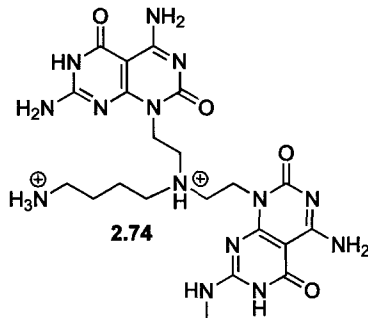
Compound **2.71** (0.120 g, 0.082 mmol) was stirred in 95% TFA in thioanisole (10 mL) for 48 h. Et₂O (60 mL) was then added to the reaction mixture to give a white precipitate, which was centrifuged down. The residual solid was resuspended in Et₂O, sonicated and centrifuged down. This process was repeated until the spotting of the Et₂O produced no UV active spot. The yellow solid was dried, then dissolved in 1 M hydrochloric acid (10 mL) and evaporated. This process was repeated two more times before the solid was dried under vacuo for 72 h to yield **2.72** (0.060g, 87%) as an off-white powder; ¹H NMR (600 MHz, d₆-DMSO): δ = 12.20 (bs, 2H), 11.20 (bs, 1H), 9.18 (bs, 2H), 8.93 (bs, 2H), 8.45 (bs, 2H), 7.88 (bs, 3H), 4.42 (m, 4H), 3.48-3.32 (m, 10H), 2.78 (m, 2H), 1.75 (m, 2H), 1.59 (m, 2H), 1.09 (t, *J* = 6.9 Hz, 6H); ¹³C NMR (150 MHz, d₆-DMSO): δ = 161.0, 160.3, 156.6, 155.6, 148.4, 83.1, 51.6, 50.0, 38.5, 36.6, 36.4, 24.5, 20.3, 14.8; HRMS: calcd for C₂₄H₃₇N₁₄O₄ [M+H]⁺: 585.3117; found: 585.3106; elemental analysis calcd (%) for (C₂₄H₃₇N₁₄O₄)(HCl)₆(H₂O)_{1.5}(Et₂O)_{0.25}: C 35.37, H5.64, N 23.10; found: C 35.48, H 5.46, N 22.72.

Compound 2.73



Compound **2.59** (0.075 g, 0.103 mmol) was added to a solution of *tert*-butyl 4-aminobutylcarbamate (0.020 mL, 0.103 mmol) in 1,2 DCE (20 mL) at room temperature under N₂ and stirred for 30 min. Sodium triacetoxy borohydride (0.023 g, 0.110 mmol) was added and the resulting mixture was stirred for 1 h. The reaction mixture was diluted with CH₂Cl₂ (50 mL) and then washed with water (10 mL), brine (15 mL), dried over Na₂SO₄ and concentrated. Fresh 1,2 DCE (20 mL) and **2.13** (0.066 g, 0.103 mmol) was added to the residue and stirred for 30 min, prior to the addition of sodium triacetoxy borohydride (0.023 g, 0.110 mmol), and stirring was continued for another 36 h. The reaction mixture was diluted with CH₂Cl₂ (50 mL) and washed with water (10 mL), NaHCO₃ (10 mL), brine (15 mL), dried over Na₂SO₄ and concentrated. Flash chromatography of the residue over silica gel using (0-50% EtOAc in hexanes) gave **2.73** (0.062 g, 40%) as a colourless oil. R_f = 0.28 (50% EtOAc in hexanes); ¹H NMR (600 MHz, CDCl₃): δ = 7.44-7.30 (m, 10H), 5.56 (s, 2H), 5.51 (s, 2H), 4.92 (m, 1H), 4.38 (t, *J* = 6.9 Hz, 4H), 3.48 (s, 3H), 3.04 (m, 2H), 2.91 (t, *J* = 6.9 Hz, 2H), 2.87 (t, *J* = 7.2 Hz, 2H), 2.64 (m, 2H), 1.55 (s, 9H), 1.53 (s, 18H), 1.40 (s, 9H), 1.39 (s, 9H), 1.34-1.30 (m, 4H), 1.30 (s, 18H), 1.28 (s, 9H); ¹³C NMR (150 MHz, CDCl₃): δ = 166.7, 166.3, 165.6, 161.3, 161.2, 161.1, 161.0, 160.2, 160.1, 158.6, 156.0, 155.5, 155.2, 155.1, 149.4, 149.2, 149.1, 135.5, 134.4, 128.7, 128.6, 128.6, 128.5, 128.5, 128.4, 128.4, 94.1, 92.8, 84.6, 84.5, 83.9, 83.8, 83.6, 83.2, 82.8, 70.4, 70.0, 53.7, 51.0, 50.4, 41.3, 41.2, 40.5, 35.0, 28.4, 28.1, 27.9, 27.8, 27.8, 27.7, 27.6, 25.0 ppm; HRMS: calcd for C₇₅H₁₀₆N₁₄O₂₀Na [M+Na]⁺: 1545.7600; found: 1545.7582.

Compound 2.74



Compound **2.73** (0.055 g, 0.036 mmol) was stirred in 95% TFA in thioanisole (10 mL) for 48 h. Et₂O (60 mL) was then added to the reaction mixture to give a white precipitate, which was centrifuged down. The residual solid was resuspended in Et₂O, sonicated and centrifuged down. This process was repeated until the spotting of the Et₂O produced no UV active spot. The yellow solid was dried, then dissolved in 1 M hydrochloric acid (10 mL) and evaporated. This process was repeated two more times before the solid was dried under vacuo for 72 h to yield **2.74** (0.021 g, 70%) as an off-white powder; ¹H NMR (600 MHz, d₆-DMSO): δ = 12.24 (bs, 2H), 11.32 (bs, 1H), 9.14 (bs, 2H), 8.77 (bs, 2H), 8.72 (bs, 1H), 8.33 (bs, 1H), 8.03 (bs, 3H), 7.91 (bs, 1H), 4.46-4.30 (m, 4H), 3.48 (bs, 6H, merged with H₂O peak), 2.95 (d, *J* = 3.5 Hz, 3H), 2.80 (m, 2H), 1.79 (m, 2H), 1.63 (m, 2H); ¹³C NMR (150 MHz, d₆-DMSO): δ = 161.4, 161.2, 160.7, 160.3, 157.5, 156.7, 156.5, 156.1, 148.6, 83.1, 38.5, 36.7, 28.4, 24.5, 20.4 ppm; HRMS: calcd for C₂₁H₃₁N₁₄O₄ [M-H]⁺: 543.2652; found: 543.2647; elemental analysis calcd (%) for (C₂₁H₃₀N₁₄O₄)(HCl)_{6.5}(H₂O)_{2.5}(Et₂O)_{0.25}: C 31.24, H 5.26, N 23.26; found: C 31.24, H 5.11, N 22.89.

2.6. References

1. Seeman, N. C. *Angew. Chem. Int. Ed.* **1998**, *37*, 3220-3238.
2. (a) Klug, A. *Angew. Chem. Int. Ed.* **1983**, *22*, 565-582. (b) Schlick, T. L.; Ding, Z.; Kovacs, E. W.; Francis, M. B. *J. Am. Chem. Soc.* **2005**, *127*, 3718-3723.
3. (a) Schmuck, C. *Angew. Chem. Int. Ed.* **2007**, *46*, 5830-5833. (b) Rebek, J. Jr. *Angew. Chem. Int. Ed.* **2005**, *44*, 2068-2078. (c) Pop, A.; Vysotsky, M. O.; Saadioui, M.; Bohmer, V. *Chem. Commun.* **2003**, 1124-1125. (d) Ajami, D.; Hou, J.-L.; Dale, T. J.; Barrett, E.; Rebek, J. Jr. *Proc. Natl. Acad. Sci. U.S.A.* **2009**, *106*, 10430-10434.
4. (a) Carmona-Ribeiro, A. M. *Chem. Soc. Rev.* **2001**, *30*, 241-247. (b) Tanaka, Y.; Miyachi, M.; Kobute, Y. *Angew. Chem. Int. Ed.* **1999**, *38*, 504-506.
5. van Nostrum, C. F. *Adv. Mater.* **1996**, *8*, 1027-1030.
6. (a) Widom, B.; Bhimalapuram, P.; Koga, K. *Phys. Chem. Chem. Phys.* **2003**, *5*, 3085-3093. (b) Pratt, L. R.; Pohorille, A. *Chem. Rev.* **2002**, *102*, 2671-2692. (c) Southall, N. T.; Dill, K. A.; Haymet, A. D. J. *J. Phys. Chem. B.* **2002**, *106*, 521-533. (d) Southhall, N. T. Dill, K. A. *Biophys. Chem.* **2002**, *101*, 295-307. (e) Dill, K. A. *Biochemistry*, **1990**, *29*, 7133-7155.
7. Hunter, C. A.; Lawson, K. R.; Perkins, J.; Urch, C. J. *J. Chem. Soc., Perkin Trans. 2*, **2001**, *5*, 651-669.
8. (a) Fenniri, H.; Deng, B. L.; Ribbe, A. E.; Hallenga, K.; Jacob, J.; Thiagarajan, P. *Proc. Natl. Acad. Sci. U.S.A.* **2002**, *99*, 6487-6492. (b) Fenniri, H.; Mathivanan, P.; Vidale, K. L.; Sherman, D. M.; Hallenga, K.; Wood, K. V.; Stowell, J. G. *J. Am. Chem. Soc.* **2001**, *123*, 3854-3855; (c) Tikhomirov, G.; Oderinde, M.; Makeiff, D.; Mansoui, A.; Lu, W.; Heirtzler, F.; Kwok, D. Y.; Fenniri, H. *J. Org. Chem.* **2008**, *73*, 4248-4251. (d) Johnson, R. S.; Yamazaki, T.; Kovalenko, A.; Fenniri, H. *J. Am. Chem. Soc.* **2007**, *129*, 5735-5743. (e) Fenniri, H.; Deng, B. L.; Ribbe, A. E. *J. Am. Chem. Soc.* **2002**, *124*, 11064-11072.
9. (a) Zhang, L.; Rodriguez, J.; Raez, J.; Myles, A. J.; Fenniri, H.; Webster, T. J. *Nanotechnology* **2009**, *20*, 17510-17522. (b) Zhang, L.; Chen, Y.; Rodriguez,

- J.; Fenniri, H.; Webster, T. J. *Int. J. Nanomed.* **2008**, *3*, 323-333. (c) Journeay, W. S.; Suri, S. S.; Moralez, J. G.; Fenniri, H.; Singh, B. *Int. J. Nanomed.* **2008**, *3*, 373-383. (d) L. Zhang, L.; Ramsaywack, S.; Fenniri, H.; Webster, T. J. *Tissue Eng.* **2008**, *14*, 1353-1364. (e) Zhang, L.; Rakotondradany, F.; Myles, A. J.; Fenniri, H.; Webster, T. J. *Biomaterials* **2009**, *30*, 1309-1320.
10. Moralez, G.; Raez, J.; Yamazaki, T.; Motkuri, R. K.; Kovalenko, A.; Fenniri, H. *J. Am. Chem. Soc.* **2005**, *127*, 8307-8309.
11. (a) Reha, D.; Hocek, M.; Hobza, P. *Chem. Eur. J.* **2006**, *12*, 3587-3595. (b) Morozov, V. F.; Badasyan, A. V.; Grigoryan, M. A.; Mamasakhlisov, Y. S.; *Biopolymers* **2004**, *75*, 434-439. (c) Sen, A.; Nielsen, P. E. *Biophys. Chem.* **2009**, *141*, 29-33. (d) Brotschi, C.; Haberli, A.; Leumann, C. J. *Angew. Chem. Int. Ed.* **2001**, *40*, 3012-3014.
12. (a) Muir, T.; Morales, E.; Root, J.; Kumar, I.; Garcia, B.; Vellandi, C.; Jenigian, D.; Marsh, T.; Henderson, E.; Vesenska, J. *J. Vac. Sci. Technol. A* **1998**, *16*, 1172-1177. (b) DeRose, J. A.; Revel, J. P. *Thin Solid Films* **1998**, *331*, 194-202. (c) Kasumov, A. Y.; Klinov, D. V.; Roche, P. E.; Gueron, S.; Bouchiat, H. *Appl. Phys. Lett.* **2004**, *84*, 1007-1009.
13. (a) Persson, I. *Pure & Appl. Chem.* **1986**, *58*, 1153-1161. (b) Reichardt, C. *Solvents and Solvent Effects in Organic Chemistry*, Wiley-VCH, Germany, **2003**, pp 1-629.
14. (a) Vazquez-Campos, S.; Crego-Calama, M.; Reinhoudt, D. N. *Supramolecular Chemistry* **2007**, *19*, 95-106. (b) Feringa, B. L.; van Delden, R. A. *Angew. Chem. Int. Ed.* **1999**, *38*, 3419-3438. (c) Yashima, E.; Maeda, K.; Nishimura, T. *Chem. Eur. J.* **2004**, *10*, 42-51. (d) Zahn, S.; Canary, J. W. *Science* **2000**, *288*, 1404-1407. (e) Hill, D. J.; Mio, M. J.; Prince, R. B.; Hughes, T. S.; Moore, J. S. *Chem. Rev.* **2001**, *101*, 3893-4011. (f) Yashima, E.; Maeda, K.; Okamoto, Y. *Nature* **1999**, *399*, 449-451. (g) Ribó, J. M.; Crusats, J.; Sagués, F.; Claret, J.; Rubires, R. *Science* **2001**, *292*, 2063-2066. (h) Huck, N. P. M.; Jager, W. F.; de Lange, B.; Feringa, B. L. *Science* **1996**, *273*, 1686-1688. (i) Fenniri, H.; Deng, B. L.; Ribbe, A. E. *J. Am. Chem. Soc.*

- 2002, 124, 11064-11072. (j) Hembury, G. A.; Borovkov, V. V.; Inoue, Y. *Chem. Rev.* **2008**, 108, 1-73. (k) De Greef, T. F. A.; Smulders, M. J. M.; Wolffs, M.; Schenning, A. P. H. J.; Sijbesma, R. P.; Meijer, E. W. *Chem. Rev.* **2009**, 109, 5687-5754.
15. (a) Kovalenko, A. Three-dimensional RISM theory for molecular liquids and solid-liquid interfaces, in: *Molecular Theory of Solvation*, Hirata, F. (ed.) Series: *Understanding Chemical Reactivity*, Vol. 24, Mezey, P.G. (ed.) Kluwer Academic Publishers, Dordrecht, **2003**, 169-275. (b) A. Kovalenko, A.; Hirata, F. *J. Chem. Phys.* **1999**, 110, 10095-10112. (c) Kovalenko, A.; Hirata, F. *J. Chem. Phys.* **2000**, 112, 10391-10417.
16. Chin, D. N.; Simanek, E. E.; Li, X.; Wazeer, M. I. M.; Whitesides, G. M. *J. Org. Chem.* **1997**, 62, 1891-1895.
17. Muler, E. A.; Rull, L. F.; Vega, L. F.; Gubbins, K. E. *J. Phys. Chem.* **1996**, 100, 1189-1196.
18. (a) Dominguez, J. N. *Curr. Top. Med. Chem.* **2002**, 2, 1173-1185. (b) Ridley, R. G. *Nature* **2002**, 415, 686-693. (c) Yang, X.; Robinson, H.; Gao, Y.-G.; Wang, A. H.-J. *Biochemistry* **2000**, 39, 10950-10957. (d) Baguley, B. C.; Wakelin, L. P. G.; Jacintho, J. D.; Kovacic, P. *Curr. Med. Chem.* **2003**, 10, 2643-2649. (e) Teulade-Fichou, M.-P.; Perrin, D.; Boutorine, A.; Polverari, D.; Vigneron, J.-P.; Lehn, J.-M.; Sun, J.-S.; Garestier, T.; Helene, C. *J. Am. Chem. Soc.* **2001**, 123, 9283-9292. (f) Demeunynck, M.; Charmantray, F.; Martelli, A. *Curr. Pharm. Des.* **2001**, 7, 1703-1724. (g) Denny, W. A. *Med. Chem. Rev.* **2004**, 1, 257-266.
19. (a) Pritchard, N. J.; Blake, A.; Peacocke, A. R. *Nature* **1966**, 212, 1360-1361. (b) Belmont, P.; Dorange, I. *Expert Opin. Ther. Patents*, **2008**, 18, 1211-1224. (c) Chow, C. S. *Chem. Rev.* **1997**, 97, 1489-1513. (d) Aoki, S.; Kimura, E. *Chem. Rev.* **2004**, 104, 769-787. (e) Thomas, J. R.; Hergenrother, P. J. *Chem. Rev.* **2008**, 108, 1171-1224.
20. (a) Lowde, R. D.; Phillips, D. C.; Wood, R. G. *Acta Crystallogr.* **1953**, 6, 553-556. (b) Mei, X.; Wolf, C. *Cryst. Growth Des.* **2004**, 4, 1099-1103. (c)

- Musumeci, D.; Hunter, C. A.; McCabe, J. F. *Cryst. Growth Des.* **2010**, *10*, 1661-1664.
21. (a) Sangster, A. W.; Stuart, K. L. *Chem. Rev.* **1995**, *65*, 69-130. (b) Perez-Flores, L.; Ruiz-Chica, A. J.; Delcros, J. G.; Sanchez-Jimenez, F.; Ramirez, F. *J. J. Mol. Struct.* **2005**, 699-704. (c) Reichardt, C.; Che, D.; Heckenkemper, G.; Schäfer, G. *Eur. J. Org. Chem.* **2001**, 2343-2361. (d) Spange, S.; Kunzmann, D.; Sens, R.; Roth, I.; Seifert, A.; Thiel, W. R. *Chem. Eur. J.* **2003**, *9*, 4161-4167. (e) Chako, N. Q. *J. Chem. Phys.* **1934**, *2*, 644-653. (e) Bayliss, N. S.; McRae, E. G. *J. Phys. Chem.* **1954**, *58*, 1002-1006.

Chapter 3

Thermo-reversible supramolecular chirality from achiral self-assembling molecules

“Where nature finishes producing its own species, man begins, using natural things and in harmony with this very nature, to create an infinity of species.”

- Leonardo da Vinci

3.1. Introduction

Circular dichroism¹ (CD) spectroscopy has emerged as a common probe for the measurement of chiroptical data due to its great sensitivity related to chiral perturbations of the system being studied. While it was initially developed for evaluating molecular chirality of chromophoric molecules,^{1,2} it later evolved as a method for the study of supramolecular chirality of self-assembling systems.³ As such, a number of reports pertaining to the expression of molecular chirality at macromolecular level,⁴ Sergeants and Soldiers' principle⁵ and induced circular dichroism (ICD)⁶⁻¹⁰ appeared. There have been cases of spontaneous symmetry breaking in crystallization¹¹ and liquid crystals¹² resulting in an excess of one of the enantiomers, however it was not possible to predict which enantiomer would form. Defying these norms, achiral systems adopting a preferred helical sense as a result of a macroscopic chiral bias have also been reported.¹³⁻¹⁵ In some cases, the reliability of these data were questioned due to CD artifacts, which can greatly affect the data.

This chapter introduces an achiral molecule (But-TBL) that has unexpectedly shown CD activity in methanol. Variable temperature CD (VT-CD) experiments revealed almost mirror-image CD profiles at 10 and 40 °C in certain solvents upon self-assembly. Though, these data were initially treated as an artifact, extensive experiments revealed that this was not the case. Consequently a number of derivatives of But-TBL were synthesized,¹⁶ and found to display a similar behaviour (Figure 3.1). These modules, which possess two donor-donor-acceptor

H-bond arrays of guanine and two acceptor-donor-donor arrays of cytosine, have been shown to undergo a dynamic self-assembly process to yield rosette nanotubes (RNTs) of high aspect ratio.¹⁷ The RNTs were characterized extensively using various microscopy and spectroscopic techniques for a better understanding of this phenomenon.

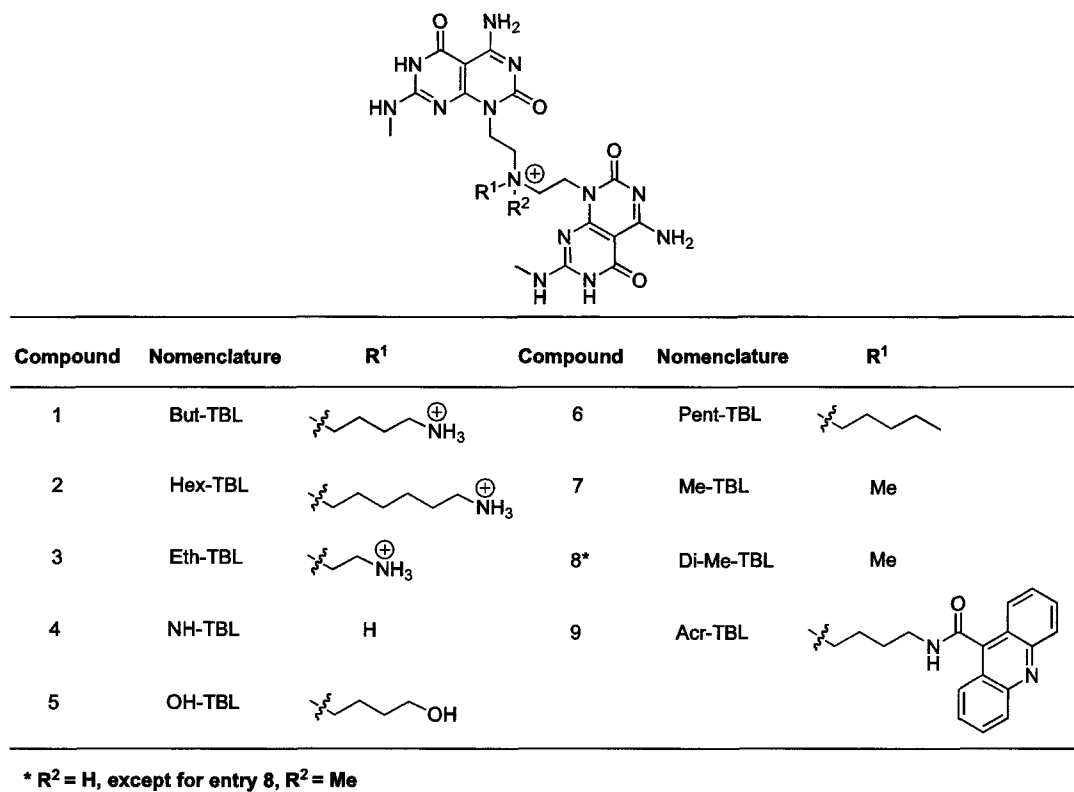


Figure 3.1: Achiral twin RNT monomers that give a CD signal in methanol upon self-assembly.

3.2. Results

Compound But-TBL, which was isolated as the hydrochloride salt, is achiral and, in principle, it was expected to give a CD-silent racemic mixture of *P* and *M* RNTs. However when a CD measurement was carried out on a sample assembled at 0.5 mg/mL (0.685 mM) in methanol and aged for 1 week, a strong negative monosignate CD signal was observed at dilute concentrations (0.017 mM in methanol). The measurement was carried out in a quartz cuvette of 1 cm pathlength at 10 °C. At these concentrations, the G_AC derivative **1** undergoes the

formation of a six-membered twin rosette, maintained by 36 H-bonds, which then stacks into a tubular architecture with a 4 Å stacking distance and an average calculated outer diameter of 3.8 nm.¹⁸ The measured diameter obtained from TEM measurements is 3.5 nm ± 0.2 nm.

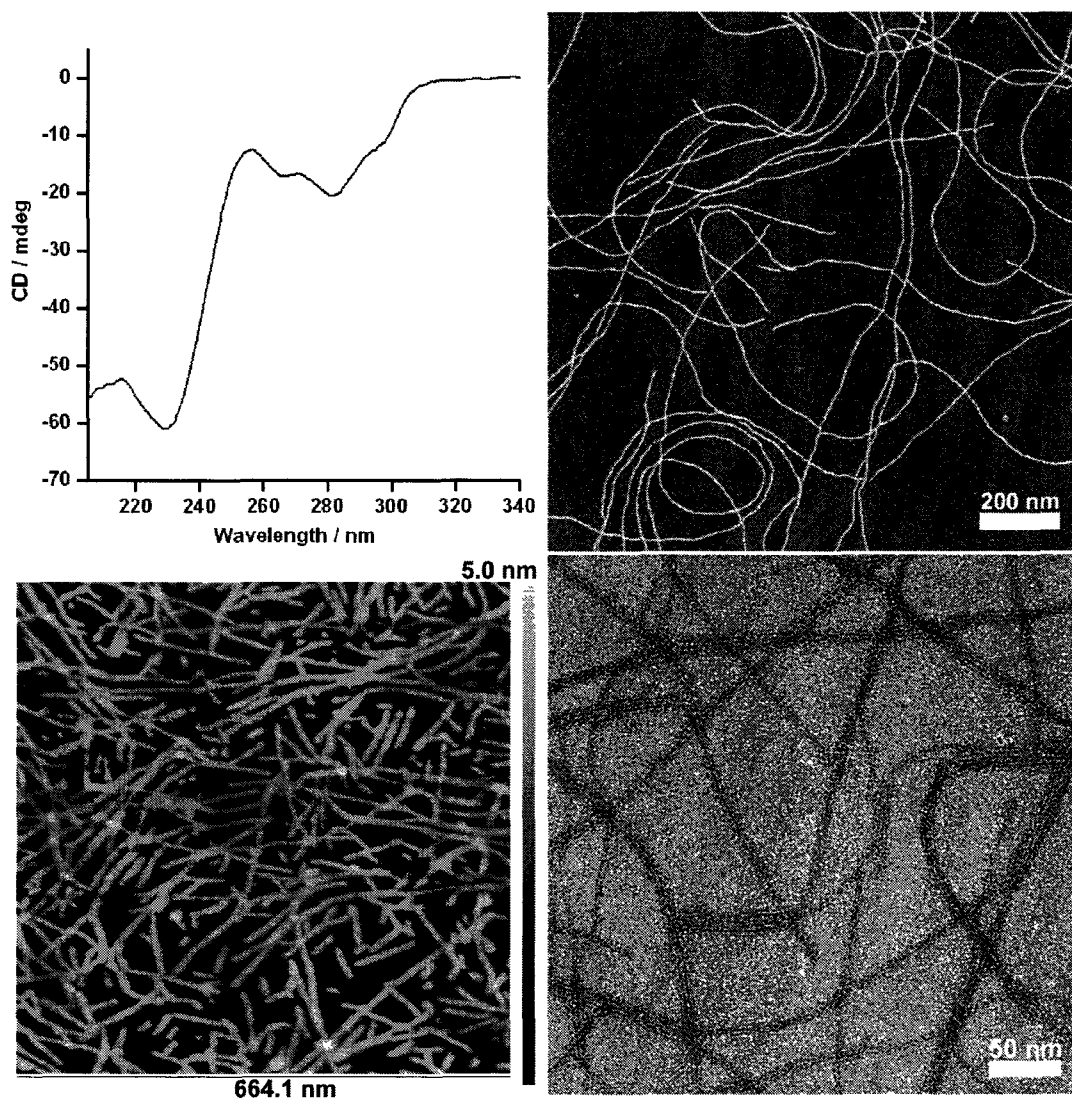


Figure 3.2: CD at 10 °C (top left), SEM (top right), AFM (bottom left) and TEM (bottom right) of RNTs derived from monomer But-TBL (1) in methanol. Microscopy images show the formation of long nanotubes after aging for 1 week at 0.5 mg/mL and then diluting to 0.0125 mg/mL (0.017 mM) in methanol. This diluted solution also gave the CD profile indicated.

3.3. Solution phase characterization

Time dependent UV-Vis and CD spectroscopies along with dynamic light scattering (DLS) experiments were done to investigate whether the observed CD signal, was related to the presence and growth of the RNTs. The stock solution was assembled at 0.5 mg/mL in methanol and aged at room temperature.

The UV-vis spectroscopy for But-TBL was monitored over time. But-TBL absorbs UV light between 220-320 nm due to chromophores present in the G \wedge C base. A significant hyperchromic effect (0.5 h \rightarrow 10 d) and a small hypsochromic effect ($\lambda_{\text{max}} = 234$ nm, 0.5 h \rightarrow $\lambda_{\text{max}} = 229$ nm, 10 d) were observed. UV-vis spectroscopy has been used extensively for investigating nucleic acid structure and stability. It is often predicted that a hyperchromic effect is equivalent to the melting of DNA, however Williams¹⁹ reported that in some cases UV-vis spectroscopy fails to be an adequate technique in correlating the hyperchromic effect to disassembly. In our case, RNTs formation in methanol starts immediately after dissolution (as observed by SEM), so the UV absorbance might just be associated with the formation of RNTs. Over time, RNTs concentration and length increased, and this may be correlated to the hyperchromic effect observed. This is also consistent with increased scattering observed as the particles grow from shorter to longer tubes.

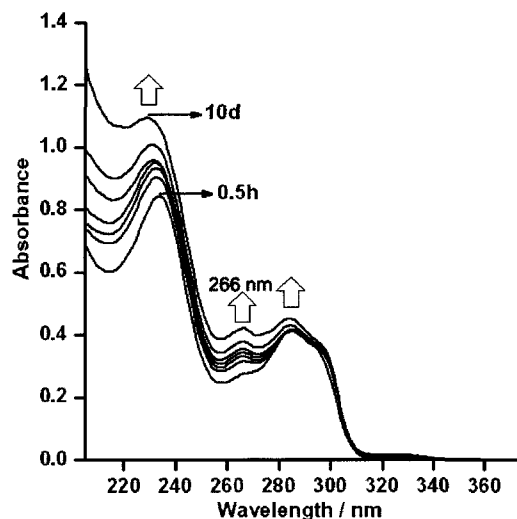


Figure 3.3: Time-dependent UV-vis spectra of But-TBL in methanol - (0.01 mg/mL, 20 °C).

In addition, a new but relatively weak hypsochromic-shifted absorption band ($\lambda = 266$ nm) emerged upon interaction of the chromophores after 10 days. This peak was absent from the spectrum obtained (0.5 h) at the beginning of aggregation. We presumed that this new band could be due to H-type aggregates.²⁰ Unlike J-type aggregates²¹ (bathochromic shifted absorption band) which stems from a head-to-tail configuration, H-aggregates result from a face-to-face arrangement. For H-aggregates, an increase in the HOMO-LUMO gap is observed when chromophores are in the aggregated state. The theory behind the increase in HOMO-LUMO gap for H-aggregates and decrease in HOMO-LUMO gap for J-aggregates upon aggregation was developed by Kasha²² and was explained by exciton theory (Figure 3.4). Prior to excitation in a system containing N chromophores, there is an N-fold degeneracy that exists. However upon electrostatic perturbation resulting from intermolecular dipole-dipole interaction of transition dipoles, an exciton band of N discrete exciton states is produced.

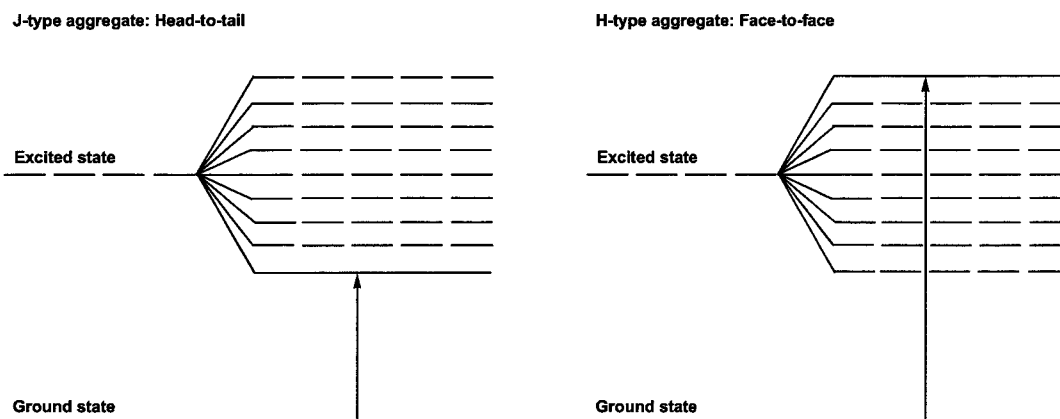


Figure 3.4: Exciton band structure for J- and H-aggregates.²²

Though RNTs are the main aggregates in our system, formation of H-type aggregates are still possible. The latter probably arise from the face-to-face stacking of the two GAC units from the twin GAC monomer during the self-assembly process.

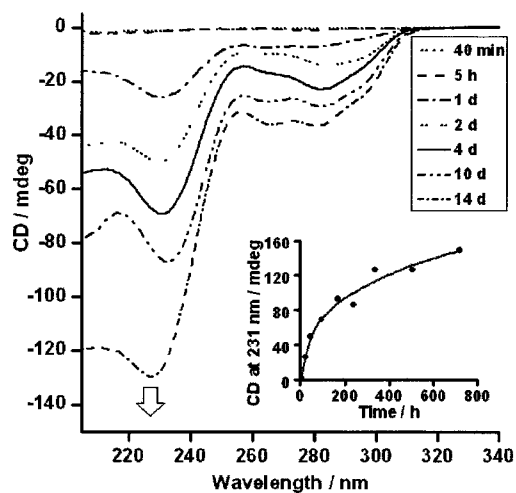


Figure 3.5: CD growth of But-TBL with time (CD recorded at 10 °C).

For the time dependent CD experiment, aliquots from the stock solutions were taken at different time intervals and diluted to 0.0125 mg/mL (0.017 mM) with methanol, before the CD spectra were recorded at 10 °C. No measurable CEs were observed at the start of the self-assembly process, however as the sample aged, a monosignate CD signal appeared, which intensified over time (Figure

3.5). Unlike most optically active systems that give bisignated CE, having an entirely negative CE initially seemed unusual, however a literature survey revealed a number of such cases.²³

A small aliquot (2.0 μL) from each solution used for the CD measurement was deposited on a carbon-coated TEM grid at different time intervals and SEM was done to confirm the presence and growth of the RNTs (Figure 3.6). At the beginning of the self-assembly process, only a few long RNTs were observed and the grid mostly consisted of short RNTs. After aging for 7 days, the RNTs were longer and more abundant. Since the CD signal was absent at the beginning of the self-assembly process, there seemed to be a correlation between the existence of the RNTs and CD effects.

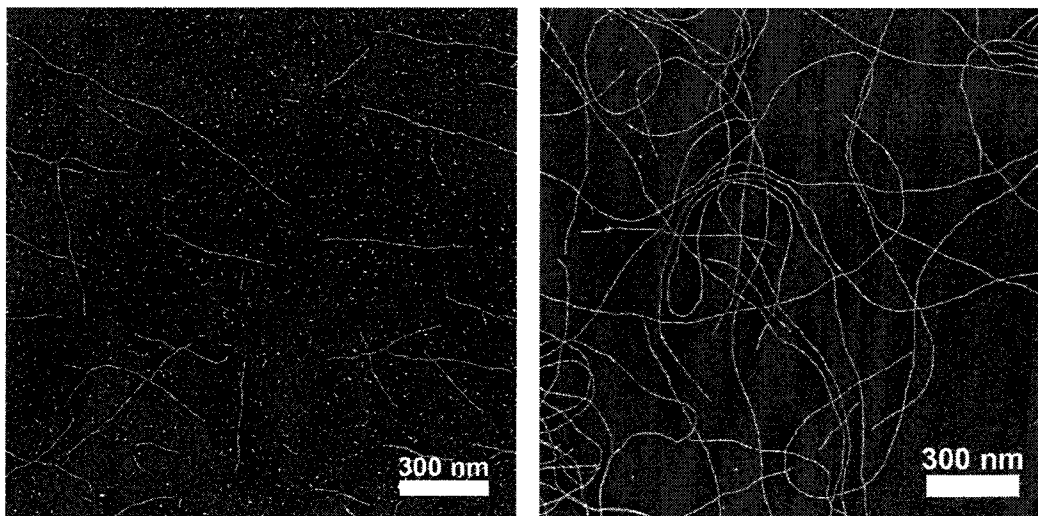


Figure 3.6: Growth of But-TBL RNTs after 30 min (left) and 7 days (right) monitored by SEM.

A time-dependent DLS experiment was also used to determine the relative sizes of the structures formed in methanol over time. The exact values for average hydrodynamic diameter in this DLS experiment is not directly related to the RNT size distribution but it follows the growth kinetics of the RNTs. The sample was prepared at 0.5 mg/mL in methanol and filtered through a 200 nm pore-size Whatmann filter, and the measurements were recorded at different time intervals

at room temperature. The average hydrodynamic diameter values were plotted against time (Figure 3.7) and a sigmoid curve was obtained (clearly visible from the inset, which shows the growth of the RNTs within the first few hours), reflecting the autocatalytic nature of the RNTs.^{10c} The rate-determining step in the self-assembly process is most likely the formation of RNT seeds, which catalyzes the growth process. The increased growth of the RNTs after one day is most probably due to a larger number of seed aggregates, which template longer RNTs and bundles in solution as the sample aged.

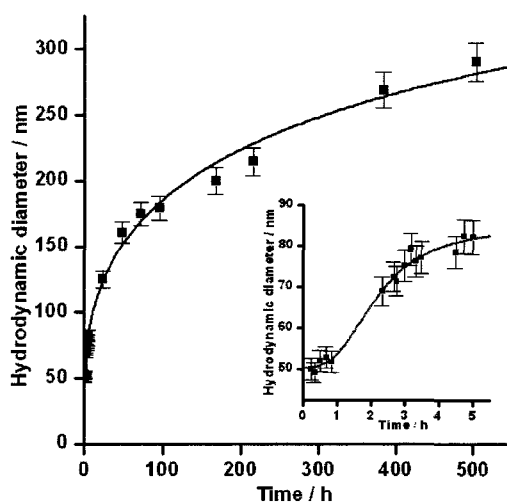


Figure 3.7: Time-dependent DLS spectrum of But-TBL in methanol (sigmoid fit).

Simultaneous growths of the RNTs (demonstrated by the SEM images in Figure 3.6 and the DLS curve in Figure 3.7) and the CD signals over time suggest that the existence of the CD signal is not a random process, but rather a process that is directly related to the presence and abundance of the RNTs. The CD dependence on the RNT's abundance was further supported by the disappearance of the CD signal upon disassembly of the RNTs via acidification. As shown in Figure 3.8, TFA breaks up the RNTs, most likely by the protonation of the Watson-Crick hydrogen bond acceptor sites, thus leading to a CD silent spectrum.

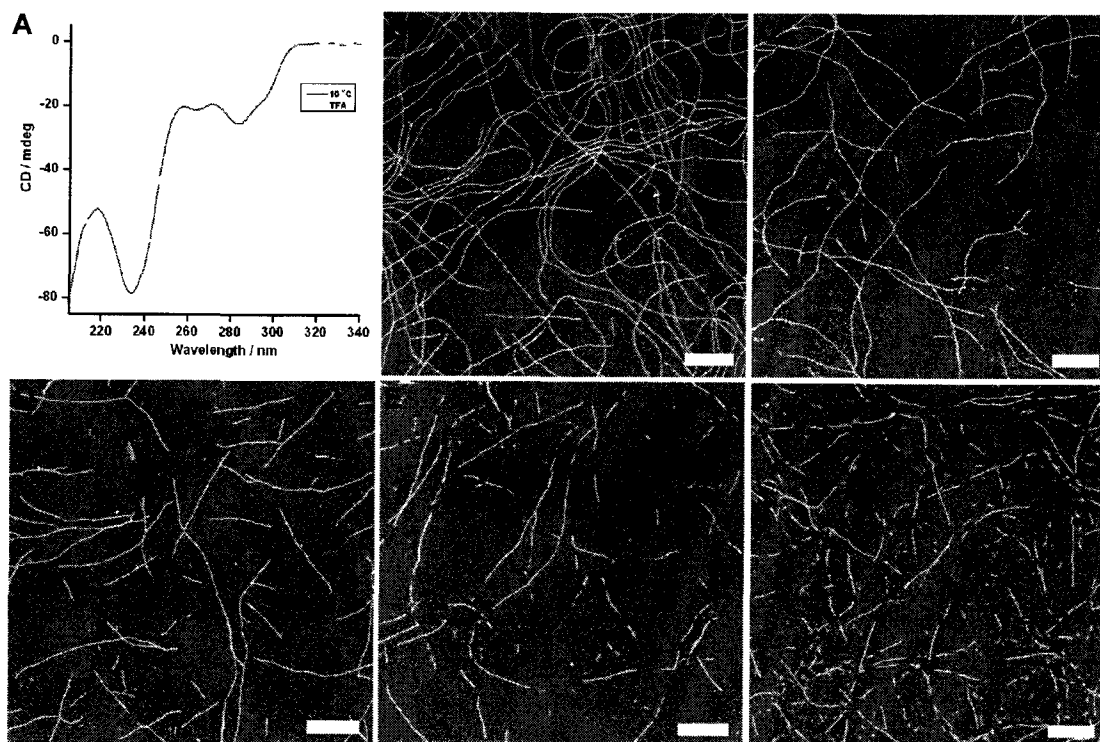


Figure 3.8: CD spectra of But-TBL before and after (10 min) addition of 10 μ L of neat TFA in 2 mL of But-TBL RNT solution in methanol of a 0.017 mM concentration (A). The SEM images (B-F) show the RNT morphologies before (B) and after addition of TFA at 5 min (C), 15 min (D), 30 min (E) and 1 h (F) intervals. Scale bar = 200 nm.

3.4. Thermo-reversibility of the CD profiles

To verify the origin of the CD signal for But-TBL RNTs and their thermal stability, a VT-CD experiment on a diluted But-TBL sample (0.0125 mg/mL, 0.017 mM in methanol) was performed. The supramolecular chirality of a RNT sample with a built-in stereogenic centre in the monomer is biased by its point chirality, which leads to one of the two possible diastereomeric forms.³ The CD spectrum monitors the formation and growth of these chiral supramolecular assemblies by displaying a CE in the UV range. These CEs decrease in intensity with increasing temperatures in a VT-CD experiment, due to disassembly of the non-covalent assemblies.²⁴ The chiral analogue K-TBL,²⁵ as its TFA salt, which self-assembled readily in methanol, was subjected to a VT-CD experiment. This

compound, with a built-in L-lysine moiety, was assembled at 0.5 mg/mL in methanol and aged for 14 days. An aliquot of the stock solution was diluted to 0.0125 mg/mL in methanol and the measurement was carried out in a quartz cell of 1 cm pathlength between 20 and 50 °C. The CEs observed at 234, 251 and 301 nm showed a decrease in intensity as the temperature was increased (Figure 3.9), as expected for a chiral RNTs sample.²⁴

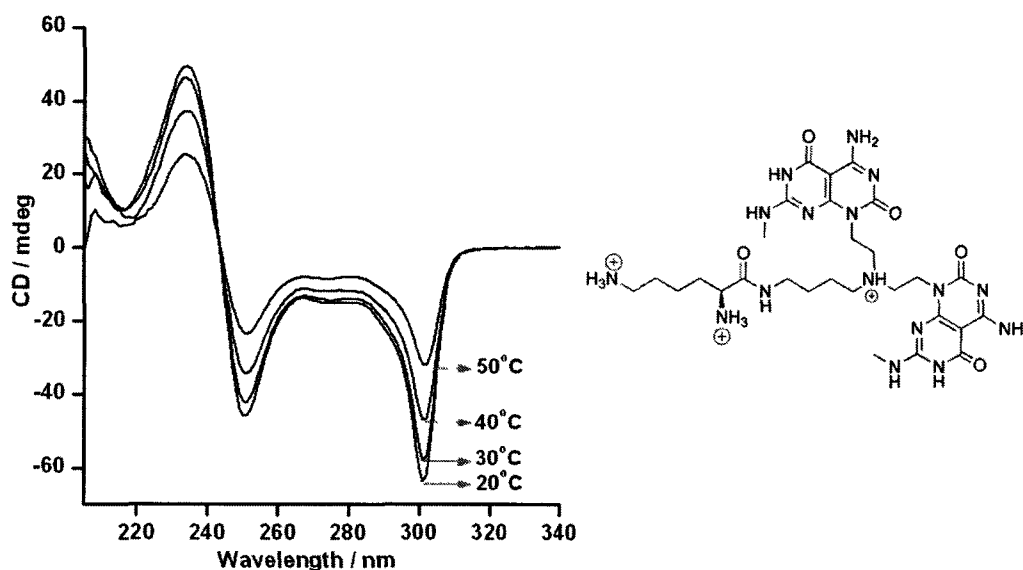


Figure 3.9: VT-CD of K-TBL (TFA salt) in methanol.

Similarly, But-TBL was subjected to a VT-CD experiment between 10 and 50 °C. However in this case the results obtained were very different - a gradual inversion of the CD signal was observed (Figure 3.10). The monosignate CD signal, which had an intensity of about -160 mdeg at 239 nm at 10 °C, became CD silent at about room temperature. As the temperature reached about 40 °C, a positive monosignate CD signal emerged. This was a pseudo mirror image CD signal as compared to the one obtained at 10 °C. The positive CD signal at 40 °C was slightly lower in intensity as compared to the CD at 10 °C, which can be attributed to disruption of some of the non-covalent assemblies at higher temperatures.²⁴

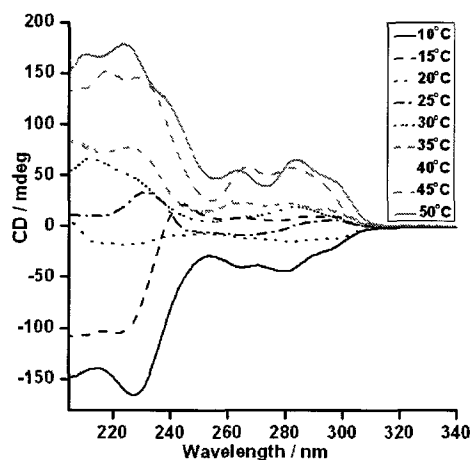


Figure 3.10: VT-CD on But-TBL RNTs as the HCl salt in methanol.

Different batches of the But-TBL monomer were screened and in each case the RNTs still exhibited pseudo mirror-image CD signals at 10 and 40 °C. This process was found to be reversible, albeit with a gradual loss of CD activity at both temperatures (attributed to a slow disassembly of the RNTs) (Figure 3.11).

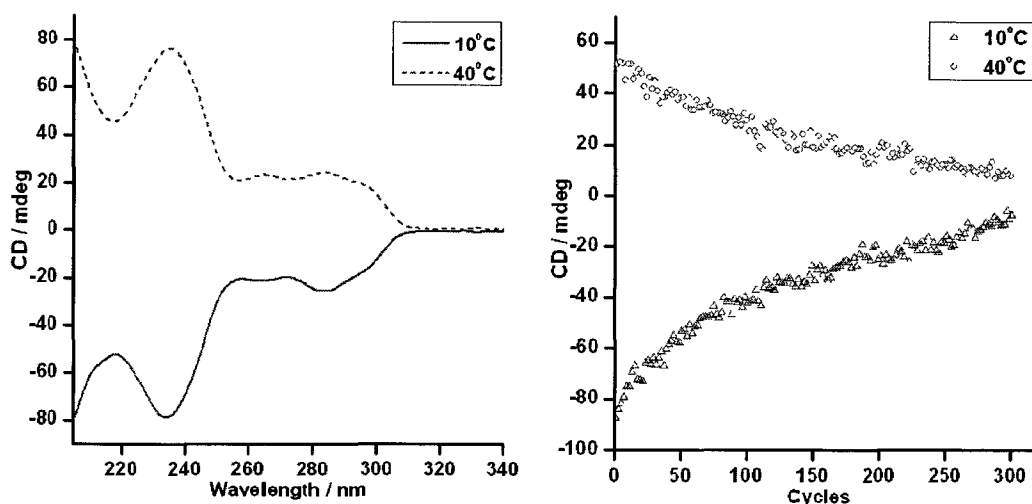


Figure 3.11: Mirror image CD profiles at 10 and 40 °C (left) and graph showing the CD intensities at 231 mdeg while But-TBL was subjected to a series of 300 VT-CD cycles at 10 and 40 °C (right).

The density of the RNTs found in solution at the CD concentration was estimated by casting these solutions on TEM grids before and after the continuous VT-CD experiments. These cast samples were then visualized using SEM imaging (Figure 3.12). Though at the end of the 300 cycles, there is still the presence of long and well-dispersed RNTs, the density of the nanostructures on the carbon coated TEM grid seems less than those obtained prior to subjecting the sample to the VT-CD cycles.

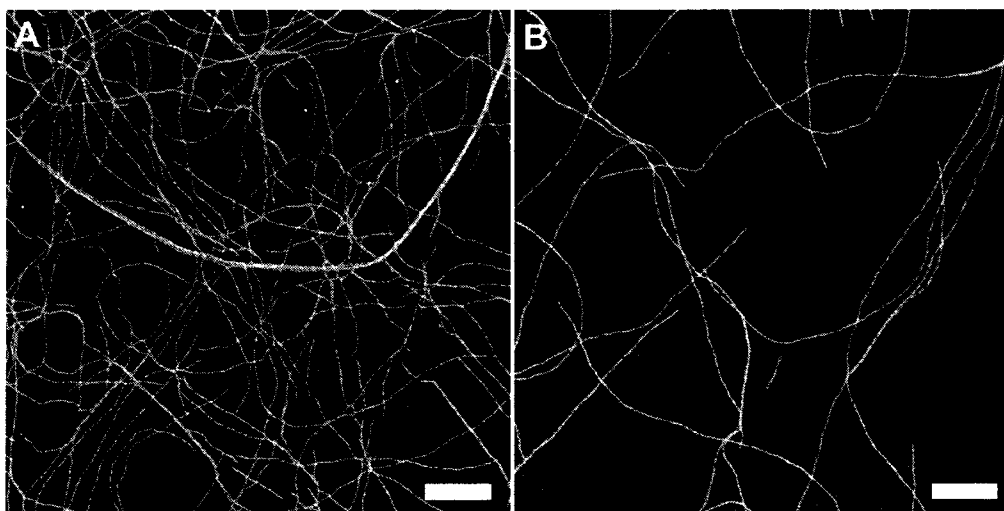


Figure 3.12: SEM images of But-TBL RNTs in methanol before (A) and after (B) 300 VT-CD cycles from 10 to 40 °C. Scale bar = 200 nm.

3.5. RNTs derived from single G \wedge C base systems do not show any CD activity.

The CD behaviour discussed previously was observed for the twin base system. To verify whether a similar phenomenon occurs for the monobase system, the CD and self-assembly of the K1 module,^{10b} isolated as a hydrochloride salt, was monitored in methanol at a similar concentration as But-TBL. A stock solution of 0.36 mg/mL of K1 (0.685 mM in methanol) was prepared and aged at room temperature. Aliquots from the stock solution were diluted to 0.017 mM and CD measurements were carried out after 1 day and 1 week. The diluted solutions were also cast on carbon-coated TEM grids for SEM visualization. While a CD

signal is usually observed for the But-TBL solution at a similar concentration after 1 day, for a 1-day old solution of the K1 module, no CD activity was observed. From SEM imaging, no RNT structures were visible on the grid. Aging the stock solution for a week did not promote a CD appearance. This result correlated with the SEM images obtained, which showed the absence of long and abundant RNTs, as in the case of But-TBL (Figure 3.13). While both monomers had the built-in ability to form RNTs in solution, the twin base system gives more stable RNTs at a faster rate due to lower functional group density, reduced net charge, enhanced stability arising from preorganization, increased amphiphilic character, greater number of H-bonds per module, higher H-bonds per rosette (36 H-bonds instead of 18), less steric congestion and lower electrostatic repulsion.²⁴

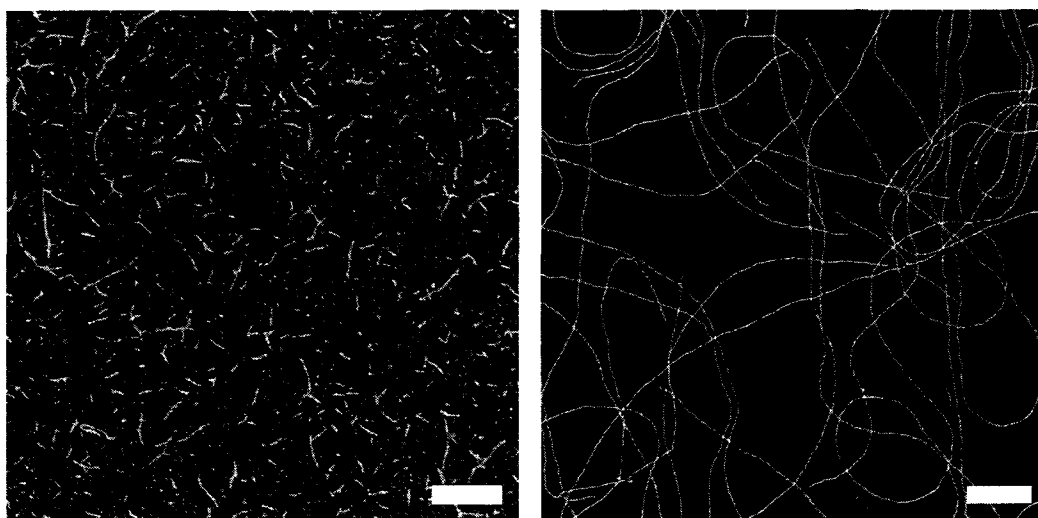


Figure 3.13: SEM images of K1 RNTs (left) and But-TBL RNTs (right) in methanol at a concentration of 0.017 mM in methanol, after 1 week of aging. Scale bar = 200 nm. The K1 module displays very short RNTs compared to the TBL monomer.

3.6. Effect of solvent, side-chain, functional group and counterions

The CD experiments performed on But-TBL RNTs revealed interesting behaviour, which had not been previously observed for any RNTs. At this point, different hypotheses were made to rationalize the CD results and experiments were designed to test the validity of each of these possibilities.

One main concern was possible contamination of the But-TBL sample by chiral impurities, resulting in the chirality induction and amplification to yield an observable CD signal according to the Sergeants and Soldiers' principle⁵. As such, the synthesis of But-TBL was repeated six times to rule out the possibility of errors and contamination from chiral compounds. The synthesis was also carried out by another group member (Dr Ross S. Johnson). All the batches synthesized gave similar CD results. Other derivatives synthesized (discussed in section 3.6.2.) also showed similar CD effects.

3.6.1. Effect of solvent on CD activity

Due to solubility issues of some of the derivatives in methanol (see next section), we probed the effect of binary mixtures of DMSO and MeOH on the CD signal. All stock solutions were made at a concentration of 0.5 mg/mL in the respective mixtures, which were diluted for CD and SEM (Figures 3.14, 3.15). While in the 100% DMSO stock solution, only a few RNTs were found, the DMSO-MeOH mixtures gave long, abundant and well-dispersed RNTs.

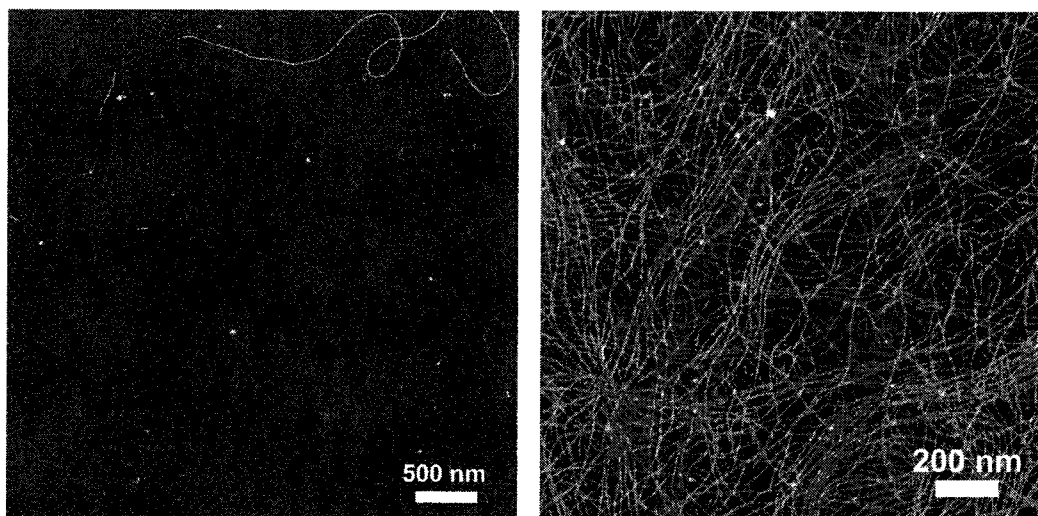


Figure 3.14: SEM images of But-TBL from a 100% DMSO (left) and 75% DMSO-MeOH stock solution

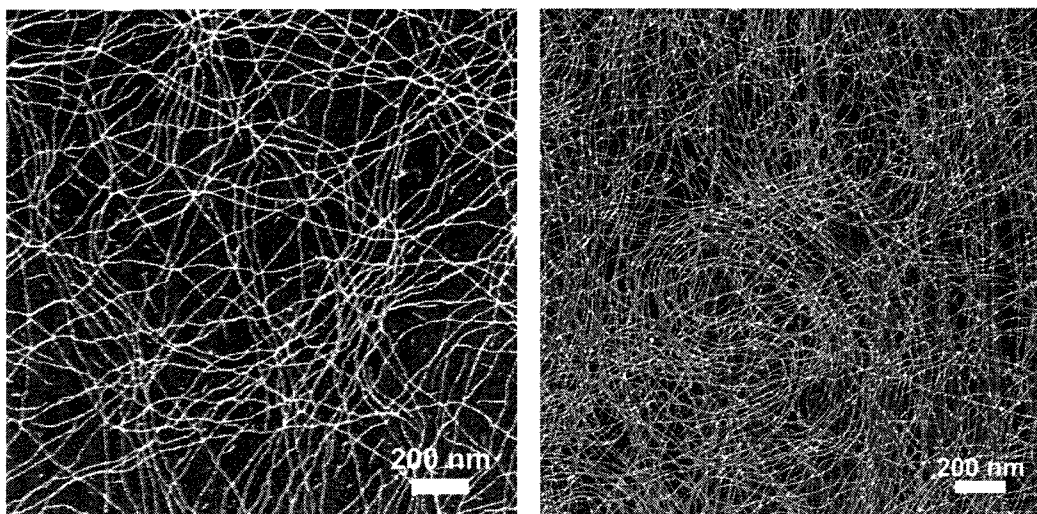


Figure 3.15: SEM images of But-TBL from a 50% DMSO (left) and 25% DMSO-MeOH stock solution

The CD spectra were also recorded for the DMSO and DMSO-MeOH mixtures. For CD measurements, a 50 μ L aliquot of the stock solutions (solutions prepared in DMSO or DMSO-MeOH mixtures) was diluted to 2 mL using HPLC grade methanol and the CD spectra were recorded at 10 $^{\circ}$ C. With the exception of the 100% DMSO solution, all the DMSO-MeOH samples (75%, 50% and 25%) showed CD activity (Figure 3.16). The CD spectra resembled the CD profile obtained in methanol only But-TBL solution and the intensities of the CEs were proportional to the percentage of methanol within the mixture (i.e. the higher MeOH content, the stronger the CE). The CD obtained for But-TBL in 25% DMSO-MeOH was comparable to the signal obtained in neat methanol, and the binary mixture also displayed similar thermo-reversibility properties. This system was also very useful for the CD experiments of some analogues of But-TBL, which had low solubility in pure methanol.

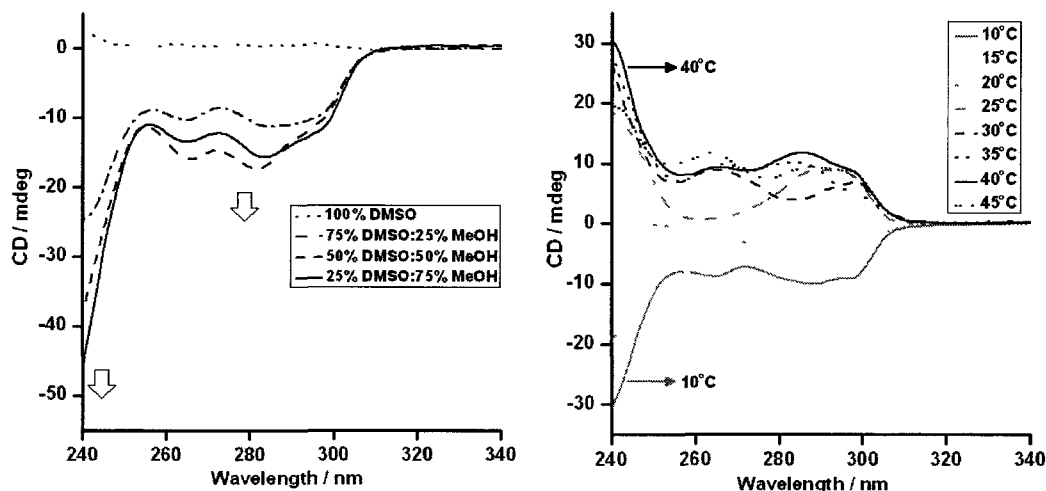


Figure 3.16: CD spectrum of DMSO-MeOH mixtures (left) and VT-CD spectrum for the 25% DMSO-MeOH solution (right) of But-TBL

Similar CD experiments were carried in binary mixtures of water and methanol. Binary mixtures of methanol and water were made by preparing stock solutions in the required ratio using 99.8% HPLC grade MeOH and deionized water. Aliquots from the stock solution were taken at different time intervals and diluted with the same solvent ratios. The CD measurements were carried out at 10 °C. Unlike the MeOH-DMSO mixtures, the CD effects were greatly affected. As little as 5% of water was enough to erase the CEs. In fact, 1% water-MeOH solution (Figure 3.18, A) resulted in about 66% decrease in CEs (Figure 3.17). A decrease in length and abundance of the RNTs was observed with increasing polarity of the solvent system.²⁶

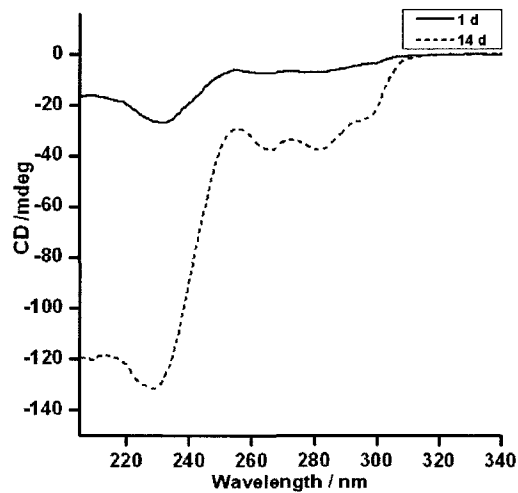


Figure 3.17: CD profiles of But-TBL in neat MeOH at 10 °C after 1 day and 14 days of aging.

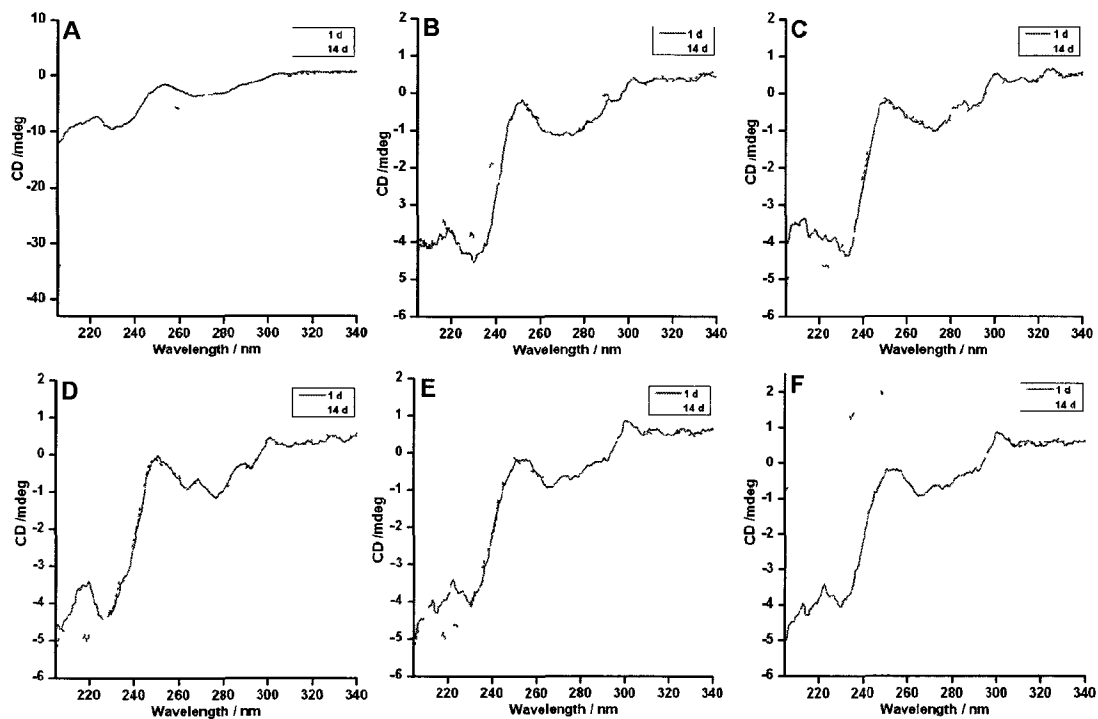


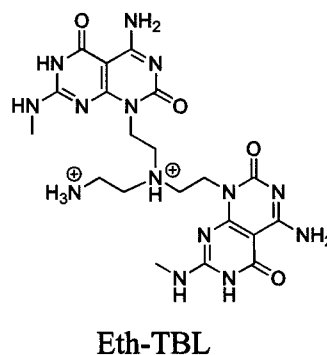
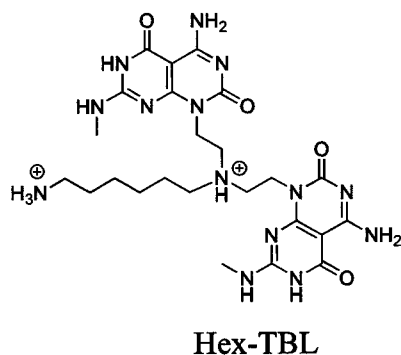
Figure 3.18: CD profiles of But-TBL recorded at 10°C in binary mixtures of MeOH and water: 99% MeOH (A), 95% MeOH (B), 75% MeOH (C), 50% MeOH (D), 25% MeOH (E), 100% water (F) after 1 day and 14 days of aging.

3.6.2. Effect of molecular structure on CD activity

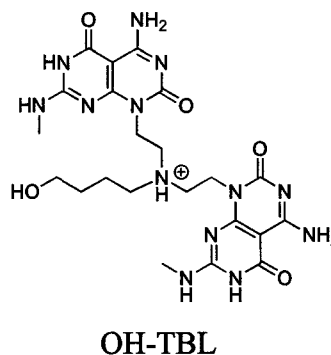
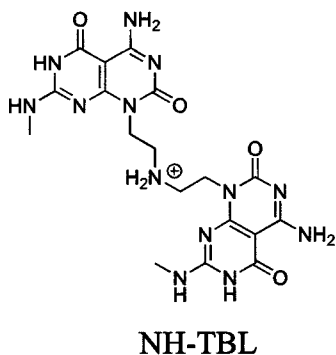
We have previously shown that a single chiral molecule can express mirror image conformers depending on how the side-chain orients itself upon interaction with achiral solvent molecules.²⁷ To gain more insight into how the CD behaviour may be related to the structure and conformation of functional groups of the self-assembling molecules, we designed a number of analogues (2-8, Figure 3.1) by varying the nature of the side-chain. These derivatives were important targets, as they allowed us to test the possible sources of anisotropy within the molecules and resulting assemblies.

If the CD signal observed for the But-TBL sample was due to the protonation of the central nitrogen atom connecting the two GAC units and the alkyl ammonium chain or due to the disymmetric interactions between the two GAC cores, the length of the linker chain should not affect the CD spectrum. This is because in all these analogues, the chromophores would still be at the same distance from the point of disymmetry. However, if the CE originates from the preferential orientation of the alkyl ammonium chain (e.g. H-bonding between the ammonium ions and solvent molecules and/or GAC moiety), the length of the side-chain should affect the CD signal. A longer side-chain could act as a solvent molecule and affect the CE.^{1a}

The analogues Hex-TBL and Eth-TBL have a terminal ammonium ion as But-TBL, but the charge is separated from the twin GAC motif by six and two methylene units, respectively. In the monomer NH-TBL the alkyl ammonium motif is missing.

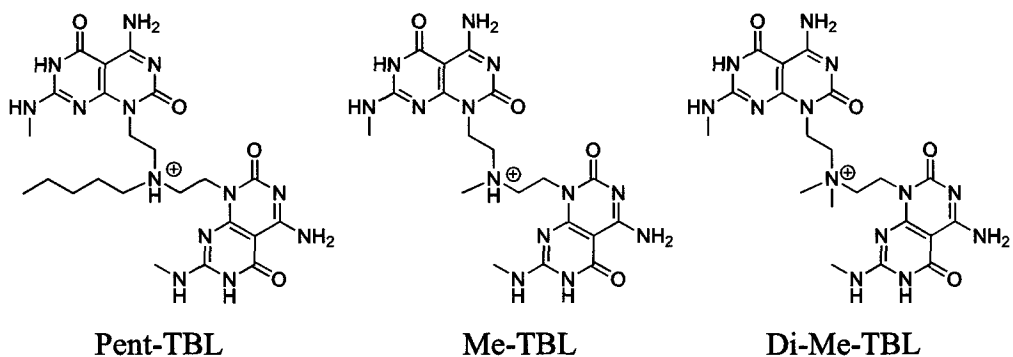


The OH-TBL derivative had the same number of side chain methylene units as But-TBL, but no charge (OH instead of $^+NH_3$) at the end of the chain. While the ammonium (But-TBL) will form stronger electrostatic H-bonds with acceptors in MeOH, the hydroxyl group (OH-TBL) can provide H-bond acceptor sites.



The But-TBL, Hex-TBL, Eth-TBL, NH-TBL and OH-TBL modules all have an ammonium or hydroxyl group that can be a potential site for hydrogen bonding. As such the heteroatoms could possibly lead to a dominant conformer within the RNTs sample.

The Pent-TBL, Me-TBL and Di-Me-TBL derivatives have no terminal heteroatom on the side chain, and were synthesized to provide further insight into the potential role of the side chain heteroatoms of But-TBL, Hex-TBL, Eth-TBL, NH-TBL and OH-TBL.



CD measurements were carried out on these analogues in methanol at 10 °C (Figures 3.19-3.25). Due to lower solubility of NH-TBL, Me-TBL and Di-Me-TBL, self-assembly was carried out in 25% DMSO-MeOH mixtures. Since DMSO absorbs strongly in the UV region (< 240 nm), the CD spectra were recorded from 240-350 nm.

Molecular modeling²⁸ done on But-TBL and NH-TBL predicts that the two G \wedge C bases are syn to each other, however, if we overlook the computation and imagine that the two bases are off-set relative to each other, in both the protonated or unprotonated states, all the molecules (But-TBL, Hex-TBL, Eth-TBL, NH-TBL, Pent-TBL and Me-TBL) can result in chiral assemblies. In all these cases, the central nitrogen atom will be in an asymmetric environment within the RNTs. As such, if this is really the source of the abnormal CD behaviour, the Di-Me-TBL building block, which does not have the free lone pair of electrons and instead bears two methyl groups on the nitrogen atom, should be CD inactive.

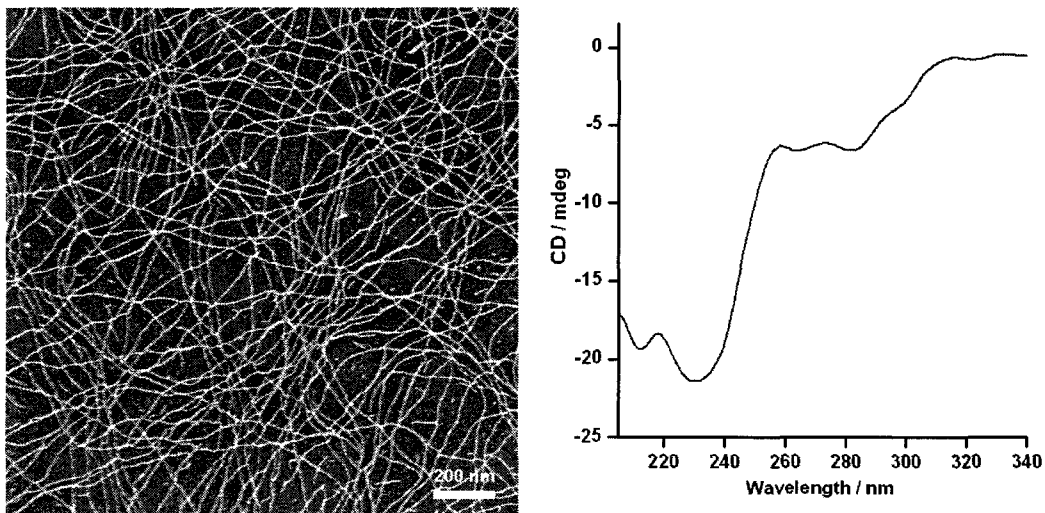


Figure 3.19: SEM image of Hex-TBL at CD concentration (left) and its CD spectrum at 10 °C in methanol after aging for 15 days (right).

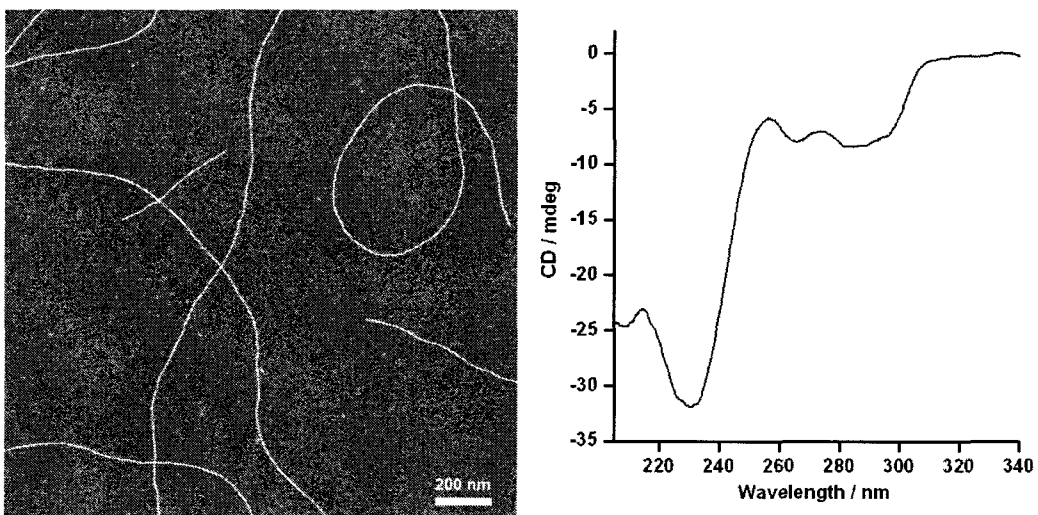


Figure 3.20: SEM image of Eth-TBL at CD concentration (left) and its CD spectrum at 10 °C in methanol after aging for 1 day (right).

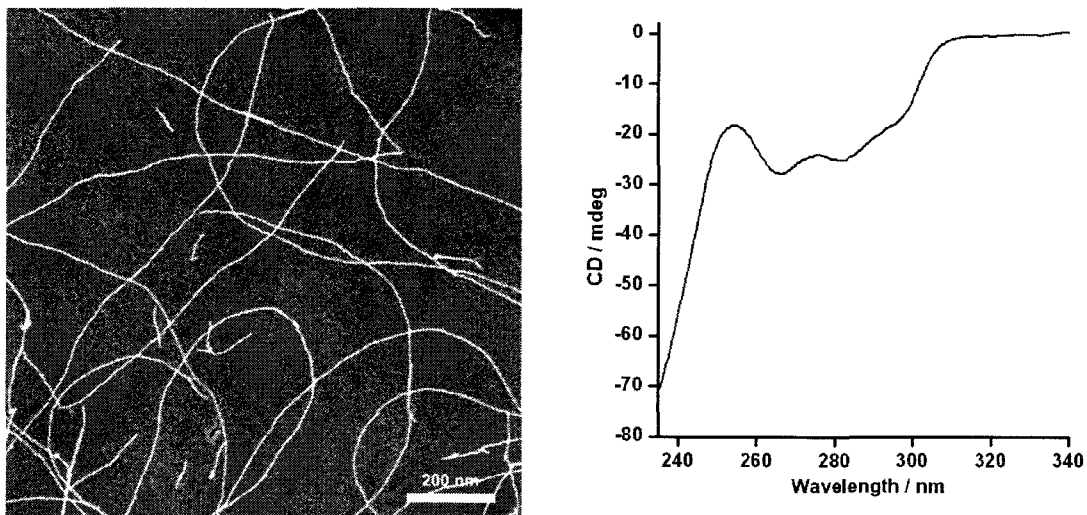


Figure 3.21: SEM image of NH-TBL at CD concentration (left) and its CD spectrum at 10 °C from a 25% DMSO-MeOH stock solution for 7 days (right).

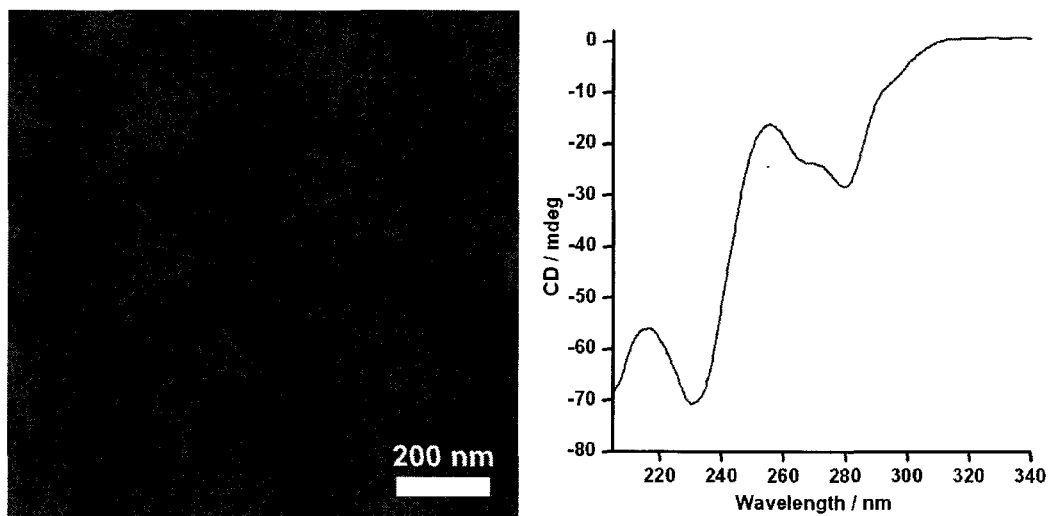


Figure 3.22: SEM image of OH-TBL at CD concentration (left) and its CD spectrum at 10 °C in methanol after aging for 3 days (right).

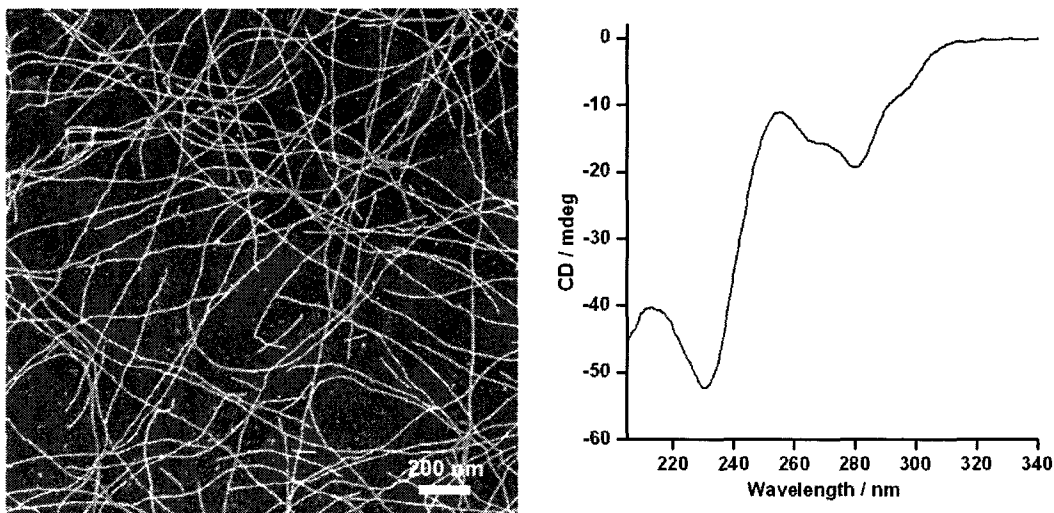


Figure 3.23: SEM image of Pent-TBL at CD concentration (left) and its CD spectrum at 10 °C in methanol for 7 days (right).

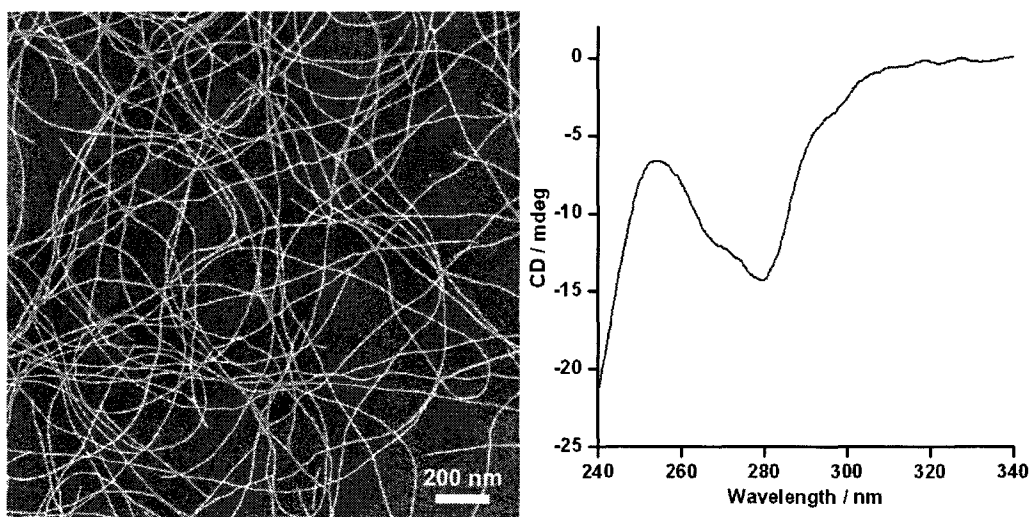


Figure 3.24: SEM image of Me-TBL at CD concentration (left) and its CD spectrum at 10 °C from a 25% DMSO-MeOH stock solution for 7 days (right).

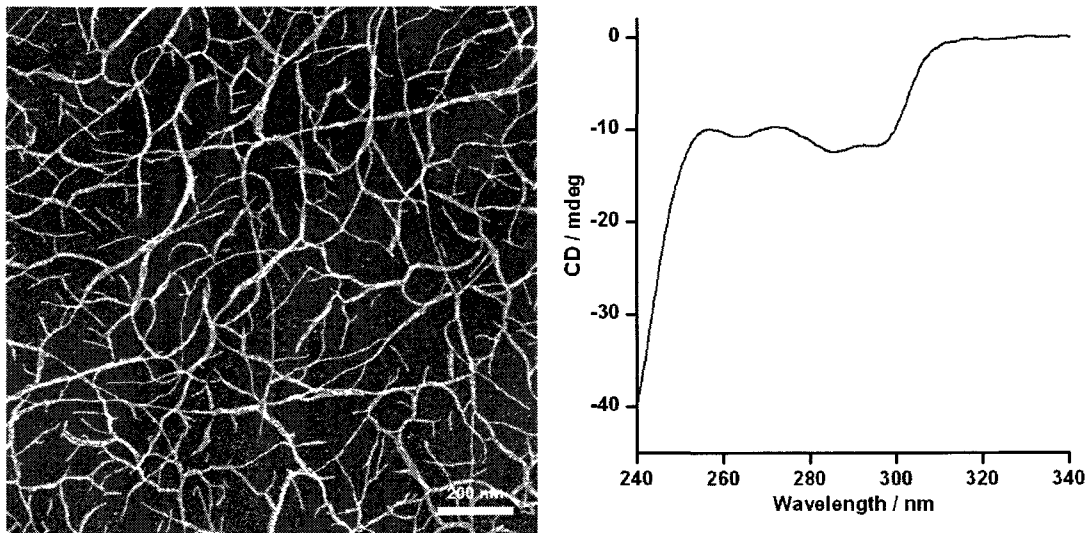


Figure 3.25: SEM image of Di-Me-TBL at CD concentration (left) and its CD spectrum at 10 °C from a 25% DMSO-MeOH stock solution for 7 days (right).

The emergence of CEs for these monomers established that neither the substitution on the nitrogen atom connecting the GAC units nor the side-chain affected the CD behaviour.

3.6.3. Effect of counterions on CD activity

So far, all the CD results presented were for achiral self-assembling monomers isolated as HCl salts. No CD activity was obtained for monomers isolated as TFA salt. SEM was used to image the morphologies exhibited by the HCl and TFA salts of But-TBL over time (Figure 3.26). Longer RNTs were observed from monomers isolated as HCl salts.

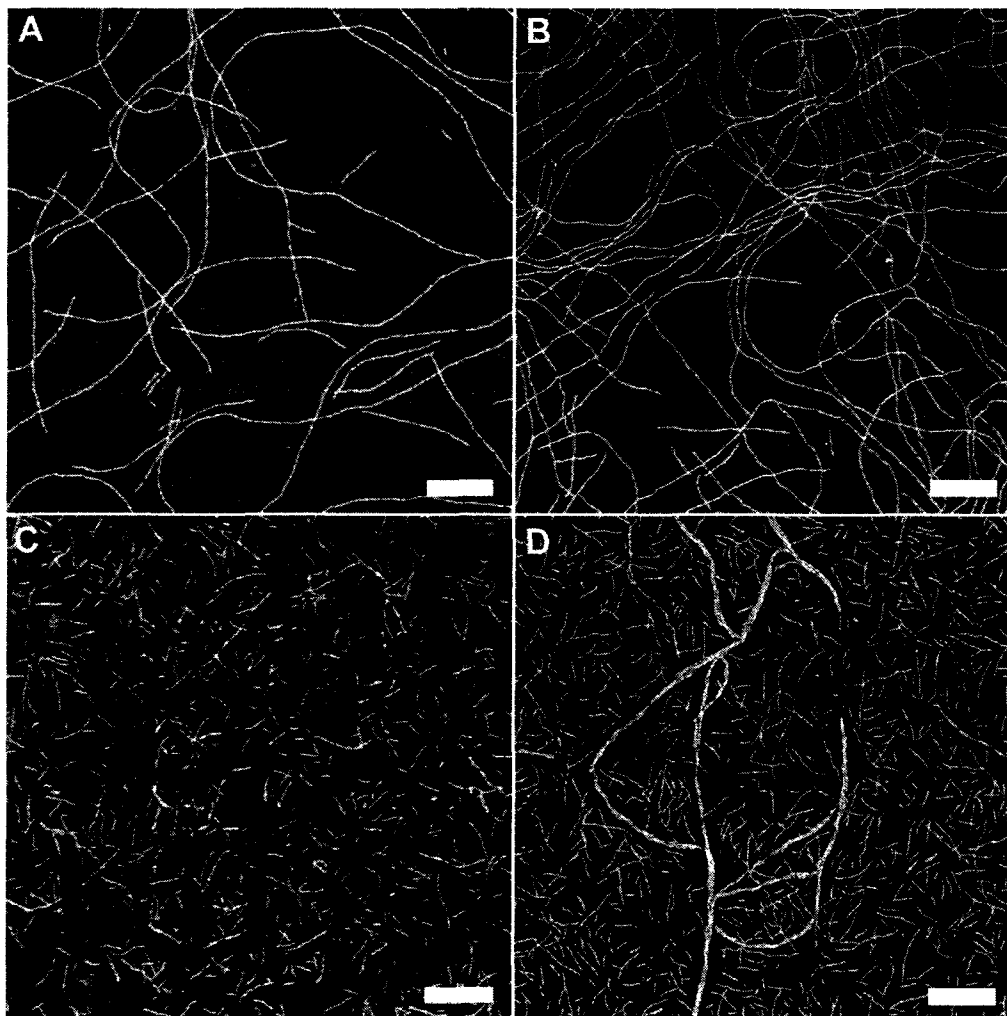


Figure 3.26: SEM of RNTs derived from But-TBL monomer as HCl (A, B) and TFA (C, D) salts. All samples are at a concentration of 0.0125 mg/mL in methanol after 1 day (A, C) and after a week (B, D) of aging the stock solution. Scale bar = 200 nm

The CD activity of But-TBL was also tested for the monomer isolated as HBr salt. Like the HCl salt, in this case too a CD signal, including the thermo-reversibility feature was obtained (Figure 3.27). SEM imaging of the RNT sample revealed the presence of long RNTs (Figure 3.28), which was consistent with the correlation we drew earlier about the CD signal and degree of aggregation of the RNTs.

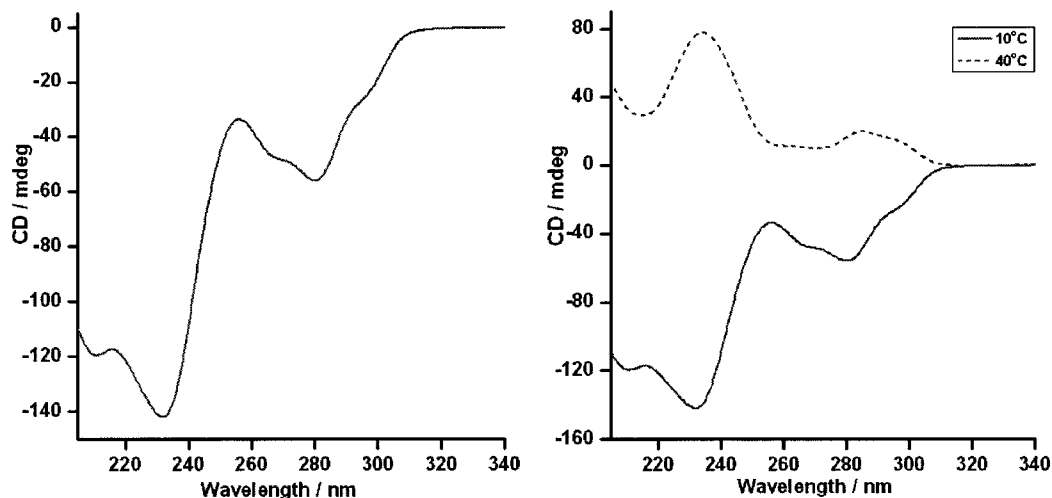


Figure 3.27: CD at 10 °C (left) and VT-CD (right) spectra of RNTs in MeOH derived from the But-TBL monomer isolated as HBr salt, aged for 5 days.

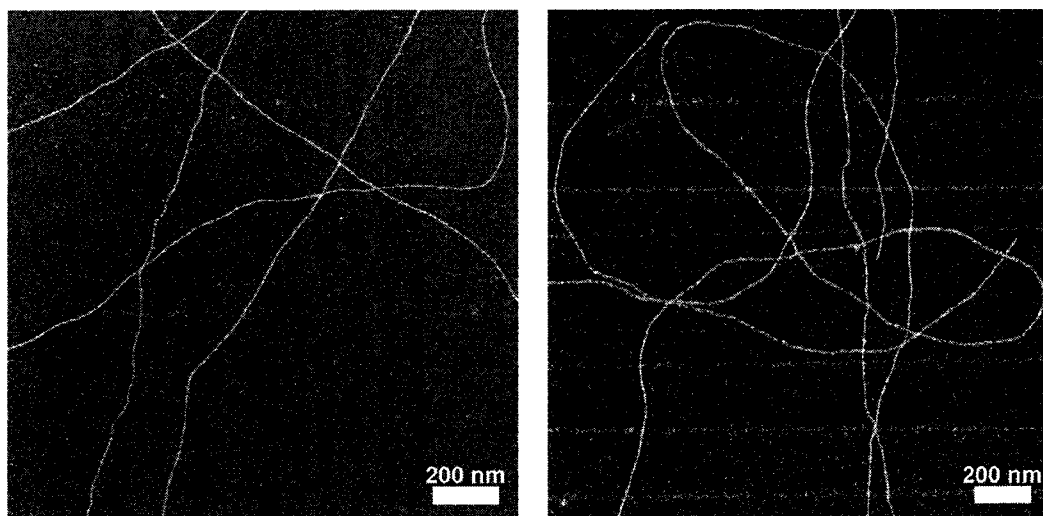


Figure 3.28: SEM of RNTs in MeOH derived from the But-TBL monomer isolated as the HBr salt, after 5 days of aging.

3.7. Cotton effects in acridine functionalized RNTs

So far we have established that the CD behaviour observed is a property intrinsic to this class of achiral twin RNTs. Compounds 1-8 (Figure 3.1) have the same CD signature since they all possess the same chromophores. Molecule 9 (Acr-TBL) which is endowed with an acridine chromophore attached to the twin G \wedge C side chain also shows the same CD profile in addition to new CEs at about 260

and 360 nm, resulting from the aromatic tricycle. Contrary to the other molecules, this molecule shows a bisignate CD signal (Figure 3.29).

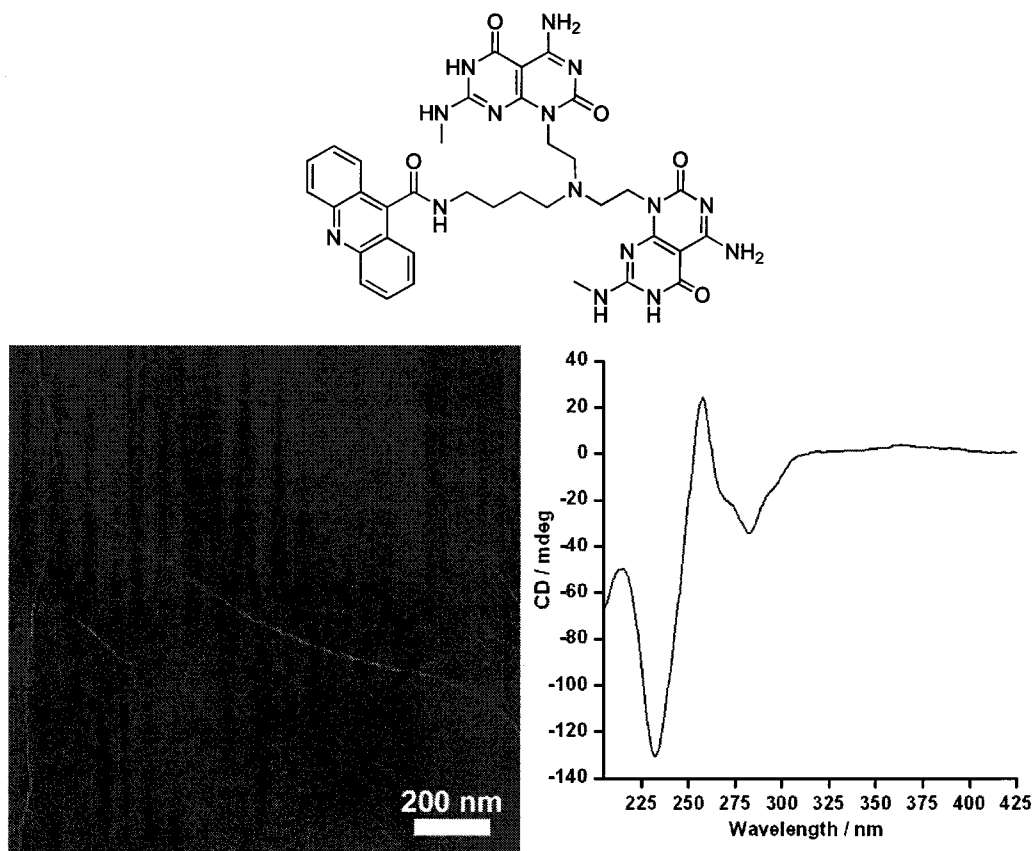


Figure 3.29: SEM image (left) after 3 days of aging and CD spectrum at 10 °C (right) after 17 days of aging of Acr-TBL at a concentration of 0.025 mg/mL in methanol.

A VT-CD experiment on the Acr-TBL RNTs in methanol revealed a thermo-reversible CD profile, which mimicked similar properties as compounds 1-8.

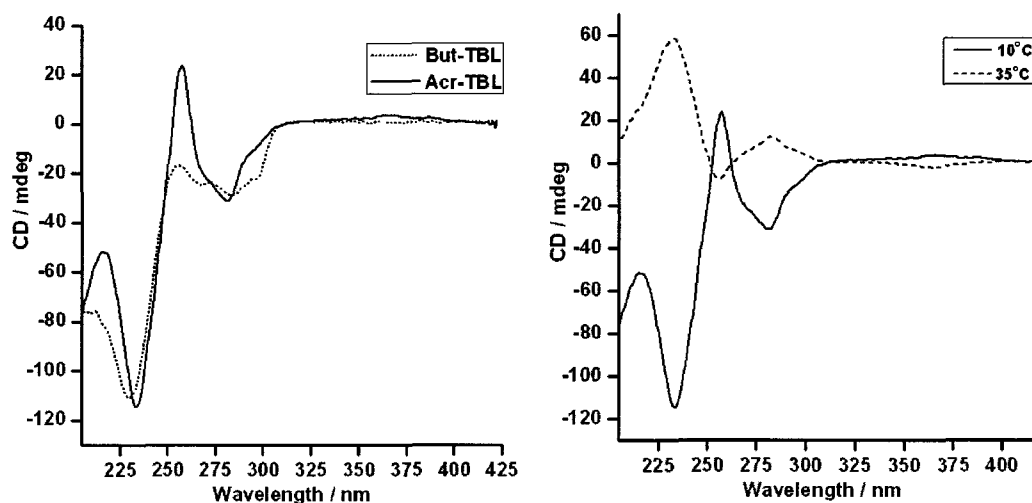


Figure 3.30: Comparison of CD spectra of But-TBL and Acr-TBL in methanol (left) and VT-CD spectra for Acr-TBL in methanol (right).

3.8. Substitution on exocyclic nitrogen

The fact that the CD behaviour also manifests itself for NH-TBL and Di-Me-TBL implies that the CD is directly related to the core of the twin G \wedge C rosettes, which are in turn responsible for RNT formation and stacking preferences. Speculation that the CD effects might arise from the relative rotation of the rosettes within a twin rosette assembly (Figure 3.31) prompted us to study the effect of substitution on the exocyclic nitrogen theoretically and experimentally. For this theoretical calculation, NH-TBL was used instead of But-TBL since it lacked the butyl ammonium chain and was therefore easier to model.

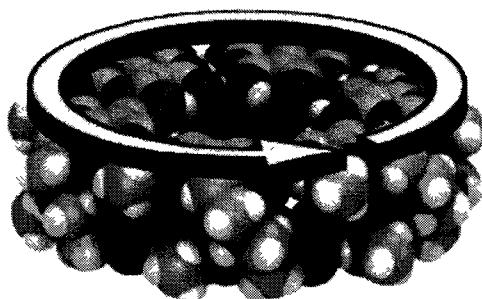


Figure 3.31: Rotation of the G \wedge C discs in NH-TBL

We investigated the possibility of the sliding of one of the G \wedge C units as being the source of the chirality inversion by molecular modeling.²⁸ The NH-TBL motif used had a syn conformation. The potential was found to be a symmetric double well and the barrier height to overcome the sliding of the upper G \wedge C base was ca. 20 kcal/mol. Replacing the methyl attached to the G \wedge C base with hydrogen, or turning off the partial charges of the motif, did not alter the potential height (Figures 3.32 and 3.33).

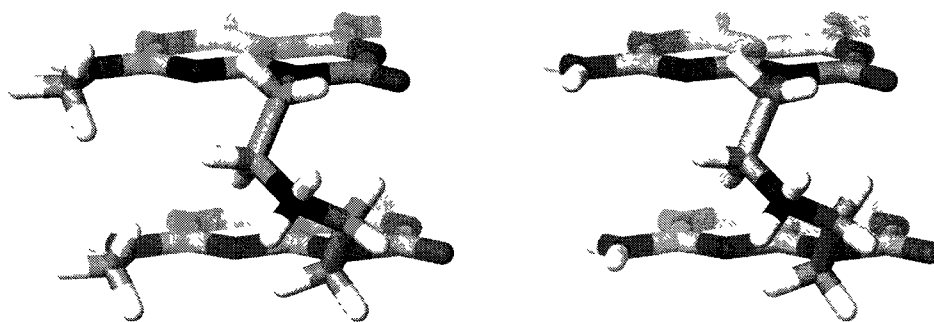


Figure 3.32: Conformers of twin G \wedge C with NHCH₃ (left) and NH₂ (right) exocyclic substituent on the guanine face.

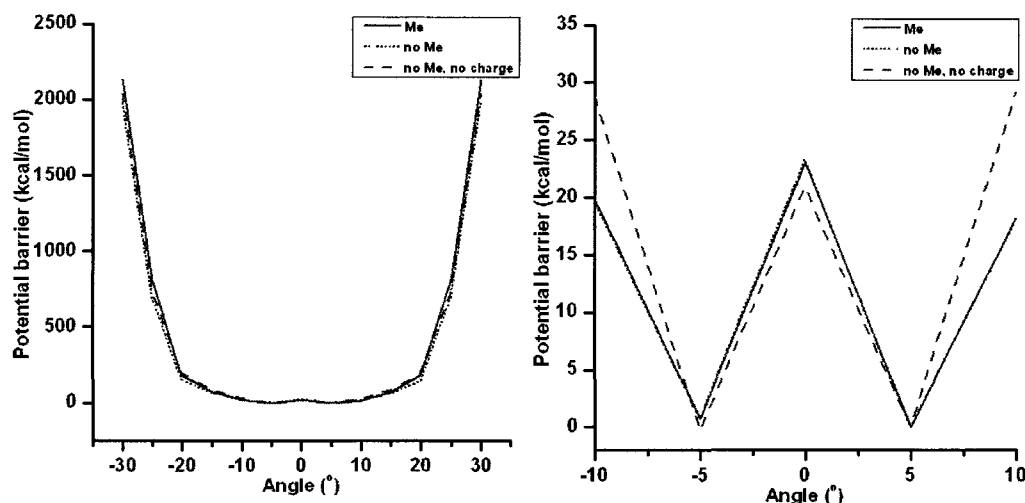


Figure 3.33: Potential barriers for rotation of most stable conformation of NH-TBL motif (with Me, no Me and no Me + no partial charges). A section of the graph (left) was magnified to show the symmetric double well potential (right).

The above calculation was carried out using methanol and chloride ions at 10 °C. The calculation was also performed in water under similar conditions, and both results were in agreement.

The potential barriers to rotate the upper G \wedge C base in each twin G \wedge C motif in one, two and three twin-rosette discs for NH-TBL were calculated at 10 °C. By carrying out the conformational search for the five twin-rosette discs, the optimal stacking distance and staggered angle between the discs were determined.

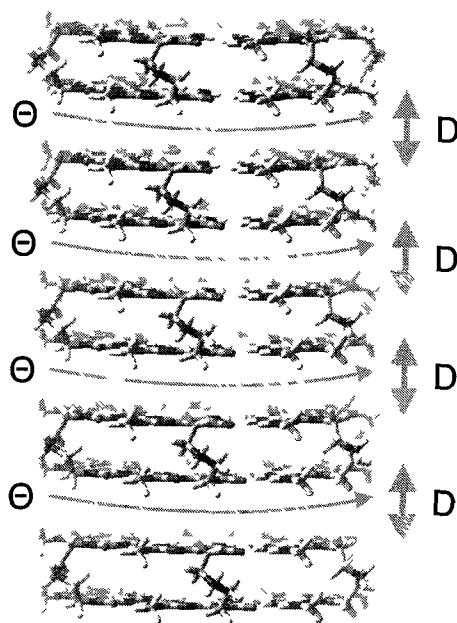


Figure 3.34: Conformational search to obtain the optimum values for the staggered angle (θ) and the stacking distance (D) between twin rosettes. The optimum values calculated for NH-TBL were: $\theta = 20^\circ$ and $D = 3.3 \text{ \AA}$.

Using $\theta = 20^\circ$ and $D = 3.3 \text{ \AA}$, one, two, and three twin-rosette discs were constructed. The upper G \wedge C base in each twin G \wedge C motif of the top twin-rosette disc was then rotated while keeping the rest of the conformation intact (Figure 3.35).

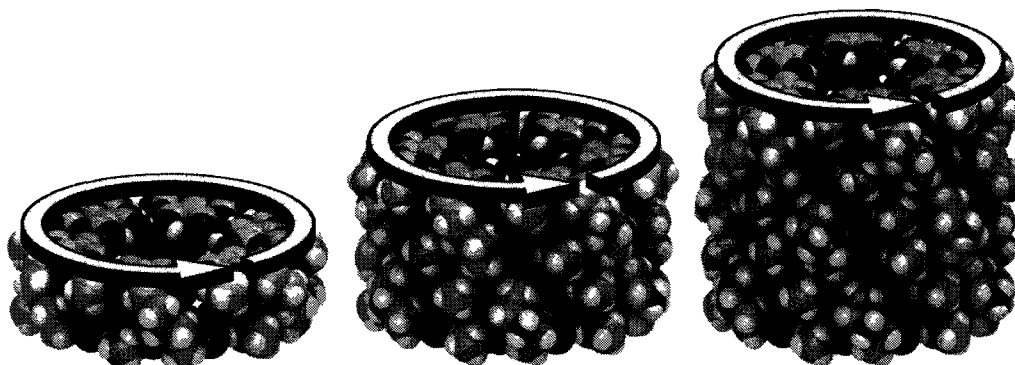


Figure 3.35: One (left), two (centre), and three (right) twin-rosette discs for NH-TBL motif constructed using $\theta = 20^\circ$ and $D = 3.3 \text{ \AA}$.

It was found that the potential becomes asymmetric for the rotation in the case of two or three twin-rosette discs. The most stable point in the potential curve corresponds to the point in which the motif in the top disc takes the same conformation as that of the lower discs (Figure 3.36). This can be considered as the manifestation of the template effect on the top disc from the lower discs.

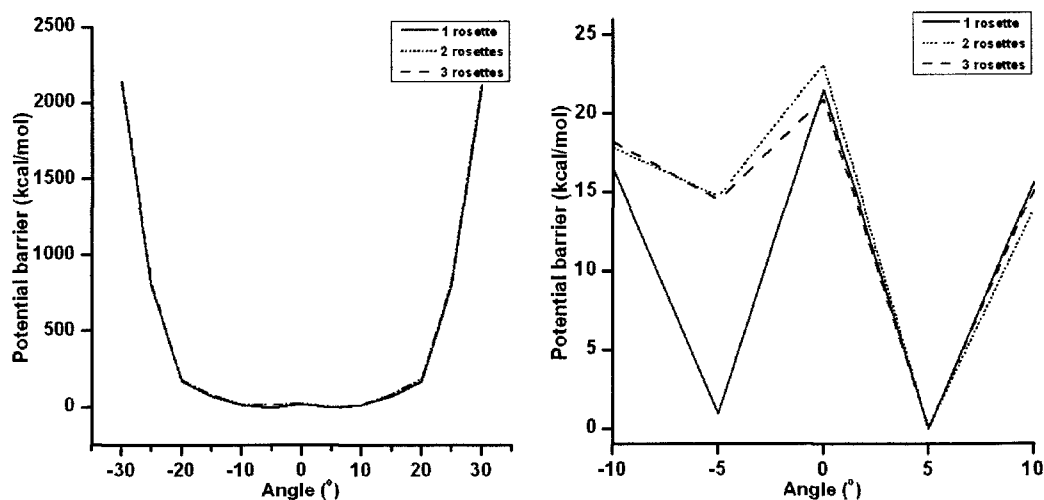


Figure 3.36: Potential barriers for rotation of NH-TBL for 1, 2 and 3 rosette rings at 10°C . A section of the graph (left) was magnified to show how the symmetric double well potential becomes asymmetric upon stacking of more rosettes (right).

The potential barriers for 1, 2 and 3 rosette rings were also calculated at 40 °C, however there was no change in the energy profiles (Figures 3.37-3.39).

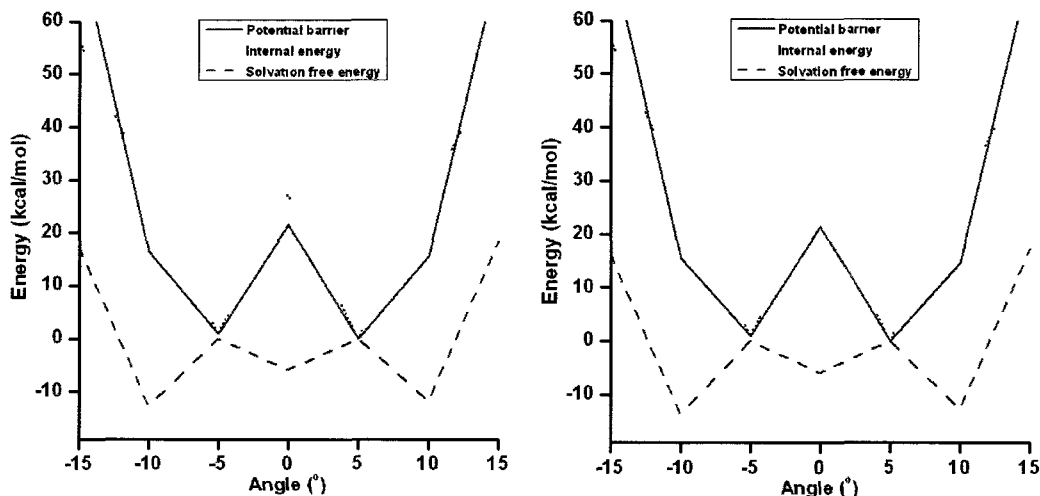


Figure 3.37: Potential barrier, internal energy and solvation free energy for NH-TBL for 1 rosette ring at 10 °C (left) and 40 °C (right).

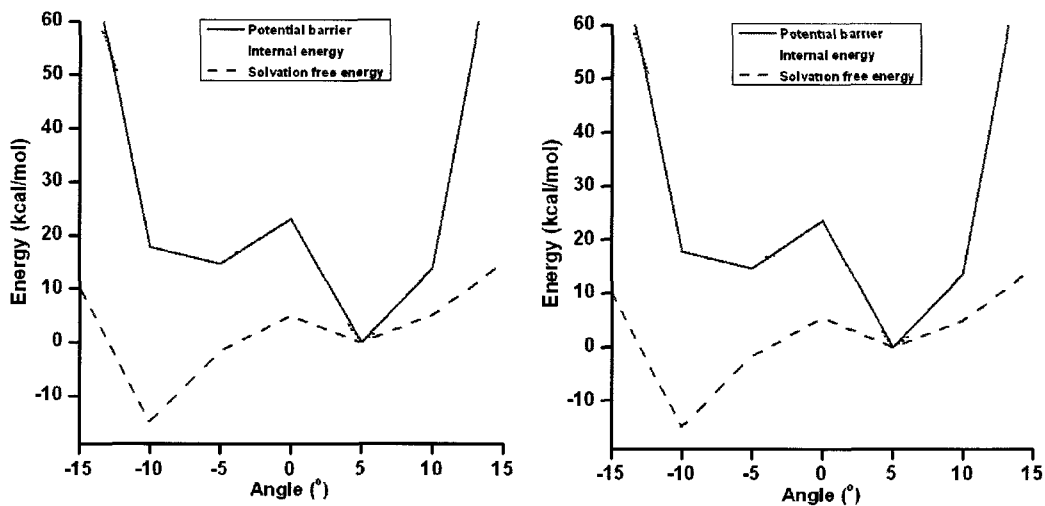


Figure 3.38: Potential barrier, internal energy and solvation free energy for NH-TBL for 2 rosette rings at 10 °C (left) and 40 °C (right).

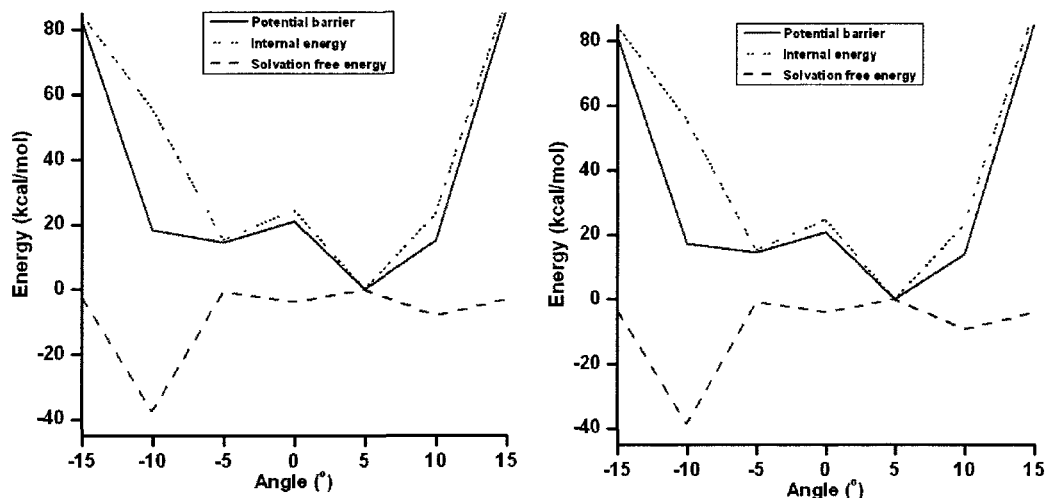


Figure 3.39: Potential barrier, internal energy and solvation free energy for NH-TBL for 3 rosette rings at 10 °C (left) and 40 °C (right).

The effect of substitution on the exocyclic nitrogen was also studied experimentally. Analogues of motif But-TBL (1) were synthesized²⁹ with the substitution illustrated in Figure 3.40.

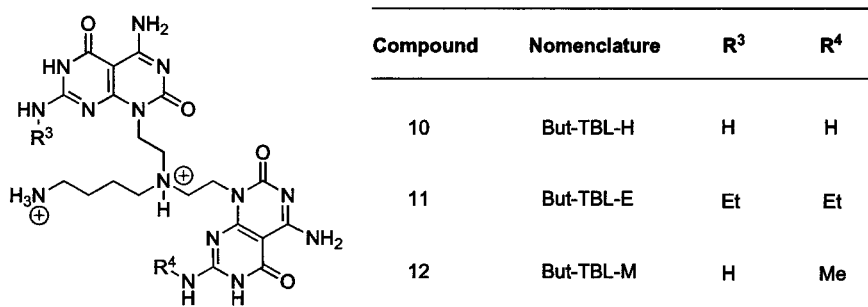


Figure 3.40: Core modification of the G \wedge C motif of the twin RNTs monomers

Stock solutions of But-TBL-H (10) were prepared at a concentration of 0.5 mg/mL in methanol. Aliquots from the stock solutions were diluted and used for CD measurements and imaging. SEM showed the presence of RNTs (Figure 3.41). The RNTs were observed at the beginning of the self-assembly process and as the sample aged, the extent of aggregation increased. Time-dependent CD study showed the presence of a strong CD signal, resembling the one obtained for

But-TBL, but also had about the same intensity. The CD signal for But-TBL-H also displayed the thermo-reversibility property when it was subjected to a VT-CD experiment. These results were in agreement with the outcome predicted by molecular modeling, whereby no difference was observed when the substitution was changed.

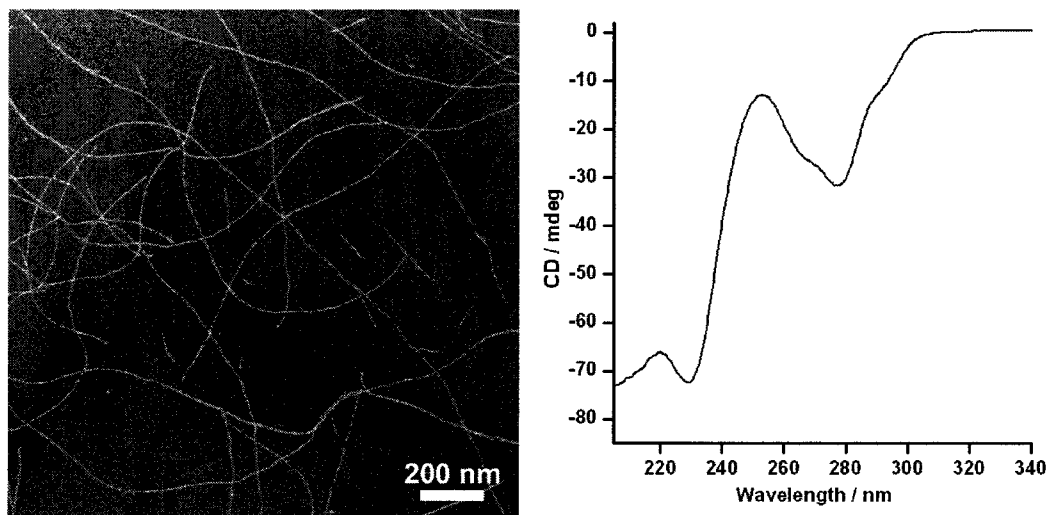


Figure 3.41: SEM image (left) and CD (right) of the HCl salt of But-TBL-H in methanol after 4 days of aging.

Stock solution of But-TBL-E (11) was prepared at a concentration of 0.5 mg/mL in methanol and the CD measurements were taken. As speculated, the spectrum obtained at the beginning of the self-assembly process, was CD-silent. Through SEM, it was possible to observe nanostructures similar to RNTs, however the nanotubes looked shorter (Figure 3.42). But-TBL-E has an ethyl group on the exocyclic nitrogen, which can increase the inter- and intra-molecular repulsion between the rosettes. Formation of longer tubes is expected to be less stable. As the methanol sample aged, no CD signal emerged, even after 2 weeks of aging. As such, a more concentrated solution of But-TBL-E (1.0 mg/mL) was prepared and the CD behaviour was monitored. However in this case too no CD signal emerged, even after two months of aging. Results from this experiment and others discussed previously strongly suggested that the RNT length was the key to observing the anomalous CD signal.

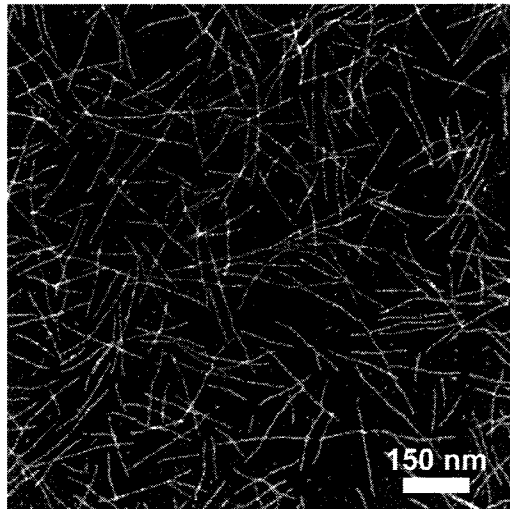


Figure 3.42: SEM image of HCl salt of But-TBL-E in methanol after 2 weeks of aging.

Heterogeneous But-TBL-M would be more prone to give strong CEs due to desymmetrization of the motif, provided long RNTs are formed. This sample showed long RNTs and similar CD behaviour as But-TBL (Figure 3.43).

The intent behind the CD experiments of But-TBL-E (**11**) was to investigate whether a potential barrier resulting from the staggered angle between the $G^A C$ units, triggered by the methyl groups, was the root of the CD signal observed for But-TBL. The RNTs derived from But-TBL-H (**10**) and But-TBL-M (**12**) showed similar CD activity as RNTs derived from the But-TBL monomer (**1**), which suggests that the substitution at this position does not have a role in the existence of the CD signal. We had speculated that if But-TBL-E gave a CD signal, it should be more pronounced due to a higher potential barrier. However we could not verify this theory experimentally since But-TBL-E did not yield any measureable CE, most probably due to the shorter nanotubes obtained.

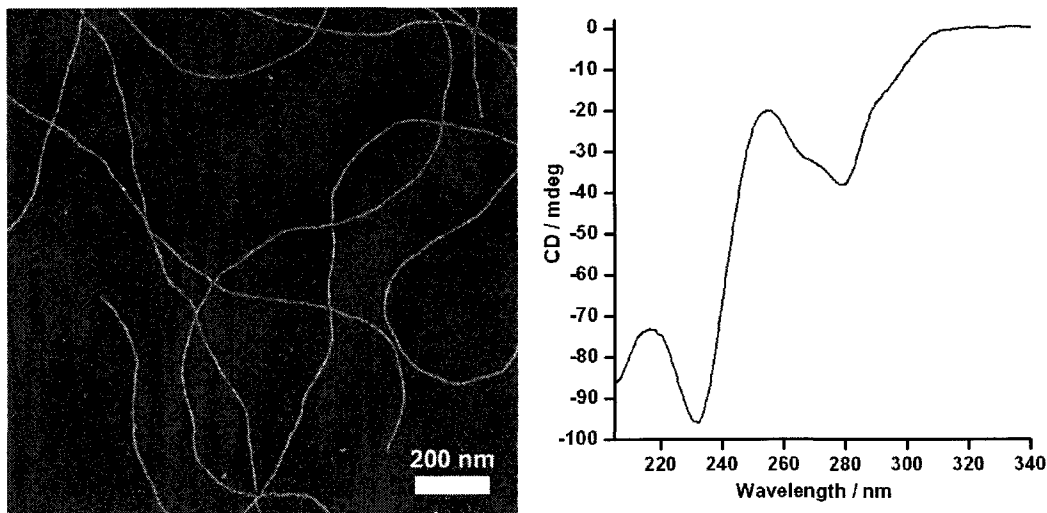


Figure 3.43: SEM image (left) and CD spectrum (right) of HCl salt of But-TBL-M in methanol after 4 days of aging.

3.9. Comparing the TBL system to previously reported systems

Though the CD effects observed for But-TBL and related molecules are unique and have not been reported previously, a number of features can be compared to recent literature reports. These include work by Ribo and coworkers who were able to disymmetrize homoassociates of diprotonated meso-sulfonatophenyl substituted porphyrins by vortex forces.¹³ Aida and coworkers reported the emergence of CD and LD signals when their nanofibres were stirred during spectroscopic measurements.¹⁴ Finally, Meijer and coworkers observed a CD signal when their self-assembled fibres were slowly cooled.¹⁵ As such, some of the experiments reported therein, have been adopted for comparison purposes. These three reports (described in more detail in chapter 1, section 1.5 of this thesis) invoked systems with macroscopic chirality - a spontaneous symmetry-breaking scenario triggered by an external stimulus.

3.9.1. Effect of stirring on TBL's supramolecular chirality

We suspected that our system too showed macroscopic chirality and to investigate whether it was induced during the stirring or rotary evaporation (as in the case of Ribo's work where chirality in diprotonated porphyrins was induced during rotary evaporation),¹³ a sample of But-TBL was synthesized by stirring in a *counter-*

clockwise manner and evaporating in a *clockwise* fashion. Normally, most magnetic stir plates stir in a clockwise manner, while the rotary evaporator spins in a counter-clockwise manner. To reverse the direction of stirring and spinning during the synthesis, the magnetic stir plate used was inverted upside down, allowing the magnetic stir bar to spin in a counter-clockwise direction. The rotary evaporator was manually spun in a clockwise direction to reverse the spin. The centrifugation step for separation of the solid and liquid phases was replaced by filtration.

The But-TBL product, obtained by reversing the direction of magnetic stirring and rotary evaporation, was self-assembled in methanol and the CD was monitored. Presence of RNTs, CD effects and thermo-reversibility of the CD signal were observed, suggesting that stirring and removal of solvent using the rotary evaporator in the opposite directions did not result in reversal of chirality. These results also suggest that this system behaves differently from Ribo's system as the sign of the macroscopic chirality is independent of the stirring/spinning direction.

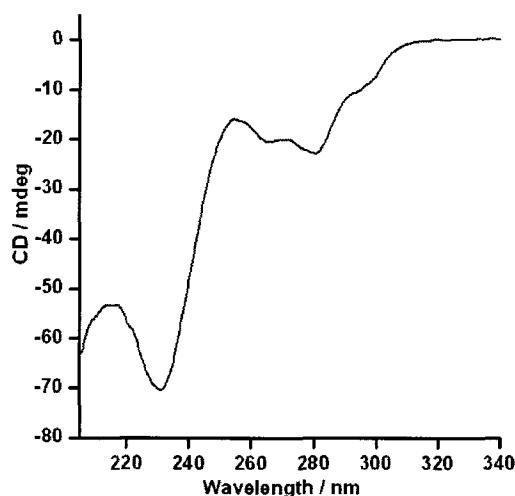


Figure 3.44: CD of But-TBL sample at 10 °C (0.0125 mg/mL, 0.017 mM, aged for 5 days at room temperature) made by changing the direction of the vortex during synthesis.

3.9.2. Effect of temperature and stirring on the CD of the RNTs

To see the effect of stirring and temperature on self-assembly and CD, the But-TBL salt was dissolved in HPLC grade methanol (0.5 mg/mL, 0.685 mM), divided into five vials (A, B, C, D and E) and the solution in each vial was aged under the conditions indicated below:

A: Vial kept at room temperature (21-23 °C).

B: Vial kept in the refrigerator (2-8 °C).

C: Vial kept in a warm oil bath (33-38 °C).

D: Vial contained a magnetic bar, which stirred the sample in the clockwise (CW) direction at room temperature (21-23 °C).

E: Vial contained a magnetic bar, which stirred the sample in the counter-clockwise (CCW) direction at room temperature (21-23 °C).

The spectroscopic measurements were carried out on unstirred and diluted methanolic samples (0.0125 mg/mL, 0.017 mM) at 10 °C. Time dependent CD and SEM were done to investigate whether the macroscopic chirality observed was related to any external stimuli such as temperature and magnetic stirring. Aliquots from the stock solutions were taken at different time intervals and diluted with methanol, before the CD spectra were recorded at 10 °C. No measurable CE was observed at the start of the self-assembly process. However, as the sample aged, a monosignate CD signal appeared, which intensified over time. This observation further confirms that the CD effects are due to the RNTs.

A small aliquot from each solution was deposited on a carbon-coated TEM grid at different time intervals and SEM was done to confirm the presence and the growth of the RNTs. The CD was monitored at 0.5, 5 h and 1, 2, 4, 7, 10, 14, 21 and 30 days. However for simplicity in visualizing the CD signals, only 0.5 h, 1, 2, 4, 7, 14 and 30 days have been plotted. SEM images taken after 7 days growth in each case did not show major differences in the type or extent of aggregation of

the RNTs. The figures 3.45-3.49 show the CD growth and SEM images for the diluted But-TBL samples aged under different conditions.

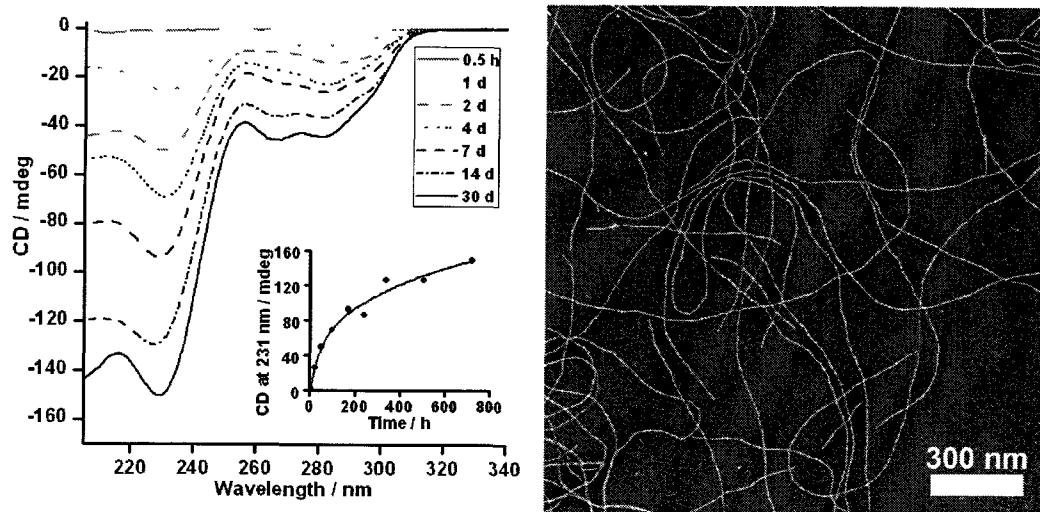


Figure 3.45: CD growth of But-TBL sample A (stock solution aged at 21-23 °C) with time (left) and SEM image of a 7-day diluted But-TBL sample (right).

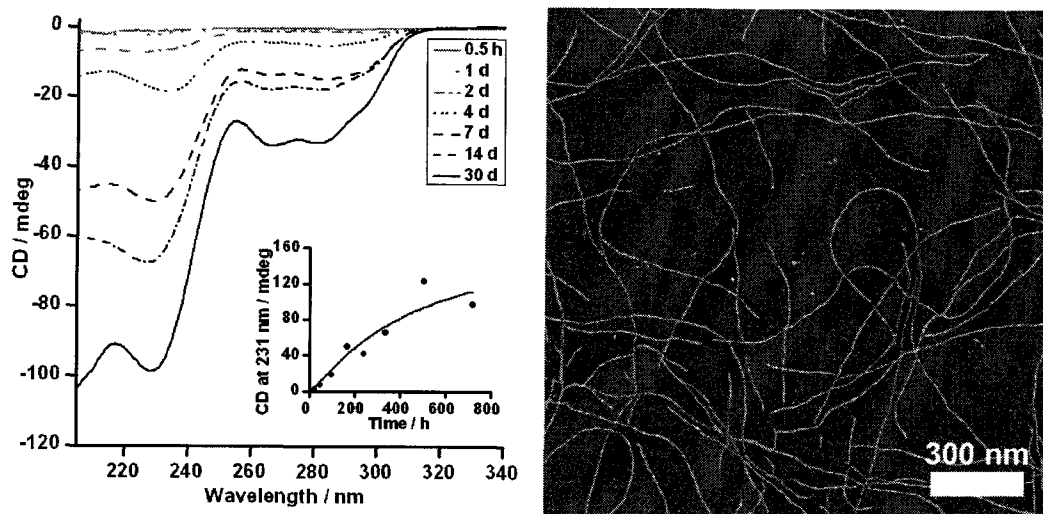


Figure 3.46: CD growth of But-TBL sample B (stock solution aged at 2-8 °C) with time (left) and SEM image of a 7-day diluted But-TBL sample (right).

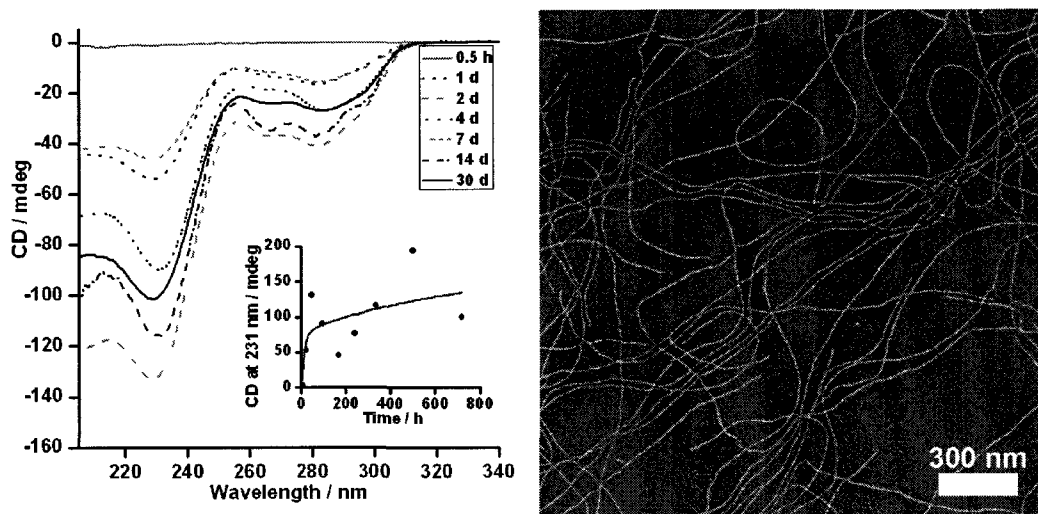


Figure 3.47: CD growth of But-TBL sample C (stock solution aged at 33-38 °C) with time (left) and SEM image of a 7-day diluted But-TBL sample (right).

Though A and B have similar CD growth trend, the rate of growth is slower in the case of B since the sample was aged at a lower temperature (2-8 °C) than A (21-23 °C). Higher temperatures tend to favour the self-assembly process of the RNTs, which is why the sample C (aged at 33-38 °C) has the highest CD intensity. Samples D and E follow similar CD growth and CD decay. Initially, the CD intensity increased and this was most likely due to increased self-assembly of the RNTs. However the intensities of both D and E are lower than A, implying that stirring in either direction affects the CD signal. Both samples (D and E) reached a CD maximum before undergoing a gradual decay. We propose that stirring in either direction hinder RNTs growth or break the existing aggregation, resulting in the CD decay. These stirring experiments suggest that unlike Ribo's work, this system does not memorize the stirring effect, and hence, it does not assume any mechanically-induced supramolecular chirality.

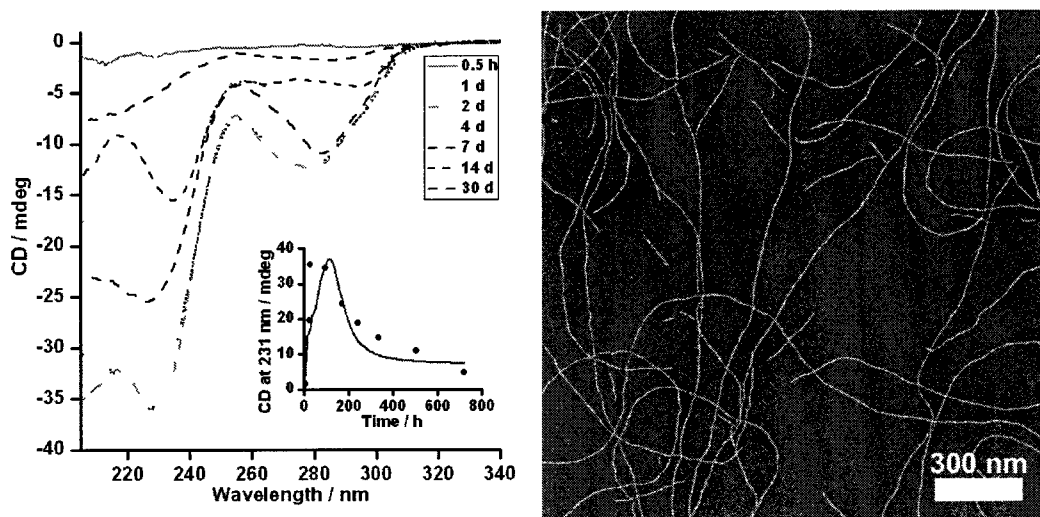


Figure 3.48: CD growth of But-TBL sample D (stock solution aged at 21-23 °C and stirred CW) with time (left) and SEM image of a 7-day diluted But-TBL sample (right).

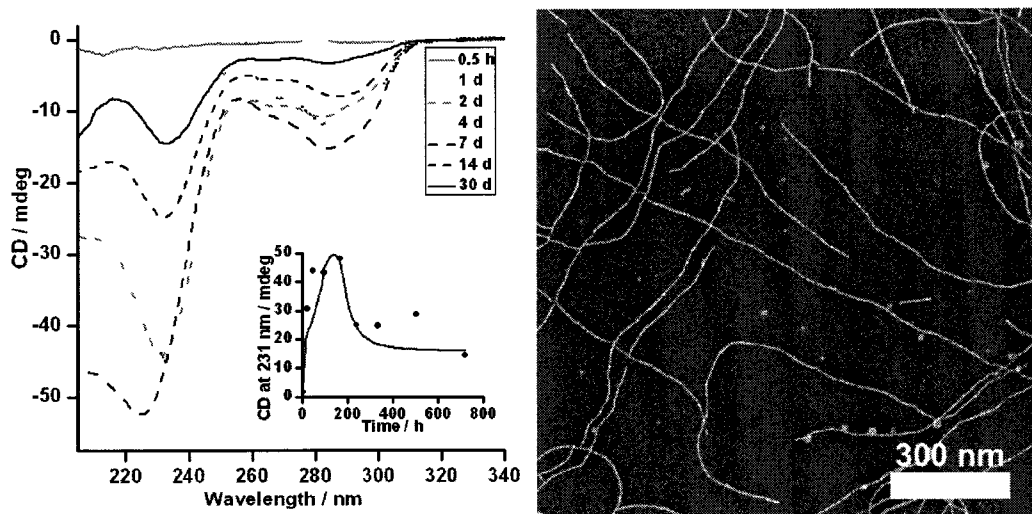


Figure 3.49: CD growth of But-TBL sample E (stock solution aged at 21-23 °C and stirred CCW) with time (left) and SEM image of a 7-day diluted But-TBL sample (right).

3.9.3. Contamination of CD by LD

Linear dichroism^{1c} (LD) is a spectroscopic technique based on the difference in absorption of linearly polarized light parallel and perpendicular to an orientation axis. This instrumentation is very useful for studying oriented samples. In a

number of reports, alignment of samples led to an apparent CD signal.³⁰ In some cases, the true CD was obtained by subtracting the LD component from the observed CD. To verify whether the CD signal in our case was contaminated by a LD component, both CD and LD of the But-TBL sample were measured. An aliquot from the stock solution (0.5 mg/mL, aged at room temperature for 9 days) was diluted with methanol (0.0125 mg/mL, 0.017 mM) and the corresponding CD and LD spectra were recorded at 10 °C (Figure 3.50).

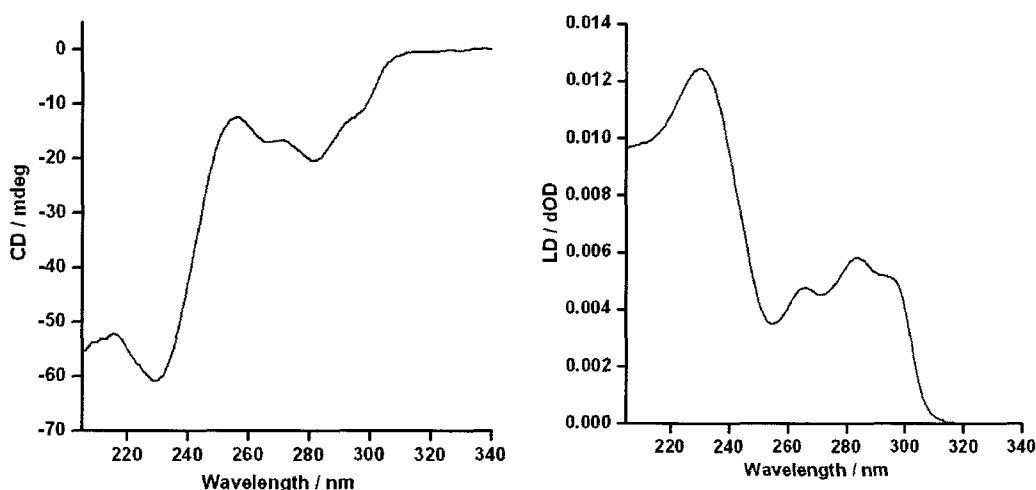


Figure 3.50: CD (left) and LD (right) of But-TBL methanolic solution at 10 °C.

Since the highest intensities for both CD and LD were mostly at 231 nm, the contamination of CD by LD was calculated at that wavelength using the equations below.^{1c,14,30}

$$CD_{\text{true}} = CD_{\text{obs}} - 0.02 (LD_{\text{obs}}) \quad (1)$$

$$\% \text{ Contamination of CD by LD} = 100 \times (|CD_{\text{true}} - CD_{\text{obs}}| / |CD_{\text{obs}}|) \quad (2)$$

Maximum observed CD ($\lambda = 231 \text{ nm}$, 10 °C) = -60.923 mdeg

Maximum observed LD ($\lambda = 231 \text{ nm}$, 10 °C) = 0.0124 (equivalent to 40.92 mdeg)^{1c}

Contamination of CD by LD ($\lambda = 231 \text{ nm}$, 10 °C) = 13%

Similar to other systems,¹³ the CD signal obtained for the But-TBL sample had a minor LD contribution. After unit conversion^{1c} and applying the experimental values to the above equation, the contamination of CD by LD in solution phase was found to be 13%.

To further assess the origin of these CD effects, the But-TBL sample was dip-coated from a two weeks aged 0.5 mg/mL methanolic solution onto a 1 mm thick quartz substrate (experiment done in duplicate). The quartz slides were dipped vertically into the RNT solution so as to preferentially align the nanotubes along the dipping direction and the corresponding CD and LD for both films were measured (Figures 3.51 and 3.52).

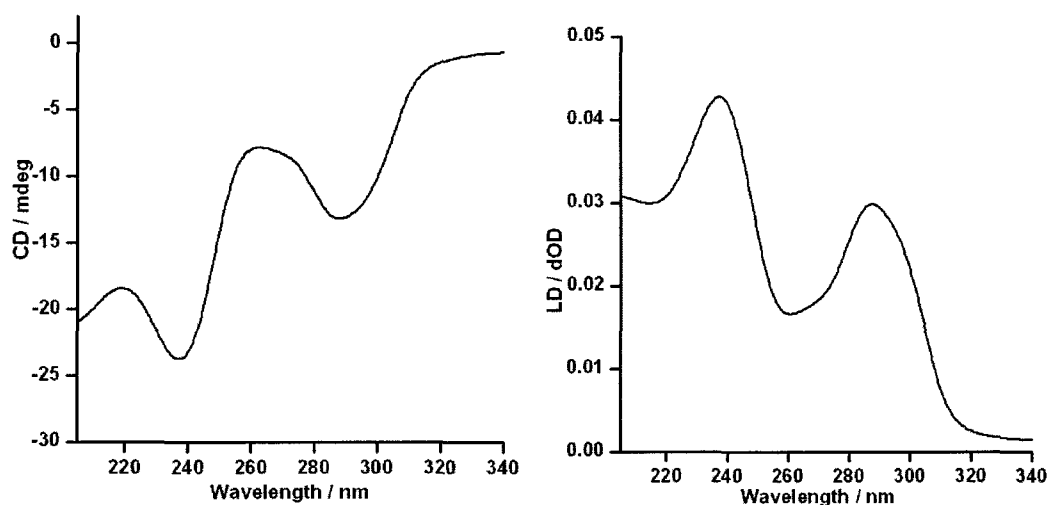


Figure 3.51: CD (left) and LD (right) of But-TBL RNTs dip-coated film 1.

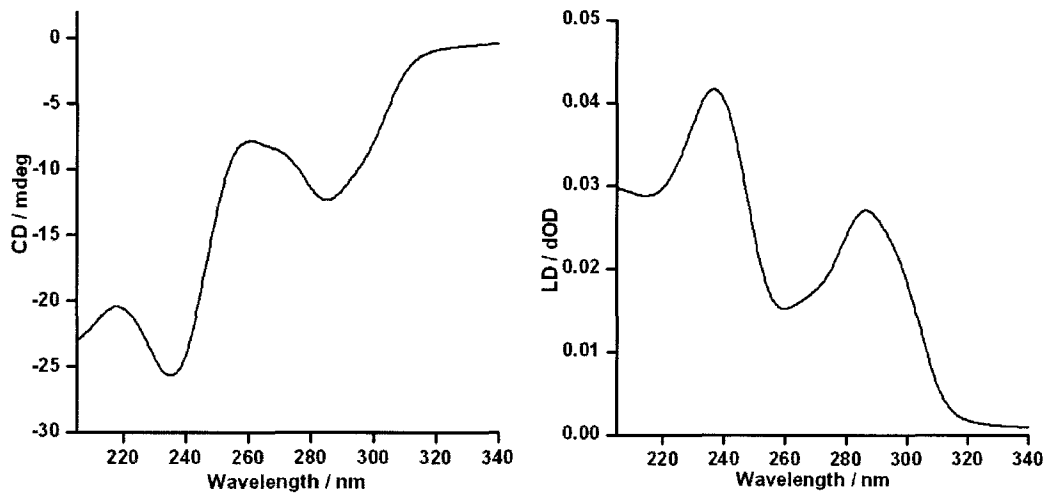


Figure 3.52: CD (left) and LD (right) of But-TBL RNTs dip-coated film 2.

Applying equations 1 and 2, the contamination of CD by LD for both films were found to be over 100% (118% and 103% respectively, calculated for $\lambda = 238$ nm). This implied that for the cast films, the CD signals observed were entirely due to alignment of the RNTs on the quartz surfaces. Hence the apparent CD signals for the cast substrates are not due to molecular anisotropy, but are rather the LD components displayed by the cast samples as a result of alignment of the RNTs.

To further confirm that the RNTs were aligned along the dipping axis, the quartz substrate was rotated by 90° relative to the beam of light and the LD spectrum was recorded. An inversion of the LD spectral sign was observed (Figure 3.53), which proved that the RNTs were anchored along the dipping direction of the quartz slide.

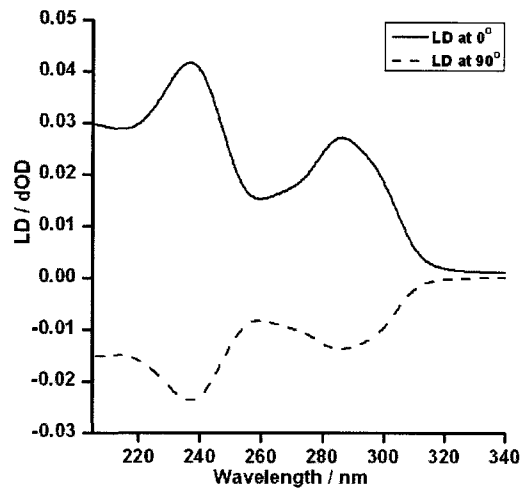


Figure 3.53: LD spectra of RNTs dip-coated film 1 recorded when the substrate was at 0° and 90° relative to the beam of light.

Sometimes the presence of LD in a sample can give rise to an apparent CD signal. Aida and coworkers observed CD signals when their sample made of nanofibres was stirred during spectroscopic measurements.¹⁴ They found that the observed CD obtained in presence of a vortex could be replicated by superimposing two cast films. Similar experiments were performed to verify the angle dependency of the optical activity and whether our system behaved in a similar fashion as Aida's.

As such, two new films (F1 and F2) cast with But-TBL (by dip-coating) were prepared. In these cases too, the CD signals were due to alignment (contamination of CD by LD for F1 and F2 (at 238 nm) = 119%, 95% respectively). The films were subjected to CD spectroscopy while varying the dihedral angle (φ) as shown in Figure 3.54.

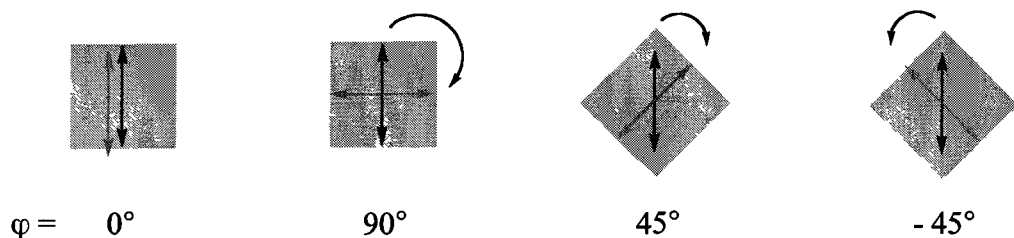


Figure 3.54: Overlap of 2 films (cast with But-TBL RNTs) at different dihedral angles, φ .

The spectra below show the LD obtained for the two films (F1 and F2). These spectra were mathematically added and subtracted to reveal two new spectra (Figure 3.55). The LD was also recorded for the two films by changing the dihedral angle of the overlap. When the films were 90° to each other, the spectrum was similar to $F2 - F1$ spectrum, while the 0° , 45° , -45° spectra were closer to the $F2 + F1$ spectrum, notably due to alignment of the RNTs along the same direction.

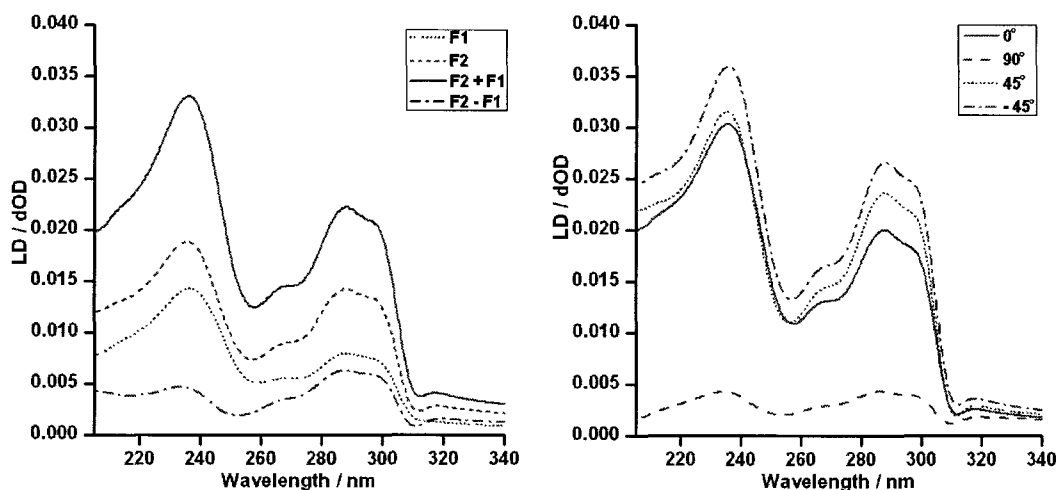


Figure 3.55: LD spectra of But-TBL cast on films and upon overlap of two such films by varying the dihedral angle.

The purpose of recording LD of two overlapped films in previous reports^{13,14} was done to reproduce the CD effect obtained in presence of a macroscopic factor such as the vortex. In our case, with the exception of $\varphi = 90^\circ$, all other angles

gave fairly significant LD intensities, which was equivalent to at least LD of F1 + F2.

While CD and LD measurements for the cast samples established that LD was the sole contributor to the apparent CD signal, calculation of the contamination of CD by LD for the samples in the solution phase only pointed to LD as being a minor contributor. As such, it was important to evaluate the origin of the remaining CD signal for those But-TBL methanolic solutions.

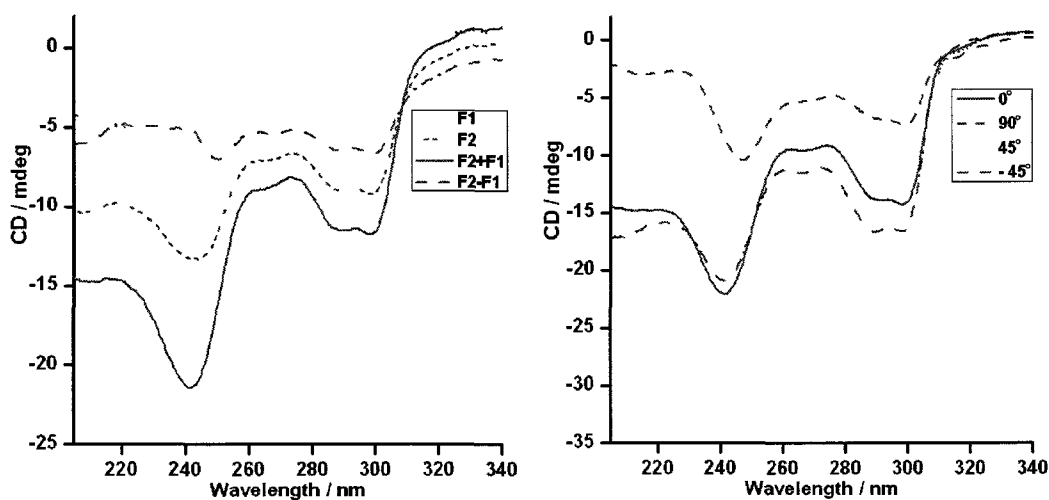


Figure 3.56: CD spectra of But-TBL films cast on quartz slides and upon overlap of two such films at various dihedral angles.

3.9.4. Effect of temperature and stirring while recording the CD spectra

Since the TBL samples exhibited temperature induced-spectroscopic reversibility in solution, it was important to study the effect of stirring the samples in either direction during CD measurement. Aida and coworkers observed CD signals when their sample was stirred while the spectra were being recorded.¹⁴ Meijer observed a monosignate CD profile when an achiral oligo(*p*-phenylene vinylene) derivative (A-OPV) was slowly cooled (363 K to 293 K at a rate of 60 K h⁻¹). Stirring of these A-OPV nanofibres led to the emergence of very intense bisignate CD profiles. In fact, like Aida, Meijer too was able to reproduce similar CD signals (obtained upon stirring) by measuring the chiroptical activity using the

angle dependence of two films. However both of these CD signals obtained (on stirring or using two films) were different from the monosignate CD profile obtained on cooling. This prompted the authors to conclude that the origin of the CD effects for stirring and cooling were different.

Stirring experiments were carried out during spectroscopic measurements on But-TBL at 10, 23 and 40 °C using a magnetic stir bar (0.9 cm x 0.35 cm), stirring at a speed of 640 rpm. As discussed earlier, for the unstirred solutions, a strong negative monosignate CD signal was obtained at 10 °C, while a similar but positive CD signal prevailed at 40 °C. Stirring clockwise at any of these temperatures gave negative CD signals while stirring counter-clockwise gave positive CD signals (Figures 3.57 and 3.58). Generally, CD obtained for the stirred samples had a higher intensity than the unstirred sample at any of these temperatures.

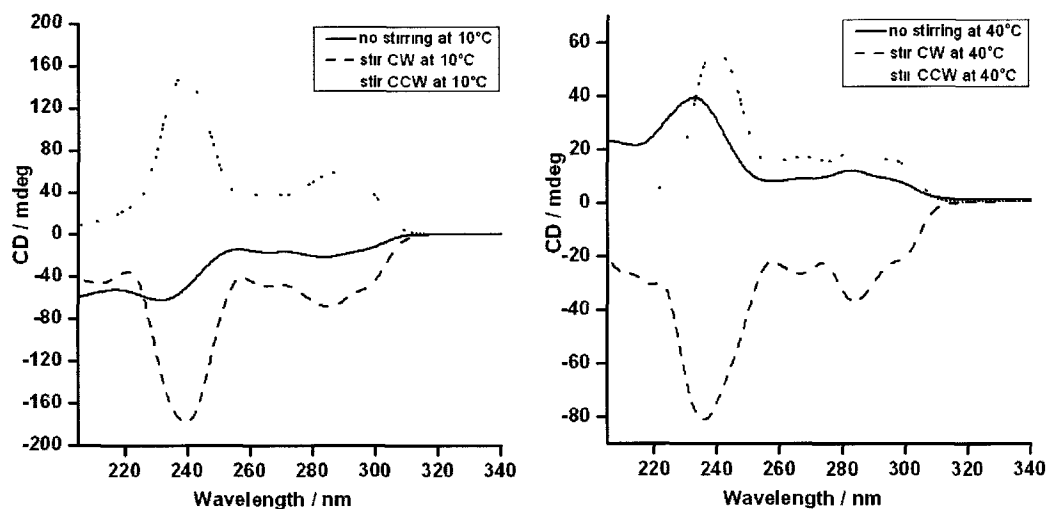


Figure 3.57: CD signals of stirred and unstirred But-TBL solutions at 10 °C (left) and 40 °C (right).

CD measurement for the unstirred But-TBL solution at 23 °C gave no CD activity. Stirring at this temperature in either direction resulted in the emergence of CEs. However as soon as the stirring was stopped, the CD signal disappeared.

Though stirring induced CD signals at this temperature, there was no memorization of the CD signal.

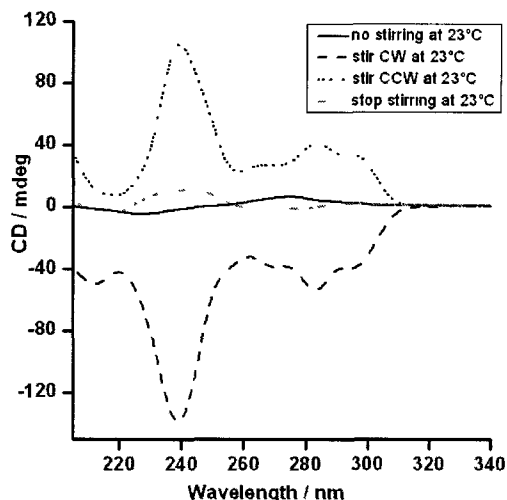


Figure 3.58: CD signals of stirred and unstirred But-TBL samples at 23 °C.

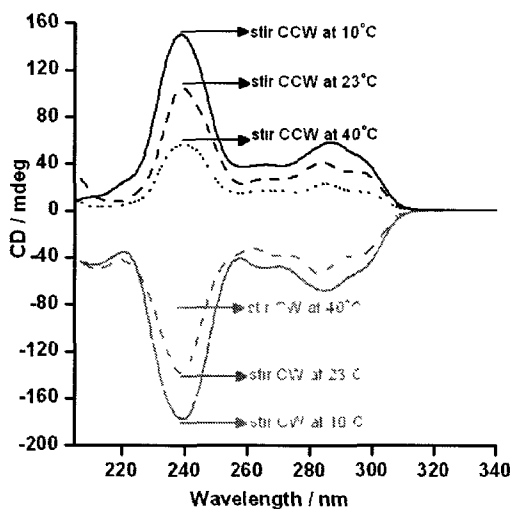


Figure 3.59: CD signals of But-TBL at 10, 23 and 40 °C when stirred CW and CCW.

Figure 3.59 summarizes the CD effects of But-TBL upon stirring at different temperatures. In all cases, strong CEs emerged. While stirring CW led to the emergence of negative CD signals, stirring CCW gave positive CD signals

exclusively. The effect of stirring became more pronounced at lower temperatures, irrespective of the stirring direction.

Since stirring at 10 °C in either directions gave the highest CD intensities among the three temperatures chosen, the ability to memorize the CD effects at this temperature was tested by stirring But-TBL from clockwise to counter-clockwise direction alternatively while the CD signal was being recorded (Figure 3.60). Though it was not verified experimentally, it is anticipated that the CD signals will follow an exponential decay as in the case of the CD recorded for the continuous VT-CD experiment at 10 and 40 °C (Figure 3.11). This is because at this concentration, the RNTs will slowly disassemble and stirring will only contribute to the disassembly process, leading to CD loss.

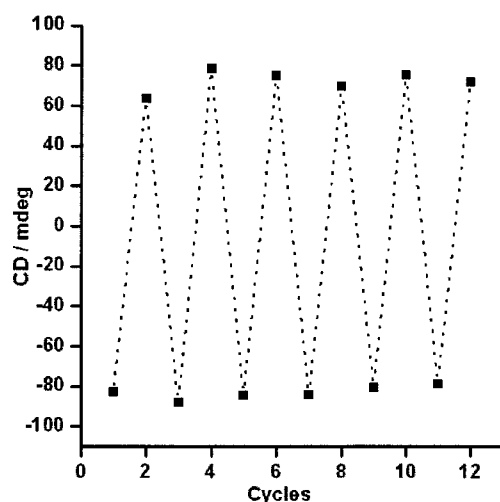


Figure 3.60: CD signals of But-TBL samples when stirred clockwise and counter-clockwise alternately at 10 °C.

Stirring in opposite directions gives mirror-image CD signals, similar to Aida's work¹⁴ and in absence of any vortex flows, the CD persists (at 10 and 40 °C), as observed for Meijer's system. However our system differs from these two systems in several ways. But-TBL gives more intense CD signal upon stirring, however, a monosignate CD profile still exists (at 10 and 40 °C) when stirring is

stopped. In addition, the fact that the CD effects obtained in the presence of convective or vortex flows have similar profiles, suggests that the CD spectrum induced by stirring must follow similar mechanism as the one induced by convective flows.

The LD experiments were also performed while stirring in the clockwise and counter-clockwise direction alternatively at 10 °C (Figure 3.61). Unlike the CD experiments, the LD spectral sign was independent of the stirring direction, implying that stirring in either direction does not alter the alignment vector, however, an increase in the intensity of the LD signals (102% for CW and 117% for CCW) was observed. Since the LD spectral sign for the film (RNTs were aligned along dipping axis) and stirred solution are the same, the RNTs are most likely aligned along the vortex created during stirring. The contamination of CD by LD was found to be 9% (CW) and 12% (CCW) at 10 °C.

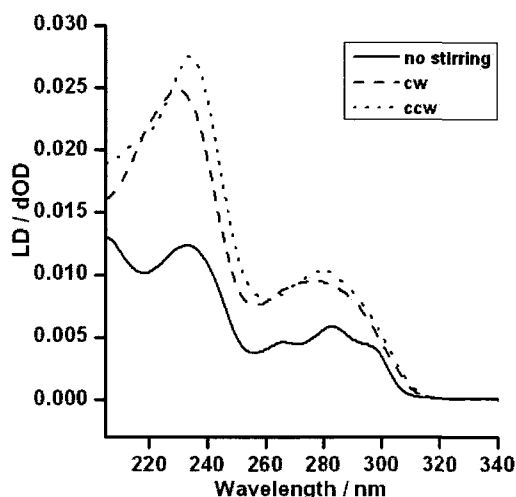


Figure 3.61: LD signals of But-TBL samples at 10 °C when unstirred, stirred in clockwise and stirred in counter-clockwise directions.

The LD signal was also measured upon addition of TFA (Figure 3.58) and a significant reduction of the LD effects (75%) was observed. This confirmed that the LD observed originated from the alignment of the RNTs in solution and since

TFA is known to disrupt self-assembly (see Figure 3.8), the alignment was greatly reduced.

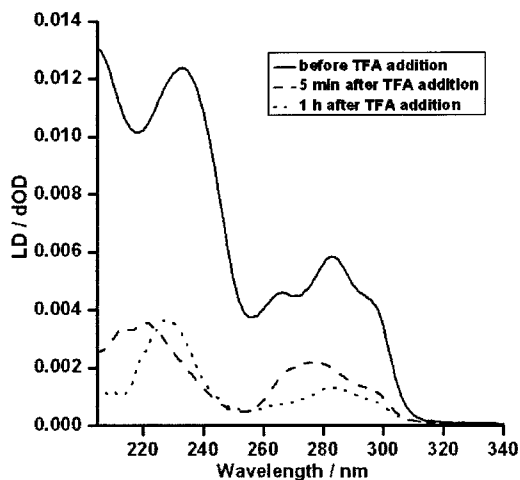


Figure 3.62: LD signals of But-TBL samples at 10 °C before and after TFA addition.

To gain more insight on how the RNTs were aligning themselves in the solution during stirring, we recorded the LD spectra with the optical cell selectively masked in the centre or along the edges (Figure 3.63), as per the published work of Aida.¹⁴ Aida used this experiment to demonstrate that their sample was aligning along the vortex created when the solution was stirred.

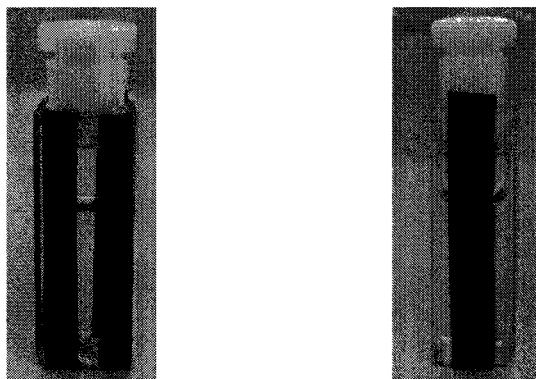


Figure 3.63: Edge mask (left): the edges of the cuvette were masked using 4 mm wide black tapes on both sides leaving a 2 mm central slit; and Central mask

(right): the centre of the optical faces was masked by 6 mm wide black tape, leaving 2 mm margins on each side of the optical windows.

As a control experiment, the LD signal for the unmasked cuvette was also measured and a positive monosignate signal was obtained. Since LD has the same spectral sign as those obtained for the cast films, the RNTs were primarily aligned along the walls of the cuvette, which is perpendicular to the beam of light. The LD of the cuvette masked along the edges gave a LD spectrum similar to the unmasked cell, which implied this LD signal could be treated as a representation of the whole system. While the LD signal for the centrally masked cuvette was lower in intensity, it also had the opposite sign as the signal observed for the whole solution (Figure 3.64). This finding pointed towards the horizontal alignment of the RNTs, found close to the edges of the optical windows.

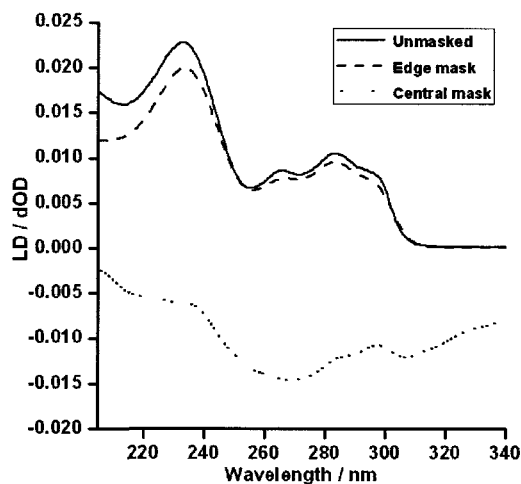


Figure 3.64: LD signals of But-TBL samples at 10 °C when the optical cell was unmasked, masked on the edges and in the centre.

3.10. Mueller matrix and standard commercial CD instrument

The optical properties of our RNTs were studied with a home-built spectroscopic polarimeter,³¹ which uses the configuration known as two-modulator generalized ellipsometer (2-MGE).³² The optical characterization was based on the spectroscopic measurement of the Mueller matrix³³ of the samples. The

transmission Mueller matrix is 4 x 4 real-valued matrix (Figure 3.65) that describes the transformation of an incident polarization state after it traverses an optical medium. The polarization-dependent properties of the medium are contained in its Mueller matrix. For a non-depolarizing system six parameters³⁴ are used, namely, CD, circular birefringence (CB), two parameters that define the projection of linear birefringence at 0° and 45° (LB and LB') and two parameters for the projection of linear dichroism at 0° and 45° (LD and LD'). In general none of the 16 elements of the Mueller matrix (Figure 3.66) are simply related to any of these polarization effects, although in some circumstances, especially for non-oriented samples, it is possible to find that certain elements of the Mueller matrix are mostly contributed by one single effect.³⁵ In our case, the relevant optical effects were obtained by the analytic inversion of the Mueller matrix of a homogeneous medium.³⁶

$$\begin{pmatrix} M_{00} & M_{01} & M_{02} & M_{03} \\ M_{10} & M_{11} & M_{12} & M_{13} \\ M_{20} & M_{21} & M_{22} & M_{23} \\ M_{30} & M_{31} & M_{32} & M_{33} \end{pmatrix}$$

Figure 3.65: Mueller matrix – a 4 x 4 matrix

$$M = e^{-2k} \begin{pmatrix} 1 + 1/2 (LD'^2 + LD^2) & -LD & -LD' & CD + 1/2 (LBLD' - LB'LD) \\ -LD & 1 + 1/2 (LD^2 - LB'^2) & CB + 1/2 (LBLB' + LDLD') & LB' \\ -LD' & -CB + 1/2 (LBLB' + LDLD') & 1 + 1/2 (LD'^2 - LB^2) & -LB \\ CD - 1/2 (LBLB' - LB'LD) & -LB' & LB & 1 + 1/2 (LB'^2 + LB^2) \end{pmatrix}$$

Figure 3.66: The Mueller matrix for a general sample with mixed anisotropies

In general, fused quartz cuvettes used for CD measurement show low birefringence values. However, some degree of strain-induced birefringence in

the walls of the cuvette is always present, which becomes significant in the UV region. This birefringence is expected to vary with the quality of cuvette, but sometimes even higher-grade cuvettes are not exempt of birefringence. The combination of linear birefringence of the walls of the cuvette, and the linear dichroism of an oriented sample can give rise to a measureable CD signal when using a commercial instrument.³⁰ While we initially attempted to subtract the LD contamination from CD as previously done in a number of reports,^{14,37} we later realized that this was not the correct approach. This is because the remaining CD component obtained upon extraction of the LD component could still contain a LB component. To avoid these undesired artifacts,³⁸ the Mueller matrix approach³³ was used for CD measurement. Standard CD instruments such as our Jasco 810 spectropolarimeter, typically measure the M_{03} element of the Mueller matrix (Figure 3.66), where $M_{03} \approx CD + \frac{1}{2}(LBLD' - LB'LD)$. The measurement of Mueller matrix allows the use of model descriptions for the light propagation through the medium, and when properly used, permits a complete and accurate identification of the polarization effects contained in the sample.

Measurements were taken *in situ* while stirring the RNT solutions with a magnetic stirrer, capable of stirring in CW and CCW directions. The light beam was incident to the central part (1.5 mm in diameter) of the cuvette at about 10 mm above the stirrer bar. Samples were scanned from 235-340 nm and the spectroscopic Mueller matrix normalized to the M_{00} element for the stirred and unstirred But-TBL was obtained (Figure 3.67).

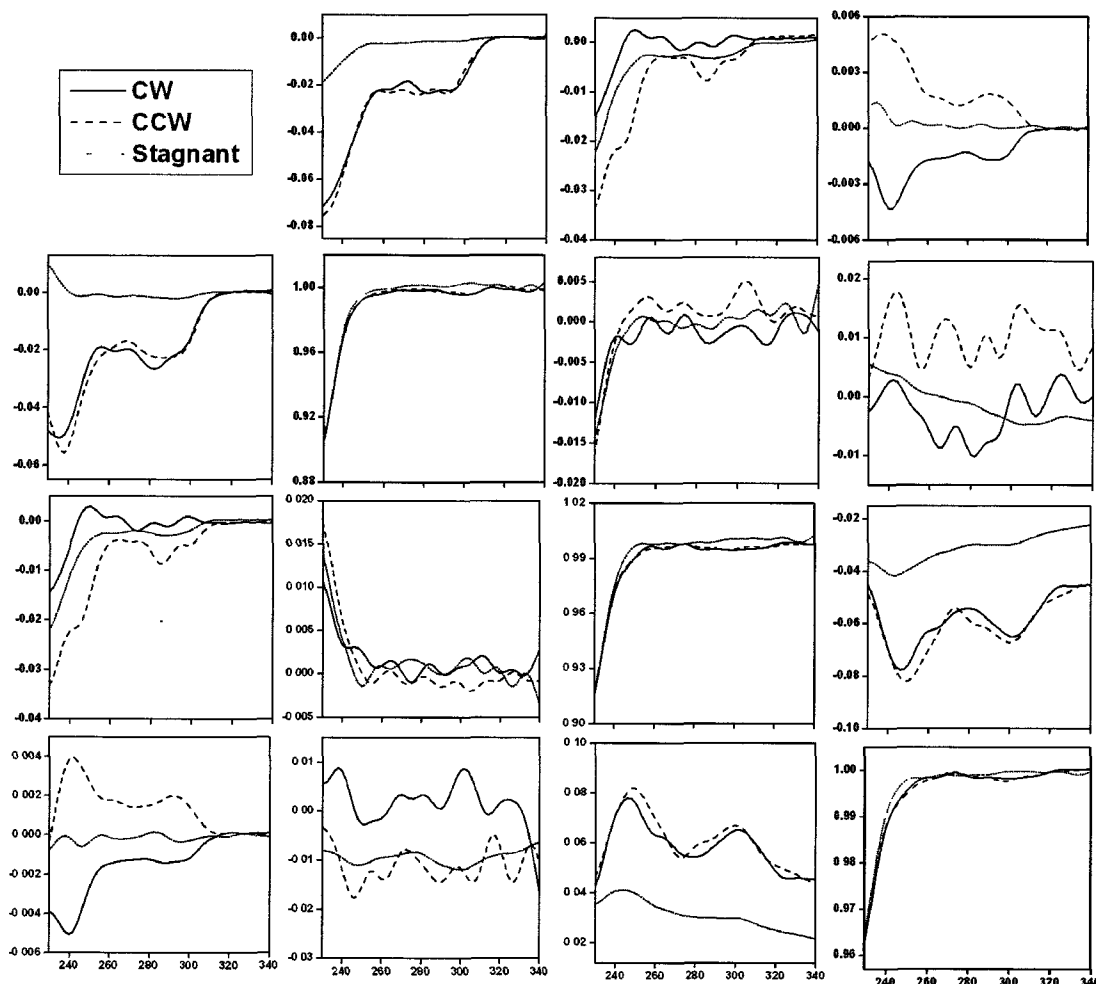


Figure 3.67: Mueller matrix obtained for But-TBL RNTs at room temperature (23°C).

The CD profiles of the RNTs (Figure 3.68) were calculated from the analytical inversion of the Mueller matrix from Figure 3.67 and evidence of chiral induction as function of the direction of stirring was found.³⁹ The total in-plane linear dichroism LD_m is taken as $LD_m=(LD^2+LD'^2)^{1/2}$ and the total in-plane linear birefringence LB_m is $LB_m=(LB^2+LB'^2)^{1/2}$ and are shown in Figure 3.68 (B and C) respectively. The higher values of LD_m and LB_m obtained for CW and CCW stirring show that the RNTs have a greater degree of orientation with respect to the stagnant configuration as result of the vortex flows.

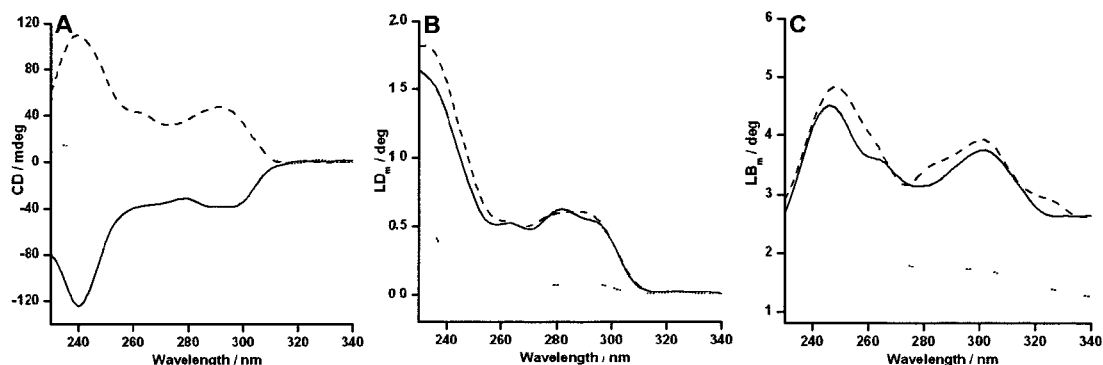


Figure 3.68: Optical effects derived from the Mueller matrix obtained for But-TBL RNTs at 23 °C when stirred CW (solid), CCW (dash) and when unstirred (dot).

CD measurement of the unstirred RNTs sample with 2-MGE (Figure 3.68) did not yield any discernible value of CD at room temperature. These results were in agreement with the spectra obtained on our commercial Jasco J-810 spectropolarimeter, with only subtle difference in intensities (Figure 3.58). Stirring CW gave negative monosignate CD signals while stirring CCW produced positive CD profiles. The difference in intensities at different temperatures (see Figure 3.59) clearly depicted a thermally induced phenomenon in addition to the vortex triggered CD behaviour.

3.11. Convection and interaction with quartz surface

In most cases, we obtained a strong negative monosignate CD signal at 10 °C and a positive CD profile at 40 °C when carrying out CD measurements on a Jasco 810 spectropolarimeter. The thermal control during CD measurement was achieved using a Peltier accessory, which operates with an external circulation bath. Unless stated otherwise, the cuvette used had a rectangular shape (see Figure 3.63), with a pathlength of 1 cm and fits exactly into the sample holder shown in Figure 3.69. The latter shows the sample holder used for CD and LD measurements in the solution phase. Light passing through the aperture is incident on the optical windows on the **C** and **D** faces. The water circulation (used for cooling) is closer to the face **A**, while the thermocouple is found next to

the face **B**. Any temperature change will therefore affect the solution next to the cuvette wall on the **A** face first.

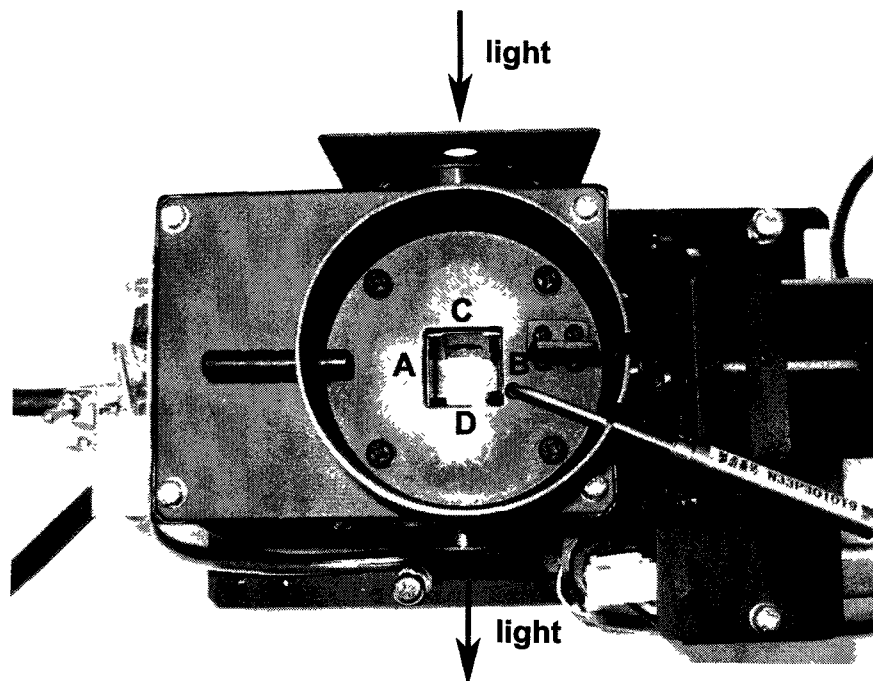


Figure 3.69: Top view of the sample holder used for CD and LD measurements in the solution phase.

The temperature of the circular bath was set to room temperature (23 °C), resulting into a temperature gradient. We presumed that the CD effects could be related to the convection flows present in the cuvette, which were responsible for the orientation of the RNTs in solution. When the temperature of the circulation bath is similar to that of the Peltier accessory, the temperature gradient in the cuvette is lower, leading to less oriented particles. This hypothesis was further supported by the opposite preferential orientations at 10 and 40 °C (obtained the LD and LD' values) that could be attributed to the different sense of the convection flows when cooling or heating (Figure 3.70). As such, the source of the macroscopic chirality for the unstirred TBL samples could arise from the convective flows created in the RNT solutions.

Average preferential directions	
10 °C (Unstirred)	40 °C (Unstirred)
	

Figure 3.70: Average preferential orientations of But-TBL at 10 and 40 °C

CD measurements for the unstirred solutions with 2-MGE at 10, 23 and 40 °C (Figure 3.71) gave essentially no CD signal due to the absence of a temperature gradient (temperature of circulation bath was set at 10, 23 and 40 °C respectively).

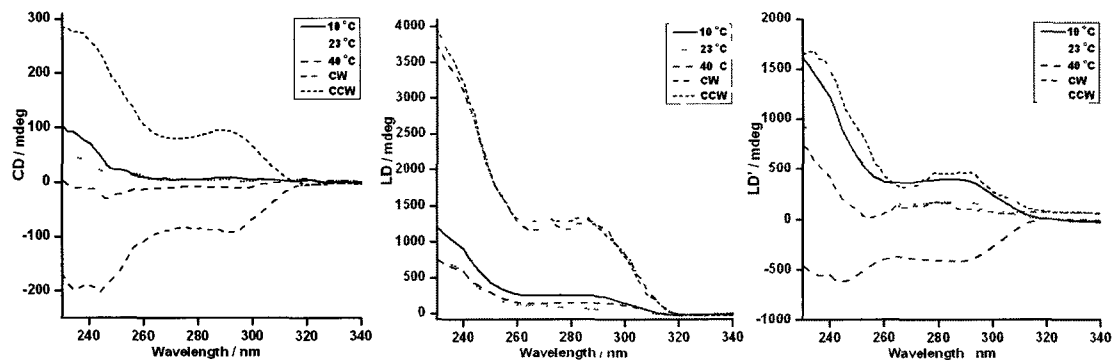


Figure 3.71: Optical effects – CD (left), LD (centre) and LD' (right) obtained from the analytical measurements using the 2-MGE at 10, 23 and 40 °C for the unstirred methanolic But-TBL sample and when stirring CW and CCW at 23 °C.

So far all the CD studies were conducted with pre-formed RNTs aged at room temperature and aliquots of those stock solutions were diluted prior to the CD measurements at 10 °C. The growth of RNTs is an autocatalytic process^{10c} (DLS, Figure 3.7) and in principle, if the CD effects arise from the intrinsic chirality of the nanotubes, the CD should also follow a sigmoidal growth. The CD activity of a freshly made RNTs solution (0.3 mg/mL in methanol) was monitored at a constant temperature of 10 °C over 2 weeks in a cuvette having a pathlength of 0.1 cm. No CD signal emerged during this time interval. This result reiterates the

importance of a convection flow as the key to observing a CD signal for the unstirred But-TBL sample.

The thermo-reversibility of the CD profiles was also affected when using a cuvette of a smaller volume (0.45 mL) and a shorter pathlength (0.3 cm). Though an intense CD signal was observed at 10 °C, the temperature-induced CD switch in this cuvette occurred at a lower temperature (Figure 3.72) compared to the previously used cuvettes (3.5-5 mL volume, 1 cm pathlength).

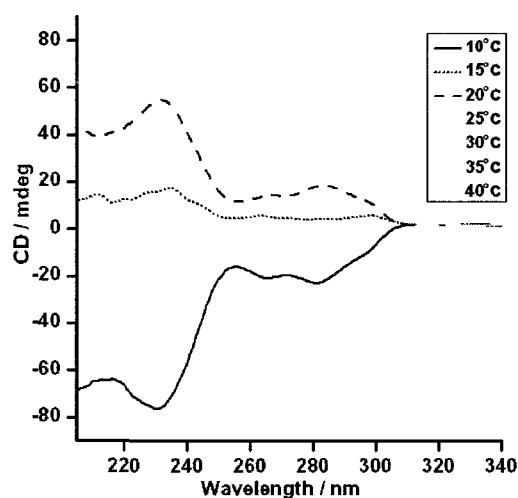


Figure 3.72: VT-CD signals of But-TBL in methanol in a cuvette having a volume of 0.45 mL and a pathlength of 0.3 cm.

Generally, the CD measurements for cuvettes of 1-cm pathlength had a volume of 3.5-5mL. A sample volume of 2 mL was used for spectroscopic measurements. The CD activity was however not affected when the measurement was carried out with the cuvette (3.5 mL) filled up to the rim. Though the solution level affects the convective flows in the medium, it does not have an impact on the CD activity (Figure 3.73).

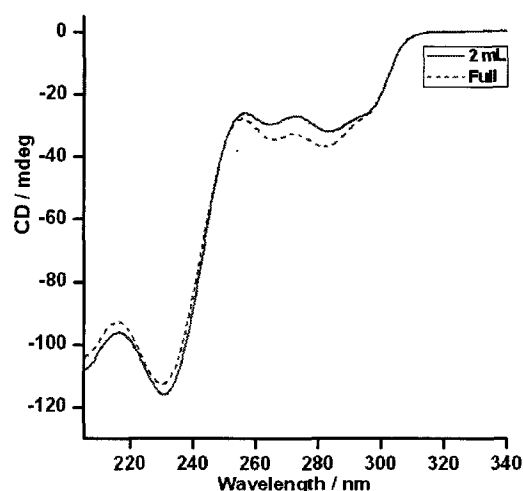


Figure 3.73: CD profiles of But-TBL in methanol in the rectangular cuvette of 1-cm pathlength. The measurements were recorded with 2 mL and 3.5 mL (full) of solution.

CD measurements were also conducted in a cylindrical quartz cuvette (1-cm pathlength). The geometry of this cuvette allows limited heat conduction, resulting into a lower degree of fluctuation in temperature. This decrease in the convective flows led to a lower CD intensity for unstirred But-TBL as compared to a similar measurement carried out in the rectangular cuvette at 10 °C (Figure 3.74).

Similar CD experiments carried out for the stirred But-TBL sample showed no major difference for measurements carried out in the cylindrical or rectangular cuvette (Figure 3.75). This implied that unlike the convective flows, the shape of the cuvette did not affect the vortex flows created upon stirring.

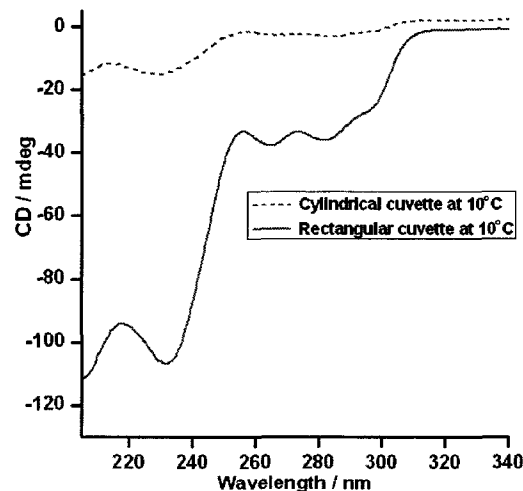


Figure 3.74: CD spectra of But-TBL RNTs, recorded in cylindrical and rectangular cuvettes at 10 °C. Both cuvettes have pathlength of 1 cm.

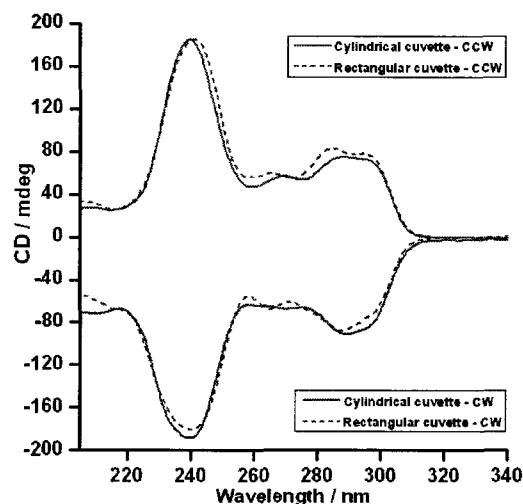


Figure 3.75: CD profiles of But-TBL RNTs upon stirring (at 640 rpm) CW and CCW in cylindrical and rectangular cuvettes at 10 °C.

At this point, the effect of stirring speed on the CD signals was also investigated. Since no major difference was observed between the two cuvettes upon stirring, the next experiment was carried out in the cylindrical cuvette in an attempt to eliminate any CD effects created by convective flows. CD measurements were carried out when the sample was stirred in the clockwise direction at 10 °C using a magnetic stir bar (0.8 cm x 0.1 cm x 0.2 cm). The CD effects initially increase

with increasing revolutions per minute (rpm) until a maxima is reached, after which an exponential decay is observed (Figure 3.76). Most CD measurements obtained upon stirring were carried out in the region where there were minimal CD fluctuations.

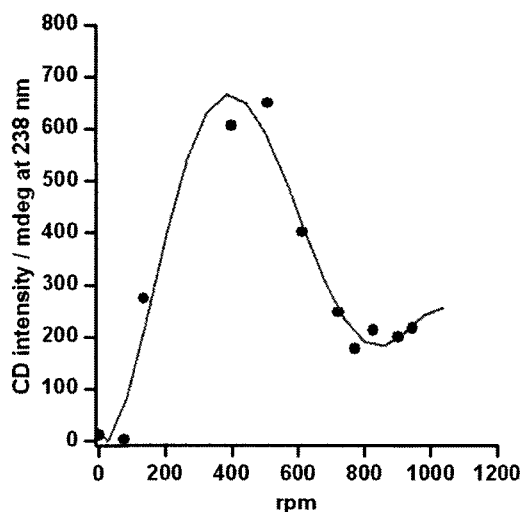


Figure 3.76: CD signals of But-TBL samples at 10 °C when stirred in clockwise direction at varying stirring speeds in the cylindrical cuvette.

Certainly the convective flows had a role in the macroscopic chirality observed for the unstirred RNT solution, however, it was not the only cause of the CD effects. A difference in the intensity of the CD signals based on the cuvette used prompted us to believe that the surface of the optical cell might play a role in the CD activity. As such, CD signals of a 20-day old But-TBL solution were recorded in two cuvettes having a 1 cm pathlength. Though the CD profiles were similar, the intensities were clearly different (Figure 3.77).

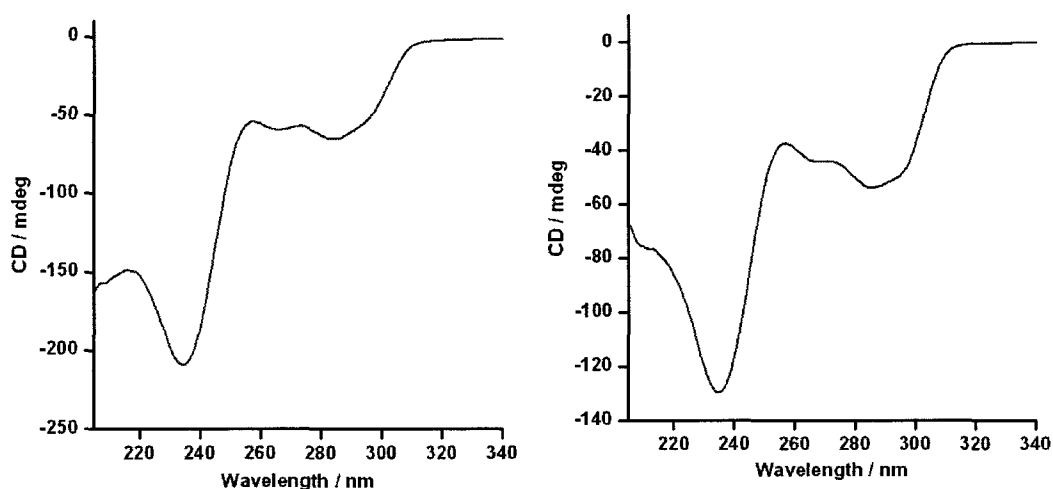


Figure 3.77: CD signals of But-TBL in methanol at 10 °C in cuvette 1 (left) and cuvette 2 (right) having 1-cm pathlength

Similar CD fluctuations were observed when our collaborator, Dr Nathan Cowiesson from Monash University carried out the CD measurements in Australia.⁴⁰ We were able to rule out the effect of the Earth's magnetic field⁴¹ on our sample since we obtained similar CD and VT-CD profiles as the ones obtained in our laboratory. However, obvious intensity differences were observed when the measurements were repeated using a different cuvette (Figure 3.78).

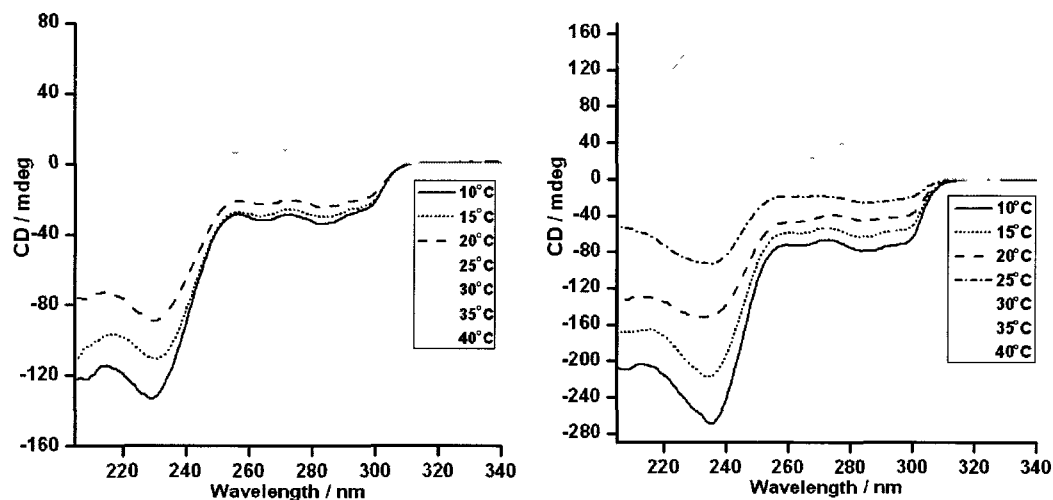


Figure 3.78: VT-CD signals of But-TBL in methanol in cuvette 3 (left) and cuvette 4 (right) having 1-cm pathlength. The measurements were carried out in Australia.

Some materials are known to preferentially adhere to the hydrophilic quartz surfaces.⁴² We anticipate that the preferential interaction between the RNTs and the quartz surface, coupled with linear dichroism, linear birefringence and the convective flows are the causes for the CD effects observed for the unstirred solutions at 10 °C (or 40 °C). When the sample is subjected to a VT-CD experiment, the direction of the alignment changes with the convective flows, resulting in opposite CD signal at 40 °C.

3.12. Effect of chiral substituents

In the case of the achiral monomers, it was clear that the CD for the unstirred samples was derived from LB present in the walls of the quartz cuvettes and the orientation of RNTs as a result of convective flows. However separation of this CD (termed artifactual CD - a combination of the macroscopic chirality resulting from the convective flows, alignment (LD) of the RNTs and LB of the optical windows) from the real CD of the chiral RNTs (due to molecular anisotropy) (Figure 3.79) was important in evaluating the supramolecular chirality of such

systems. It was suspected that the artifacts due to LB and LD resulting from long fibres were masking the chirality due to the anisotropy from the molecules.

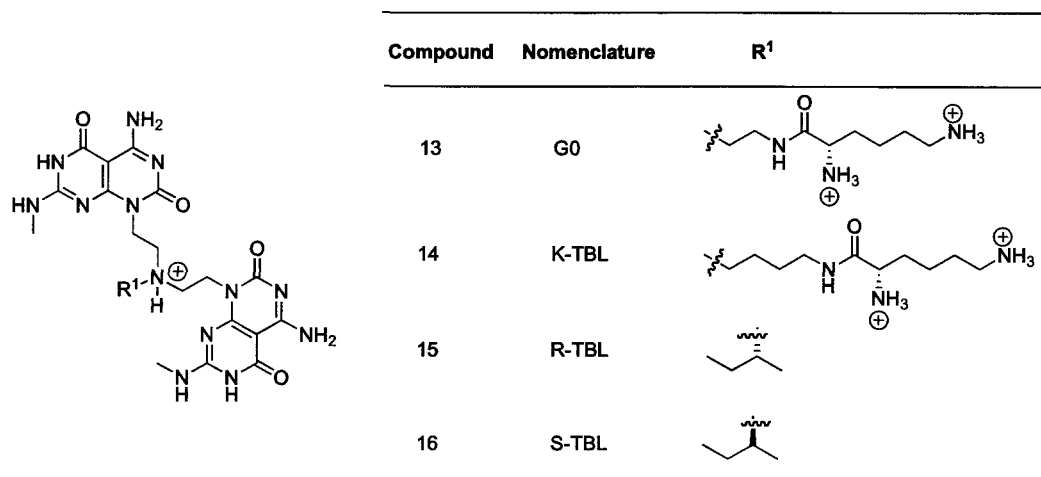


Figure 3.79: Functionalized chiral twin RNTs monomers.⁴³

We initially recorded the CD of RNTs derived from monomers G0²⁴ (13) and K-TBL (14), which were isolated as HCl salts. CD signals resembling the CD profiles of RNTs 1-8 were obtained.

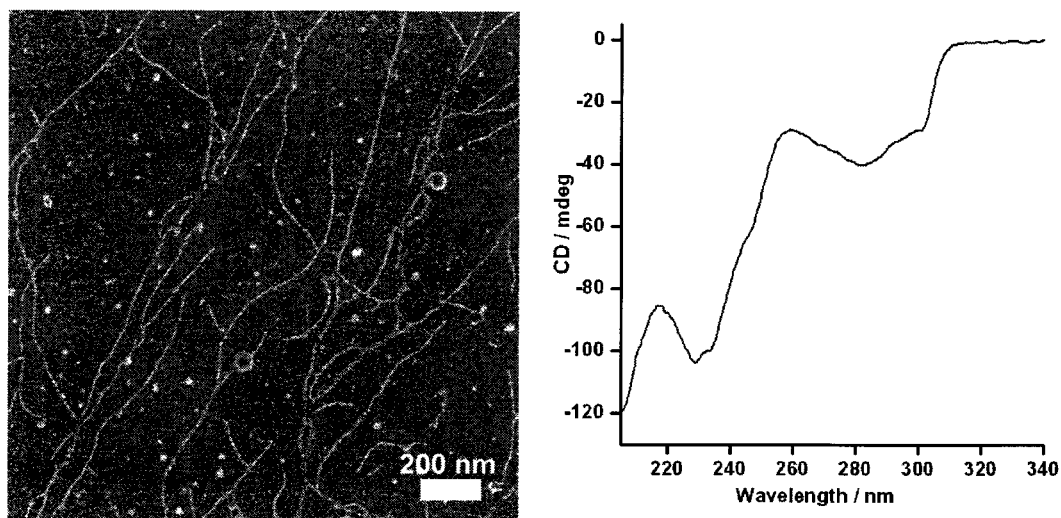


Figure 3.80: SEM image of the HCl salt of G0 (13) in methanol (left) and its CD spectrum at 10 °C (right) after 7 days of aging.

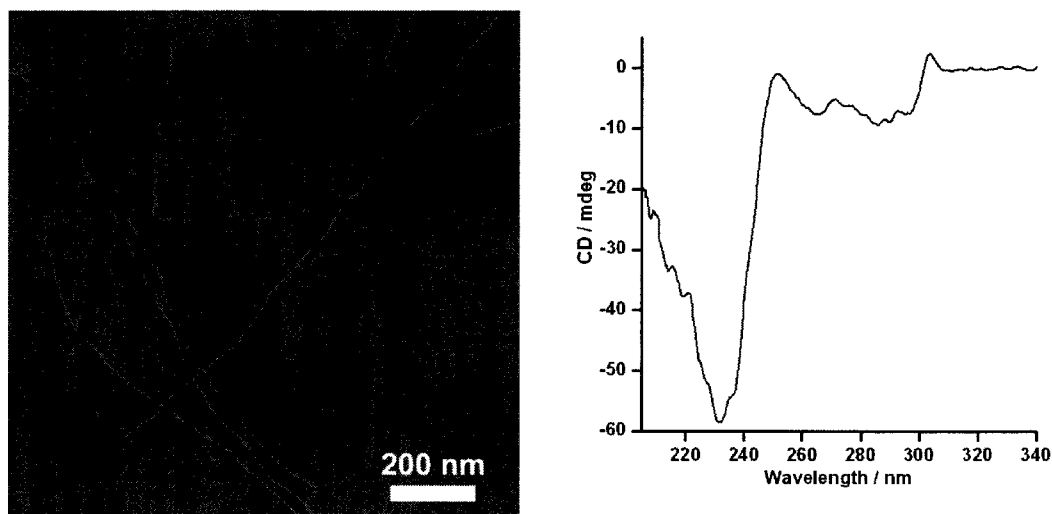


Figure 3.81: SEM image of the HCl salt of K-TBL (**14**) in methanol, aged for 1 day (left) and its CD spectrum at 10 °C (right) after 7 days of aging.

The artifactual contributions to the CD signals were dominant for RNTs **13** and **14** as the chiral centres were further away from the chromophores (Figures 3.80 and 3.81). Studying the CD effects for R-TBL (**15**) and S-TBL (**16**) RNTs was more successful since the point of chirality was closer to the chromophores. R-TBL and S-TBL have mirror-image structures and in principle, their RNTs should exhibit opposite supramolecular chirality³ (Figures 3.82 and 3.83).

In both cases, CD measurements after 1 day of aging resulted in intense CEs. However only R-TBL was suitable for our CD study as S-TBL RNTs displayed mostly negative CEs, which was hard to differentiate from the artifactual CD (Figure 3.83). R-TBL RNTs initially showed mostly positive CEs after 1 day of aging (Figure 3.82). This CD signal can be considered to arise from anisotropy due to the chiral centre within the motif. This is because upon VT-CD, the CD intensity at 40 °C is lower than that obtained at 10 °C, which can be related to a phenomenon similar to the melting of DNA (Figure 3.84). The signal arising from the anisotropy in the monomer was gradually taken over by the artifactual negative monosignate CD. This is apparent from the decrease in intensity of the CD signal at 10 °C as the sample was aged from 1 to 3 days. In addition, a more

positive CD signal was observed for the 3-day solution at 40 °C during the VT-CD experiment.

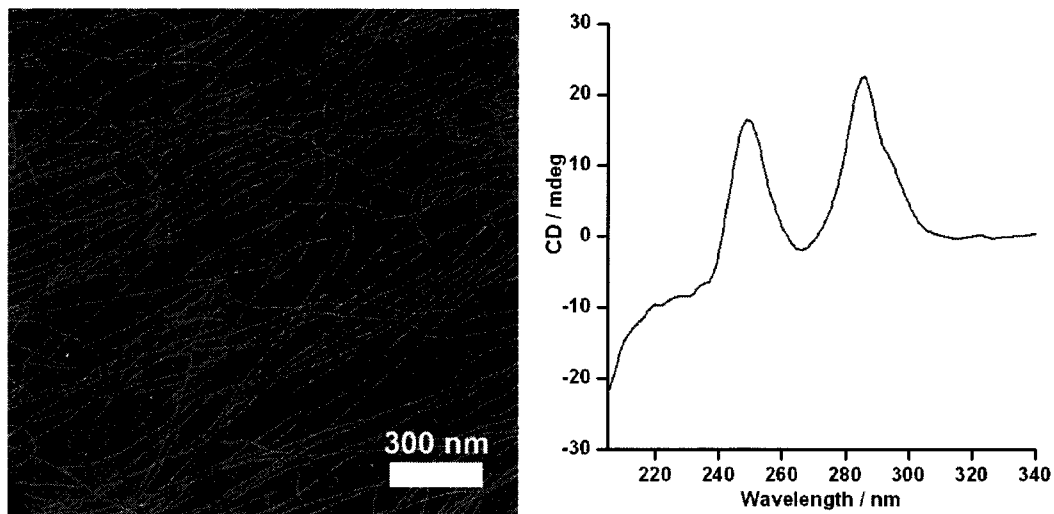


Figure 3.82: SEM image of the HCl salt of R-TBL (15) (left) and CD signal at 10 °C (right) after 1 day of aging in methanol.

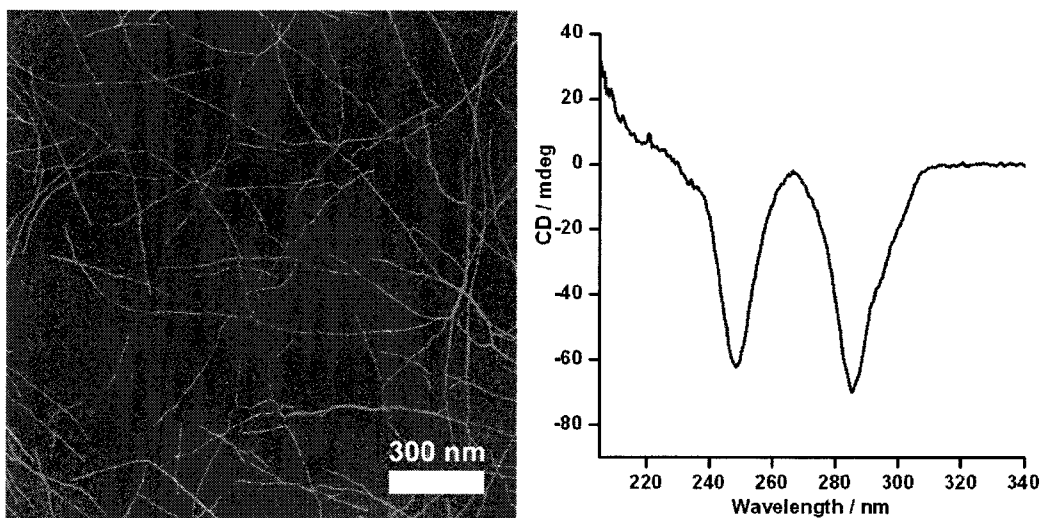


Figure 3.83: SEM image of the HCl salt of S-TBL (16) (left) and CD signal at 10 °C (right) after 1 day of aging in methanol.

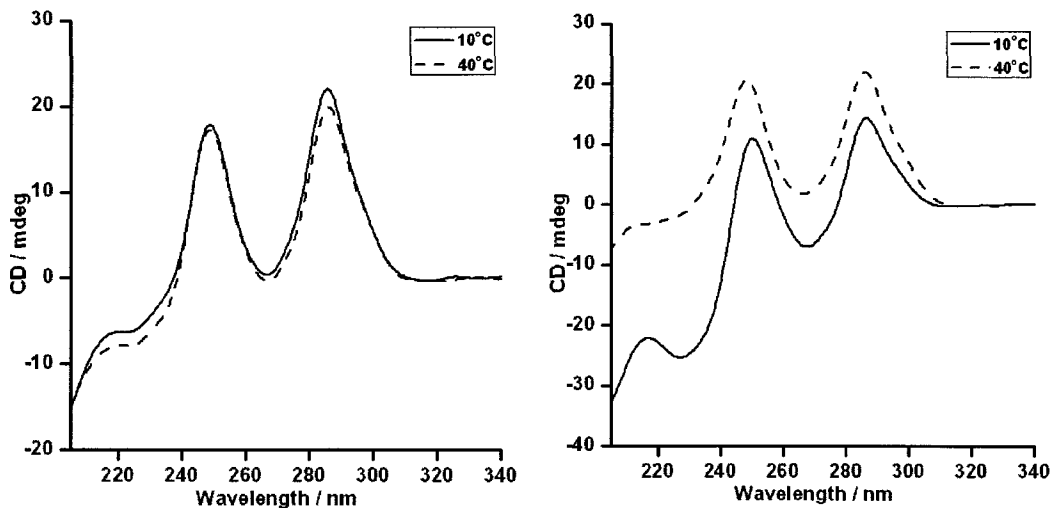


Figure 3.84: VT-CD spectra of the HCl salt of R-TBL in methanol for a 1-day aged solution (left) and for a 3-day aged solution (right).

As the sample was aged for a longer time, the positive CEs turned into an exclusively monosignate negative CD signal, which underwent thermo-reversible CD switch at 40 °C (Figure 3.85), similar to what was observed for But-TBL and related RNTs.

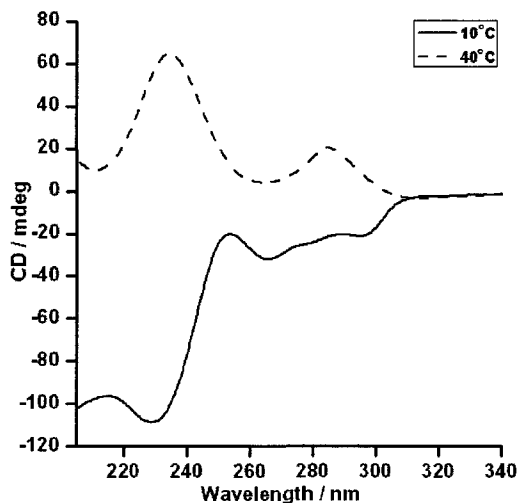


Figure 3.85: VT-CD spectra of the HCl salt of R-TBL in methanol for a two-month aged solution.

This experiment has allowed us to establish that the CD effects are present for both the achiral and chiral twin RNTs (unstirred samples). The only way these two groups seems to differ is that for the achiral RNTs only the artifactual chirality (macroscopic chirality from convective flows coupled with LD and LB) is observed, while in the case of the chiral RNTs the CD signal is a combination of the intrinsic chirality resulting from molecular anisotropy and artifactual chirality of the twin RNTs system.

One way to suppress the artifactual component of CD for the intrinsically chiral RNTs was to control the length of the RNTs, thus restricting the degree of alignment. This was possible by using the monomers as the TFA salts, whereby the resulting RNTs are much shorter and are devoid of artifacts when recording their CD activity. Figures 3.86-3.89 show the morphologies and CD signals of the RNTs with trifluoroacetate counterions, recorded at 10 °C in methanol.

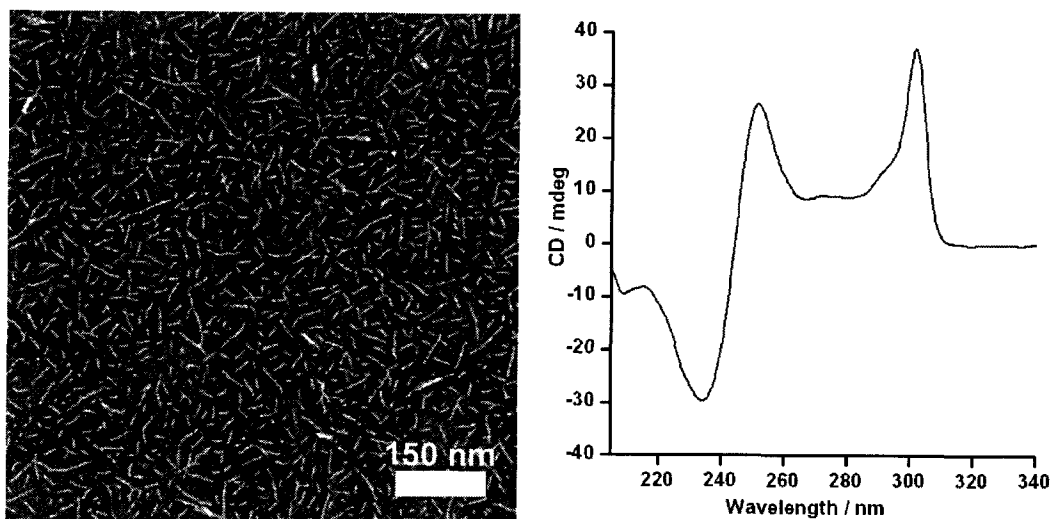


Figure 3.86: SEM image of the TFA salt of G0 in methanol (left) aged for 2 days and its CD (right) 14 days of aging.

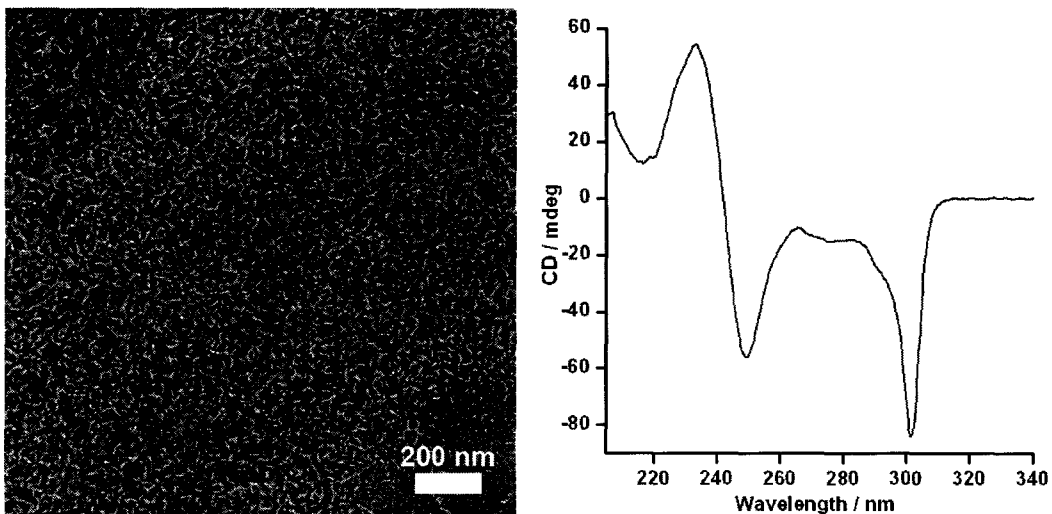


Figure 3.87: SEM images of the TFA salt of K-TBL in methanol (left) for 1 day, CD after 14 days of aging.

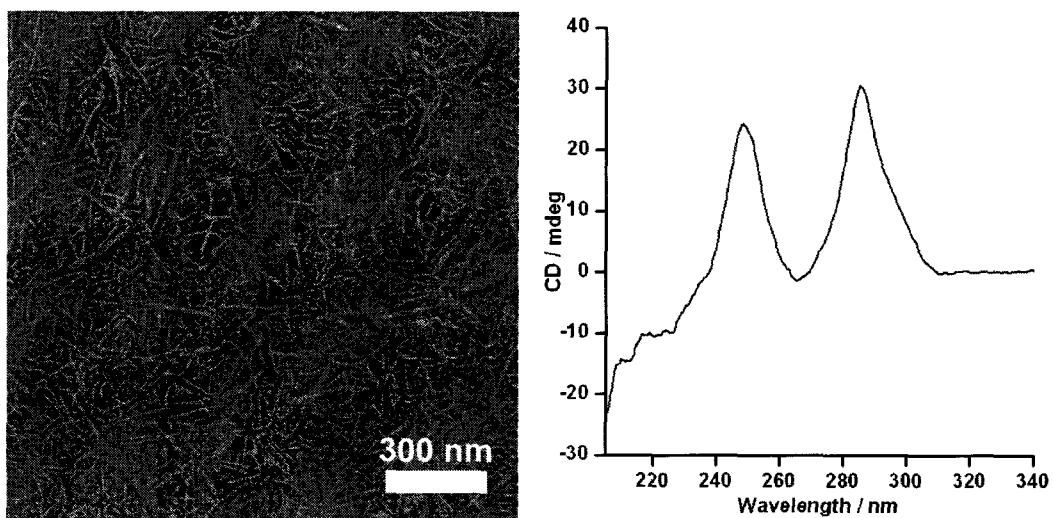


Figure 3.88: SEM images of the TFA salt of R-TBL in water (left) and in methanol (right).

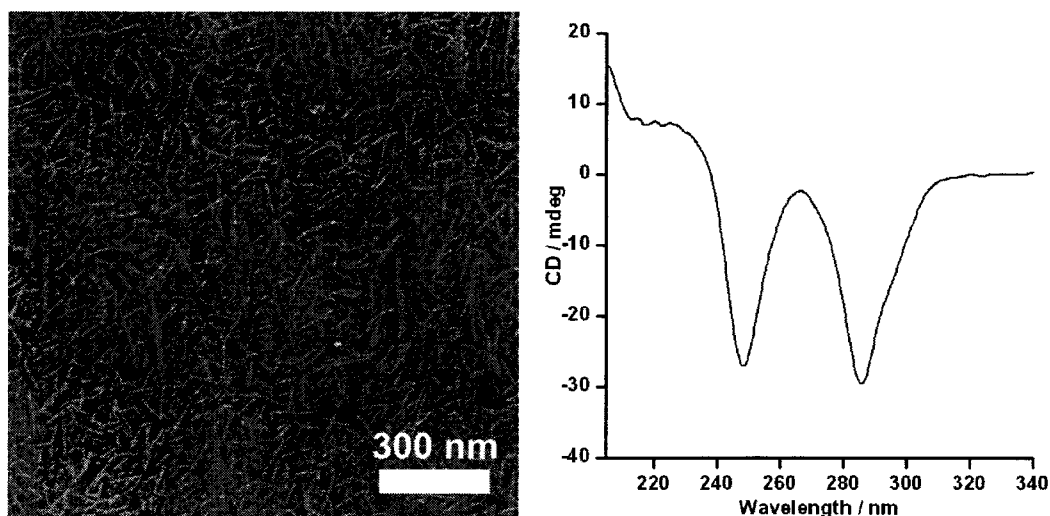


Figure 3.89: SEM images of the TFA salt of S-TBL in water (left) and in methanol (right).

3.14. Conclusion

An achiral molecule, shown to self-assemble into RNTs, gave an unexpected CD signal in methanol at 10 °C. The CD profiles at 10 and 40 °C were thermo-reversible and mirror-image. We demonstrated that the presence of CD for these samples was not a random process, but rather a consequence of self-assembly. These CD effects amplified with RNT growth, but were absent when RNT growth was sluggish or disrupted. These CD effects were presented for a number of achiral twin RNT forming analogues. RNTs derived from the single G \wedge C motif failed to show similar CD activity. With the exception of one module (ethyl-substituted derivative on the exocyclic nitrogen, which formed shorter nanostructures), the RNTs derived from the modified core structure also showed similar CD properties.

These achiral RNTs also displayed mirror-image thermo-reversible CD signals when the samples were stirred in the clockwise and counter-clockwise directions. The Mueller matrix approach was adopted to verify the authenticity of the CD signals and it was found that macroscopic factors such as vortex produced true supramolecular chirality. While for the stirred solutions data from the commercial

and the custom-made instruments were in agreement, no measureable CD was detected for the unstirred solution on the home-built spectroscopic polarimeter in the absence of convective flows. The CD obtained on the commercial Jasco instrument for the unstirred samples was attributed to linear dichroism arising from the alignment of the long RNTs and the birefringence of the optical cell walls and the convective flows in the medium.

With the exception of a higher intensity upon stirring, the CD profiles obtained in the presence of convective or vortex flows were similar. This implies that temperature change and mechanically stirring create the same type of flow. The flows created during stirring are stronger, leading to more intense CEs. Simulations are currently being run to obtain more details about the flows created in the medium under various conditions and how these flows may affect the supramolecular chirality.

Similar CD effects were also observed for unstirred chiral samples, which overshadowed the molecular anisotropy. One way to observe the supramolecular chirality of the chiral RNTs was to control the length of the nanostructures formed and this was done by self-assembling the TFA salt of the monomers. As such these shorter RNTs showed negligible alignment in solution and therefore displayed the true chirality of the system, which could be recorded by a commercial CD instrument.

In summary, this project involved the observation of unique optical properties present for a class of achiral and chiral twin RNTs. The study of this system established the presence of vortex induced supramolecular chirality for the achiral twin RNTs. It would be interesting to attempt organic reactions in the presence of these RNTs while stirring in the clockwise and counter-clockwise directions. Since these RNTs adopt a preferred helical sense on stirring in either direction, interaction of the reactants with the RNTs might result in a transfer of chirality from the supramolecular RNTs to the molecular products.

3.15. Experimental section

3.15.1. CD spectroscopy

All circular dichroism spectra were recorded on a JASCO J-810 spectropolarimeter. Samples were scanned from 350-205 (All samples except Acr-TBL) or 450-205 nm at a rate of 100 nm/min. The stock solutions were prepared at a concentration of 0.5 mg/mL (unless stated otherwise) in HPLC grade MeOH or MeOH-DMSO mixtures or dH₂O or dH₂O-MeOH mixtures and aged for different time intervals at room temperature. Their CD spectra were recorded at 10 °C by taking aliquots of the stock solutions and diluting them to 0.025 mg/mL using MeOH or other solvent mixtures as indicated. In most cases, the CD spectra were recorded in cuvettes of 3-5 mL with a pathlength of 1 cm. For the VT-CD experiments, the measurement was carried out from 10 to 50 °C, at a heating rate of 2 °C/min and the spectra were recorded at 5 or 10 °C intervals. For the stirring experiments on the Jasco instrument, magnetic stir bars of 2 x 7 mm dimensions were used.

3.15.2. DLS measurements

A dynamic light scattering experiment (DLS) was used to determine the relative sizes of the structures formed in methanol over time. The exact values for average hydrodynamic diameter in this DLS experiment do not reflect the actual sizes of the structures formed in methanol since the RNTs are non-spherical. However, the change in the average hydrodynamic correlated with a change in size of the RNTs. The sample was prepared by dissolving 1.5 mg in 3 mL of methanol by sonication for 10 min. The solution was then filtered into a 12 x 75 mm glass culture tube through a 0.2 µm pore diameter non-sterile PVFD membrane filter (Whatman) and capped. The growth of the RNTs was monitored by recording measurements at different time intervals at room temperature. DLS experiments were performed from 0.25-504 h (74 measurements were carried out at 24 different time intervals) using a Brookhaven BI-200SM Multi-angle Light Scattering System working at a 90° scattering angle at 23° C. The instrument is equipped with a 40 mW He-Ne laser ($\lambda = 632.8$ nm) and an avalanche photodiode

detector. Size distributions were calculated using an inverse Laplace transform algorithm, and the hydrodynamic radii were calculated using the Stokes-Einstein equation. The average hydrodynamic diameter values were plotted against time.

3.16. References

1. (a) Nakanishi, K.; Berova, N.; Woody, R. W. *Circular dichroism – Principles and applications*, Wiley-VCH, New York, **1994**. (b) Berova, N.; Di Bari, L.; Pescitelli, G. *Chem. Soc. Rev.* **2007**, *36*, 914-931. (c) Rodger, A.; Norden, B. *Circular dichroism & linear dichroism*, Oxford University Press, **1997**. (d) Fasman, G. D. *Circular dichroism and the conformational analysis of biomolecules*, Plenum Press, New York, **1996**. (e) Harada, N.; Nakanishi, K. *Circular Dichroic Spectroscopy Exciton Coupling in Organic Stereochemistry*; University Science Book: Mill Valley, CA, **1983**.
2. (a) Harada, N.; Saito, A.; Ono, H.; Gawronski, J.; Gawronska, K.; Sugioka, T.; Uda, H.; Kuriki, T. *J. Am. Chem. Soc.* **1991**, *113*, 3842-3850. (b) Wiesler, W. T.; Nakanishi, K. *J. Am. Chem. Soc.* **1990**, *112*, 5574-5583. (c) Berova, N.; Gargiulo, D.; Nakanishi, K.; Harada, N. *J. Am. Chem. Soc.* **1993**, *115*, 4769-4775. (d) Gargiulo, D.; Cai, G.; Ikemoto, N.; Bozhkova, N.; Odingo, J.; Berova, N.; Nakanishi, K. *Angew. Chem., Int. Ed.* **1993**, *32*, 888-891. (e) Gargiulo, D.; Ikemoto, N.; Odingo, J.; Bozhkova, N.; Iwashita, T.; Berova, N.; Nakanishi, K. *J. Am. Chem. Soc.* **1994**, *116*, 3760-3767. (f) Matile, S.; Berova, N.; Nakanishi, K.; Novkova, S.; Philipova, I.; Blagoev, B. *J. Am. Chem. Soc.* **1995**, *117*, 7021-7022. (g) Matile, S.; Berova, N.; Nakanishi, K.; Fleischhauer, J.; Woody, R. W. *J. Am. Chem. Soc.* **1996**, *118*, 5198-5206. (h) Rele, D.; Zhao, N.; Nakanishi, K.; Berova, N. *Tetrahedron* **1996**, *52*, 2759-2776.
3. (a) Amabilino, D. B. *Chirality at the Nanoscale*, Wiley-VCH, Weinheim, **2009**. (b) Lehn, J-M. *Supramolecular chemistry*, VCH, New York, **1995**. (c) Lough, W. J.; Wainer, I. W. *Chirality in Natural and Applied Science*, CRC Press, Oxford, **2002**. (d) Crego-Calama, M.; Reinhoudt, D. N. *Supramolecular Chirality, Top. Curr. Chem.*, **2006**. (e) Vazquez-Campos, S.; Crego-Calama, M.; Reinhoudt, D. N. *Supramolecular Chemistry* **2007**, *19*, 95-106. (f) Lee, C. C.; Grenier, C.; Meijer, E. W.; Schenning, A. P. H. *J. Chem. Soc. Rev.* **2009**, *38*, 671-683.

4. (a) Engelkamp, H.; Middelbeek, S.; Nolte, R. J. M. *Science* **1999**, *284*, 785-788. (b) Schenning, A. P. H. J.; Jonkheijm, P.; Peeters, E.; Meijer, E. W. *J. Am. Chem. Soc.* **2001**, *123*, 409-416. (c) Jeukens, C. R. L. P. N.; Jonkheijm, P.; Wijnen, F. J. P.; Gielen, J. C.; Christianen, P. C. M.; Schenning, A. P. H. J.; Meijer, E. W.; Maan, J. C. *J. Am. Chem. Soc.* **2005**, *127*, 8280-8281.
5. (a) Green, M. M.; Peterson, N. C.; Sato, T.; Teramoto, A.; Cook, R.; Lifson, S. *Science* **1995**, *268*, 1860-1866. (b) Green, M. M.; Rediy, M. P.; Johnson, R. J.; Darling, G.; O'leary, D. J.; Willson, G. *J. Am. Chem. Soc.* **1989**, *111*, 6452-6454. (c) Palmans, A. R. A.; Vekemans, J. A. J. M.; Havinga, E. E.; Meijer, E. W. *Angew. Chem. Int. Ed. Engl.* **1997**, *36*, 2648-2651. (d) Brunsveld, L.; Meijer, E. W.; Prince, R. B.; Moore, J. S. *J. Am. Chem. Soc.* **2001**, *123*, 7978-7984. (e) Prince, R. B.; Moore, J. S.; Brunsveld, L.; Meijer, E. W.; *Chem. Eur. J.* **2001**, *7*, 4150-4154. (f) Brunsveld, L.; Lohmeijer, B. G. G.; Vekemans, J. A. J. M.; Meijer, E. W. *Chem Commun.* **2000**, 2305-2306. (g) Brunsveld, L.; Vekemans, J. A. J. M.; Hirschberg, J. H. K. K.; Sijbesma, R. P.; Meijer, E. W. *Proc. Natl. Acad. Sci.* **2002**, *99*, 4977-4982. (h) Schenning A. P. H. J.; Kilbinger, A. F. M.; Biscarini, F.; Cavallini, M.; Cooper, H. J.; Derrick, P. J.; Feast, W. J., Lazzaroni, R.; Leclere, Ph.; McDonell, L. A.; Meijer, E. W.; Meskers, S. C. J. *J. Am. Chem. Soc.* **2002**, *124*, 1269-1275. (i) El-ghayoury, A.; Schenning A. P. H. J.; van Hal, P. A.; van Duren, J. K. J.; Janssen, R. A. J.; Meijer, E. W. *Angew. Chem. Int. Ed.* **2001**, *40*, 3660-3663. (j) Brunsveld, L.; Schenning, A. P. H. J.; Broeren, M. A. C.; Janssen, H. M.; Vekemans, J. A. J. M.; Meijer, E. W. *Chem. Lett.* **2000**, 292-293.
6. (a) Cram, D. J. *Angew. Chem., Int. Ed.* **1988**, *27*, 1009-1020. (b) Lehn, J.-M. *Angew. Chem., Int. Ed.* **1988**, *27*, 89-112. (c) Schneider, H.-J.; Dürr, H.; Lehn, J.-M., Eds. *Frontiers in Supramolecular Organic Chemistry and Photochemistry*; VCH: Weinheim, **1988**. (d) Pirkle, W.; Pochapsky, T. C. *Chem. Rev.* **1989**, *89*, 347-362. (e) Rebek, J. Jr. *Angew. Chem., Int. Ed. Engl.* **1990**, *29*, 245-255. (f) Seel, C.; Vögtle, F. *Angew. Chem., Int. Ed.* **1992**, *31*, 528-549. (g) Webb, T. H.; Wilcox, C. S. *Chem. Soc. Rev.* **1993**, 383-395. (h)

- Böhmer, V. *Angew. Chem. Int. Ed.* **1995**, *34*, 713-745. (i) Kirby, A. J. *Angew. Chem., Int. Ed.* **1996**, *35*, 706-724. (j) Bender, M. L.; Komiyama, M. *Cyclodextrin Chemistry*; Springer-Verlag: New York, **1977**. (k) Breslow, R. *Acc. Chem. Res.* **1980**, *13*, 170-177. (l) Tabushi, I. *Acc. Chem. Res.* **1982**, *15*, 66-72. (m) Li, S.; Purdy, W. C. *Chem. Rev.* **1992**, *92*, 1457-1470. (n) Wenz, G. *Angew. Chem., Int. Ed.* **1994**, *33*, 803-822. (o) Rekharsky, M. V.; Goldberg, R. N.; Schwarz, F. P.; Tewari, Y. B.; Ross, P. D.; Yamashoji, Y.; Inoue, Y. *J. Am. Chem. Soc.* **1995**, *117*, 8830-8840. (p) Diederich, F. *Angew. Chem., Int. Ed.* **1988**, *27*, 362-386. (q) Yashima, E.; Matsushima, T.; Okamoto, Y.; *J. Am. Chem. Soc.* **1997**, *119*, 6345-6359. (r) Yashima, E.; Maeda, K.; Okamoto, Y. *Science* **1999**, *399*, 449-451.
7. (a) Gutsche, C. D. *Calixarenes*; Royal Society of Chemistry: Cambridge, UK, **1989**. (b) Gutsche, C. D.; Iqbal, M.; Nam, K. S.; See, K.; Alam, I. *Pure Appl. Chem.* **1989**, *60*, 483-488. (c) Diamond, D.; McKervey, M. A. *Chem. Soc. Rev.* **1996**, 15-24. (d) Takeshita, M.; Shinkai, S. *Bull. Chem. Soc. Jpn.* **1995**, *68*, 1088-1097.
8. (a) Whitesides, G. M.; Simanek, E. E.; Mathias, J. P.; Seto, C. T.; Chin, D. N.; Mammen, M.; Gordon, D. M. *Acc. Chem. Res.* **1995**, *28*, 37-44. (b) Seto, C. T.; Whitesides, G. M., *J. Am. Chem. Soc.* **1990**, *112*, 6409-6411. (c) Zerkowski, J. A.; Seto, C. T.; Wierda, D. A.; Whitesides, G. M. *J. Am. Chem. Soc.* **1990**, *112*, 9025-9026. (d) Seto, C. T.; Whitesides, G. M. *J. Am. Chem. Soc.* **1991**, *113*, 712-713. (e) Whitesides, G. M.; Mathias, J. P.; Seto, C. T. *Science* **1991**, *254*, 1312-1319. (f) Seto, C. T.; Whitesides, G. M. *J. Am. Chem. Soc.* **1993**, *115*, 1330-1340. (g) Seto, C. T., Mathias, J. P.; Whitesides, G. M. *J. Am. Chem. Soc.* **1993**, *115*, 1321-1329. (h) Mathias, J. P.; Simanek, E. E.; Seto, C. T.; Whitesides, G. M. *Angew. Chem. Int. Ed.* **1993**, *32*, 1766-1769. (i) Zerkowski, J. A.; Seto, C. T.; Wierda, D. A.; Whitesides, G. M.; *J. Am. Chem. Soc.* **1994**, *116*, 2382-2391. (j) Zerkowski, J. A., Mathias, J. P. and Whitesides, G. M., *J. Am. Chem. Soc.* **1994**, *116*, 4305-4315. (k) Mathias, J. P.; Seto, C. T.; Simanek, E. E.; Whitesides, G. M. *J. Am. Chem. Soc.* **1994**, *116*, 1725-1736.

9. (a) Prins, L. J.; De Jong, F.; Timmerman, P.; Reinhoudt, D. N. *Nature* **2000**, *408*, 181-184. (b) Prins, L. J.; Jolliffe, K. A.; Hulst, R.; Timmerman, P.; Reinhoudt, D. N. *J. Am. Chem. Soc.* **2000**, *122*, 3617-3627. (c) Prins, L. J.; Huskens, J.; De Jong, F.; Timmerman, P.; Reinhoudt, D. N. *Nature* **1999**, *398*, 498-502. (d) Prins, L. J.; Timmerman, P.; Reinhoudt, D. N. *J. Am. Chem. Soc.* **2001**, *123*, 10153-10163. (e) Vreekamp, R. H.; Van Duynhoven, J. P. M.; Hubert, M.; Verboom, W.; Reinhoudt, D. N. *Angew. Chem. Int. Ed.* **1996**, *35*, 1215-1218. (f) Timmerman, P.; Vreekamp, R. H.; Hulst, R.; Verboom, W.; Reinhoudt, D. N.; Rissanen, K.; Udachin, K. A.; Ripmeester, J. *Chem. Eur. J.* **1997**, *3*, 1823-1832. (g) Crego Calama, M.; Fokkens, R.; Nibbering, N. M. M.; Timmerman, P.; Reinhoudt, D. N. *Chem. Commun.* **1998**, 1021-1022.
10. (a) Fenniri, H.; Deng, B. L.; Ribbe, A. E.; Hallenga, K.; Jacob, J.; Thiyagarajan, P. *Proc. Natl. Acad. Sci.* **2002**, *99*, 6487-6492. (b) Fenniri, H.; Mathivanan, P.; Vidale, K. L.; Sherman, D. M.; Hallenga, K.; Wood, K. V.; Stowell, J. G. *J. Am. Chem. Soc.* **2001**, *123*, 3854-3855. (c) Fenniri, H.; Deng, B. L.; Ribbe, A. E. *J. Am. Chem. Soc.* **2002**, *124*, 11064-11072.
11. (a) Jacques, J.; Collet, A.; Wilen, S. H. *Enantiomers, Racemates, Resolutions* Wiley, New York, **1981**. (b) Kondepudi, D. K.; Kaufman, R. J.; Singh, N.; *Science* **1990**, *250*, 975-976. (c) Kondepudi, D. K.; Bullock, K. L.; Digits, J. A.; Hall, J. K.; Miller, J. M. *J. Am. Chem. Soc.* **1993**, *115*, 10211-10216. (d) Kondepudi, D. K.; Laudadio, J.; Asakura, K. *J. Am. Chem. Soc.* **1999**, *121*, 1448-1451.
12. (a) Schwartz, D. K.; Viswanathan, R.; Zasadzinski, J. A. N.; *Phys. Rev. Lett.* **1993**, *70*, 1267-1270. (b) Vanakaras, A. G.; Photinos, D. J. *J. Phys. Rev. E* **1998**, *57*, R4875-R4878. (c) Hough, L. E.; Jung, H. T.; Krueerke, D.; Heberling, M. S.; Nakata, M.; Jones, C. D.; Chen, D.; Link, D. R.; Zasadzinski, J.; Heppke, G.; Rabe, J. P.; Stocker, W.; Koerblova, E.; Walba, D. M.; Glaser, M. A.; Clark, N. A. *Science*, **2009**, *325*, 456-460.
13. Ribo, J. M.; Crusats, J.; Sagues, F.; Claret, J.; Rubires, R. *Science*, **2001**, *292*, 2063-2066.

14. Tsuda, A.; Alam M. A.; Harada, T.; Yamaguchi, T.; Ishii, N.; Aida, A. *Angew. Chem. Int. Ed.* **2007**, *46*, 8198-8202.
15. Wolffs, M.; George, S.J.; Tomovic, Z.; Meskers, S.C.J.; Shenning, A.; Meijer E.W. *Angew. Chem. Int. Ed.* **2007**, *46*, 8203-8205.
16. The synthesis of the achiral twin RNT monomers is described in the second chapter (Section 2.2) of this thesis work.
17. The self-assembly behaviour of these RNTs are described in the second chapter (Section 2.3) of this thesis work.
18. Davis, T. M.; McFail-Isom, L.; Keane, E.; Williams L. D. *Biochemistry* **1998**, *37*, 6975-6978.
19. (a) Gadde, S.; Batchelor, E. K.; Kaifer, A. E.; *Chem. Eur. J.* **2009**, *15*, 6025-6031. (b) Eisfeld A.; Briggs, J. S. *Chem. Phys.* **2006**, *324*, 376-384. (c) Lau, V.; Heyne, B. *Chem Comm.* **2010**, *46*, 3595-3597.
20. (a) Jelley, E.E. *Nature* **1936**, *138*, 1009-1010. (b) Scheibe G.; *Angewandte Chem.* **1937**, *50*, 51.
21. (a) Kasha, L. *Radiation Res.* **1963**, *20*, 55-71. (b) M. Kasha, H. R. Rawls and M. A. El-Bayoumi, *Pure Appl. Chem.* **1965**, *11*, 371-392.
22. (a) Hayward, L. D. *Chem. Phys. Lett.* **1975**, *33*, 53-56. (b) Dragomir, I.; Hagarman, A.; Wallace, C.; Schweitzer-Stenner R. *Biophysical* **2007**, *92*, 989-998. (c) Okamoto, Y.; Matsuda, M.; Nakano, T.; Yashima, E. *J. Polym. Sci. Part A: Polym. Chem.* **1994**, *32*, 309-315.
23. Morales, G.; Raez, J.; Yamazaki, T.; Motkuri, R. K.; Kovalenko, A.; Fenniri, H. *J. Am. Chem. Soc.* **2005**, *127*, 8307-8309.
24. The synthesis of the K-TBL monomer is described in the second chapter (Section 2.2, Figure 2.7) of this thesis work.
25. The study of solvent ratios of methanol and water on length and abundance of the RNTs is presented in the second chapter (Section 2.3.1) of this thesis work.
26. A detailed study on length and abundance of the RNTs is presented in the second chapter (Section 2.3.1) of this thesis.

27. Johnson, R. S.; Yamazaki, T.; Kovalenko, A.; Fenniri, H. *J. Am. Chem. Soc.* **2007**, *129*, 5735-5743.
28. (a) Kovalenko, A. Three-dimensional RISM theory for molecular liquids and solid-liquid interfaces, in: *Molecular Theory of Solvation*, Hirata, F. (ed.) Series: *Understanding Chemical Reactivity*, Vol.24, Mezey, P.G. (ed.) Kluwer Academic Publishers, Dordrecht, (2003), pp.169-275. (b) A. Kovalenko, A.; Hirata, F. *J. Chem. Phys.* **1999**, *110*, 10095-10112. (c) Kovalenko, A.; Hirata, F. *J. Chem. Phys.* **2000**, *112*, 10391-10417.
29. The synthesis of analogues of But-TBL with modified core structure is described in the second chapter (Section 2.3.3.1) of this thesis work.
30. (a) Schellman, J.; Jensen, H. P. *Chem. Rev.* **1987**, *87*, 1359-1399. (b) Francke, C.; Otte, S. C. M.; van der Heiden, J. C.; Spurious, A. J. *Biochim. Biophys. Acta* **1994**, *1186*, 75-80.
31. These experiments were carried out by our collaborators Oriol Arteaga and Professor Josep Ribo from University of Barcelona, Spain.
32. (a) Jellison, G. E.; Modine F. A. *Appl. Opt.* **1997**, *36*, 8190-8198. (b) Jellison, G. E.; Modine F. A. *Appl. Opt.* **1997**, *36*, 8184-8189.
33. Tunis-Schneider, M. J. B.; Maester, M. F. *J. Mol. Biol.* **1970**, *52*, 521-541.
34. Jones R. C. *J. Opt. Soc. Am.* **1948**, *38*, 671-683.
35. Arteaga, O.; Canillas, A. *J. Opt. Soc. Am. A*, **2009**, *26*, 783-793.
36. Arteaga, O.; Canillas, A. *Opt. Lett.* **2010**, *35*, 559-561.
37. (a) Gillgren, H.; Stenstam, A.; Ardhammar, M.; Nordón, B.; Sparr, E.; Ulvenlund, S. *Langmuir* **2002**, *18*, 462-469. (b) Ohira, A.; Okoshi, K.; Fujiki, M.; Kunitake, M.; Naito, M.; *Adv. Mater.* **2004**, *16*, 1645-1650.
38. (a) Shindo, Y.; Ohmi, Y. *J. Am. Chem. Soc.* **1985**, *107*, 91-97. (b) Shindo, Y.; Nakagawa, M. *Rev. Sci. Instrum.* **1985**, *56*, 32-39. (c) Shindo, Y.; Nakagawa, M.; Ohmi, Y. *Appl. Spectrosc.* **1985**, *39*, 860-868. (d) Shindo, Y. *Appl. Spectrosc.* **1985**, *39*, 713-715.
39. Arteaga, O.; Canillas, A.; Purrello, R.; Ribo, J. M. *Opt. Lett.* **2009**, *34*, 2177-2179.

40. These CD measurements were carried out by our collaborator, Dr Nathan Cowiesson, from Monash University in Australia.
41. (a) Dougherty, R. C. *J. Am. Chem. Soc.* **1980**, *102*, 380-381. (b) Edwards, D.; Cooper, K.; Ralph R. C. *J. Am. Chem. Soc.*, **1980**, *102*, 381-382.
42. (a) Escudero, C.; El-Hachemi, Z.; Crusats, J.; Ribo, J. M. *J. Porphyrins Phthalocyanines* **2005**, *9*, 852-863. (b) Monti, D.; Venanzi M.; Russo, M.; Bussetti, G.; Goletti, C; Montalti, M.; Zaccheroni, N.; Prodi, L.; Rella, R.; Manera, M. G.; Di Natale C.; Paolesse, R. *New J. Chem.* **2004**, *28*, 1123-1128.
43. The synthesis of the chiral monomers is described in the second chapter (Section 2.2) of this thesis.

Chapter 4

Solvent effects on the self-assembly of RNTs

4.1. Introduction

The creation of supramolecular structures from the interaction of two or more neutral or charged species, held together by noncovalent intermolecular forces, has been thoroughly investigated due to its importance of molecular recognition in biochemical processes.¹ Such activities have been primarily observed in aqueous medium, however other solvents are also known to have a great impact on the stability of such superstructures.² The function of such solvent systems is not just limited to the dissolution of the solute in the medium. They also contribute immensely to the existence and stability of such architectures by favourable solute-solvent interactions.

The first RNT system made up of a $G\wedge C^3$ moiety was formulated from a water-soluble module, K1 (Figure 4.1).⁴ This molecule possessed an amino acid fragment (L-lysine) attached via an ethylene linker to the $G\wedge C$ core. Another important RNT system that followed from the Fenniri group was the G0 module.⁵ The latter had two $G\wedge C$ bases connected to an ethylene linker, which was in turn linked to the carboxy terminus of the lysine moiety.

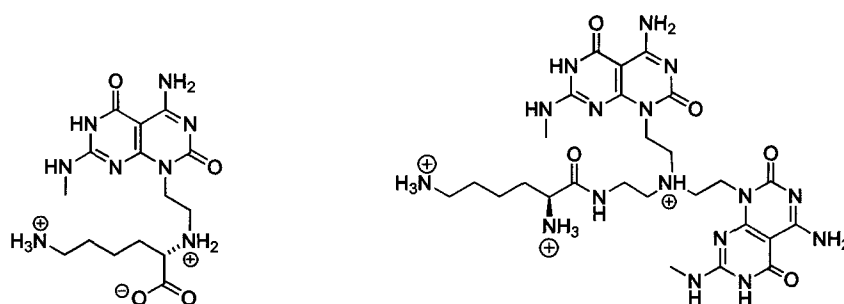


Figure 4.1: Water-soluble K1 module bearing a single $G\wedge C$ unit (left) and G0 analogue with two $G\wedge C$ units (right). Both motifs contain a L-lysine pendant.

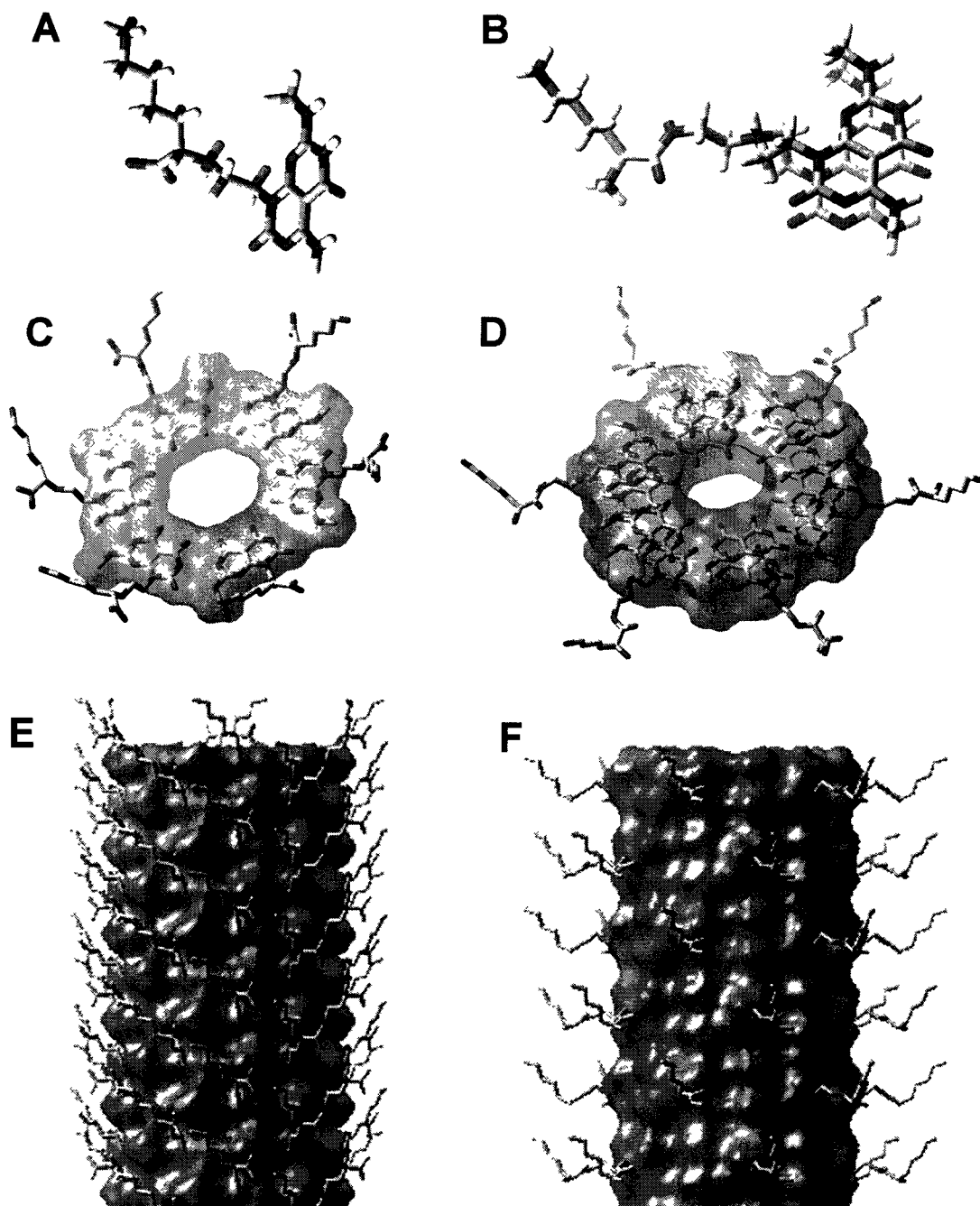


Figure 4.2: Self-assembling modules K1 (A) and G0 (B). Single (C) and twin (D) rosettes obtained from the self-assembly of K1 and G0, respectively. RNTs obtained from K1 (E) and G0 (F). The figures are not drawn to scale.

While both molecules had the built-in ability to form RNTs in solution, G0 had a number of advantages over K1 - (a) the functional group density and the net

charge were lower (b) the RNTs had enhanced stability as a result of preorganization, increased amphiphilic character, and greater number of H-bonds per module, (c) the rosettes were maintained by 36 H-bonds instead of 18, and (d) the RNTs were sterically less congested, resulting in lower electrostatic repulsion. Nevertheless, both modules formed RNTs readily in solution and the mode by which they self-assembled are shown in Figure 4.2.

Another molecule (**4.1**) possessing some of the structural features of the above two compounds was synthesized.^{5,6} According to the initial studies on this compound, it was found that this motif, which had only one G \wedge C base as K1 and similar lysine attachment as G0, did not self-assemble in solution. One of the hypotheses put forward to explain this behaviour was the possibility of intramolecular hydrogen bonding, which could prevent the cytosine face of the G \wedge C base from engaging in intermolecular hydrogen bonding as shown in Figure 4.3.⁶ Another possibility for the non-assembly of the monomers could be related to the structural (net charge of monomer) and environmental factors (such as solvent properties), which could dictate the stability and self-assembly of the RNTs. Compared to K1, which has net charge of +1, **4.1** has net charge of +3.

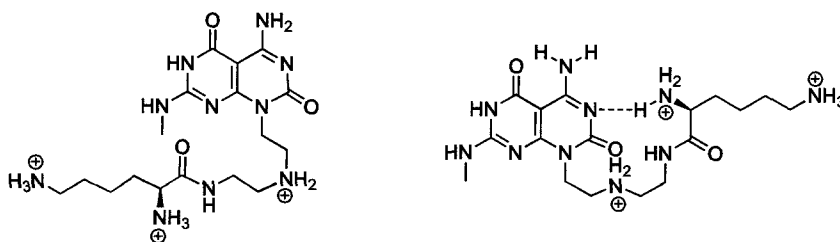


Figure 4.3: Structure of **4.1** and intramolecular hydrogen bonding, which could prevent the cytosine face of the G \wedge C base from engaging in intermolecular hydrogen bonding.

In this chapter we test the possible hypotheses resulting in the non-assembly of the monomers. In this process, other molecules possessing only one G \wedge C core, different side-chains and varying net charge were synthesized. The self-assembly

of these monomers were then investigated in various solvent systems. In addition, two dimensional nuclear magnetic resonance (2D-NMR) experiments were carried out to verify if the monomers were engaging in intramolecular hydrogen bonding. From these experiments, it was found that these monomers were not involved in intramolecular hydrogen bonding and exhibited nanostructures when they had minimal net charge or when they were self-assembled in hydrogen-bond acceptor (HBA) solvents.

4.2. Results

The table below shows all the molecules that are discussed in this chapter, along with their net charge.

Entry	Structure	Net charge	Entry	Structure	Net charge
4.1		+ 3	4.5		+ 1
4.2		+ 3	4.7		+ 1
4.3		+ 2	4.16		0

Figure 4.4: Table showing the molecules studied in this chapter

Molecule **4.3** was obtained upon deprotection of its precursor **2.21**⁸ using 95% TFA/thioanisole, and was subsequently converted to the hydrochloride salt via anion exchange in 88% yield (Figure 4.6). This analogue has a terminal ammonium group, which can act a H-bond donor to any structurally accessible H-bond acceptor site available on the G \wedge C core.

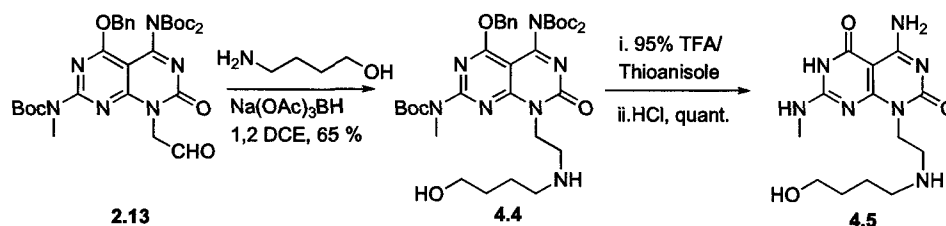


Figure 4.7: Synthetic scheme for G \wedge C analogue **4.5**

The commercially available 1,4 aminobutanol was reductively coupled with aldehyde **2.13**⁹ to afford **4.4** in 65% yield. The acid labile protecting groups were cleaved under acidic conditions, after which the TFA salt was converted to the hydrochloride salt via anion exchange in 95% yield (Figure 4.7). The analogue **4.5** has a terminal hydroxyl group, which possesses both H-bond donor and acceptor sites.

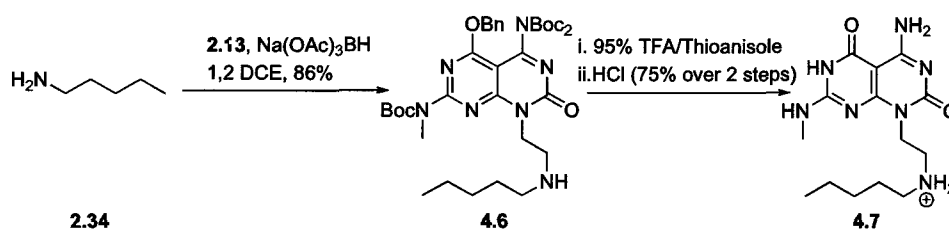


Figure 4.8: Synthetic scheme for G \wedge C analogue **4.7**

Commercially available pentylamine **2.34** was reductively coupled to aldehyde **2.13**⁹ to produce **4.6** in 86% yield. Removal of all protecting groups from compound **4.6** under acidic conditions, followed by anion exchange afforded the derivative **4.7** as the hydrochloride salt in 75% yield (Figure 4.8).

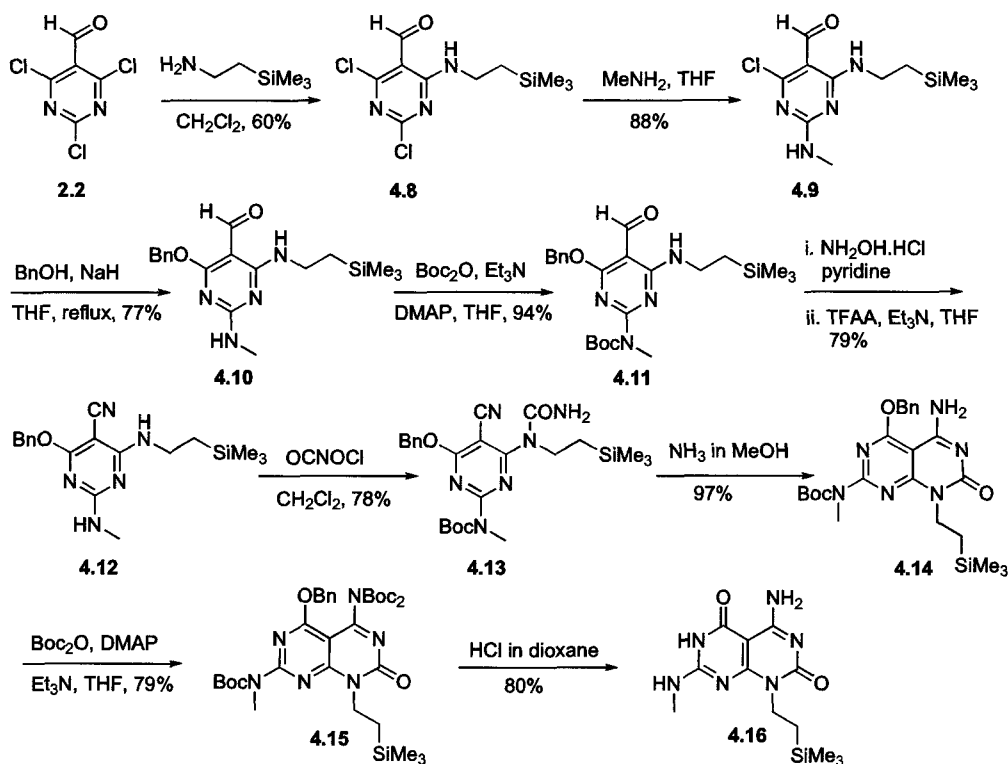


Figure 4.9: Synthetic scheme for GAC analogue 4.16

The monomer **4.16** was obtained as per the synthetic scheme shown in Figure 4.9.¹⁰ Nucleophilic aromatic substitution reaction of 2,4,6-trichloro-pyrimidine-5-carbaldehyde (**2.2**)⁹ to trimethylsilylethylamine hydrochloride afforded 2,4-dichloro-6-(2-(trimethylsilyl)ethylamino)pyrimidine-5-carbaldehyde (**4.8**). The latter was then subjected to another nucleophilic aromatic substitution reaction to afford 4-chloro-2-(methylamino)-6-(2-(trimethylsilyl)ethylamino)pyrimidine-5-carbaldehyde (**4.9**) in 88% yield. Subsequent reaction with benzyl alcohol under basic conditions produced 4-(benzyloxy)-2-(methylamino)-6-(2-(trimethylsilyl)ethylamino)pyrimidine-5-carbaldehyde (**4.10**). Selective Boc protection of the methylamine fragment in **4.10** gave rise to *t*-butyl 4-(benzyloxy)-5-formyl-6-(2-(trimethylsilyl)ethylamino)pyrimidin-2-yl(methyl) carbamate (**4.11**). Oxime synthesis followed by a dehydration process using trifluoroacetic anhydride yielded *t*-butyl 4-(benzyloxy)-5-cyano-6-(2-(trimethylsilyl)ethylamino)pyrimidin-2-yl(methyl) carbamate (**4.12**) in 79% over

2 steps. Reaction with *N*-chlorocarbonyl isocyanate produced *t*-butyl 4-(benzyloxy)-5-cyano-6-(1-(2-(trimethylsilyl)ethyl)ureido)pyrimidin-2-yl(methyl)carbamate (**4.13**), which was then cyclized in a methanolic solution of ammonia to give *t*-butyl 4-amino-5-(benzyloxy)-1,2-dihydro-1-(2-(trimethylsilyl)ethyl)-2-oxopyrimido[4,5-*d*]pyrimidin-7-ylmethylcarbamate (**4.14**). Deprotection of the protected derivative **4.15** under acidic conditions afforded 4-amino-7-(methylamino)-1-(2-(trimethylsilyl)ethyl)pyrimido[4,5-*d*]pyrimidine-2,5(1*H*,6*H*)-dione (**4.16**) in good yield.

4.2.2. Self-assembly

Similar to compound **4.1**, which did not show the formation of RNTs in water,^{5,6} modules **4.2** and **4.3** also did not form any nanostructures in the aqueous media. We therefore proceeded in studying the molecule **4.7**, which did not possess any hydrogen bond donor atom at the end of the side-chain.

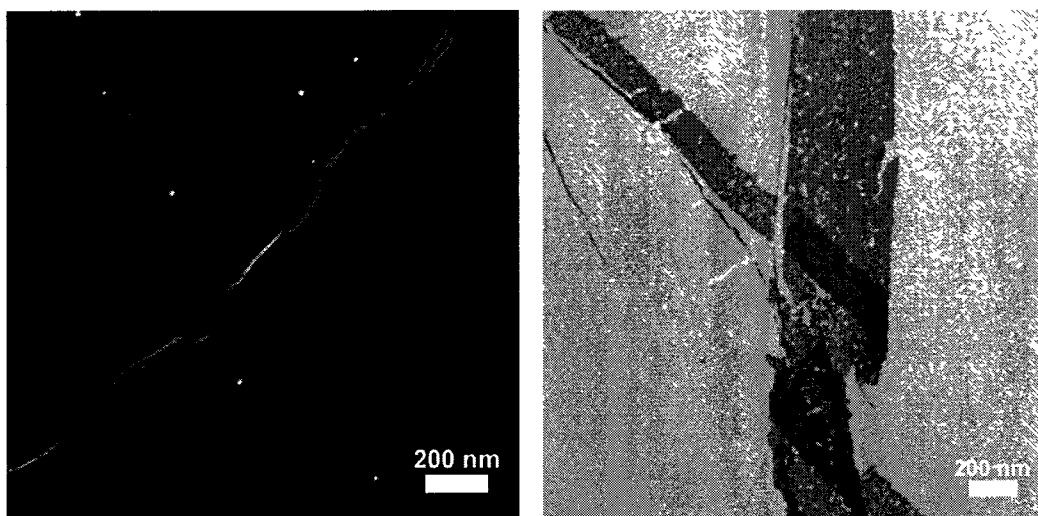


Figure 4.10: SEM images of **4.7** in water at a concentration of 0.33 mg/mL (left) and stained using 2% uranyl acetate solution in water (right, TE mode).

Attempts to self-assemble analogue **4.7** in water proved to be successful. A 1.0 mg/mL solution was prepared in water and the sample was aged for 1 day. An aliquot of the solution was then diluted to 0.33 mg/mL and was cast on carbon-coated TEM grid. Visualization of the latter revealed structures that resemble bundles or sheets of RNTs (Figure 4.10).

To improve the dispersion of the RNTs, the extent of aggregation of **4.7** in water was reduced by sonication of a more dilute nanotube solution. Sonication successfully dispersed the RNTs more evenly in the solution by breaking the intermolecular interactions between the RNTs (Figure 4.11).

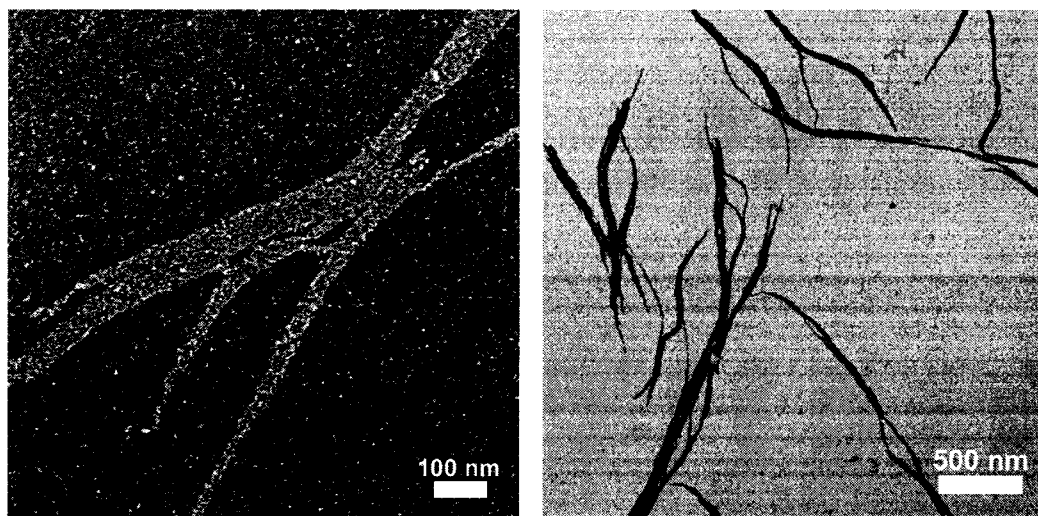


Figure 4.11: SEM images of **4.7** in water at a concentration of 0.1 mg/mL, stained with 2% uranyl acetate solution in water in SE mode (left) and in TE mode (right).

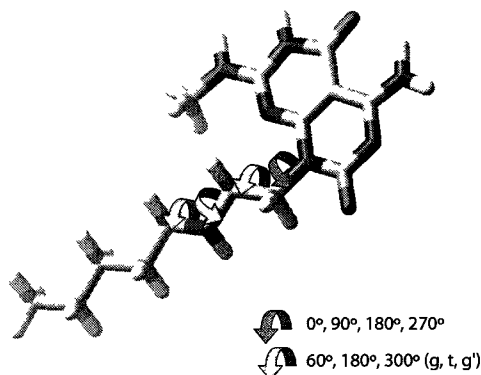


Figure 4.12: Initial conformations ($4 \times 3 \times 3 \times 3 = 108$) were generated by varying the dihedral angles around the four bonds indicated by arrows.

Molecular modeling was conducted by Dr Takeshi Yamazaki on compound **4.7**. In this process, 108 RNTs were generated with a staggered angle of -20° and the stacking distance of 4.8 \AA between the rosette rings (Figure 4.12). The RNT conformation was then optimized and RNTs composed of one to ten rosette stacks using the optimized conformer was generated using Macromodel and 3D-RISM theory.¹¹

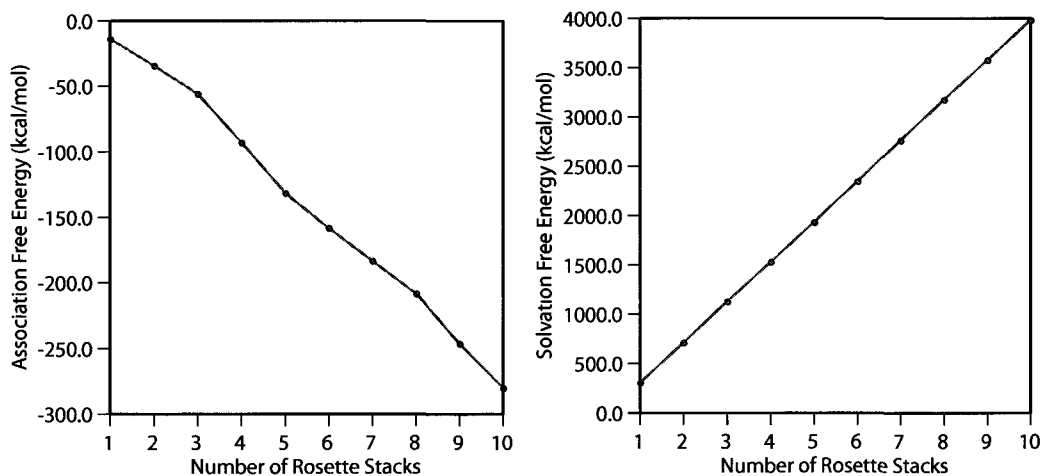


Figure 4.13: Association free energy (left) and solvation free energy (right) of the most stable RNT in water.

The association free energy and the solvation free energy were obtained for the most stable RNT in water (Figure 4.13). The negative trend for the association

free energy graph suggests that RNT formation of this motif in water is preferable with increasing number of rosettes. The opposite trend was observed for the solvation free energy of this RNT, which implies that water does not like to surround the RNT due to which this RNT tends to aggregate.

As seen for the RNT generated by molecular modeling in Figure 4.14, there is a dense network of aliphatic chains hanging around the nanotube. These side-chains are hydrophobic and therefore the RNTs arrange themselves in such a way as to minimize interactions with water molecules. The solvation free energy trend calculated for this RNT justifies the bundles and sheets of nanostructures observed by the microscopy techniques.

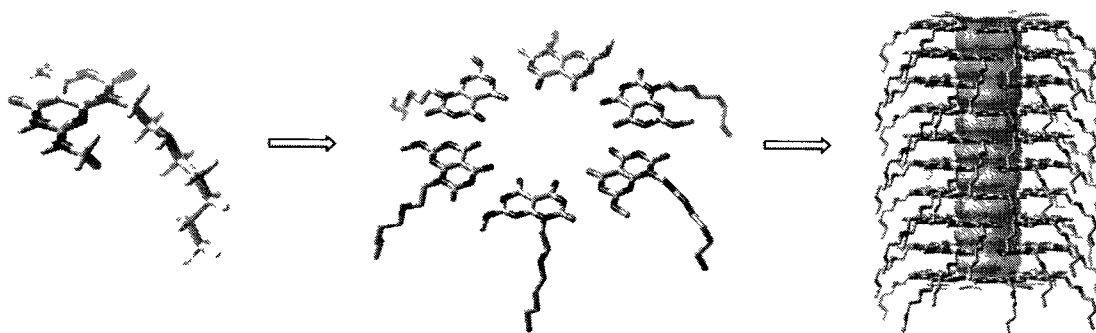


Figure 4.14: Formation of rosette and a nanotube from the assembly of the most stable conformer of molecule 4.7 in water.

Most of the RNTs made earlier have been known to self-assemble readily in both water and methanol, giving rise to long, abundant and well-dispersed nanostructures within hours of dissolution.^{2a,4-6,12} The formation of RNT in methanol are generally faster and give rise to longer nanostructures than in water due to the decreased solvation of the donor and acceptor sites on the GAC cores. However attempts to observe any nanostructures or other types of aggregates for 4.7 failed in methanol.

The self-assembly of compound **4.5** was also investigated in water and methanol. In water, no self-assembly was observed. The self-assembly process was attempted in methanol. A 0.5 mg/mL methanolic solution of **4.5** was prepared and aged for 2 days. The sample was then diluted to 0.05 mg/mL and deposited on a TEM grid. The sample was stained using a 2% uranyl acetate solution in methanol. The SEM images (Figure 4.15) depicted morphologies similar to rosette nanotubes, however, these nanostructures were not very long and well-dispersed as the rosette nanotubes resulting from the twin-base system.^{5,12}

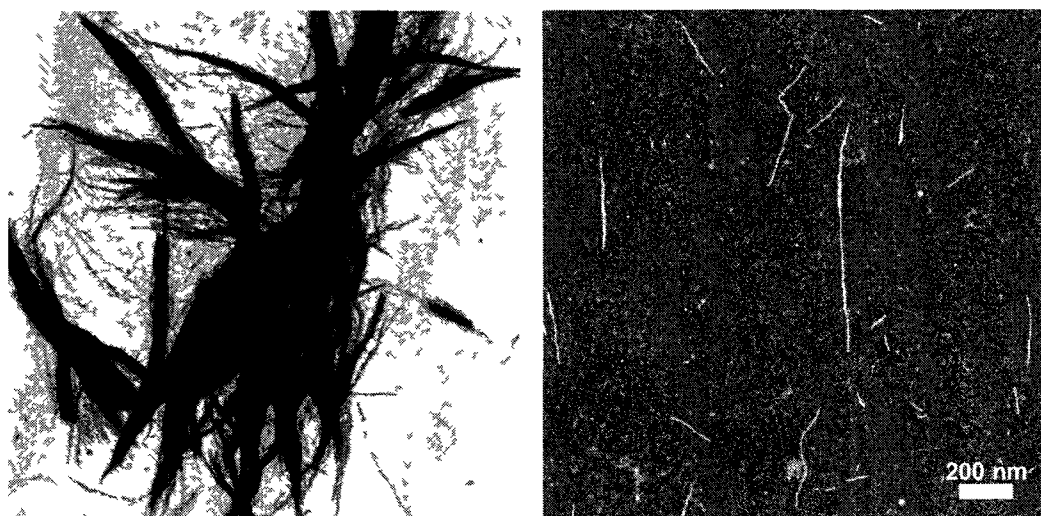


Figure 4.15: SEM images of **4.5** at a concentration of 0.05 mg/mL in methanol in TE mode (left) and in SE mode (right).

Unlike the SEM images, the AFM images obtained displayed a denser network of bundles of rosette nanotubes, when visualized on a mica substrate. This was presumably due to the stronger interactions (including hydrogen-bonding) between the hydroxyl group of the nanostructures and the mica substrate. For the sample cast on the TEM carbon grid, such favourable sample-substrate interactions were missing.

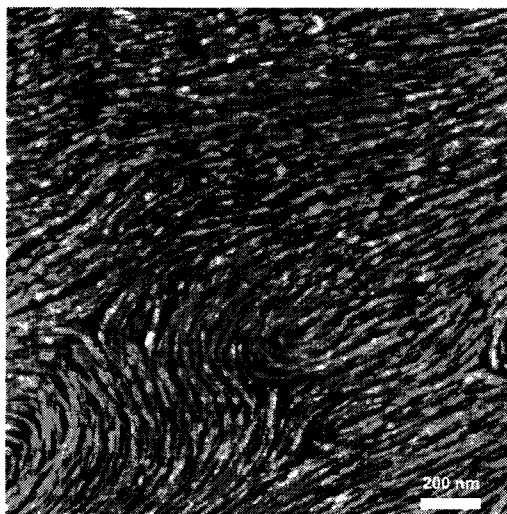


Figure 4.16: AFM image of **4.5** at a concentration of 0.05 mg/mL in methanol, cast on a freshly cleaved mica substrate.

The self-assembly of the neutral molecule **4.16** was also investigated. A 1.0 mg/mL solution of **4.16** was prepared in methanol and the sample was then allowed to age. Aliquots of that stock solution was diluted and then cast on carbon-coated TEM grids. Visualization of the cast samples using SEM revealed RNTs of high aspect ratio. Compared to the positively charged salts, this monomer gave rise to long and well-dispersed nanofibres as seen with the images obtained through SEM (Figure 4.17) and AFM imaging (Figure 4.18). Though we had expected the presence of aggregates in the aqueous medium, solubility issues related to compound **4.16** in water prevented its self-assembly.

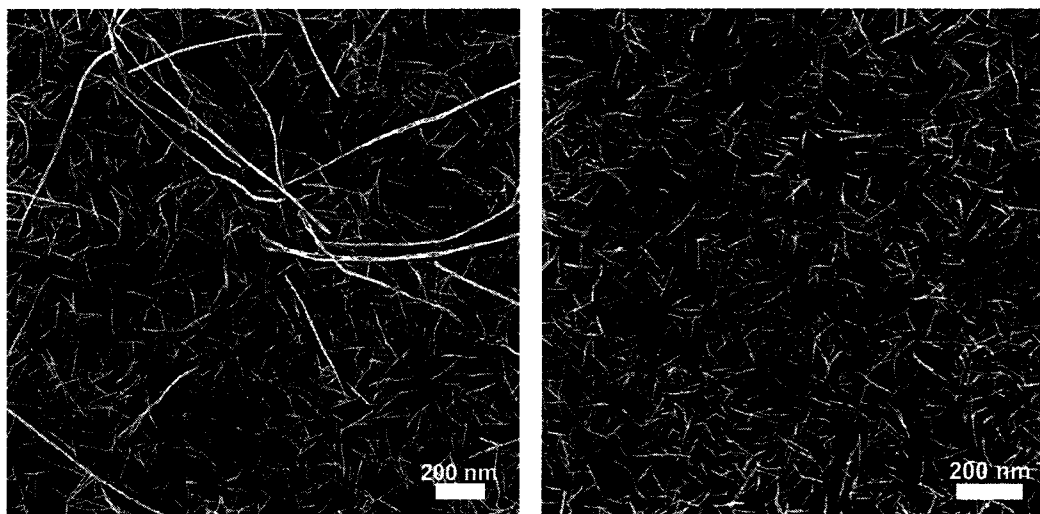


Figure 4.17: SEM images of compound **4.16** aged for 4 days in methanol and diluted to 0.2 mg/mL (left) and 0.1 mg/mL (right).



Figure 4.18: AFM images of compound **4.16** aged for 4 days in methanol and diluted to 0.2 mg/mL. Sample was cast on a mica substrate.

The sample was also imaged using scanning tunneling microscopy (STM). STM is a powerful tool, which is used to image surfaces at the atomic level.¹³ While we had tried STM imaging for other samples, the experiments were not very successful due to the non-conductivity of the samples. Compound **4.16** has silicon (a metalloid) atoms on the periphery of the RNTs, resulting in more electron tunneling between the tip and the sample, leading to a current that can be

measured. As the tip is moved across the sample, changes in current occur, which can be mapped into images.



Figure 4.19: STM images of compound **4.8** aged for 4 days in methanol and diluted to 0.2 mg/mL. Sample was cast on HOPG.

So far, whenever aqueous solutions of the monomers were prepared, the pH of the resulting solutions was acidic (pH ~ 4) since the compounds were isolated as hydrochloride salts. In an attempt to promote self-assembly of the monobase derivatives, their respective solutions of a concentration of 0.5 mg/mL were prepared in CAPS (0.05 M) buffer at pH 11. At this pH, most of the nitrogens would be unprotonated, thus reducing the charge repulsion, leading to promotion of self-assembly.⁵ Initial investigation of one-month old solutions, which were diluted to 0.05 mg/mL, showed aggregates only for compounds **4.5**, **4.7** and **4.16** (Figure 4.20). From the previous experiments at pH 4, only monomer **4.7** had shown aggregation.

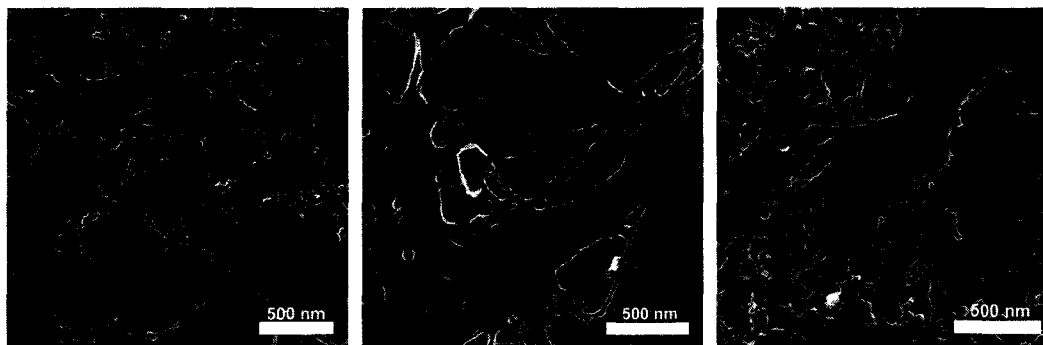


Figure 4.20: SEM images of **4.5** (left), **4.7** (centre) and **4.16** (right) at pH 11

So far, only the molecules with the lowest net charges (**4.5**, **4.7** and **4.16**) showed higher order aggregation. We proceeded in attempting the self-assembly of **4.1**, **4.2** and **4.3** in other solvent systems. Solutions of these compounds were prepared in DMF at a concentration of 0.5 mg/mL and aged for 1 day. The solutions were cast on carbon-coated TEM grids, which were then visualized by SEM. For compound **4.1**, no self-assembly was observed at this concentration, however, both **4.2** and **4.3** showed morphologies resembling single RNTs or RNT bundles.

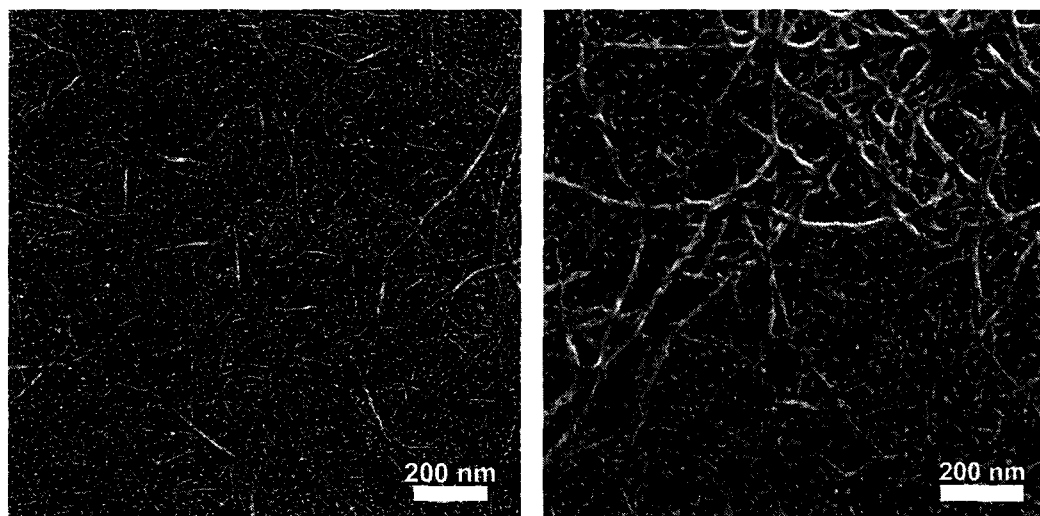


Figure 4.21: SEM images of **4.2** at a concentration of 0.5 mg/mL in DMF upon aging for 1 day (left) and 3 days (right).

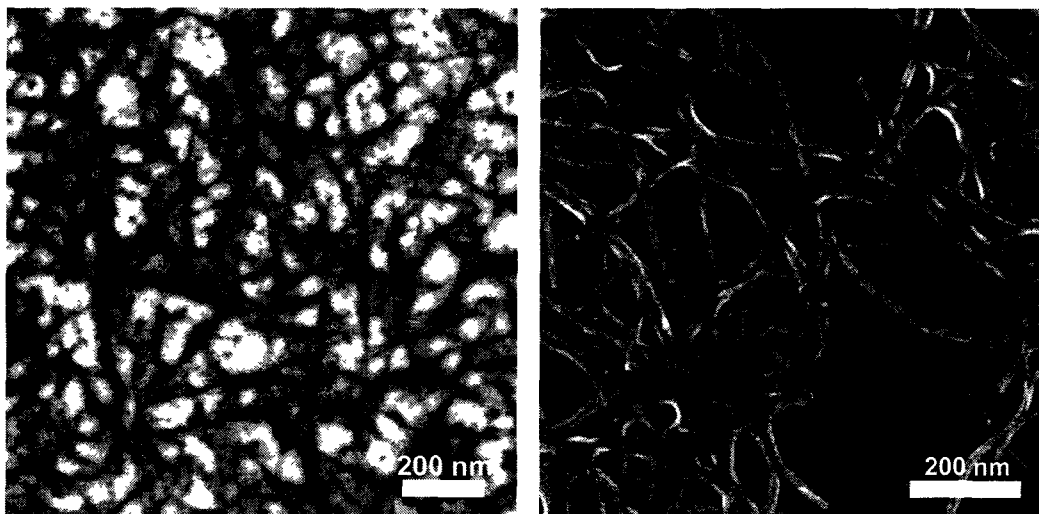


Figure 4.22: SEM images of **4.3** at a concentration of 0.5 mg/mL in DMF upon aging for 1 day and stained using uranyl acetate (left), and after 3 days of aging (right).

We attempted to self-assemble molecule **4.1** at a higher concentration (2.0 mg/mL) in DMF. The sample was then aged for 1 day. An aliquot of the solution was diluted to 0.5 mg/mL and then cast on a TEM grid. SEM imaging of the sample showed RNTs of high aspect ratio as well as agglomerates of RNTs. We believe that the self-assembly of molecule **4.1** did not proceed at the lower stock concentration as the monomers **4.2** and **4.3**, is because compound **4.1** was used in the form of the TFA salt. As shown in chapter 2 of this thesis work, monomers isolated as hydrochloride salts tend to self-assemble to a greater extent as compared to the TFA counterparts.

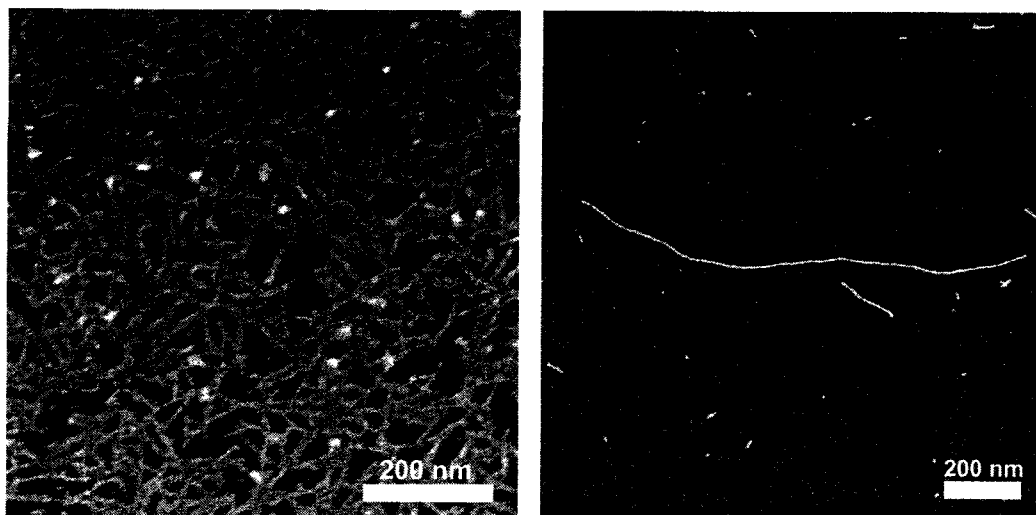


Figure 4.23: SEM images of **4.1** in DMF upon aging for 1 day at a concentration of 2.0 mg/mL (left) and diluting the 2.0 mg/mL solution into 0.5 mg/mL (right).

We also investigated the self-assembly of the samples in DMA. We initially prepared 0.5 mg/mL solutions, but none of these samples displayed nanostructures visible through SEM imaging. We thus attempted to make 2.0 mg/mL solutions, however only **4.1** formed a homogeneous solution in DMA. For samples **4.2** and **4.3**, we opted for a concentration of 1.0 mg/mL and due to the solubility issues, these compounds formed a suspension in DMA. These samples were aged for 1 day and aliquots of these samples were diluted to 0.5 mg/mL for SEM imaging.

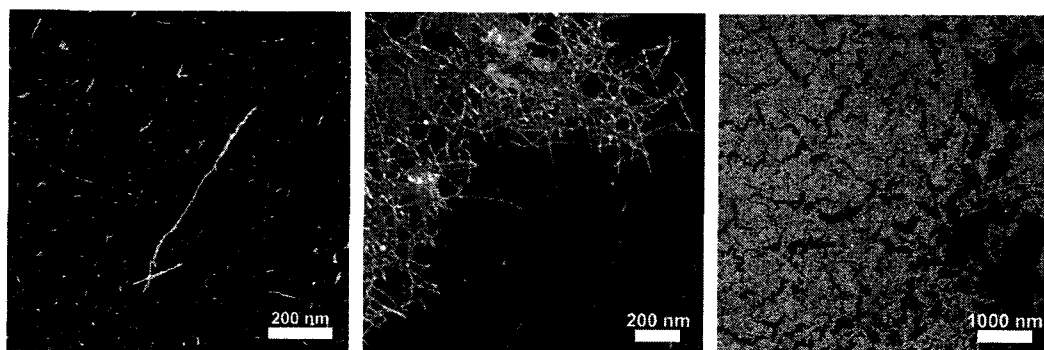


Figure 4.24: SEM images of **4.1** at a concentration of 0.5 mg/mL in DMA upon aging for 1 day, visualized at different locations on the same TEM grid.

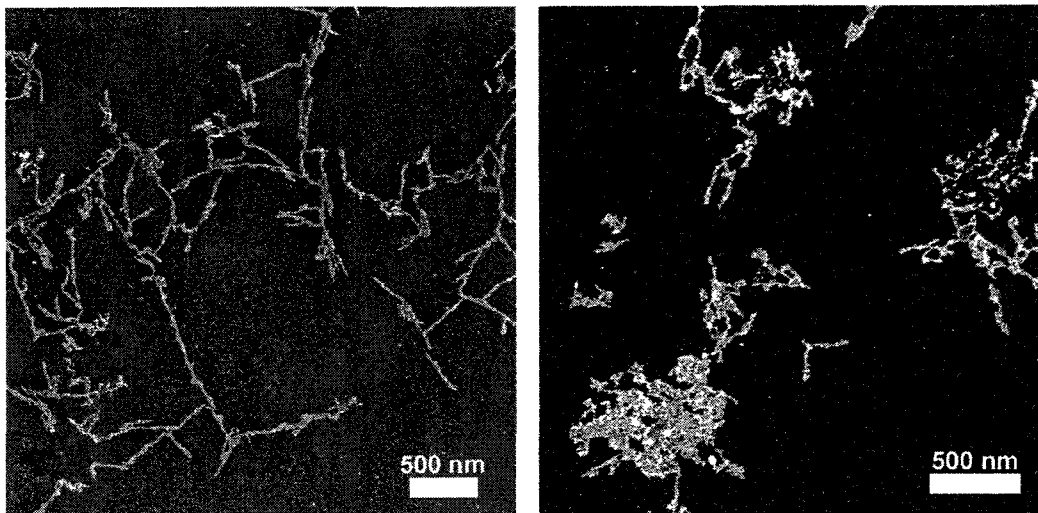


Figure 4.25: SEM images of **4.2** at a concentration of 0.5 mg/mL in DMA upon aging for 1 day, showing agglomerates of short and long RNTs.

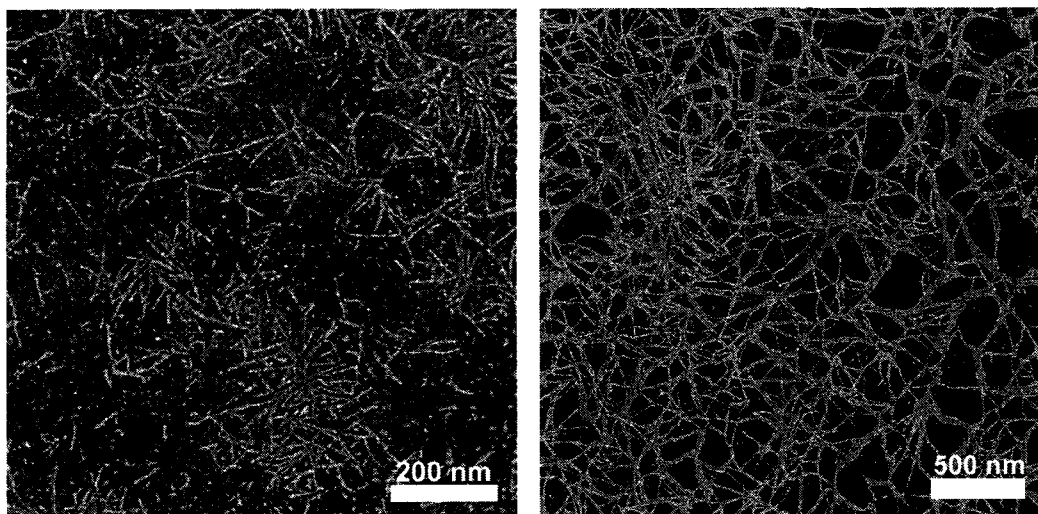


Figure 4.26: SEM images of **4.3** at a concentration of 0.5 mg/mL in DMA upon aging for 1 day, visualized at different locations on the same TEM grid.

Unlike the DMF and DMA samples, the DMSO samples failed to display any nanostructures.

4.2.3. NMR experiments

We had successfully self-assembled all the monobases by varying the solvent systems, which indicated that the intramolecular H-bonding between the side-chain and the endocyclic nitrogen of the cytosine ring was unlikely. Nevertheless, 2D-NMR experiments were carried out to confirm the absence of such interaction. NOESY experiment was initially run on compound **4.1** in 90% H₂O/D₂O. Under these conditions it was difficult to identify the exchangeable amino protons, since some of the peaks were either absent or very broad in the proton NMR spectrum. Consequently, the data obtained were inconclusive and unreliable. We therefore carried out those NMR experiments in deuterated DMSO to suppress proton exchange, which was prevalent in the aqueous medium. DMSO does not have exchangeable protons. TROESY experiments for the newly synthesized molecules **4.1**, **4.2**, **4.3** and **4.5** were carried out in deuterated DMSO. The NOESY, ROESY and TROESY are similar 2D-NMR techniques that provide correlations based on through-space interactions of protons as opposed to correlations based on through bond interactions.¹⁴ In our case, the NOESY experiment was undesirable since under certain combination of field and molecular weight, the NOE can be zero despite the close proximity of the protons in space. The ROESY and TROESY experiments do not possess this undesirable feature, however the TROESY is preferred over the ROESY. This is because ROESY sometimes includes some unwanted contributions from coupling in addition to the through-space correlations. The NOESY experiments are best suited for small or large molecules. Since molecules **4.1**, **4.2**, **4.3** and **4.5** did not self-assemble in DMSO, the existence of any correlation would be easy to detect since the analogues would exist in the monomeric state. As a result, the TROESY experiment was best suited for our medium sized molecules.

The TROESY spectra of the compounds displayed clear cross-peaks, which corresponded to the nuclei being considered or were due to exchange. The dark cross-peaks were real correlation, which implied closeness in space. The figures 4.27-4.30 show the TROESY spectra obtained for molecules **4.1**, **4.2**, **4.3** and **4.5**

in deuterated DMSO. In all cases, interaction between the cytosine nitrogen and the side-chain might result into the formation of a 12-membered ring.

For compound **4.1**, intramolecular hydrogen bonding, if present, can occur between the ammonium ion of the lysine moiety and the endocyclic nitrogen of the cytosine ring, as shown below (Figure 4.27).

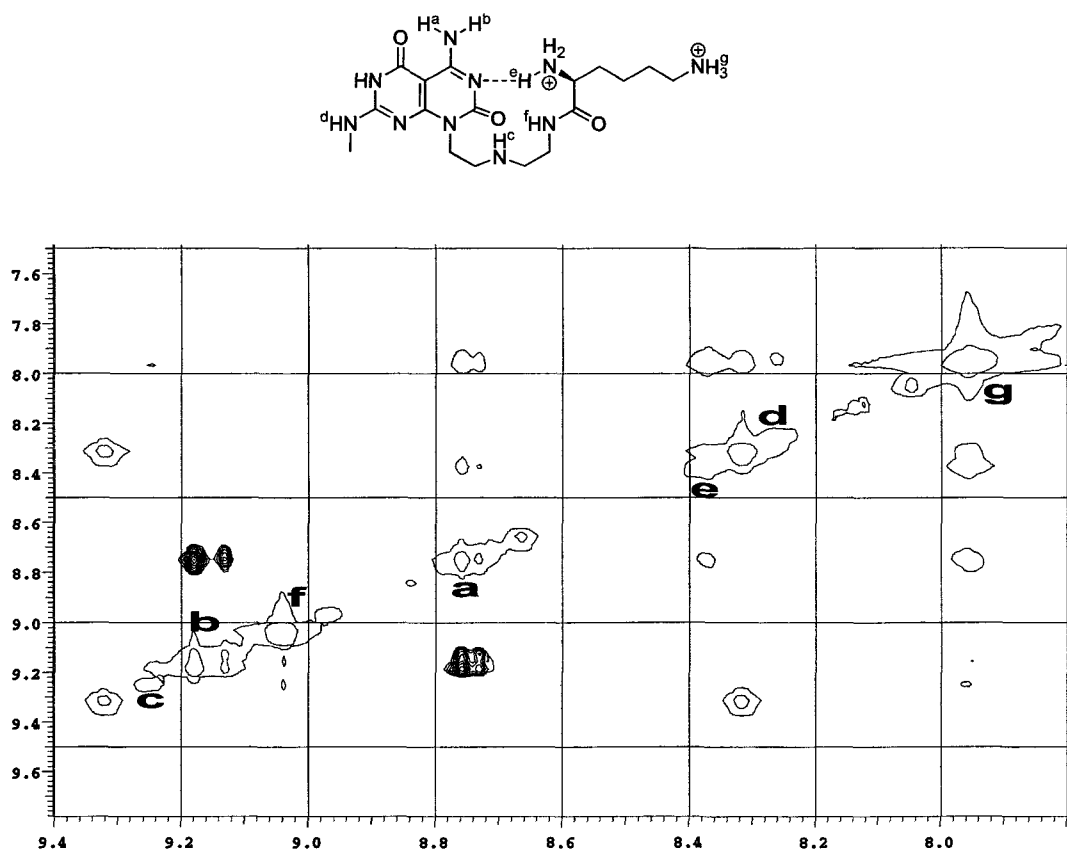


Figure 4.27: TROESY spectrum for molecule **4.1** in deuterated DMSO. The clear cross-peaks correspond to the nuclei being considered and dark cross-peaks signify ROE correlations due to close proximity in space.

As seen from the TROESY spectrum, no ROE correlation was observed between H^b and H^c . The only correlation, which existed, was between the geminal protons H^a and H^b due to their close proximity in space.

For molecule **4.2**, interaction (if any) resulting from intramolecular hydrogen-bonding would occur between the endocyclic nitrogen and the amide proton. From the TROESY spectrum such correlation was absent between the protons H_b and H_e . As in the case of **4.1**, the only observed ROE was for H_a and H_b .

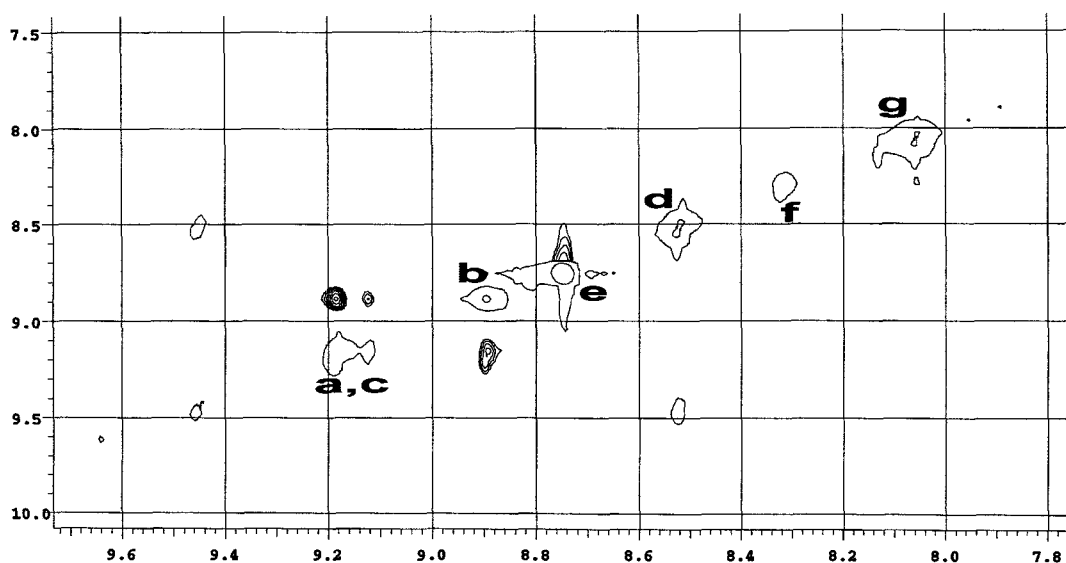
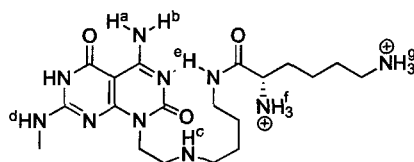


Figure 4.28: TROESY spectrum for molecule **4.2** in deuterated DMSO

Similar experiment carried out on molecule **4.3**, showed the absence of ROE between H_b and H_e , which proves that there is no interaction between the cytosine ring and the ammonium ion.

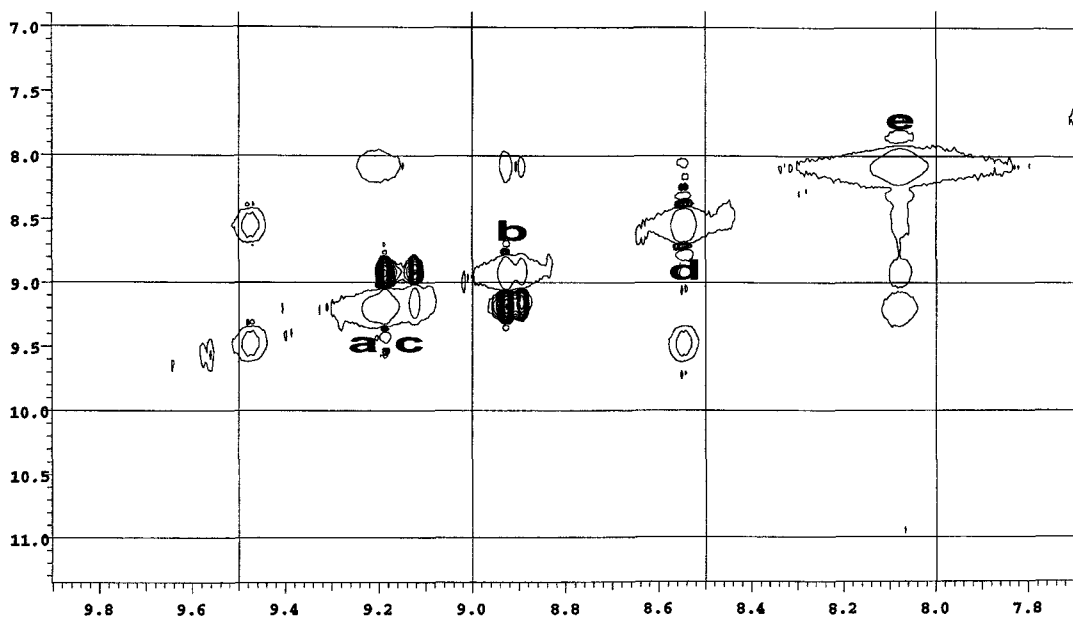
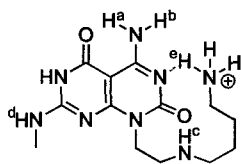


Figure 4.29: TROESY spectrum for molecule **4.3** in deuterated DMSO

TROESY experiment was also conducted on monomer **4.5**. Unlike the derivatives **4.1**, **4.2** and **4.3**, which were potential proton donors due to accessible NHs on the side-chain, **4.5** had a hydroxyl group, which could serve a proton. From the 2D spectrum obtained no ROE was observed between H_b and H_c . The only existing ROE for the exchangeable protons were between H_a and H_b .

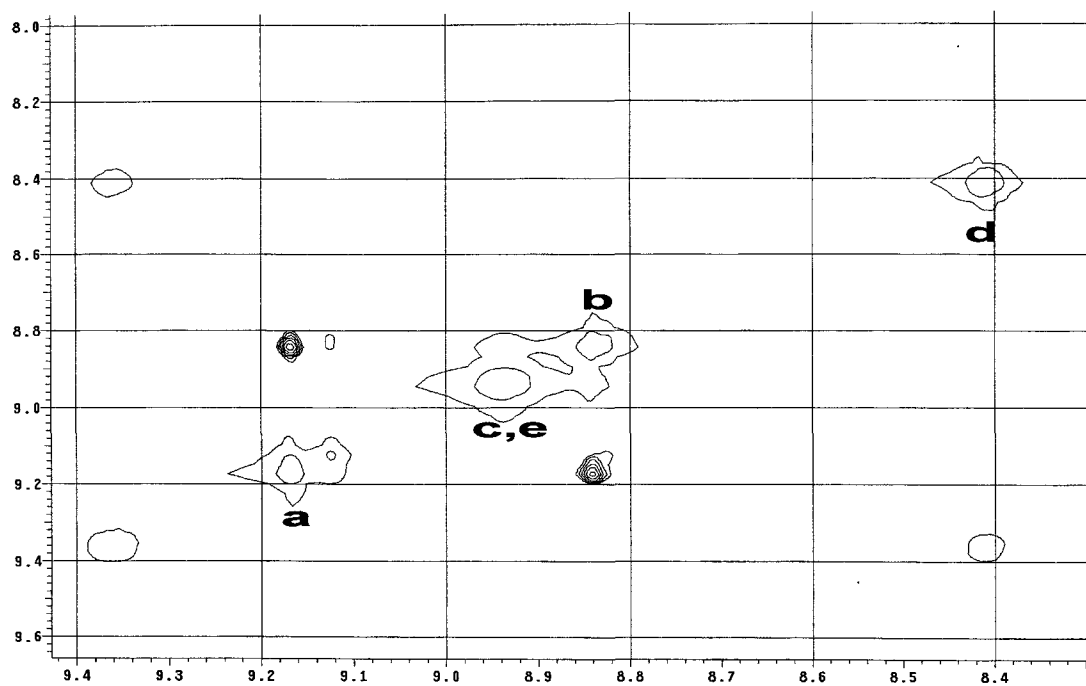
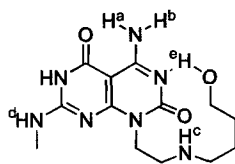


Figure 4.30: TROESY spectrum for molecule 4.5 in deuterated DMSO

4.3. Discussion

A summary of the self-assembly behaviour of the monomers in different solvent systems is illustrated in the table below.

Molecule	4.1	4.2	4.3	4.5	4.7	4.16
Net charge	+3	+3	+2	+1	+1	0
Self-assembly in H ₂ O (pH 4)	No	No	No	No	Yes	No
Self-assembly in CH ₃ OH	No	No	No	Yes	No	Yes
Self-assembly at pH 11	No	No	No	Yes	Yes	Yes
Self-assembly in DMF	Yes	Yes	Yes			
Self-assembly in DMA	Yes	Yes	Yes			
Self-assembly in DMSO	No	No	No			

Figure 4.31: Table summarizing the net charge of the monobases and their self-assembly behaviour in methanol or in the aqueous media.

For most derivatives (with the exception of 4.7), no self-assembly was observed upon dissolution in water. From Figure 4.31, a trend is observed between the net charge on the monomers and their ability to self-assemble. Since the monomers were isolated as either HCl or TFA salts, the pH of the resulting solutions is about 4. Under these conditions, the nitrogen atoms on the side-chain of the monomers exist in the protonated form, leading to high charge repulsion, which hinder RNT formation.

Despite lower net charge as compared to 4.7, monomer 4.16 failed to show aggregation due to its limited solubility in water. Similarly though compound 4.5 had similar net charge as 4.7, no nanostructures were observed in solution. This could be related to the stability and solvation of the monomer, resulting from the hydrophilicity of the terminal hydroxyl group in the medium. In water, aggregation is driven by entropy and water molecules are released into the bulk solvent as rosettes are sequestered onto the growing RNTs. In addition, the hydrophobic nature of the side-chain in 4.7 contribute to the self-assembly.¹⁵

Evidence that the net charge plays a significant role in the self-assembly of these monomers was demonstrated by successful RNT formation in the case of **4.5** and **4.16** at pH 11. Under basic conditions, most of the nitrogens would be unprotonated, due to which electrostatic repulsion is reduced, thus leading to self-assembly.⁵ However these conditions were still not favourable for the self-assembly of **4.1**, **4.2** and **4.3**.

In methanol, there are stronger electrostatic interactions between the ammonium groups on the G \wedge C base and the chloride anions than in water due to decreased cation and anion solvation.¹⁶ The charge neutralization resulting from the tighter ion pair, reduces the charge density on the RNTs. This justifies the presence of nanostructures for **4.5** in methanol and its non-assembly in water. Decreased solvation of the donor and acceptor sites on the G \wedge C heterocycles, which stabilizes the hexameric rosettes within the RNTs through stronger H-bonding interactions, along with improved solubility of **4.16** in methanol RNTs led to the observation of RNTs.

So far, only the molecules with the lowest charge density (**4.5**, **4.7** and **4.16**) showed higher order aggregation. Compared to these three molecules, the monomers **4.1** and **4.2** have higher functional group densities, which can lead to a sterically more congested supramolecule. We had utilized water, methanol or alkaline buffer conditions (pH 11) as solvent media for triggering the self-assembly resulting from solvophobic effects. Water and methanol are amphiprotic solvents, which can act both as a hydrogen-bond donor (HBD) and hydrogen-bond acceptor (HBA).¹⁷ We envisaged that the high positive charge density on the RNTs would be better stabilized in a HBA solvent. We thus investigated dimethyl sulfoxide (DMSO) and *N,N*-dimethylformamide (DMF) and *N,N*-dimethylacetamide (DMA) as solvents for the self-assembly of compounds **4.1**, **4.2** and **4.3**. Liquid DMF is a dipolar aprotic solvent and possesses both donor and acceptor properties. However the absence of a strong proton-donor group limits the extent of H-bonding due to which liquid DMF does not form

chains or lattices. As such, DMF can be considered as a HBA solvent.¹⁷ The table in Figure 4.32 shows the structure and some of the physical properties of the solvents investigated.

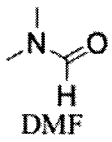
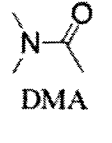
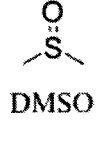
Solvent	Polarity index	Boiling pt / °C	Dipole moment	Dielectric constant	Solvent type
$\text{H}-\overset{\cdot\cdot}{\text{O}}-\text{H}$ Water	9	100	1.85	78.4	HBA/HBD
$\text{H}_3\text{C}-\text{OH}$ Methanol	5.1	68	1.70	33	HBA/HBD
 DMF	6.4	153	4.82	38.3	HBA
 DMA	6.5	166	4.72	37.8	HBA
 DMSO	7.2	189	3.96	47.2	HBA

Figure 4.32: Table showing some of the physical properties of the solvents used.¹⁷

One of the most striking differences in the physical properties of water and DMF (from Figure 4.32) is the dielectric constant. The higher the dielectric constant, existence of ion pairs would be less prevalent due to the greater charge separation. In addition, the partial molar volume of ions determines the type and the strength of the ion-pair in solution. In water, the chloride ion displays a partial molar volume of $24.3 \text{ cm}^3\text{mol}^{-1}$, whereas in DMF the partial molar volume is $2.8 \text{ cm}^3\text{mol}^{-1}$. While the change in partial molar volume of the chloride ion from water to DMF is quite alarming (20.5), the difference in partial molar volume of

the cations is relatively small. For instance, the difference in partial molar volume of tetramethylammonium ions is only 1.1.¹⁸ The lower solvation in DMF and DMA leads to a tighter ion pair between the ammonium and chloride ions, thus leading to more stable RNTs due to less electrostatic repulsion.

Unlike the DMF and DMA samples, the DMSO samples failed to display any nanostructures. Though, we do not have a definite answer to the non-assembly under these conditions, we presume that it could be related to the polarity of the solvent. Compared to DMF and DMA, DMSO has a higher dipole moment, which can lead to more interference with the H-bonding pattern within the rosettes and the stacking of the RNTs.

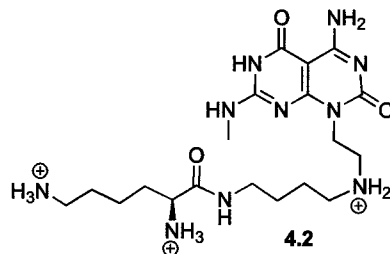
From the 2D NMR experiments carried out on 4.1, 4.2, 4.3 and 4.5, we failed to observe any through space correlation, which could justify intramolecular hydrogen bonding within the monomers. As such we can state that the non-assembly of the monomers discussed in this chapter relied on their net charge and the solvent effects.

4.4. Conclusion

We have demonstrated how the net charge and the functional group density can affect the self-assembly of RNTs. The formation of RNTs relies on a favourable association free energy for the system, which is highly dependent on the solvation energy, which in turn has to compensate for the solute-solute and solvent-solvent interaction energies. In case of unfavourable structural features, hydrogen bond donor/acceptor properties of the solvent can be successfully utilized to trigger the self-assembly of RNTs. It was found that higher pH and HBA solvents led to higher order aggregation. Absence of through space correlation from the TROESY spectra negates the intramolecular hydrogen-bonding hypothesis of the monomers in solution. This work also highlights the importance of careful structural design for monomers aimed for biological applications, in which self-assembly under physiological conditions is a requirement.

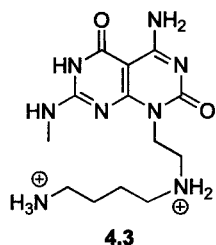
4.5. Experimental section

Compound 4.2



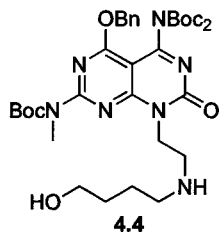
Compound **2.50** (0.447 g, 0.429 mmol) was stirred in a 95% TFA in thioanisole (10 mL) for 72 h. Et₂O (60 mL) was then added to the reaction mixture and the precipitate formed, was centrifuged down. The residual solid was resuspended in Et₂O, sonicated and centrifuged down. This process was repeated until the spotting of the Et₂O produced no UV active spot. The white solid was dried under vacuo and was then dissolved in 1 M hydrochloric acid (20 mL), followed by removal of water under reduced pressure. This process was repeated two more times before the solid was dried under vacuo for 72 h to yield the desired compound **4.2** (0.262 g, 91%) as a white solid; ¹H NMR (600 MHz, d₆-DMSO): δ = 12.31 (s, 1H), 9.18 (s, 1H), 9.13 (d, *J* = 9.0 Hz, 2H), 8.87 (s, 1H), 8.74 (t, *J* = 5.4 Hz, 1H), 8.47 (q, *J* = 5.4 Hz, 1H), 8.30 (d, *J* = 4.2 Hz, 3H), 8.03 (bs, 3H), 4.37 (t, *J* = 5.4 Hz, 1H), 4.72 (q, *J* = 5.4 Hz, 1H), 4.21 (m, 2H), 4.12 (q, *J* = 6.6 Hz, 2H), 2.99 (d, *J* = 4.8 Hz, 2H), 2.91 (m, 2H), 2.74 (m, 2H), 1.73-1.69 (m, 2H), 1.67-1.62 (m, 2H), 1.60-1.53 (m, 2H), 1.50-1.43 (m, 2H), 1.37-1.31 (m, 2H); ¹³C NMR (125 MHz, d₆-DMSO): δ = 168.6, 161.0, 160.3, 156.4, 156.1, 148.4, 82.9, 52.2, 46.8, 44.8, 38.6, 38.5, 38.1, 30.5, 28.3, 26.5, 26.0, 23.0, 21.4; HRMS calcd for C₁₉H₃₅N₁₀O₃ [M-H]⁺ 451.2888, found: 451.2892; elemental analysis calcd (%) for C₁₉H₃₃N₁₀O₃(HCl)₅(H₂O)₂ C, 34.12, H, 6.48, N, 20.94, found C, 34.36, H, 6.47, N, 20.87; elemental analysis calcd (%) for C₁₉H₃₃N₁₀O₃(TFA)_{4.5}(H₂O) C, 34.26, H, 4.16, N, 14.27, found C, 34.28, H, 4.33, N, 14.54.

Compound 4.3



Compound **2.21** (0.055 g, 0.0677 mmol) was stirred in a 95% TFA in thioanisole (10 mL) for 72 h. Et₂O (40 mL) was then added to the reaction mixture and the precipitate formed, was centrifuged down. The residual solid was resuspended in Et₂O, sonicated and centrifuged down. This process was repeated until the spotting of the Et₂O produced no UV active spot. The white solid was dried under vacuo and was then dissolved in 1 M hydrochloric acid (10 mL), followed by removal of water under reduced pressure. This process was repeated two more times before the solid was dried under vacuo for 72 h to give **4.3** (0.028 g, 88%) as an off-white powder; ¹H NMR (600 MHz, d₆-DMSO): δ = 12.30 (s, 1H), 9.16 (s, 3H), 8.90 (s, 1H), 8.53 (q, *J* = 4.8 Hz, 1H), 8.04 (bs, 3H), 4.37 (t, *J* = 6.6 Hz, 2H), 4.21 (t, *J* = 5.7 Hz, 2H), 2.99 (d, *J* = 4.8 Hz, 3H), 2.91 (app. q, *J* = 5.4 Hz, 2H), 2.77 (app. q, *J* = 7.2 Hz, 2H), 1.72-1.65 (m, 2H), 1.62-1.56 (m, 2H); ¹³C NMR (125 MHz, d₆-DMSO): δ = 161.4, 160.8, 156.9, 156.6, 148.8, 84.3, 46.9, 45.3, 39.1, 38.7, 28.7, 24.7, 24.1; HRMS calcd for C₁₃H₂₃N₈O₂ [M-H]⁺ 324.1939, found 324.1938; elemental analysis calcd (%) for C₁₃H₂₂N₈O₂(HCl)₄(H₂O)_{0.33} C, 32.93, H, 5.67, N, 23.63, found C, 33.07, H, 5.65, N, 24.35.

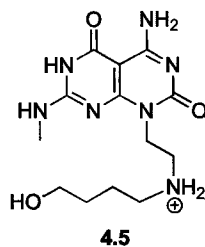
Compound 4.4



To a stirred solution of **2.13** (0.100 g, 0.157 mmol) in 1,2 DCE (20 mL), 1,4 aminobutanol (17 μL, 0.188 mmol) was added at room temperature under N₂. The mixture was stirred for 30 min before sodium triacetoxy borohydride (0.036

g, 0.186 mmol) was added and the resulting mixture was stirred for an additional 15 h. The reaction mixture was diluted with CH₂Cl₂ (50 mL) and then washed with water (2 x 10 mL), brine (15 mL), dried over Na₂SO₄ and concentrated. Flash chromatography of the residue over silica gel (0-10% MeOH in CH₂Cl₂) gave **4.4** (0.072 g, 65%) as a white foam. R_f = 0.24 (8% MeOH in CH₂Cl₂); ¹H NMR (500 MHz, CDCl₃): δ = 7.42-7.29 (m, 5H), 5.55 (s, 2H), 5.16 (bs, 1H), 4.57 (t, *J* = 6.0 Hz, 2H), 4.51 (t, *J* = 5.5 Hz, 2H), 3.48 (s, 3H), 4.20 (t, *J* = 6.0 Hz, 2H), 2.88 (t, *J* = 6.2 Hz, 2H), 1.74-1.67 (m, 2H), 1.62-1.57 (m, 2H), 1.55 (s, 9H), 1.31 (s, 18H); ¹³C NMR (125 MHz, CDCl₃): δ = 165.7, 161.1, 161.0, 160.0, 155.9, 152.4, 149.4, 134.8, 128.6, 128.3, 94.1, 84.0, 84.2, 70.2, 62.0, 48.9, 46.3, 41.6, 35.0, 30.8, 28.1, 27.8, 26.0; HRMS calcd for C₃₅H₅₂N₇O₉ [M+H]⁺ 714.3810, found 714.3818.

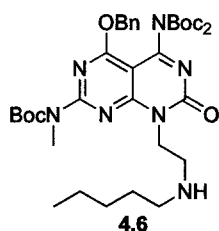
Compound 4.5



Compound **4.4** (0.065 g, 0.091 mmol) was stirred in a 95% TFA in thioanisole (10 mL) for 72 h. Et₂O (60 mL) was then added to the reaction mixture and the precipitate formed, was centrifuged down. The residual solid was resuspended in Et₂O, sonicated and centrifuged down. This process was repeated until the spotting of the Et₂O produced no UV active spot. The white solid was dried under vacuo and was then dissolved in 1 M hydrochloric acid (10 mL), followed by removal of water under reduced pressure. This process was repeated two more times before the solid was dried under vacuo for 72 h to yield the desired compound **4.5** (0.040 g, 95%) as an off-white powder; ¹H NMR (500 MHz, d₆-DMSO): δ = 12.30 (bs, 1H), 9.17 (s, 1H), 8.94 (bs, 2H), 8.85 (bs, 1H), 8.42 (app. q, *J* = 4.5 Hz, 1H), 4.37 (t, *J* = 5.5 Hz, 2H), 3.40 (t, *J* = 6.3 Hz, 2H), 4.22 (t, *J* = 5.0 Hz, 2H), 2.99 (d, *J* = 5.0 Hz, 3H), 2.93 (app. q, *J* = 5.0 Hz, 2H), 1.68-1.61 (m,

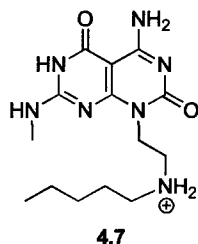
2H), 1.46-1.40 (m, 2H); ^{13}C NMR (125 MHz, d_6 -DMSO): δ = 160.8, 160.0, 156.2, 155.7, 148.3, 82.5, 60.0, 47.0, 44.5, 38.3, 29.3, 27.9, 22.4; HRMS calcd for $\text{C}_{13}\text{H}_{22}\text{N}_7\text{O}_3$ $[\text{M}]^+$ 324.1779, found 324.1779; elemental analysis calcd (%) for $\text{C}_{13}\text{H}_{21}\text{N}_7\text{O}_3(\text{HCl})_{3.67}$ C, 33.94, H, 5.42, N, 21.31, found C, 34.84, H, 5.31, N, 22.34.

Compound 4.6



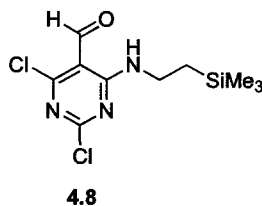
To a stirred solution of **2.13** (0.200 g, 0.313 mmol) in 1,2 DCE (20 mL), pentylamine (43 μL , 0.376 mmol) was added at room temperature under N_2 . The mixture was stirred for 30 min before sodium triacetoxy borohydride (0.078 g, 0.371 mmol) was added and the resulting mixture was stirred for an additional 12 h. The reaction mixture was diluted with CH_2Cl_2 (50 mL) and then washed with water (2 x 10 mL), brine (15 mL), dried over Na_2SO_4 and concentrated. Flash chromatography of the residue over silica gel (0-5% MeOH in CH_2Cl_2) gave **4.6** as a white foam in 86% yield. R_f = 0.43 (5% MeOH in CH_2Cl_2); ^1H NMR (500 MHz, CDCl_3): δ = 7.44-7.32 (m, 5H), 5.56 (s, 2H), 4.48 (t, J = 6.5 Hz, 2H), 3.46 (s, 3H), 3.04 (t, J = 6.5 Hz, 2H), 2.67 (t, J = 7.3 Hz, 2H), 1.58 (s, 9H), 1.48-1.44 (m, 2H), 1.32 (s, 18H), 1.30-1.22 (m, 4H), 0.86 (t, J = 7.0 Hz, 3H); ^{13}C NMR (125 MHz, CDCl_3): δ = 165.7, 161.2, 161.0, 160.4, 155.8, 152.6, 149.3, 134.9, 128.6, 128.5, 128.3, 94.3, 84.8, 84.1, 70.1, 49.5, 47.0, 42.9, 34.9, 29.3, 29.2, 28.1, 27.8, 22.5, 14.0; HRMS calcd for $\text{C}_{36}\text{H}_{54}\text{N}_7\text{O}_8$ $[\text{M}+\text{H}]^+$ 712.4028, found 712.4026.

Compound 4.7



Compound 4.6 (0.190 g, 0.267 mmol) was stirred in a 95% TFA in thioanisole (20 mL) for 72 h. Et₂O (60 mL) was then added to the reaction mixture and the precipitate formed, was centrifuged down. The residual solid was resuspended in Et₂O, sonicated and centrifuged down. This process was repeated until the spotting of the Et₂O produced no UV active spot. The white solid was dried under vacuo and was then dissolved in 1 M hydrochloric acid (10 mL), followed by removal of water under reduced pressure. This process was repeated two more times before the solid was dried under vacuo for 72 h to yield the desired compound 4.7 (0.079 g, 75%) as an off-white powder; ¹H NMR (500 MHz, d₆-DMSO): δ = 12.30 (bs, 1H), 9.14 (s, 1H), 8.90 (bs, 2H), 8.81 (bs, 1H), 8.36 (bs, 1H), 4.36 (t, *J* = 5.5 Hz, 2H), 4.22 (t, *J* = 5.0 Hz, 2H), 2.98 (d, *J* = 4.5 Hz, 3H), 2.92-2.86 (m, 2H), 1.61-1.58 (m, 2H), 1.29-1.22 (m, 4H), 0.86 (t, *J* = 6.8 Hz, 3H); ¹³C NMR (100 MHz, d₆-DMSO): δ = 160.6, 159.8, 156.1, 155.5, 148.3, 82.3, 46.7, 44.3, 38.1, 27.8, 27.7, 24.8, 21.4, 14.5; HRMS calcd for C₁₄H₂₄N₇O₂ [M]⁺ 322.1986, found 322.1986; elemental analysis calcd (%) for C₁₄H₂₃N₇O₂(HCl)₂ C, 42.65, H, 6.39, N, 24.87, found C, 42.34, H, 6.52, N, 24.17.

2,4-dichloro-6-(2-(trimethylsilyl)ethylamino)pyrimidine-5-carbaldehyde (4.8)



A solution of 2,4,6-trichloropyrimidine-5-carbaldehyde (300 mg, 1.42 mmol) in CH₂Cl₂ (2 mL) at -78°C was treated with DIEA (0.30 mL, 1.7 mmol) followed by a solution of trimethylsilylethylamine hydrochloride (0.260 g, 1.69 mmol) in

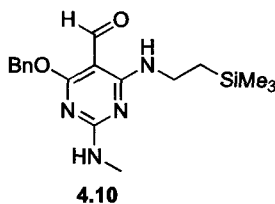
CH₂Cl₂ (2 mL). After stirring for 2 h, the reaction was warmed to room temperature and stirred for an additional 12 h. The solvents were then removed under reduced pressure and the product was purified by flash chromatography on silica gel (5-8% EtOAc in hexanes) to provide **4.8** as a white solid (0.250 g, 60%). R_f = 0.61 (15% EtOAc in hexane), mp = 159-161 °C; ¹H NMR (300 MHz, CDCl₃): δ = 10.25 (s, 1H), 9.22 (bs, 1H), 3.61-3.53 (m, 2H), 0.96-0.88 (m, 2H), 0.06 (s, 9H); ¹³C NMR (125 MHz, CDCl₃): δ = 188.1, 165.4, 161.8, 160.5, 101.5, 37.8, 17.7, -1.68; HRMS calcd mass for [M+H⁺] 292.0434, found 292.0432.

4-chloro-2-(methylamino)-6-(2-(trimethylsilyl)ethylamino)pyrimidine-5-carbaldehyde (4.9)



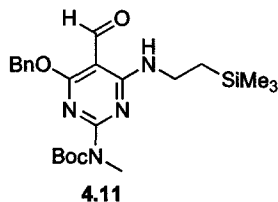
A solution of **4.8** (0.750 g, 2.57 mmol) in THF (10 mL) was treated with methylamine (2.86 mL, 2M in THF, 5.72 mmol) at 0 °C and then warmed to room temperature. After stirring for 2 h, the reaction was quenched with a saturated aqueous solution of NH₄Cl (1 mL) and the product was extracted with CH₂Cl₂ (3x). The combined organic phases were washed with water and brine, dried over anhydrous Na₂SO₄, filtered and concentrated. Purification by flash chromatography on silica gel (10-20% EtOAc in hexanes) provided 4-chloro-2-(methylamino)-6-(2-(trimethylsilyl)ethylamino)pyrimidine-5-carbaldehyde (**4.9**) as a white solid (0.650 g, 88%). R_f = 0.38 (10% EtOAc in hexanes), mp = 178-180 °C; ¹H NMR (400 MHz, CDCl₃): δ = 10.03 (s, 1H), 9.30 (bs, 1H), 5.50 (bs, 1H), 3.65-3.52 (m, 2H), 3.01 (d, J = 4.8 Hz, 3H), 1.04-0.91 (m, 2H), 0.06 (s, 9H); ¹³C NMR (100 MHz, CDCl₃): δ = 188.2, 165.3, 161.7, 161.4, 101.4, 36.9, 28.1, 17.4, -1.7; HRMS calcd mass for [M+H⁺] 287.1095, found 287.1090.

4-(benzyloxy)-2-(methylamino)-6-(2-(trimethylsilyl)ethylamino)pyrimidine-5-carbaldehyde (4.10)



Benzyl alcohol (0.046 mL, 0.45 mmol) was added to a suspension of NaH (0.013 g, 0.52 mmol) in THF (1 mL) at room temperature. After stirring for 15 min, a solution of 4-chloro-2-(methylamino)-6-(2-(trimethylsilyl)ethylamino)pyrimidine-5-carbaldehyde (0.130 g, 0.456 mmol) in THF (1 mL) was added and the mixture was refluxed for 24 h. After cooling down to 0°C, the reaction was quenched with a saturated aqueous solution of NH₄Cl and the product was extracted with EtOAc (3x). The combined organic layers were washed with water and brine, dried over anhydrous Na₂SO₄, filtered and concentrated. Purification by flash chromatography on silica gel (3-5% EtOAc in hexanes) provided **4.10** (0.125 g, 77%) as an oil. R_f = 0.60 (5% MeCN in benzene); ¹H NMR (400 MHz, CDCl₃): δ = 9.99 (s, 1H), 9.29 (bs, 1H), 7.40-7.29 (m, 5H), 5.46 (bs, 1H), 5.34 (s, 2H), 3.59-3.46 (m, 2H), 2.96 (d, *J* = 5.2 Hz, 3H), 0.99-0.92 (m, 2H), 0.06 (s, 9H); ¹³C NMR (100 MHz, CDCl₃): δ = 185.5, 171.3, 162.8, 162.5, 136.5, 128.2, 127.7, 92.4, 67.1, 36.4, 27.9, 17.6, -1.8; HRMS calcd mass for [M+H⁺] 359.1903, found 359.1895.

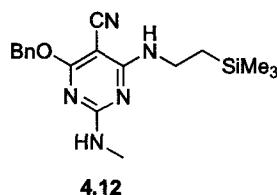
***tert*-butyl 4-(benzyloxy)-5-formyl-6-(2-(trimethylsilyl)ethylamino)pyrimidin-2-yl(methyl)carbamate (4.11)**



Boc₂O (0.288 g, 1.32 mmol) was added to a solution of 4-(benzyloxy)-2-(methylamino)-6-(2-(trimethylsilyl)ethylamino)pyrimidine-5-carbaldehyde (0.400 g, 1.11 mmol), DMAP (0.013 g, 0.11 mmol) and Et₃N (0.46 mL, 3.3 mmol) in

THF (4 mL) at room temperature. After stirring for 24 h, the reaction was quenched with water and the product was extracted with EtOAc (3x). The combined organic layers were washed with water and brine, dried over anhydrous Na₂SO₄, filtered and concentrated. Purification by flash chromatography on silica gel (2-3% EtOAc in hexanes) provided *t*-butyl 4-(benzyloxy)-5-formyl-6-(2-(trimethylsilyl)ethylamino)pyrimidin-2-yl(methyl) carbamate (0.480 g, 94%) as a foam. R_f = 0.62 (15% EtOAc in hexanes); ¹H NMR (400 MHz, CDCl₃): δ = 10.12 (s, 1H), 9.09 (bs, 1H), 7.44-7.33 (m, 5H), 5.47 (s, 2H), 3.60-3.54 (m, 2H), 3.39 (s, 3H), 1.55 (s, 9H), 0.97-0.93 (m, 2H), 0.05 (s, 9H); ¹³C NMR (100 MHz, CDCl₃): δ = 187.2, 171.3, 162.1, 161.7, 153.6, 136.2, 128.3, 128.0, 127.8, 93.9, 81.5, 68.0, 36.9, 34.4, 28.0, 17.6, -1.8; HRMS calcd mass for [M+H⁺] 459.2422, found 459.2420.

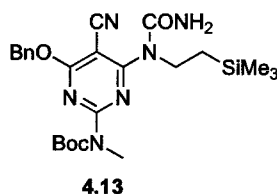
4-(benzyloxy)-2-(methylamino)-6-(2-(trimethylsilyl)ethylamino)pyrimidine-5-carbonitrile (4.12)



NH₂OH·HCl (243 mg, 3.50 mmol) was added to a solution of *tert*-butyl 4-(benzyloxy)-5-formyl-6-(2-(trimethylsilyl)ethylamino)pyrimidin-2-yl(methyl) carbamate (0.800 g, 1.75 mmol) in pyridine (5 mL) at room temperature. After stirring for 3 h, the pyridine was removed under reduced pressure and the product was extracted with EtOAc (3x). The combined organic layers were washed with saturated aqueous solution of NaHCO₃, followed by water and brine, dried over anhydrous Na₂SO₄, filtered and concentrated. The crude product (0.735 g, 1.55 mmol) was then dissolved in THF (5 mL), cooled to 0°C and treated with Et₃N (0.65 mL, 4.7 mmol). TFAA (0.33 mL, 2.3 mmol) was then added and the mixture was stirred for 15 min at 0°C, followed by 5 h at 80°C. After cooling to room temperature, EtOAc (60 mL) was added and the organic layer was washed with water and brine, dried over anhydrous Na₂SO₄, filtered and concentrated.

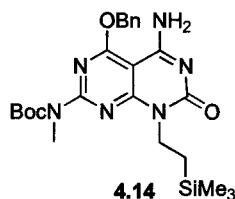
Purification by flash chromatography on silica gel (5-8% EtOAc in hexanes) afforded **4.12** as a paste (0.530 g, 79%). $R_f = 0.53$ (15% EtOAc in hexanes); ^1H NMR (400 MHz, CDCl_3): $\delta = 7.39\text{-}7.27$ (m, 5H), 5.42 (s, 2H), 5.34 (m, 1H), 3.53-3.48 (m, 2H), 3.32 (s, 3H), 1.50 (s, 9H), 0.90-0.86 (m, 2H), 0.02 (s, 9H); ^{13}C NMR (100 MHz, CDCl_3): $\delta = 170.2, 163.7, 160.8, 153.5, 135.9, 128.4, 128.1, 127.9, 114.8, 81.8, 68.7, 68.4, 38.0, 34.5, 28.1, 17.8, -1.7$; HRMS calcd mass for $[\text{M}+\text{H}^+]$ 456.2426, found 456.2425.

***tert*-butyl-4-(benzyloxy)-5-cyano-6-(1-(2-(trimethylsilyl)ethyl)ureido)-pyrimidin-2-yl(methyl)carbamate (4.13)**



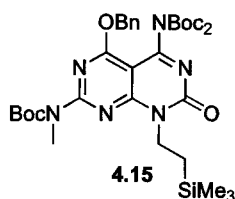
N-chlorocarbonylisocyanate (0.025 mL, 0.30 mmol) was added dropwise to a solution of **4.12** (70 mg, 0.15 mmol) in CH_2Cl_2 (3 mL) at 0°C . After stirring for 2 h, the reaction was warmed to room temperature and stirred for an additional 3 h. The mixture was then cooled to 0°C and quenched with water. The product was extracted with CHCl_3 (3x) and the combined organic layers were washed with saturated aqueous NaHCO_3 and brine, dried over anhydrous Na_2SO_4 , filtered and concentrated to provide **4.13** (0.060 g, 78%) as a white solid. The product was used in the next step without further purification. $R_f = 0.27$ (5% MeOH/ CH_2Cl_2). mp = 165°C - 166°C ; ^1H NMR (400 MHz, CDCl_3): $\delta = 7.46\text{-}7.32$ (m, 5H), 5.51 (s, 2H), 4.30-4.26 (m, 2H), 3.41 (s, 3H), 1.53 (s, 9H), 1.04-1.01 (m, 2H), 0.06 (s, 9H); ^{13}C NMR (100 MHz, CDCl_3): $\delta = 172.3, 163.3, 158.7, 155.6, 152.6, 135.4, 128.8, 128.6, 127.8, 113.8, 83.5, 69.8, 43.9, 34.6, 28.2, 17.6, -1.4$; HRMS calcd mass for $[\text{M}+\text{Na}^+]$ 521.2303, found 521.2303.

***tert*-butyl-5-amino-4-(benzyloxy)-7-oxo-8-(2-(trimethylsilyl)ethyl)-7,8-dihydropyrimido[4,5-*d*]pyrimidin-2-yl(methyl)carbamate (4.14)**



A solution of **4.13** (0.060 mg, 0.12 mmol) in MeOH (2 mL) and treated with 7*N* NH₃ in methanol (1 mL) at room temperature. After stirring for 3 h, the solution was concentrated and the yellow solid was washed with Et₂O, centrifuged, collected and dried under high vacuum to furnish *tert*-butyl 4-amino-5-(benzyloxy)-1,2-dihydro-1-(2-(trimethylsilyl)ethyl)-2-oxopyrimido[4,5-*d*]pyrimidin-7-ylmethylcarbamate (**4.14**) as a solid (0.060 g, 97%). R_f = 0.55 (5% MeOH in CHCl₃), decomposes > 315 °C; ¹H NMR (600 MHz, CDCl₃): δ = 7.71 (bs, 1H), 7.46-7.35 (m, 5H), 7.00 (bs, 1H), 5.62 (s, 2H), 4.26-4.23 (m, 2H), 3.44 (s, 3H), 1.57 (s, 9H), 1.04-1.01 (m, 2H), 0.07 (s, 9H); ¹³C NMR (150 MHz, CDCl₃): δ = 166.4, 160.8, 160.7, 160.2, 155.8, 152.9, 135.1, 128.82, 128.80, 128.6, 86.1, 82.3, 69.8, 39.4, 34.8, 28.2, 16.2, -1.7; HRMS calcd mass for [M+H⁺] 499.2489, found 499.2484.

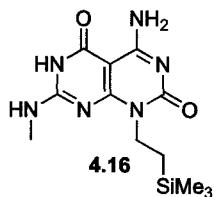
Compound 4.15



(Boc)₂O (210 mg, 0.96 mmol) was added to a solution of **4.14** (0.120 g, 0.240 mmol), Et₃N (0.10 mL, 0.72 mmol) and DMAP (0.030 g, 0.24 mmol) in THF (4 mL). After stirring for 12 h, the reaction was quenched with water and the product was extracted with EtOAc (3x). The combined organic layers were washed successively with saturated aqueous NaHCO₃ solution, water and brine, dried over anhydrous Na₂SO₄, filtered and concentrated. Purification by flash

chromatography on silica gel (15-20% EtOAc in hexanes) provided *t*-butyl 4-(benzyloxy)-5-(*di-tert*-butylaminodicarbonate)-7-oxo-8-(2-(trimethylsilyl)ethyl)-7,8-dihydropyrimido[4,5-*d*]pyrimidin-2-yl(methyl)carbamate (**4.15**) (0.135 g, 79%) as a white foam. $R_f = 0.67$ (50% EtOAc in hexanes); $^1\text{H NMR}$ (300 MHz, CDCl_3): $\delta = 7.44\text{--}7.32$ (m, 5H), 5.57 (s, 2H), 4.37-4.34 (m, 2H), 3.47 (s, 3H), 1.59 (s, 9H), 1.32 (s, 18H), 1.09-1.06 (m, 2H), 0.09 (s, 9H); $^{13}\text{C NMR}$ (100 MHz, CDCl_3): $\delta = 165.7, 161.1, 160.5, 159.9, 155.4, 152.5, 149.2, 134.9, 128.5, 128.43, 128.39, 93.0, 83.5, 82.8, 69.9, 40.5, 34.8, 28.1, 27.8, 15.8, -1.7$; HRMS calcd mass for $[\text{M}+\text{Na}^+]$ 721.3357, found 721.3351.

4-amino-7-(methylamino)-1-(2-(trimethylsilyl)ethyl)pyrimido[4,5-*d*]-pyrimidine-2,5(1*H*,6*H*)-dione (4.16**)**



A solution of **4.15** (0.200 g, 0.286 mmol) in 4*N* HCl in dioxane (1.5 mL) was stirred for 4 h at 45°C. The solution was then concentrated and Et₂O was added. The resulting mixture was centrifuged and the solid was collected, washed with Et₂O and centrifuged again. After repeating the process 3 times, the white solid was dried under high vacuum to provide **4.16** (0.088 g, 80%); $^1\text{H NMR}$ (400 MHz, d_6 -DMSO): $\delta = 12.23$ (bs, 1H), 9.14 (s, 1H), 8.55 (s, 1H), 8.01 (s, 1H), 4.08 (m, 2H), 2.93 (s, 3H), 0.94 (m, 2H), 0.04 (s, 9H); $^{13}\text{C NMR}$ (100 MHz, d_6 -DMSO): $\delta = 161.6, 159.7, 156.0, 155.8, 147.7, 82.4, 69.9, 27.9, 15.6, -1.9$; HRMS calcd mass for $[\text{M}+\text{H}^+]$ 309.1490, found, 309.1493; elemental analysis calcd (%) for $\text{C}_{12}\text{H}_{20}\text{N}_6\text{O}_2\text{Si}(\text{H}_2\text{O})_{1/3}(\text{Et}_2\text{O})_{1/3}(\text{HCl})_{4/3}$ C, 41.30, H, 6.59, N, 21.67, found, C, 41.27, H, 6.25, N, 21.44.

4.6. References

1. Lehn, J-M. *Supramolecular chemistry*, VCH, New York, **1995**.
2. (a) Johnson, R. S.; Yamazaki, T.; Kovalenko, A.; Fenniri, H. *J. Am. Chem. Soc.* **2007**, *129*, 5735-5743. (b) Ikeda, M.; Nobori, T.; Schmutz, M.; Lehn, J-M. *Angew. Chem. Int. Ed.* **2005**, *11*, 662-668. (c) Engelkamp, H.; Middelbeek, S.; Nolte, R. J. M. *Science* **1999**, *284*, 785-788. 14. (d) Schenning, A. P. H. J.; Jonkheijm, P.; Peeters, E.; Meijer, E. W. *J. Am. Chem. Soc.* **2001**, *123*, 409-416. (e) Jeukens, C. R. L. P. N.; Jonkheijm, P.; Wijnen, F. J. P.; Gielen, J. C.; Christianen, P. C. M.; Schenning, A. P. H. J.; Meijer, E. W.; Maan, J. C. *J. Am. Chem. Soc.* **2005**, *127*, 8280-8281.
3. (a) Marsh, A.; Silvestri, M.; Lehn, J. M. *Chem. Commun.* **1996**, *35*, 1527-1528. (b) Mascial, M.; Hext, N. M.; Warmuth, R.; Moore, M. H.; Turkenburg, J. P.; *Angew. Chem. Int. Ed.* **1996**, *35*, 2204-2205. (b) Mascial, M.; Hext, N. M.; Warmuth, R.; Arnall-Culliford, J. R.; Moore, M. H.; Turkenburg, J. P.; *J. Org. Chem.* **1999**, *64*, 8479-8484.
4. (a) Fenniri, H.; Deng, B. L.; Ribbe, A. E.; Hallenga, K.; Jacob, J.; Thiyagarajan, P. *Proc. Natl. Acad. Sci.* **2002**, *99*, 6487-6492. (b) Fenniri, H.; Mathivanan, P.; Vidale, K. L.; Sherman, D. M.; Hallenga, K.; Wood, K. V.; Stowell, J. G. *J. Am. Chem. Soc.* **2001**, *123*, 3854-3855. (c) Fenniri, H.; Deng, B. L.; Ribbe, A. E. *J. Am. Chem. Soc.* **2002**, *124*, 11064-11072.
5. Moralez, J. G.; Raez, J.; Yamazaki, T.; Motkuri, R. K.; Kovalenko, A.; Fenniri, H. *J. Am. Chem. Soc.* **2005**, *127*, 8307-8309.
6. Moralez, J. G. *PhD thesis*, Purdue University, USA, **2005**.
7. The synthesis of compound **2.50** has been discussed in Chapter 2, Figure 2.13.
8. The synthesis of compound **2.21** has been discussed in Chapter 2, Figure 2.6.
9. See synthetic scheme in Figure 2.3 from Chapter 2.
10. Beingessner, R. L.; Hemraz, U. D.; Moralez, J. G.; Haque, A.; Mathivanan, P.; Fenniri, H. *Application of homoallyl as a new amide protecting group*, manuscript in preparation.
11. (a) Kovalenko, A. Three-dimensional RISM theory for molecular liquids and solid-liquid interfaces, in: *Molecular Theory of Solvation*, Hirata, F. (ed.) Series:

- Understanding Chemical Reactivity*, Vol. 24, Mezey, P.G. (ed.) Kluwer Academic Publishers, Dordrecht, **2003**, 169-275. (b) A. Kovalenko, A.; Hirata, F. *J. Chem. Phys.* **1999**, *110*, 10095-10112. (c) Kovalenko, A.; Hirata, F. *J. Chem. Phys.* **2000**, *112*, 10391-10417.
12. Hemraz, U. D.; Yamazaki, Beingessner, R. L.; Cho, J. Y.; T.; Kovalenko, A.; Fenniri, H. *Structural and Environmental Factors which Tune the Stability of Rosette Nanotubes Self-Assembled from the Twin GAC Motif*, manuscript in preparation.
13. (a) Briner, B. G.; Doering, M.; Rust, H.-P.; Bradshaw, A. M.; *Science* **1997**, *278*, 257-260. (b) Heinrich, A. J.; Lutz, C. P.; Gupta, J. A.; Eigler, D. M. *Science* **2002**, *298*, 1381-1387. (c) Xu, Q. M.; Han, M. J.; Wan, L. J.; Wang, C.; Bai, C. L.; Dai, B.; Yang, J. L. *Chem. Commun.* **2003**, 2874-2875.
14. (a) Hwang, T.-L.; Shaka, A. J. *J. Am. Chem. Soc.* **1992**, *114*, 3157-3159. (b) Hwang, T.-L.; Shaka, A. J. *J. Magnetic Resonance Series B*, **1993**, *102*, 155-165.
15. (a) Widom, B.; Bhimalapuram, P.; Koga, K. *Phys. Chem. Chem. Phys.* **2003**, *5*, 3085-3093. (b) Pratt, L. R.; Pohorille, A. *Chem. Rev.* **2002**, *102*, 2671-2692. (c) Southall, N. T.; Dill, K. A.; Haymet, A. D. J. *J. Phys. Chem. B.* **2002**, *106*, 521-533. (d) Southhall, N. T.; Dill, K. A. *Biophys. Chem.* **2002**, *101*, 295-307. (e) Dill, K. A. *Biochemistry*, **1990**, *29*, 7133-7155.
16. a) I. Persson. *Pure & Appl. Chem.* **1986**, *58*, 1153-1161; b) C. Reichardt, *Solvents and Solvent Effects in Organic Chemistry*, Wiley-VCH, Germany, **2003**, pp 1-629. Kelly, C. P.; Cramer, C. J.; Truhlar, D. G. *J. Phys. Chem. B.* **2006**, *110*, 16066-16081.
17. Reichardt, C. *Solvents and Solvent effects in Organic Chemistry*, Wiley-VCH, Germany, **2003**, 1-629.
18. (a) Placzek, A.; Grzybowski, W.; Hefter, G. *J. Phys. Chem. B* **2008**, *112*, 12366-12373. (b) Marcus, Y. *Chem. Rev.* **2007**, *107*, 3880-3897. (c) Marcus, Y.; Hefter, G. *Chem. Rev.* **2004**, *104*, 3405-3452.

Chapter 5

Self-assembling system with four GAC bicycles

5.1. Introduction

So far we had investigated the self-assembly of systems with single and double GAC units.¹ Though both systems have the built-in ability to engage in intermolecular hydrogen-bonding, the twin base system gives more stable RNTs at a faster rate due to lower functional group density, reduced net charge, enhanced stability arising from preorganization, increased amphiphilic character, greater number of H-bonds per module, higher H-bonds per rosette (36 H-bonds instead of 18), less steric congestion and lower electrostatic repulsion.^{1f} This design of the twin RNTs is so robust that it can withstand big steric bulk and other competing interactions such as π - π interactions on the periphery of the RNTs as seen in the case of the Acr-TBL variant in Chapter 2.² While on a quest to develop systems which could outweigh the twin base system, we probed systems having more than two GAC units within one molecule.

In this chapter, we designed a molecule (GAC-4) bearing four GAC moieties connected through an alkyl chain. Unlike the single and twin GAC motifs that have six and twelve sites available for intermolecular hydrogen bonding, the GAC-4 module boasts up to twenty-four H-bonds per molecule (Figure 5.1). Based on this design, though a number of possible modes of interactions could be possible in solution, it was difficult to predict which one would prevail for tetra-GAC system due to a number of favourable and unfavourable intramolecular interactions. In addition, the study of this new system could shed light on how the GAC core behaves when interacting with more than one GAC moiety within the same molecule.

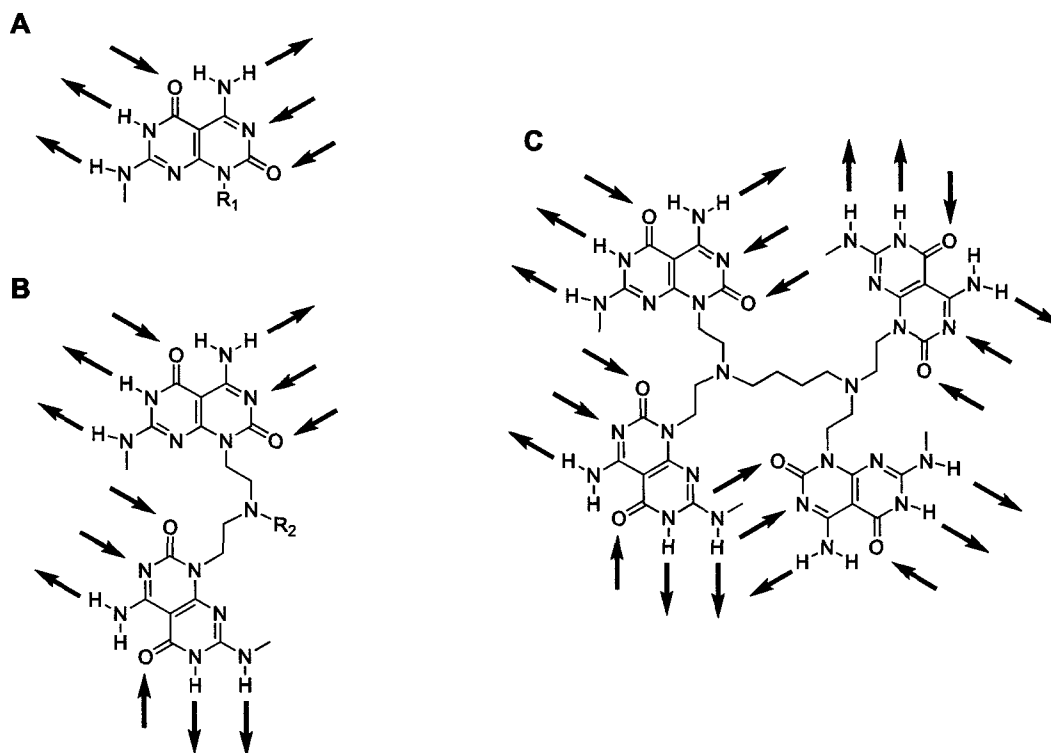


Figure 5.1: Hydrogen bonding patterns in single (A), twin (B) and tetra (also named G \wedge C-4, C) G \wedge C systems.

The G \wedge C-4 module (**5.3**) was synthesized in 2 steps starting from G \wedge C aldehyde **2.13**^{1a} (Figure 5.2). The latter was coupled with the commercially available butane-1,4-diamine through a reductive amination reaction. Though this coupling procedure was quite lengthy, it was possible to obtain the protected tetra-G \wedge C compound **5.2** in 62% yield. Removal of the protecting groups under harsh acidic conditions, followed by anion exchange from the trifluoroacetate salt to the chloride salt using a 1 M hydrochloric acid gave rise to the desired G \wedge C-4 module **5.3** as the hydrochloride salt in quantitative yield.

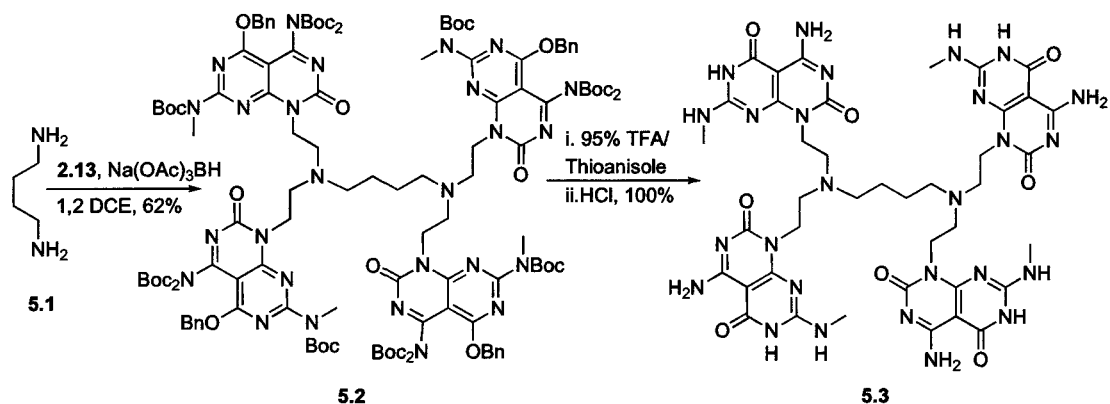


Figure 5.2: Synthetic scheme for the formation of the GAC-4 module

The investigation of the self-assembling ability of the GAC-4 module (5.3) required the dissolution of the compound in different solvents. An initial solubility test indicated that this compound had limited solubility in water and methanol compared to compounds having the single and double GAC fragments. This was most probably due to the absence of solubilising functional groups. As such, sample manipulation and solubility posed a major challenge.

5.2. Characterization of the GAC-4 module in solution

Stock solution of GAC-4 module 5.3 was prepared in water at a concentration of 0.25 mg/mL and was aged for 1 day. At this concentration, the compound was not fully dissolved and existed as a suspension though sonication and heating were used to aid the solubility. An aliquot of the stock solution (2.0 μ L) was deposited on carbon-coated TEM grids. The sample was then visualized using SEM imaging.

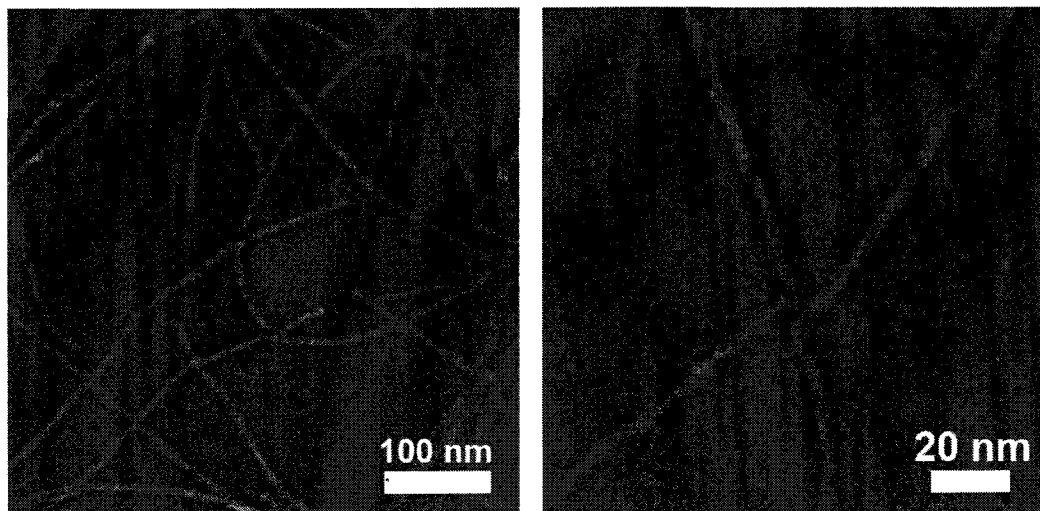


Figure 5.3: SEM images of GAC-4 module 5.3 in water

The stock solution was also cast on a freshly cleaved mica surface for visualization of the morphology by AFM imaging.

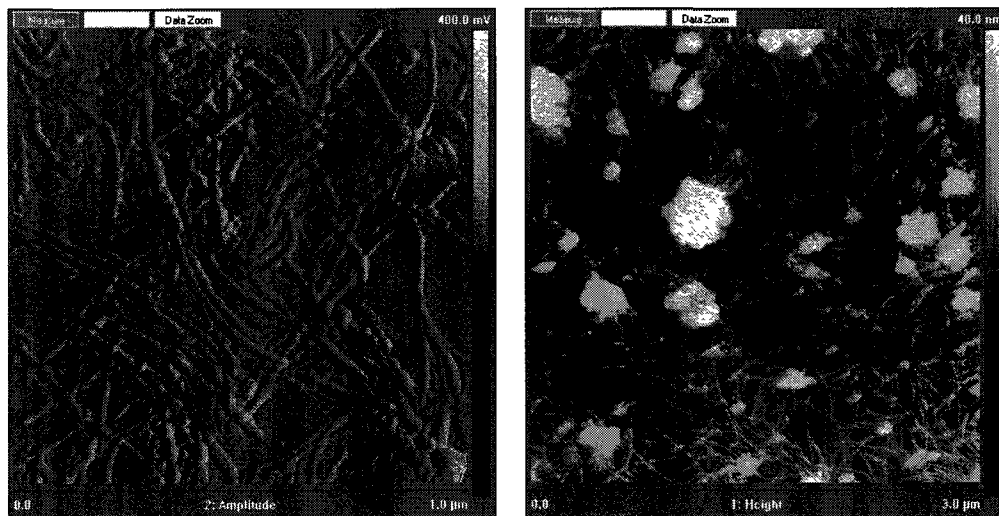


Figure 5.4: AFM images of the GAC-4 module 5.3 in water

These nanostructures looked larger in diameter than the single or twin RNTs both by SEM and AFM imaging. For a better visual comparison of the dimensions of these aggregates, GAC-4 and But-TBL³ modules were imaged on the same carbon-coated TEM grid. This was done by first casting a diluted But-TBL RNT solution (0.0125 mg/mL). The excess solution was blotted and an aliquot of the

GAC-4 solution in water was then deposited on the dried grid. Again the excess solution was blotted and the sample was then imaged by SEM.

From the SEM images, there seemed to be two distinct dimensions for the nanostructures. While But-TBL had a diameter 3.5 ± 0.2 nm (obtained from TEM measurements), the GAC-4 module appeared larger in diameter.

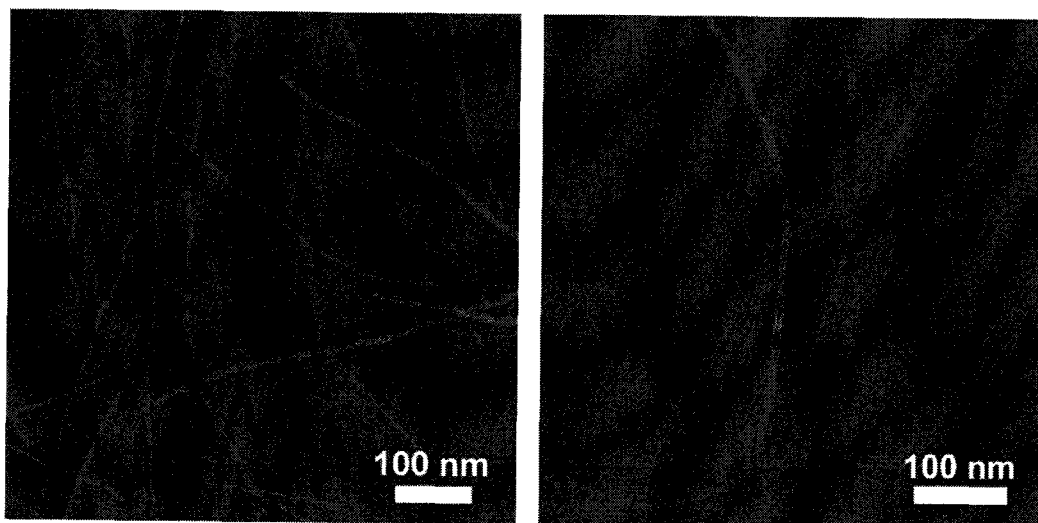


Figure 5.5: SEM images of the GAC-4 (5.3) and But-TBL modules in water cast on the same grid.

The GAC-4 module was also studied in DMSO, in which it had a higher solubility than in water. Stock solution of the salt was prepared in DMSO at a concentration of 0.25 mg/mL and was aged for 1 day. An aliquot of the stock solution (2.0 μ L) was deposited on carbon-coated TEM grids. The sample was then visualized by SEM. On certain parts of the grid, this concentration seemed to be too high to fully evaluate the type of nanostructures formed (Figure 5.6), thus part of the sample was diluted to 0.05 mg/mL.

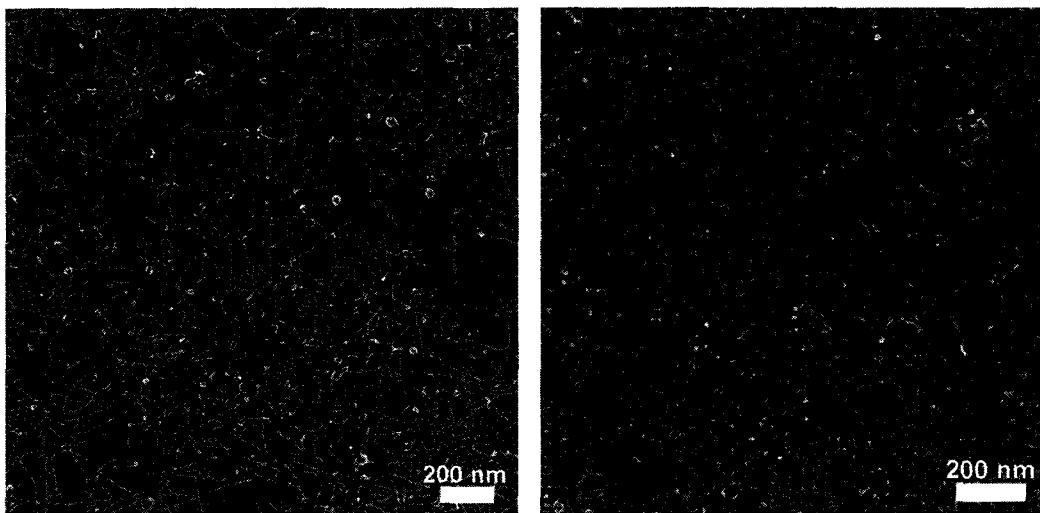


Figure 5.6: SEM images of the G \wedge C-4 5.3 in DMSO (0.25 mg/mL)

At this diluted concentration in DMSO, a better picture of the self-assembly occurring in solution was obtained (Figure 5.7). Though SEM imaging is not the best technique for estimating the dimensions, the nanostructures were similar in size as the ones obtained in water. However, unlike in water where the structures look more discrete, in DMSO the nanostructures had a tendency to bundle.

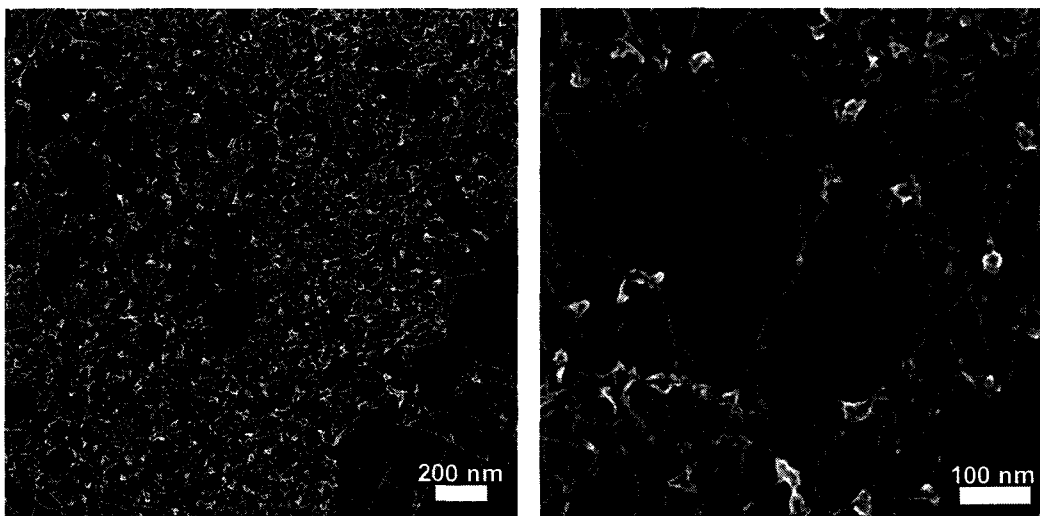


Figure 5.7: SEM images of the G \wedge C-4 5.3 in DMSO (0.05 mg/mL)

The G \wedge C-4 5.3 was also studied in methanol and unlike the solvents discussed previously the solubility in methanol was very minimal. Stock solution of the salt

was prepared in methanol at a concentration of 0.1 mg/mL and was aged for 1 day. Despite heating and sonicating the suspension to aid dissolution, the solubility of the compound did not seem to improve. Nevertheless, an aliquot of the stock solution (2.0 μ L) was deposited on carbon-coated TEM grids. The sample was then imaged by SEM. Since no nanostructures were observed after aging for 1 day, the sample was aged for 14 days. The older sample was cast on a TEM grid and imaged by SEM. This sample was more difficult to image due to the presence of insoluble material. Still, the presence of nanostructures seemed quite obvious (Figure 5.8). These aggregates appeared to have similar dimensions as the single or twin RNTs (about 4 nm).

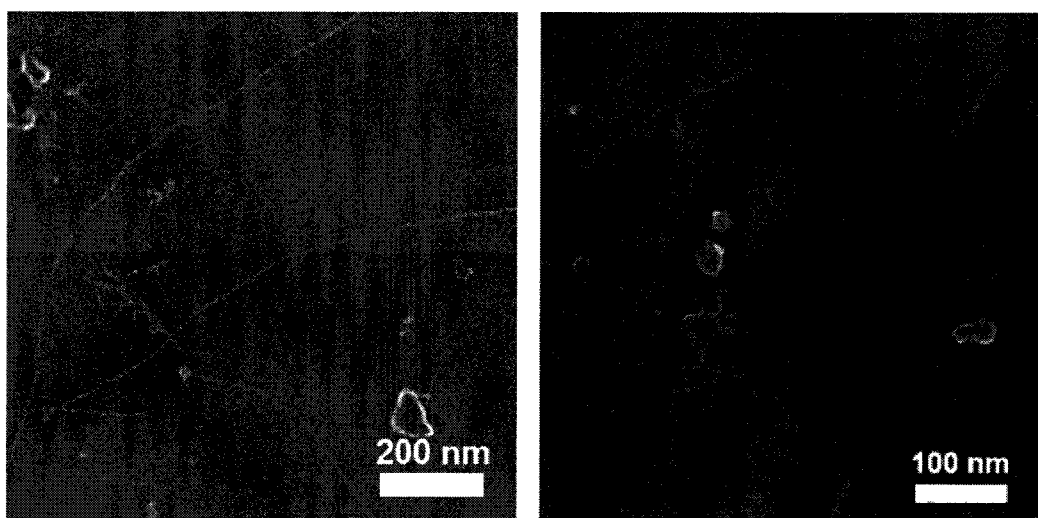


Figure 5.8: SEM images of the GAC-4 5.3 in methanol

For a better comparison of the dimensions of the nanostructures resulting from the GAC-4 module in water and methanol, TEM imaging was required. However due to the presence of a lot of insoluble material in the methanolic sample, it was difficult to conduct both TEM and AFM imaging. As a result, only the water samples were successfully visualized using TEM (Figure 5.9). For TEM, the sample was prepared in a similar fashion as for the SEM sample in water. The cast sample was then stained using 2% uranyl acetate solution in water. The TEM images showed aggregates with an average diameter of 7.3 ± 0.3 nm. This

measured value is about twice the measured diameter for But-TBL (3.5 ± 0.2 nm). Initially it was speculated that this higher value corresponded to the diameter of the self-assembled structures, however a more careful analysis of the TEM data revealed images that this larger structure was actually made up of two thinner aggregates. The average diameter of these smaller aggregates was 3.2 ± 0.1 nm. This dimerization in water could be an attempt to minimize the interaction of the hydrophobic pockets with the water molecules.

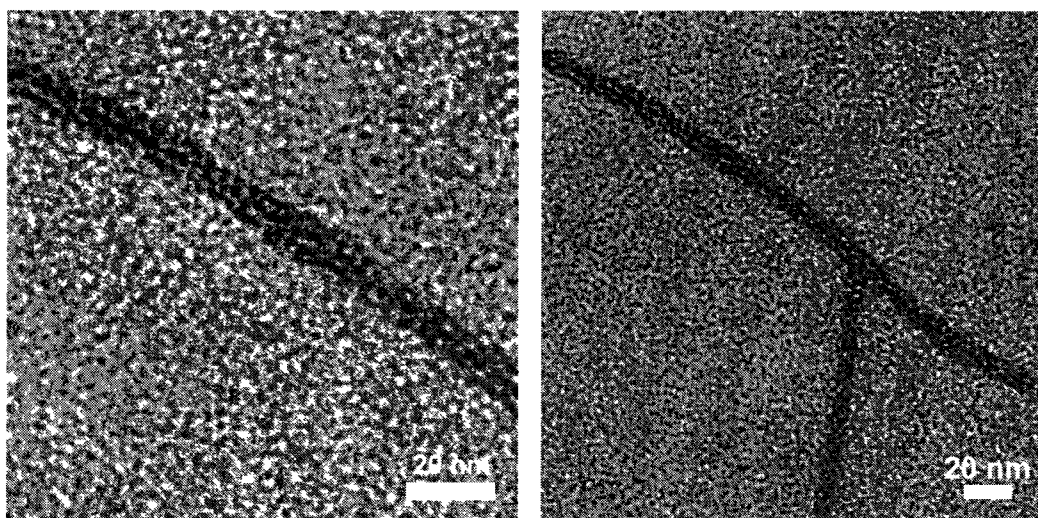


Figure 5.9: TEM images of the G \wedge C-4 5.3 in water

5.3. Molecular modeling of the G \wedge C-4 module

Molecular modeling⁴ was used in an attempt to predict how the compound was self-assembling. The computation section was conducted by Dr Takeshi Yamazaki. The conformational search for G \wedge C-4 module in the case of models 1-3 have been done in the gas phase, and therefore most of the atomic sites which carry relatively large partial charges try to establish coulombic interactions with each other.

5.3.1. Model 1

Starting from the initial structure shown below (Figure 5.10), the conformational search for this motif was carried out in gas phase, with fixing one side of two

G \wedge C bases and the conformation around the nitrogen atom linking the two G \wedge C bases (circled part) as in the case of the twin G \wedge C system. For the other two G \wedge C bases, the separation distance was the only constraint put on that part. The conformational search was then carried out.

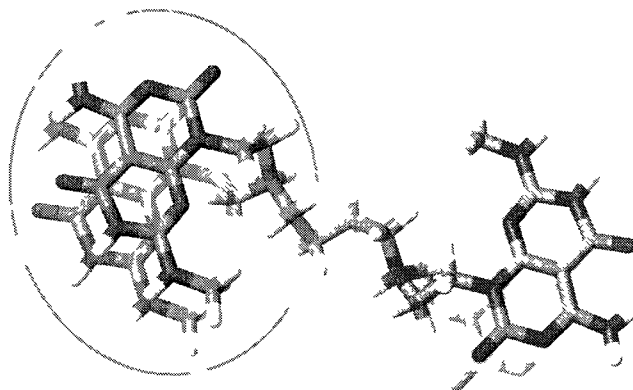


Figure 5.10: Initial structure of the G \wedge C-4 module from model 1

The most stable conformation obtained is shown in Figure 5.11. It appeared that there were strong hydrogen bonds between the ammonium ion and the cytosine oxygen, and between the cytosine oxygen and guanine NH₂.

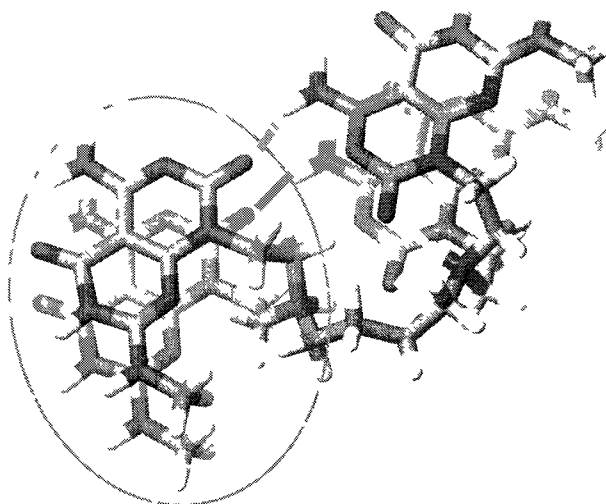


Figure 5.11: Most stable conformation of the G \wedge C-4 module obtained from the above set parameters from model 1.

Based on this conformation, a rosette consisting of four motifs was made (Figure 5.12). In this rosette, the motifs were arranged in such a way that they could have intermolecular hydrogen bonds. The outer diameter of this ring was found to be 3.6 nm, which is close to the diameter value obtained from the TEM measurements in water. However, this arrangement was unlikely because of the symmetry of the H-bonds formed. In addition, this structure did not exploit the number of hydrogen-bonding sites fully.

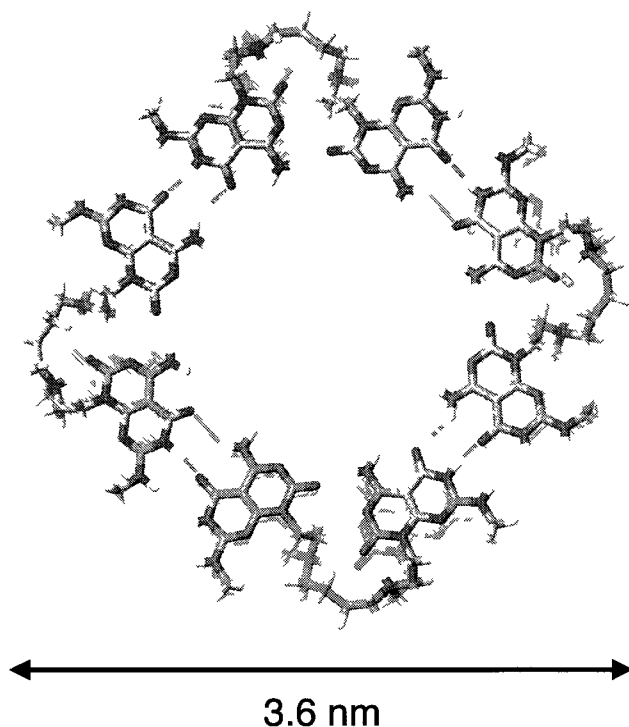


Figure 5.12: Rosette ring from the most stable conformation of the G \wedge C-4 module from model 1.

5.3.2. Model 2

Another conformational search was carried out whereby the only constraint imposed on the monomer was the G \wedge C base separation. The most stable motif was symmetric (Figure 5.13) and it had intramolecular hydrogen bond between the ammonium ion (the nitrogen is protonated) and the oxygen. From this conformer, a helical arrangement of the monomer was obtained whose diameter

ranged from 3.5-7 nm (Figure 5.14). While this structure seemed very interesting, it was quite unlikely to prevail since the interactions binding the structure together were relatively weak, hence more likely to collapse upon solvent interactions.

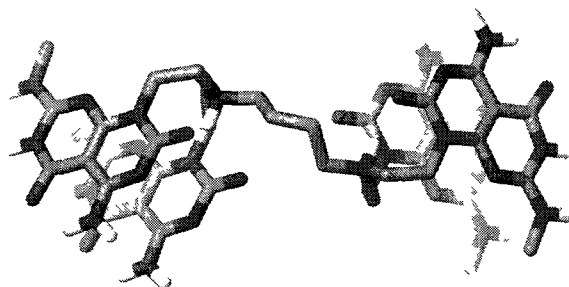


Figure 5.13: Most stable symmetrical conformation of the G^AC-4 module (from model 2), while maintaining only the G^AC base separation.

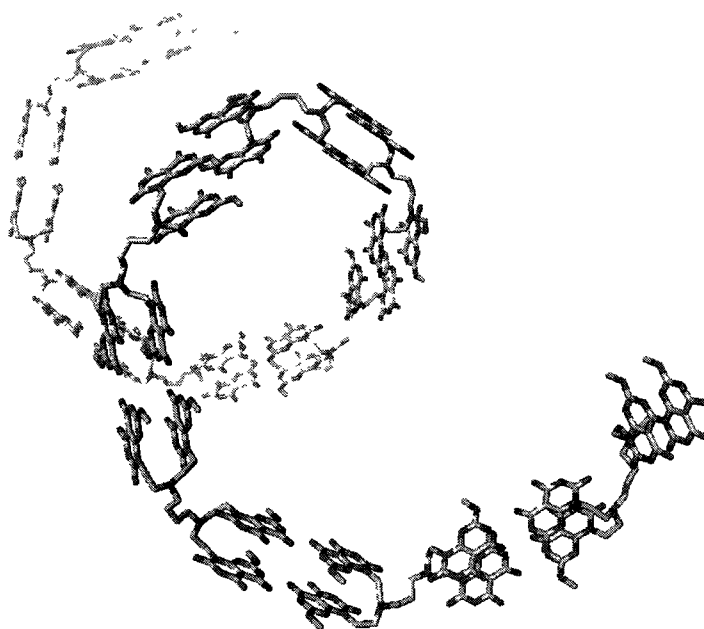


Figure 5.14: Helical tube of the G^AC-4 module from model 2

5.3.3. Model 3

Another conformational search of the G^AC-4 module was carried out in water and the conformer obtained is shown in Figure 5.15. In this structure, there was no

hydrogen bond between the ammonium ion and the oxygen atoms. The hydrogen atom of ammonium ion was facing outside to interact with water. Based on this structure, a rosette ring and rosette nanotube were constructed (Figure 5.16).



Figure 5.15: Most stable conformation of the GAC-4 module in water from model 3.

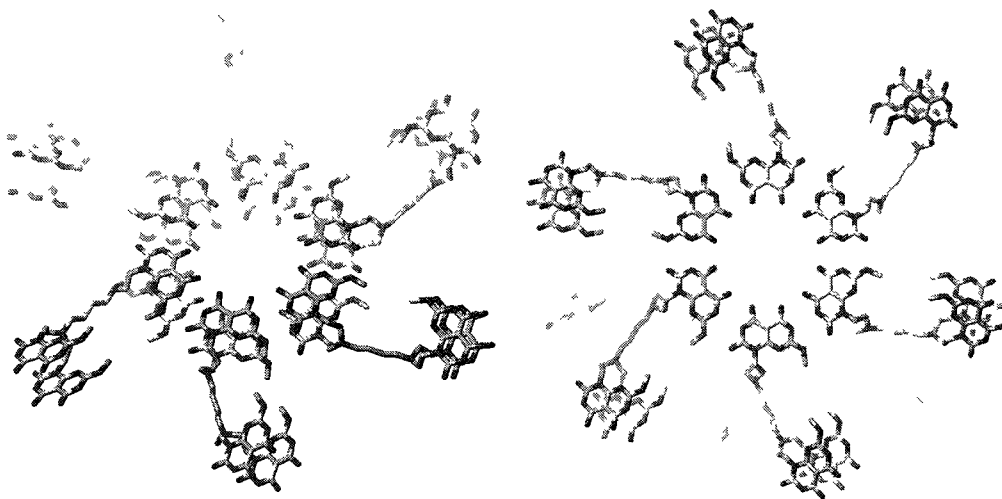


Figure 5.16: Different views of a rosette constructed from the self-assembly of six GAC-4 modules in water from model 3.

A tube with an outer diameter of 5.1 nm was obtained (Figure 5.17). This arrangement was unlikely in our case since two of its four GAC units were not engaged in the rosette formation. As such, these free hydrogen-bond donor and acceptor sites might engage in inter- and intramolecular hydrogen bonding and, instead of having discrete architectures, a network was most likely to prevail.

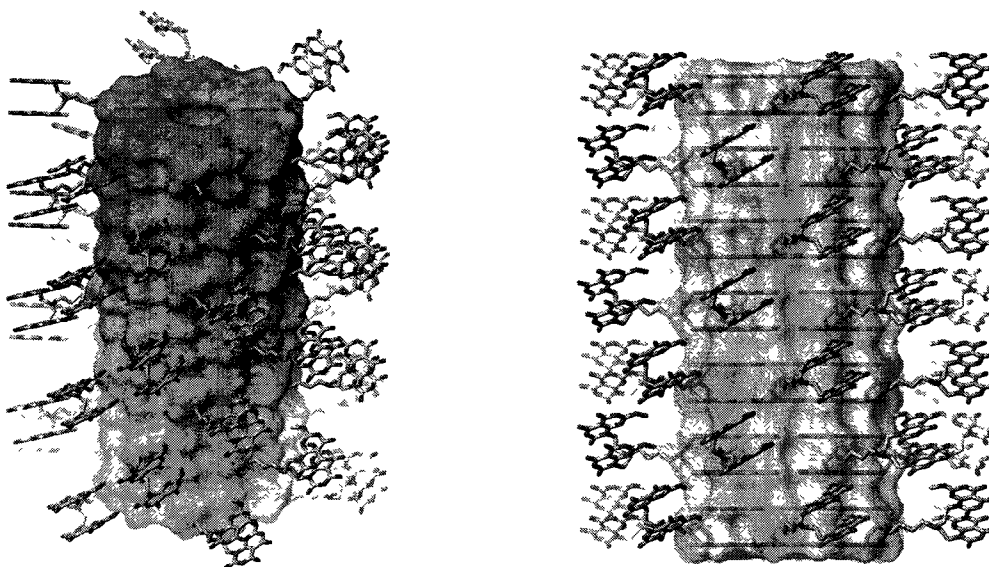


Figure 5.17: Different views of a nanotube constructed from the stacking of the rosettes shown in water from model 3.

5.3.4. Model 4

We envisaged that the most simple way that the system could yield a diameter value in agreement with the TEM measurements (3.2 ± 0.1 nm) was to mimic the self-assembly of the twin base system. In the latter, the two G \wedge C motifs from one molecule of a twin RNT monomer stack by adopting a syn conformation. Six molecules of the twin RNT monomer then formed an array of H-bonds to produce a rosette, which was held together by 36 H-bonds.^{1f, 5} In the G \wedge C-4 module, there are four G \wedge C units, which can be considered as a pair of twin G \wedge C stacks tethered by a hydrophobic linker. Due to the favourable π - π interactions between the G \wedge C units and intermolecular hydrogen bonding, we presumed that the four G \wedge C units would stack into a pile. However, the length of the linker also implied that there would be a certain degree of strain exerted on such a structure due to the limited flexibility. In an attempt to counter-attack this strain, the G \wedge C units would align themselves in a displaced stacking fashion. Six molecules of the G \wedge C-4 compound (each adopting a 4-fold stack) would then form a hexamer, held together by 72 H-bonds. This hypothesis was verified computationally.

Starting from a quad-rosette ring consisting of all-syn stack motifs, the geometry of the ring was optimized in water / Cl^- model with a nitrogen-nitrogen distance of 3.0 Å. A stacking distance of 3.3 Å was used between the two twin GAC systems (Figure 5.18), similar to the inter-rosette distance in single and twin GAC system. The stacking distance between the first and second GAC units were maintained at 3.9 Å, as in the case of the twin GAC system.

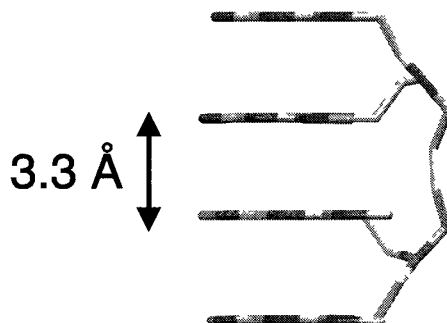


Figure 5.18: Side view of an all-syn quad-rosette from the GAC-4 monomer, showing a stacking distance of 3.3 Å between the second and third GAC moieties (model 4).

Using this unoptimized conformation, a quad-rosette ring was constructed using six GAC-4 molecules (Figure 5.19), such that each molecule would be involved in 24 H-bonds. With this arrangement, there was an optimal use of the hydrogen-bond donor and acceptor sites. There were 72 H-bonds per rosette.

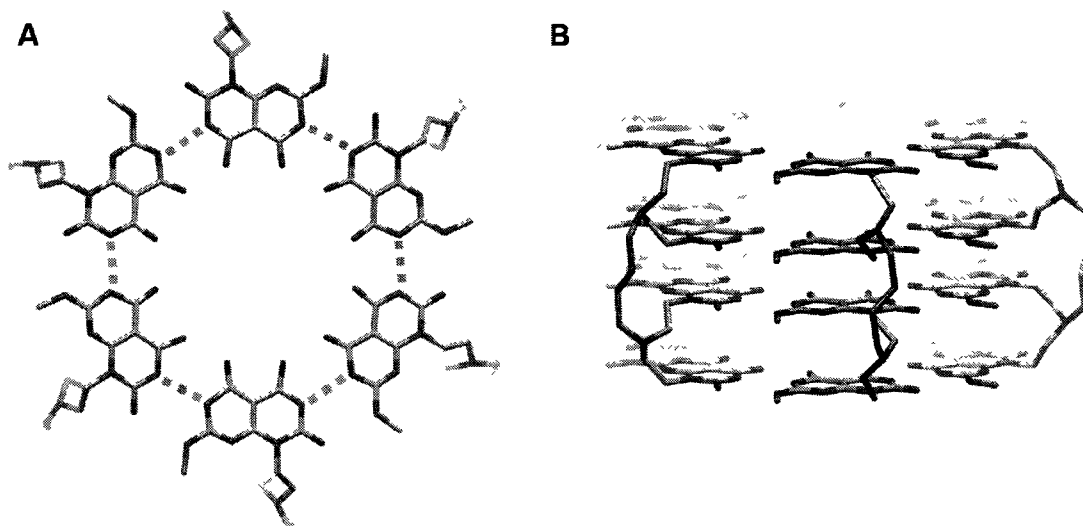


Figure 5.19: Top view, showing only the first rosette ring (A) and side view (B) of the unoptimized quad-rosette ring from $G\wedge C-4$ (model 4).

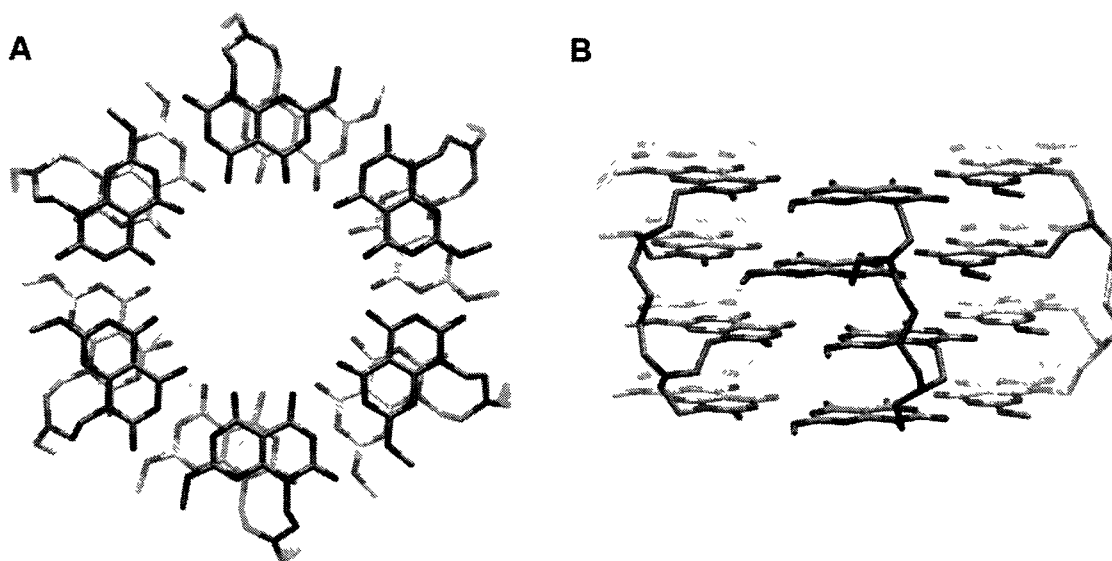


Figure 5.20: Top view (A) and side view (B) of the optimized quad-rosette ring with a syn-syn-syn conformation from $G\wedge C-4$ (model 4).

Upon optimization, it was found that the $G\wedge C$ units aligned themselves in a displaced stacking fashion, as suspected. This was clearly visible from the arrangement of the methyl groups, which adopted a zig-zag type of alignment (Figure 5.20). In this conformation, all the $G\wedge C$ units are syn to each other (syn-

syn-syn or SSS) and the outer diameter of this quad-rosette was calculated to be 3.1 nm.

A similar quad-rosette ring was constructed with a syn-anti-syn (SAS) arrangement of the GAC moieties (Figure 5.21) to give a rosette ring with an outer diameter of 3.1 nm.

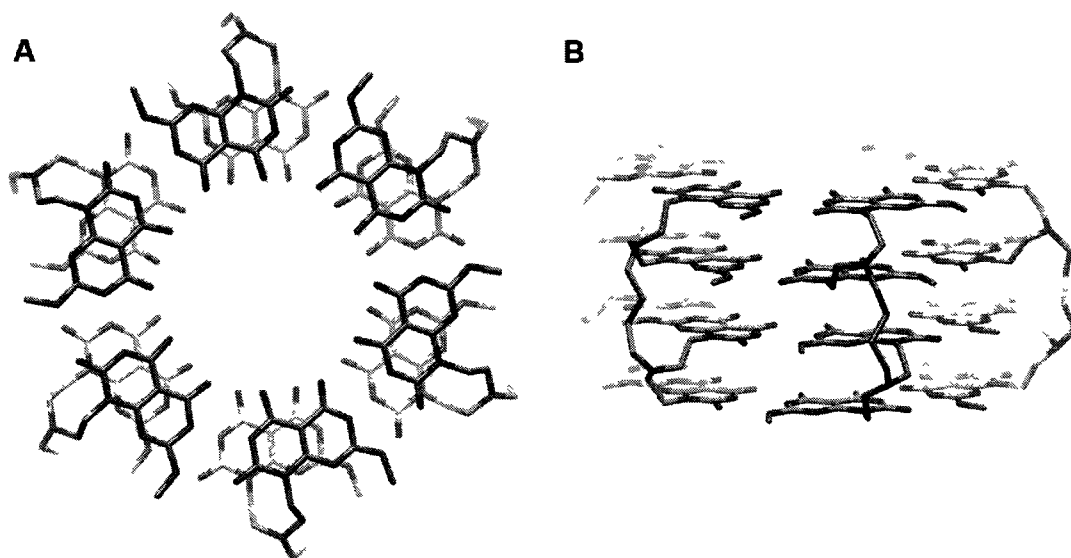


Figure 5.21: Top view (A) and side view (B) of the optimized quad-rosette ring with a syn-anti-syn conformation from GAC-4 (model 4).

Nanotubes (with an outer diameter of 3.1 nm) constructed from quad rosettes of SSS and SAS arrangements are shown below (Figure 5.22).

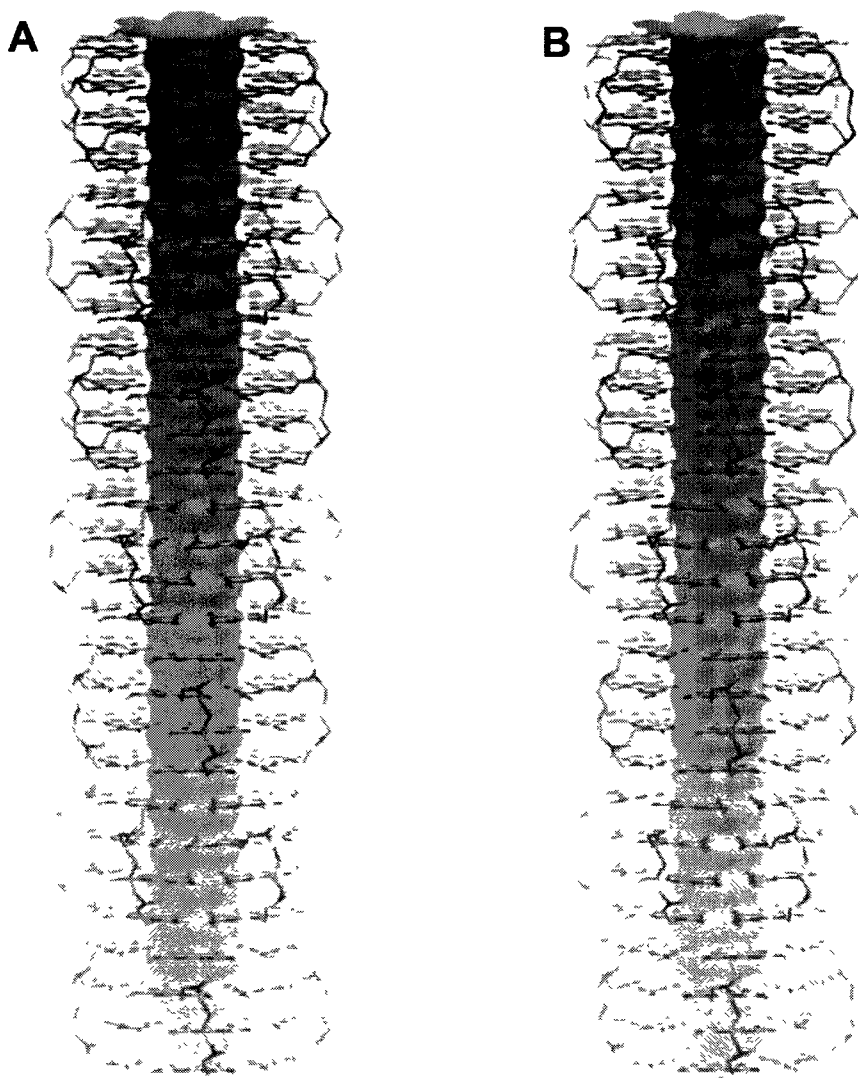


Figure 5.22: Nanotubes made up of 7 quad-rosettes from G \wedge C-4 module with SSS (A) and SAS (B) arrangements of the G \wedge C units. In both cases, the calculated diameters of the nanotubes were 3.1 nm.

The negative association free energies of the nanotubes obtained from the stacking of 7 quad-rosettes with SSS and SAS arrangements (in water and Cl⁻) imply that the formation of such superstructures is experimentally possible (Figure 5.23).

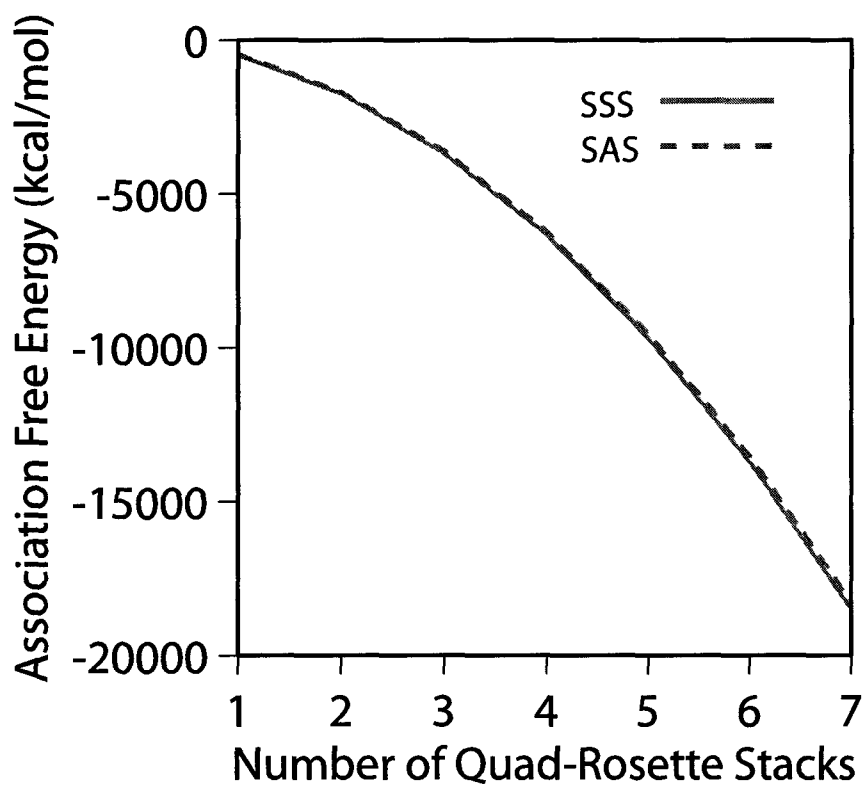


Figure 5.23: Association free energies of nanotubes from G \wedge C-4 module with SSS and SAS arrangements of the G \wedge C units with increasing number of rosette stacks.

To gain more insight on the stability of these nanostructures from G \wedge C-4, their association free energies (Figure 5.26) was compared to the twin G \wedge C motif NH-TBL.⁵ The stacking arrangements adopted by SSS G \wedge C-4, SAS G \wedge C-4 and NH-TBL are shown in Figure 5.24, which were used to construct the nanotubes (Figure 5.25)

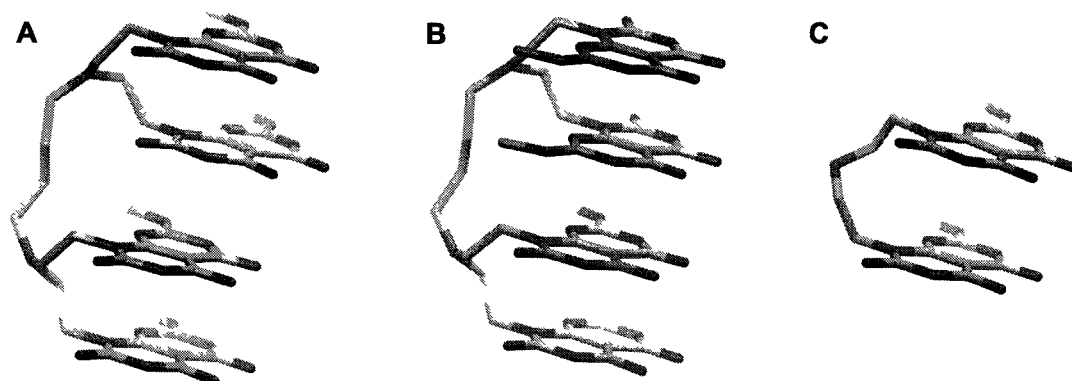


Figure 5.24: Molecular conformation adopted by SSS $G\Delta C-4$ (A), SAS $G\Delta C-4$ (B) and NH-TBL (C)

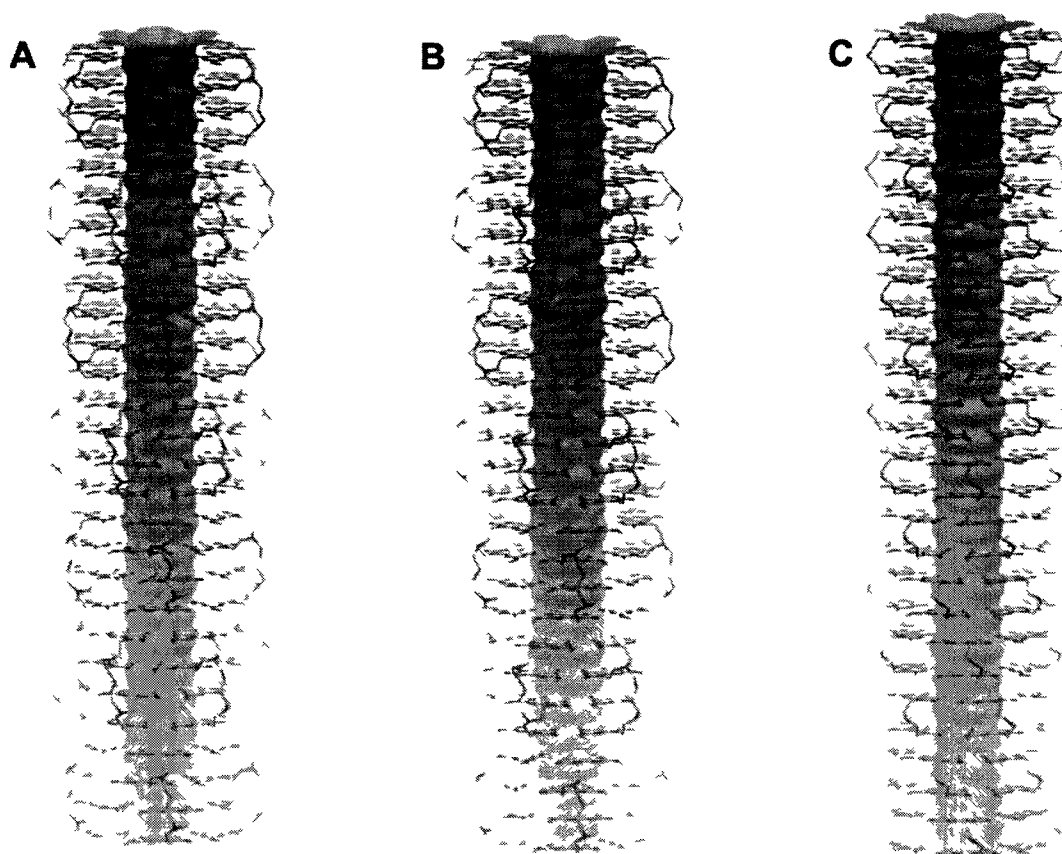


Figure 5.25: Nanotubes made up of 7 quad-rosettes from $G\Delta C-4$ module with SSS (A) and SAS (B) arrangements of the $G\Delta C$ units, and nanotube derived from NH-TBL (C), generated by the stacking of 14 twin-rosettes.

The association free energies of $G\Delta C-4$ module with SSS and SAS arrangements

of the G \wedge C units and NH-TBL were calculated and compared. In an attempt to make a valid comparison, each G \wedge C-4 rosette ring accounted for two twin rosette rings.

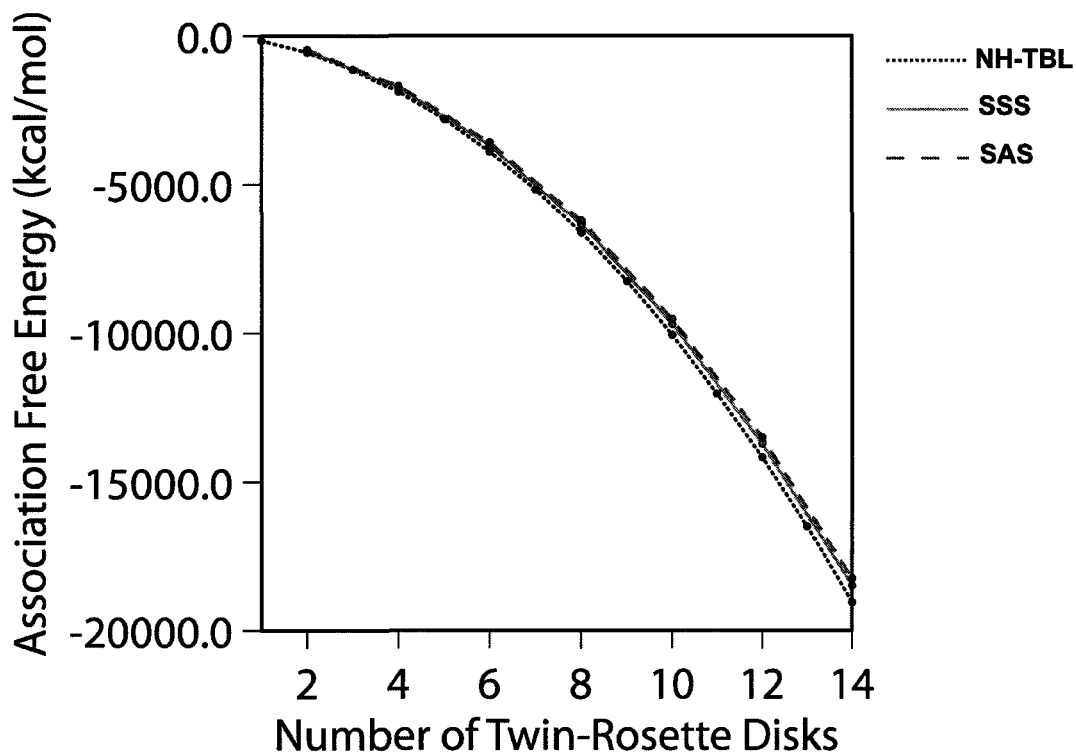


Figure 5.26: Comparison of association free energies of nanotubes from G \wedge C-4 module with SSS and SAS arrangements of the G \wedge C units with increasing number of rosette stacks (up to 7 stacks), and association free energy of NH-TBL (up to 14 stacks).

From the association free energy plot, it was found that NH-TBL and the two possible conformers of G \wedge C-4 module had comparable stabilities. This result was very promising since the G \wedge C-4 motif gave a stable association free energy in spite of having a fairly strained structure, originating from the hydrophobic butyl linker.

5.4. Conclusion

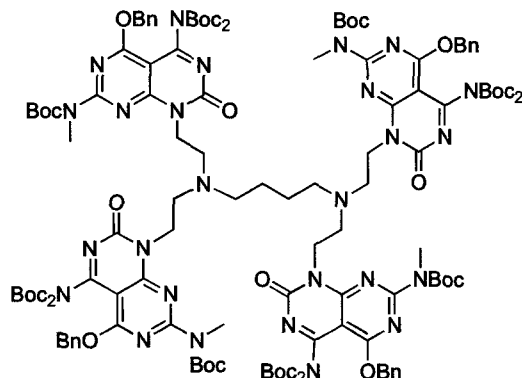
A new self-assembling molecule (G \wedge C-4) having four G \wedge C moieties was synthesized, which displayed different types of morphologies depending on the solvents. TEM results revealed that the larger aggregates formed in water were actually made of two thinner tubes, implying that a similar mode of self-assembly existed in methanol and water. The most plausible mechanism for self-assembly was model 4. Using molecular modeling, two possible molecular conformers were obtained, which could engage in rosette and nanotube formation. The nanotube diameter obtained by TEM measurements (3.2 ± 0.1 nm) was in agreement with the predicted value of 3.1 nm. In both cases, stable association free energies were obtained, which were comparable to the NH-TBL twin base system.

The main goal in making a tetra-G \wedge C system was to improve the stability of such self-assembling systems. Though along the way two possible modes of self-assembly were established, a more detailed study is desired. The main difficulty in handling the G \wedge C-4 module was related to the limited solubility of the G \wedge C-4 motif. The design and synthesis of analogues with improved solubility can be achieved by substituting the alkyl chain connecting all the G \wedge C units with an ether linkage. Another way to tweak the solubility properties is to change the substitution on the exocyclic nitrogen of the G \wedge C moiety.

With the current structure, the scope of the G \wedge C-4 module is fairly limited. However, structural diversity is possible by reductive amination of the G \wedge C aldehyde with functionalized diamines. Since the G \wedge C-4 has a higher number of hydrogen bonds, less steric congestion and lower electrostatic repulsion, the resulting nanotube will be able to support a much higher steric bulk on the periphery of the nanotube than the twin base system. In addition, the proper functionalization of the G \wedge C-4 system will ease sample manipulation due to improved solubility. It is also possible to reduce the strain in the molecule by using a longer linker or another G \wedge C aldehyde derivative.

5.5. Experimental procedure

Compound 5.2

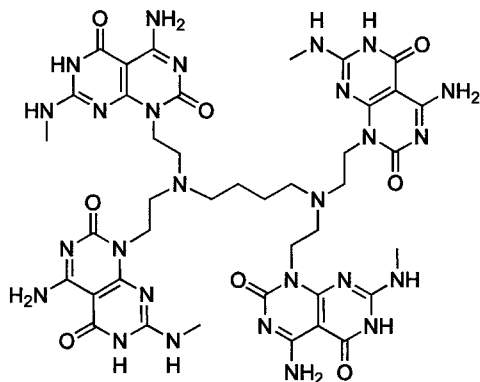


5.2

To a stirred solution of **2.13** (0.200 g, 0.313 mmol) in 1,2 DCE (20 mL), 1,4 diaminobutane (0.015g, 0.170 mmol) was added at room temperature under N₂. The solution was stirred for 30 min before sodium triacetoxy borohydride (0.070 g, 0.333 mmol) was added and the resulting mixture was stirred for an additional 24 h. The reaction mixture was diluted with CH₂Cl₂ (50 mL) and then washed with water (10 mL), NaHCO₃ (10 mL), brine (15 mL), dried over Na₂SO₄ and concentrated. Fresh 1,2 DCE (20 mL) and **2.13** (0.200 g, 0.313 mmol) were then added to the pale yellow foam and stirred. Sodium triacetoxy borohydride (0.075 g, 0.357 mmol) was then added in aliquots (0.025 g each) at 0.5 h, 4 h and 24 h. The resulting solution was stirred for another 24 h. The reaction mixture was diluted with DCM (50 mL) and then washed with water (10 mL), NaHCO₃ (10 mL), brine (15 mL), dried over Na₂SO₄ and concentrated. Flash chromatography of the residue over silica gel (0-70% EtOAc in hexanes) gave **5.2** as a white foam in 62% yield, R_f = 0.53 (70% EtOAc in hexanes); ¹H NMR (500 MHz, CDCl₃): δ = 7.46-7.29 (m, 20H), 5.57 (s, 8H), 4.38 (t, *J* = 7.5 Hz, 8H), 3.50 (s, 12H), 2.88 (t, *J* = 7.5 Hz, 8H), 2.71 (bs, 4H), 1.55 (s, 36H), 1.48 (m, 4H), 1.30 (s, 72H); ¹³C NMR (125 MHz, CDCl₃): δ = 165.5, 161.2, 161.0, 155.5, 152.5, 149.1, 135.0, 128.6, 128.5, 128.5, 128.5, 127.9, 126.9, 92.8, 83.5, 82.8, 70.0, 65.3, 54.8, 51.0, 41.7, 35.0, 28.1, 27.8, 27.8, 25.3; HRMS calcd for C₁₂₈H₁₇₃N₂₆O₃₂[M+H]⁺

2586.2704, found 2586.2716; elemental analysis calcd (%) for $C_{128}H_{172}N_{26}O_{32}$ C, 59.43, H, 6.70, N, 14.08, found C, 59.62, H, 6.83, N, 13.14.

Compound 5.3



Compound 5.2 (0.123 g, 0.048 mmol) was stirred in a 95% TFA in thioanisole (10 mL) for 72 h. Et_2O (60 mL) was then added to the reaction mixture and the precipitate formed, was centrifuged down. The residual solid was resuspended in Et_2O , sonicated and centrifuged down. This process was repeated until the spotting of the Et_2O produced no UV active spot. The white solid was dried under vacuo and was then dissolved in 1 M hydrochloric acid (10 mL), followed by removal of water under reduced pressure. This process was repeated two more times before the solid was dried under vacuo for 72 h to yield the desired compound 5.3 (0.066 g, 100%) as an off-white powder; 1H NMR (600 MHz, d_6 -DMSO): δ = 12.26 (bs, 4H), 9.21 (s, 4H), 8.96 (s, 4H), 8.15 (s, 4H), 4.45 (s, 8H), 3.54 (s, 8H), 3.78 (s, 4H), 3.30 (s, 6H), 2.90 (d, J = 1.8 Hz, 12H), 1.80 (s, 4H); ^{13}C NMR (150 MHz, d_6 -DMSO): δ = 161.2, 160.3, 156.6, 156.2, 148.5, 83.1, 52.0, 49.6, 49.1, 36.7, 28.5; HRMS calcd for $C_{40}H_{53}N_{26}O_8$ $[M+H]^+$ 1025.4534, found 1025.4526; elemental analysis calcd (%) for $C_{40}H_{52}N_{26}O_8(HCl)_8(H_2O)_3(Et_2O)_{0.5}$ C, 35.83, H, 5.08, N, 25.87, found C, 35.32, H, 4.86, N, 25.99.

5.6. References

1. (a) Fenniri, H.; Deng, B. L.; Ribbe, A. E.; Hallenga, K.; Jacob, J.; Thiagarajan, P. *Proc. Natl. Acad. Sci. U.S.A.* **2002**, *99*, 6487-6492. (b) Fenniri, H.; Mathivanan, P.; Vidale, K. L.; Sherman, D. M.; Hallenga, K.; Wood, K. V.; Stowell, J. G. *J. Am. Chem. Soc.* **2001**, *123*, 3854-3855; (c) Tikhomirov, G.; Oderinde, M.; Makeiff, D.; Mansoui, A.; Lu, W.; Heirtzler, F.; Kwok, D. Y.; Fenniri, H. *J. Org. Chem.* **2008**, *73*, 4248-4251. (d) Johnson, R. S.; Yamazaki, T.; Kovalenko, A.; Fenniri, H. *J. Am. Chem. Soc.* **2007**, *129*, 5735-5743. (e) Fenniri, H.; Deng, B. L.; Ribbe, A. E. *J. Am. Chem. Soc.* **2002**, *124*, 11064-11072. (f) Moralez, G.; Raez, J.; Yamazaki, T.; Motkuri, R. K.; Kovalenko, A.; Fenniri, H. *J. Am. Chem. Soc.* **2005**, *127*, 8307-8309.
2. Study of the Acr-TBL analogue is discussed in Chapter 2 (Section 2.3.2).
3. Synthesis and characterization of But-TBL is discussed in Chapter 2.
4. (a) Kovalenko, A. Three-dimensional RISM theory for molecular liquids and solid-liquid interfaces, in: *Molecular Theory of Solvation*, Hirata, F. (ed.) Series: *Understanding Chemical Reactivity*, Vol.24, Mezey, P.G. (ed.) Kluwer Academic Publishers, Dordrecht, (2003), pp.169-275. (b) A. Kovalenko, A.; Hirata, F. *J. Chem. Phys.* **1999**, *110*, 10095-10112. (c) Kovalenko, A.; Hirata, F. *J. Chem. Phys.* **2000**, *112*, 10391-10417.
5. See chapter 2 for a detailed study of the twin base system.

Chapter 6

Peptide modified rosette nanotubes for improved orthopedic applications

6.1. Introduction

The adult human body consists of 206 bones. They provide us with structural support, allow us to move and protect various organs of the body. Our bones behave as ball and socket joints, which control our movements, but if our bones are injured or damaged due to a number of bone disorders such as bone fractures, infections and osteoporosis, these bones no longer function properly. Instead they rub against each other in a very painful manner, due to which surgery is required to replace the damaged parts with artificial implants. These implants are commonly made of the titanium metal or its alloys. Frequently the body does not treat the implant in the same way as it is used to treat the bone and this leads to inflammation, infection and implant loosening. Unlike the natural bone that has the ability to repair itself, the artificial implant cannot do so.¹ Even in cases where the body does not seem to reject the metal implant, the relatively short longevity of orthopedic implants (mainly due to poor bone-implant integration) necessitates revision surgeries. For instance, in 2006 there were nearly 77,000 knee and hip revision surgeries performed in the United States.² The leading cause for implant failure is believed to be insufficient osseointegration – limited bonding between the implant material and the juxtaposed bone.³

Studies have shown that creating nano-surface roughness on artificial implant surfaces can promote bone deposition and this can be achieved by materials with nanoscale surface properties.⁴ One obvious way to tackle the short lifetime of the metal implants is to increase the affinity between the implants and bone cells. This can be achieved by coating the titanium implants with materials that mimic the properties of the bone. The bone is composed of nanoscale constituents such as collagen and hydroxyapatite. As such the design of biologically inspired coating materials that can transform inert titanium surfaces into biomimetic nanostructured interfaces can enhance bone cell adhesion and osseointegration.

Rosette nanotubes (RNTs) are biologically inspired nanomaterials, which are formed from synthetic DNA base analogues, namely the guanine-cytosine motif (G \wedge C).⁵ In water these RNTs self-assemble to give nanostructures that mimic collagen in the bone. Furthermore, the ability to tailor the physical properties of the RNTs by easy chemical functionality modifications, make them suitable for a number of potential applications.

Previous studies have demonstrated favourable cytocompatibility of RNTs for various tissue-engineering applications.^{4,5-11} Chun *et al.* showed that RNTs functionalized with lysine (K1) promoted osteoblast (bone-forming cell) adhesion when coated on titanium at low concentrations.^{4,6} In addition, it was shown that a mixture of K1 RNTs and nanocrystalline hydroxyapatite in hydrogels led to a two-fold increase in osteoblast adhesion when compared to hydrogel controls.⁷ In another study, Journeay *et al.* showed how RNTs have low acute toxicity in vivo.⁹ As such, it was envisioned that if the RNTs were functionalized with bioactive fragments that are known to enhance cell adhesion, they might be used as potential implant coating materials, which can also act as display/delivery system for osteogenic peptides.

The arginine-glycine-aspartic acid (RGD) peptide is a popular peptide sequence that has been widely studied for improving osteoblast adhesion. In fact, previous studies from the Fenniri and Webster groups have demonstrated increased osteoblast adhesion when lysine-serine-aspartic acid-glycine-arginine (KSDGR) was functionalized with a single G \wedge C motif.¹¹ On the other hand, Dee and co-workers have showed that lysine-arginine-serine-arginine (KRSR) peptides immobilized on glass can selectively enhance osteoblast adhesion, without causing an enhancement in endothelial cells or fibroblasts.¹² The latter have a tendency to form fibrous soft tissue around implants and are therefore undesirable for orthopedic applications.

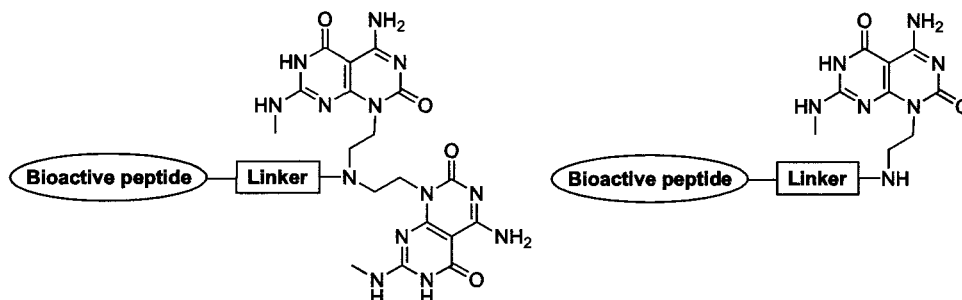


Figure 6.1: Attachment of a bioactive peptide sequence with two G \wedge C units as compared to when functionalized with one G \wedge C unit.

While one can imagine it is theoretically possible to express any moiety covalently attached to the G \wedge C motif, onto the nanotube surface, it has been a challenge to balance loss in enthalpy (H-bonds), stacking interactions, hydrophobic interactions, steric and electronic factors.^{13,14} Furthermore, it was found that KSDGR functionalized with a single G \wedge C (G \wedge C-KSDGR) unit did not self-assemble on its own under neutral pH. It had to be co-mixed with a fairly high concentration of K1 to give RNTs.¹¹ Thus, functionalizing the twin base (TB) with a peptide unit was envisaged to be a better candidate for self-assembly as opposed to the functionalization of the mono base (Figure 6.1).^{13,14}

In this chapter, the synthesis and characterization of two new RNTs derivatives functionalized with peptide units are presented. TB-KRSR was functionalized with two G \wedge C units and the KRSR peptide sequence while TB-KSDGR contained the KSDGR peptide unit along with two G \wedge C moieties (Figure 6.2).

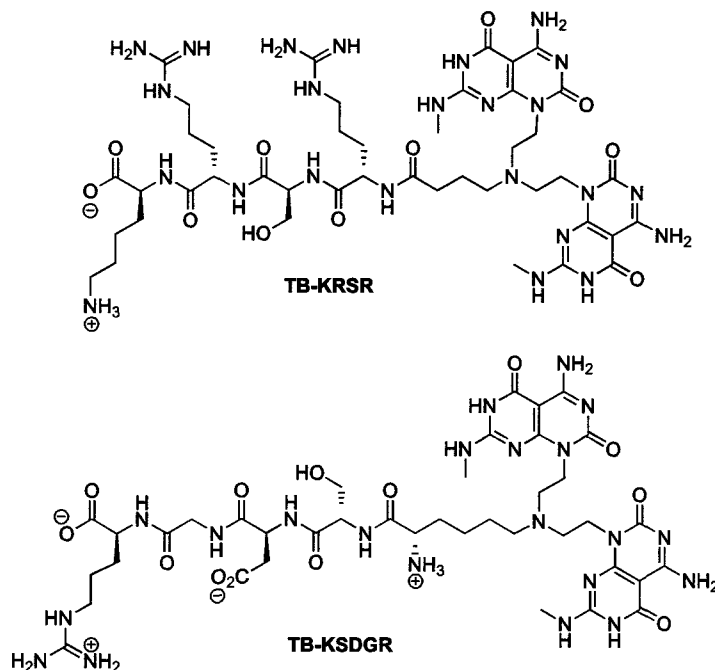


Figure 6.2: Structures of TB-KRSR and TB-KSDGR

6.2. General procedure for solid phase peptide synthesis of target molecules

Standard Fmoc solid-phase peptide synthesis (SPPS) was used to prepare the target molecules.^{15,16} SPPS is a simple procedure, which allows rapid synthesis of peptides in good yields.¹⁷ This method eliminates solubility, purification and racemization issues, common with solution phase peptide synthesis. The carboxyl groups of the first protected amino acid (Fmoc-X-OH) are first coupled to the hydroxyl groups on the Wang resin having a loading capacity of 0.65 mmol/g. The remaining free hydroxyl groups on the resin are then capped and the substitution degree on the resin is determined by spectroscopic quantification of the fulvene-piperidine adduct at 301 nm. The Fmoc group of X anchored to the resin is then removed under basic conditions, after which it is subjected to reaction with the second Fmoc-protected amino acid. The same procedure is repeated for subsequent amino acid couplings. The terminal Fmoc group on the Wang resin-supported peptide is removed and the resulting free amine is then coupled to GAC aldehyde via a reductive amination reaction. The completion of the amide coupling is verified using the Kaiser test.¹⁸ A blue colour implies incomplete reaction due to the presence of free amines in the system while a

yellow colour implies that the amide coupling has completed. The target molecule is obtained as a TFA salt upon deprotection and cleavage from the resin under strongly acidic conditions.

6.3. Synthesis of TB-KRSR

Standard Fmoc SPPS was used to prepare the Wang resin-supported KRSR peptide (Figure 6.3). The first amino acid to be anchored on the Wang resin (**6.1**) was lysine. This was done by esterification of the hydroxyl groups found on the Wang resin and the carboxyl groups of Fmoc-Lys(Boc)-OH (**6.2**). At the end of the coupling, the resin was washed and treated with a solution of 50% acetic anhydride in pyridine to cap the unreacted hydroxyl groups. The substitution degree (0.52 mmol/g) was determined by spectroscopic quantification of the fulvene-piperidine adduct at 301 nm on a resin sample. The terminal Fmoc group on the Wang resin supported lysine (**6.3**) was removed under basic conditions and the free amine was then coupled to Fmoc-Arg(Pbf)-OH (**6.4**) under amide coupling conditions (HBTU, DIEA, DMF). After the amide coupling, the resin bearing the dipeptide **6.5** was washed and the absence of free amine was confirmed using the Kaiser test. The Fmoc group in the resin supported dipeptide **6.5** was then removed and the resulting amine was coupled with Fmoc-Ser(^tBu)-OH (**6.6**). The resulting tripeptide **6.7** was then deprotected and coupled with Fmoc-Arg(PBf)-OH to give the Wang-resin supported KRSR tetrapeptide **6.8**. It was possible to attempt coupling of the free amine of **6.8** to the G \wedge C aldehyde **2.13**, however the reductive amination reaction was envisaged to be synthetically challenging due to the steric bulk of both compounds. As such, the free amine of **6.8** was coupled to the linker Fmoc- γ -Abu-OH **6.9**. The terminal Fmoc group from resulting compound **6.10** was removed, after which the free amine was coupled to the G \wedge C aldehyde **2.13** via a reductive amination reaction using sodium triacetoxyborohydride. The desired TB-KRSR (**6.12**) was obtained upon deprotection and cleavage from the resin of **6.11** under acidic conditions.

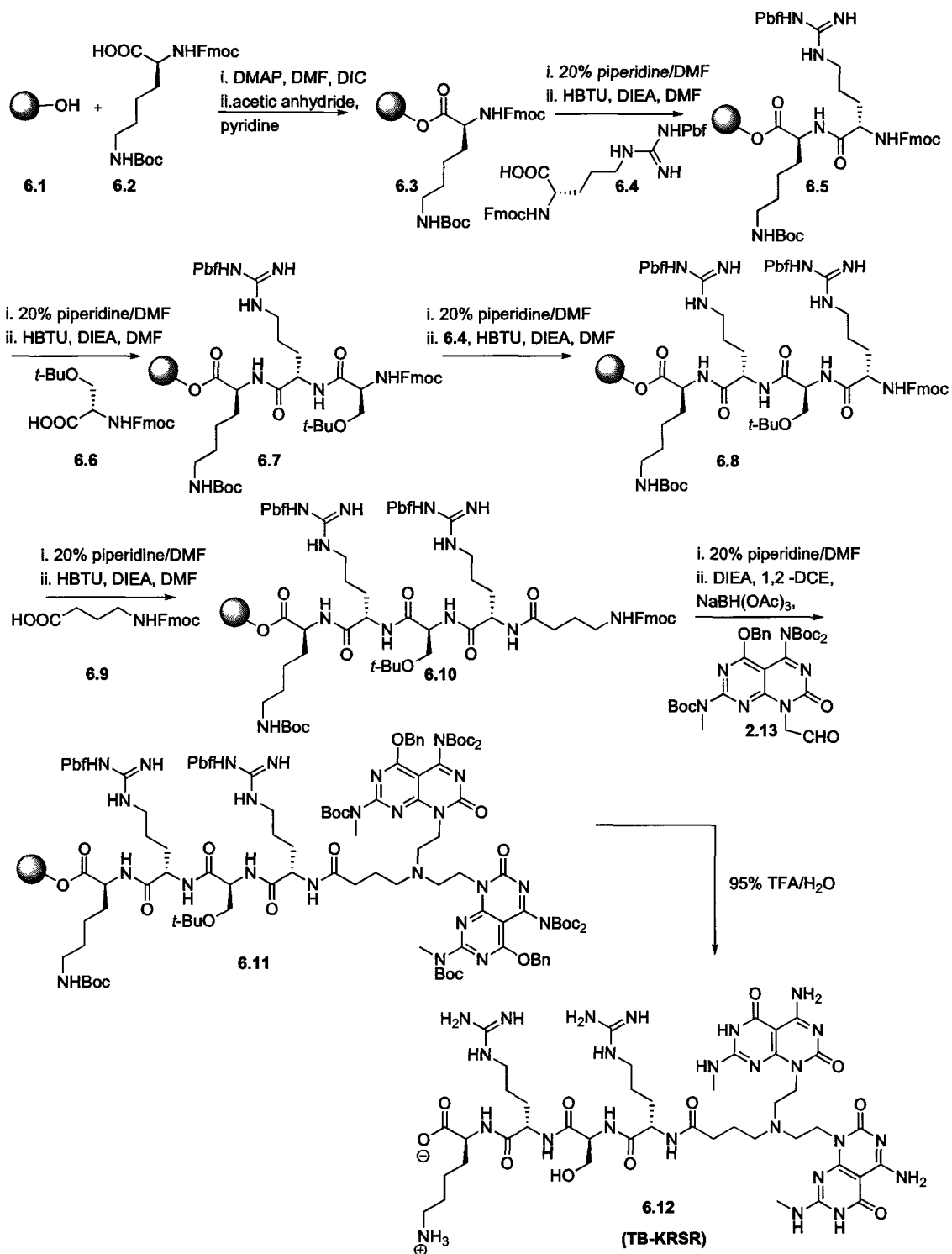


Figure 6.3: Synthetic scheme for the synthesis of TB-KRSR

6.4. Characterization and visualization of TB-KRSR

The target molecule TB-KRSR was characterized by NMR spectroscopy, mass spectrometry and elemental analysis. Though these techniques confirmed the identity of the final product, it was important to know whether this molecule would self-assemble into RNTs. Since the aim of this project was to verify the application of nanomaterials for orthopedic applications, it was important that the compound self-assembled in water.

It was predicted that the TB-KRSR modules would first form a hexameric macrocycle (referred as rosette) due to complementary hydrogen bonding patterns. These rosettes would then stack to form tubes of high aspect ratio. The formation of the RNTs would be favoured both in terms of entropy and enthalpy.

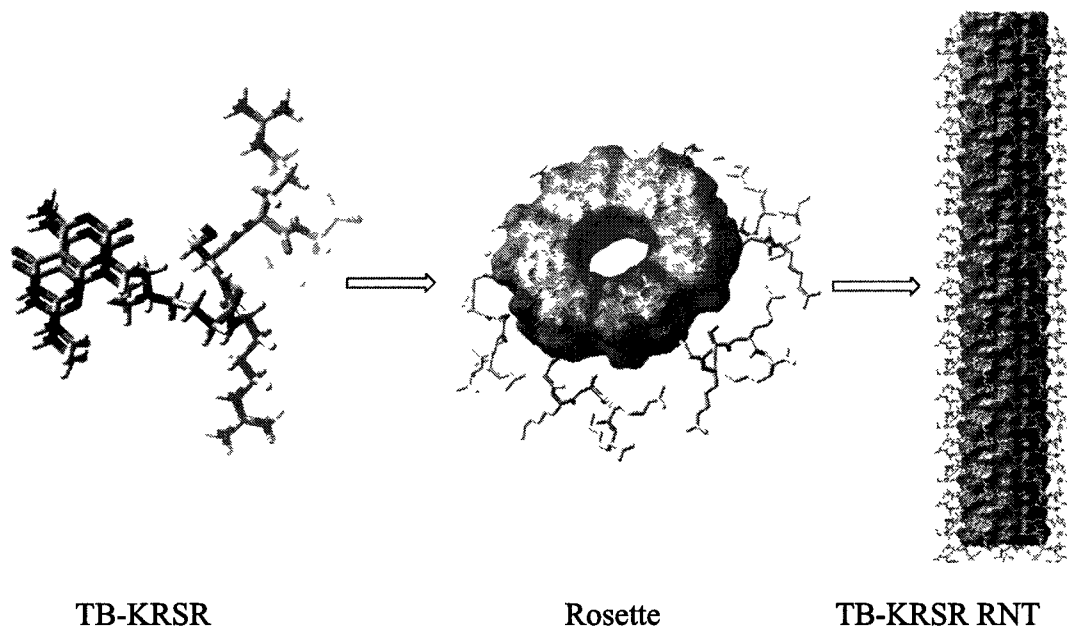


Figure 6.4: Predicted mode of self-assembly of TB-KRSR modules to form the corresponding RNTs.

A stock solution of TB-KRSR (1.0 mg/mL, 0.515 mM) was prepared in dH₂O and the solution was allowed to age for 2 days. An aliquot of the solution was diluted to 0.1 mg/mL (0.0515 mM) with dH₂O prior to imaging. SEM samples were

prepared by floating a carbon-coated 400-mesh copper grid on a droplet of the diluted RNT solution. Images revealed high aspect ratio structures, indicating that RNTs had formed.

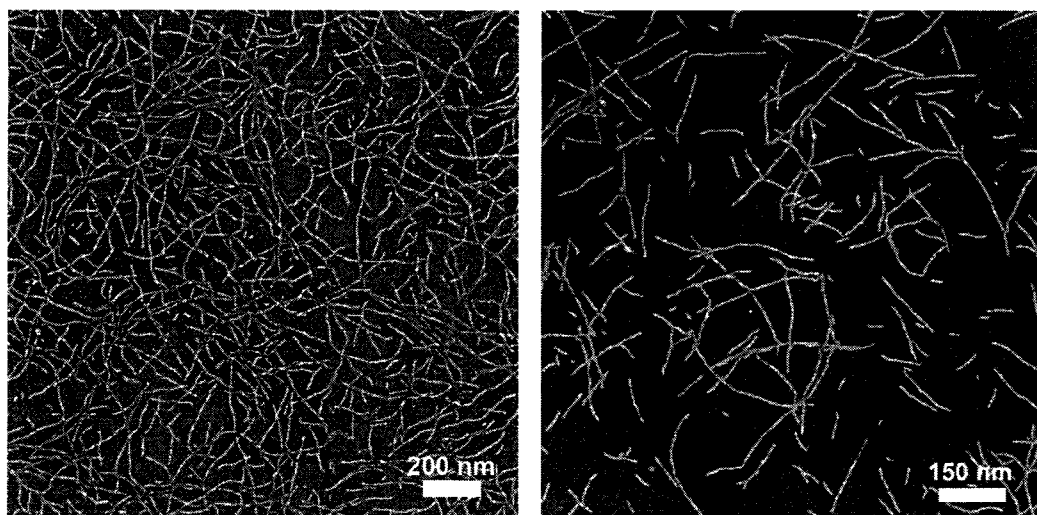


Figure 6.5: SEM images of TB-KRSR in water

The TEM sample was prepared by first depositing 2.0 μL of the diluted RNT solution (0.1mg/mL, 0.0515 mM), obtained from dilution of a 2-day old 1.0 mg/mL stock solution. The RNTs on the carbon grid were then negatively stained using a 2% uranyl acetate solution in water. The TEM images¹⁹ confirmed the formation of RNTs. A series of measurements were performed on the images and the average diameter of the nanotubes was found to be 4.4 ± 0.2 nm. This value obtained for the diameter is slightly lower than what can be predicted for a twin RNTs with such a peptide sequence. For instance, the measured diameter of TBL is 3.5 ± 0.2 nm. These values obtained for TB-KRSR RNTs can be justified by folding of the peptide, which occur to give the most stable RNT conformer in water.

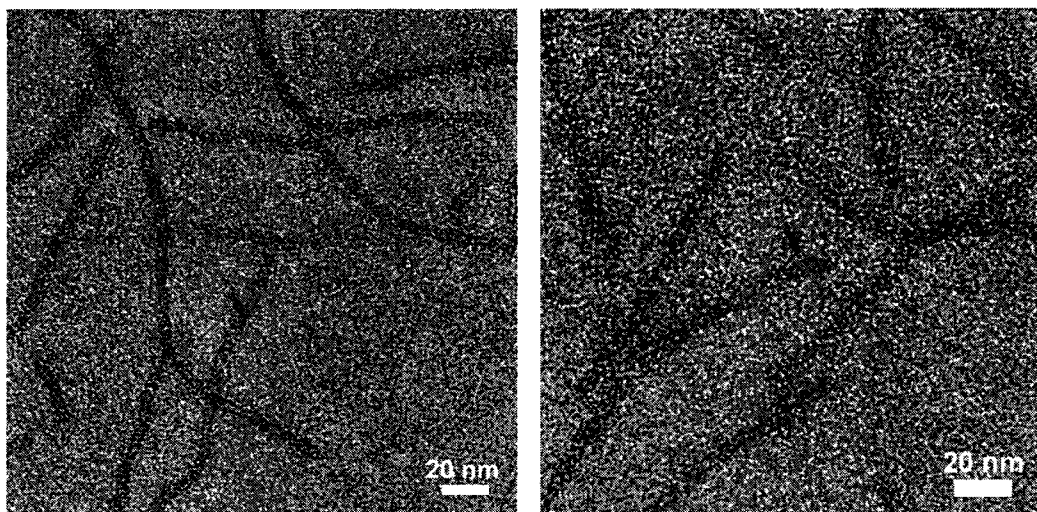


Figure 6.6: TEM images of TB-KRSR in water

For AFM imaging, one drop of the diluted RNT solution (0.1 mg/mL, 0.0515 mM) was deposited onto a freshly cleaved mica substrate and excess solution was blotted using filter paper. The sample surface was then imaged using the tapping mode. The images obtained confirmed the presence of the RNTs as in this case too, nanostructures of high aspect ratio were revealed. The height measurements for the AFM images¹⁹ gave an average height of 3.7 ± 0.2 nm. The average height value corresponds to the diameter of the RNTs and these values were lower than the values obtained from the TEM measurements. RNTs are soft materials and when AFM measurements are carried out sample deformation from substrate compression and interactions with the AFM tip can lead to flattening of the tubes, thus resulting in an inferior value.²⁰

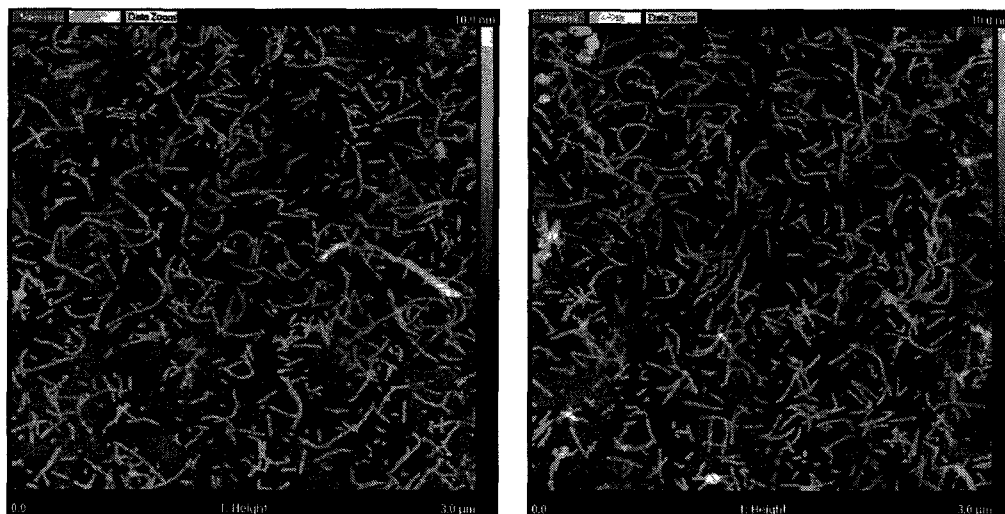


Figure 6.7: AFM images of TB-KRSR in water

6.5. Synthesis of TB-KSDGR

Similar to the synthesis of TB-KRSR, TB-KSDGR was also synthesized using Fmoc SPPS, as shown in Figure 6.8. The first amino acid arginine was anchored on the Wang resin by esterification of the hydroxyl groups on the Wang resin with the carboxyl groups of Fmoc-Arg(Pbf)-OH (**6.4**). The resin was then treated with a solution of 50% acetic anhydride in pyridine to cap the unreacted hydroxyl groups, after which the substitution degree was determined by spectroscopic quantification of the fulvene-piperidine adduct at 301 nm. The Fmoc group on the Wang resin supported arginine (**6.13**) was removed under using a solution of piperidine in DMF and the resulting free amine was coupled to Fmoc-Gly-OH (**6.14**). The Fmoc group from resin-supported dipeptide **6.15** was then cleaved and the resulting amine was coupled with Fmoc-Asp(^tBu)-OH (**6.16**) to give the tripeptide **6.17**. Deprotection of the latter, followed by coupling with Fmoc-Ser(^tBu)-OH gave the tetrapeptide **6.18**. The last amino acid was anchored after liberating the free amine from tetrapeptide **6.18** and coupling it with Fmoc-Lys(Boc)-OH (**6.2**) to give the Wang resin supported pentapeptide KSDGR. The terminal Fmoc group from compound **6.19** was cleaved and the resulting free amine was coupled to the GAC aldehyde **2.13** via a reductive amination reaction to yield the twin GAC functionalized KSDGR compound **6.20**. The latter was

then subjected to deprotection and cleavage from the resin to give the desired TB-KSDGR (6.21) as a TFA salt.

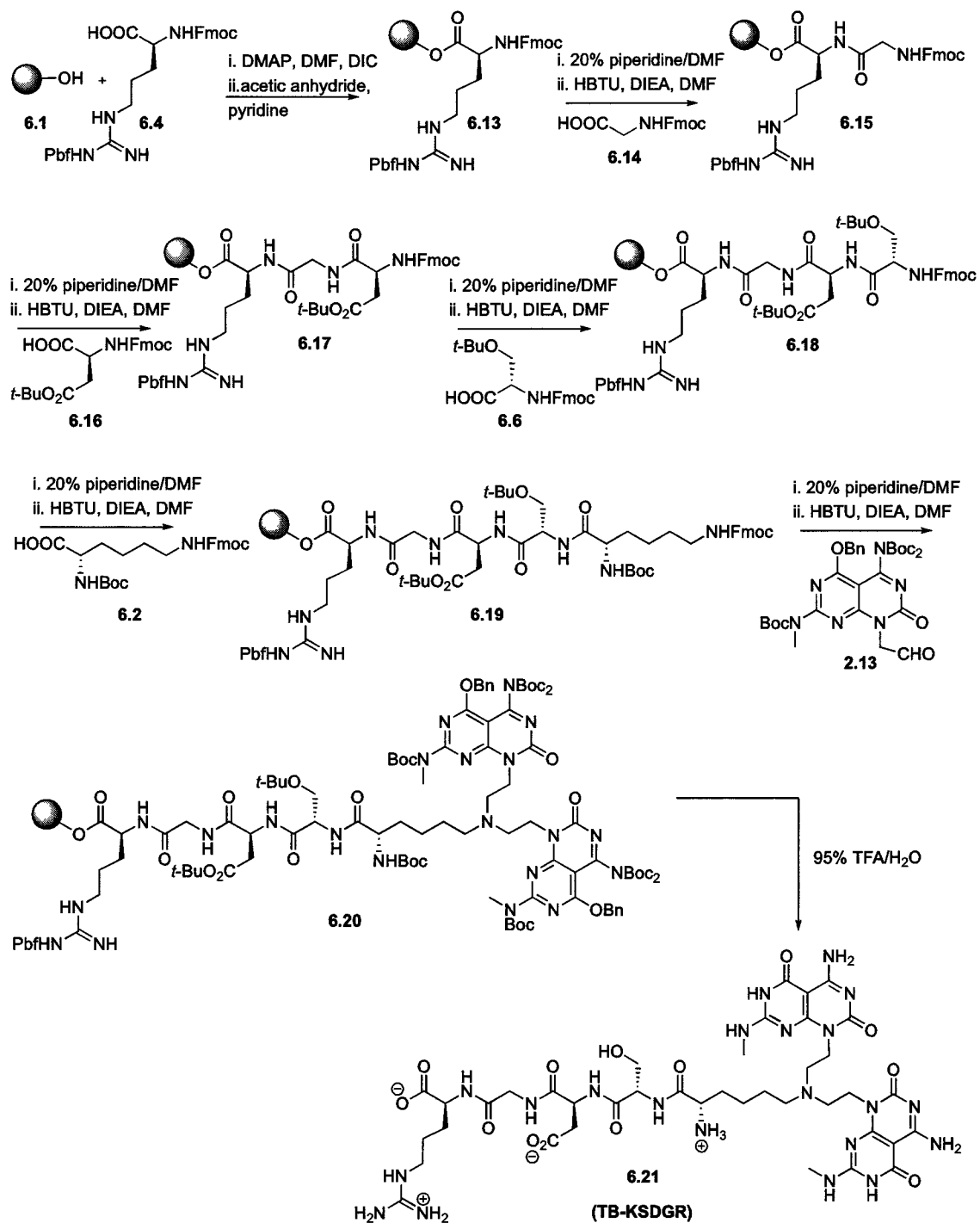


Figure 6.8: Synthetic scheme for the synthesis of TB-KSDGR

6.6. Characterization and visualization of TB-KSDGR

The molecule TB-KSDGR was characterized by NMR spectroscopy, mass spectrometry and elemental analysis. The data from these experiments confirmed the identity of the product formed. Another molecule bearing the KSDGR peptide sequence but having only one G \wedge C unit (G \wedge C-KSDGR) was previously made in the Fenniri's group. However that molecule failed to self-assemble on its own and self-assembly could only be triggered when it was mixed with another RNT forming motif.¹¹ As such it was important to know whether this molecule could self-assemble on its own in water.

It was predicted that if the TB-KSDGR modules would self-assemble readily without any help from other self-assembling modules, it would do so by first forming rosettes, which would then form RNTs (Figure 6.9).

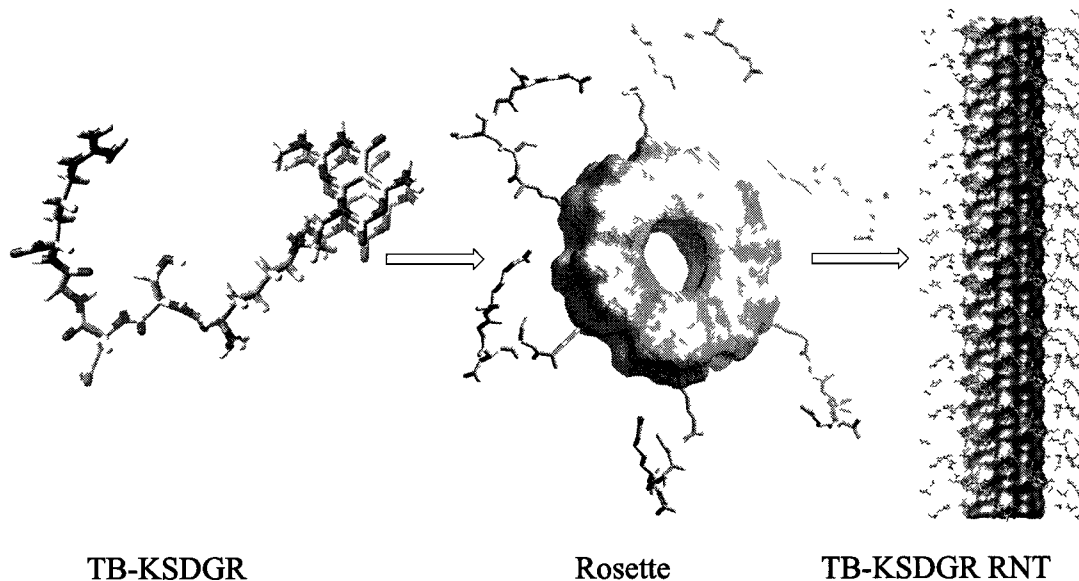


Figure 6.9: Predicted mode of self-assembly of TB-KSDGR modules to form the corresponding RNTs.

A stock solution of TB-KSDGR (1.0 mg/mL, 0.580 mM) was prepared in dH₂O and the solution was allowed to age for 4 days. An aliquot of the solution was diluted to 0.2 mg/mL (0.116 mM) with dH₂O prior to imaging. SEM samples

were prepared by depositing an aliquot of the diluting RNT solution onto a carbon-coated 400-mesh copper grid. The excess solution was blotted. The sample was then stained using 2% uranyl acetate solution in water by depositing 2.0 μL of the stain solution on the grid and the excess stain was removed by blotting. This staining procedure was repeated to improve contrast during imaging. Visualization of the RNT sample revealed images with high aspect ratio structures, indicating that RNTs had formed.

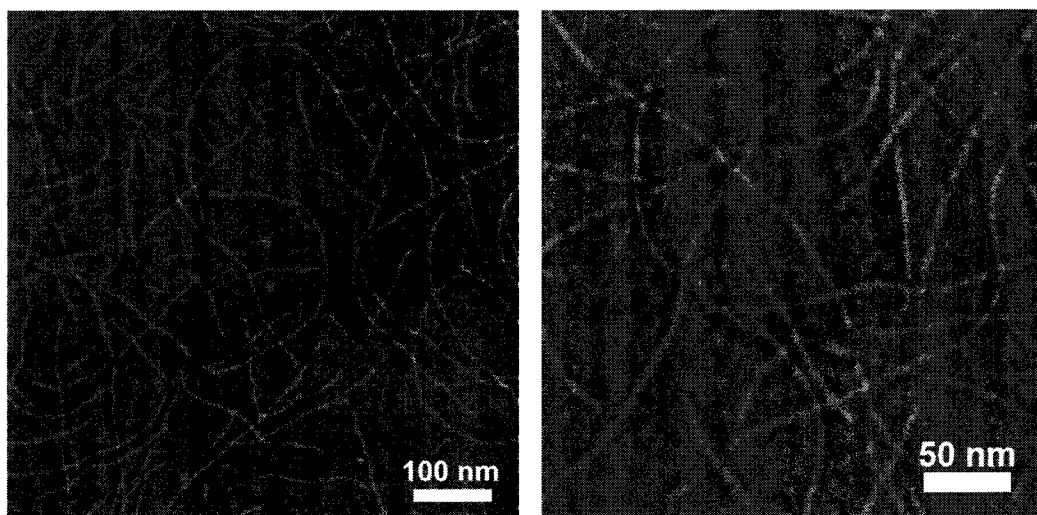


Figure 6.10: SEM images of TB-KSDGR in water

The same samples prepared for SEM imaging, were also visualized using the TEM technique. The TEM images¹⁹ also confirmed the formation of RNTs. Diameter measurements performed on the images revealed an average diameter of 4.6 ± 0.1 nm for the nanotubes.

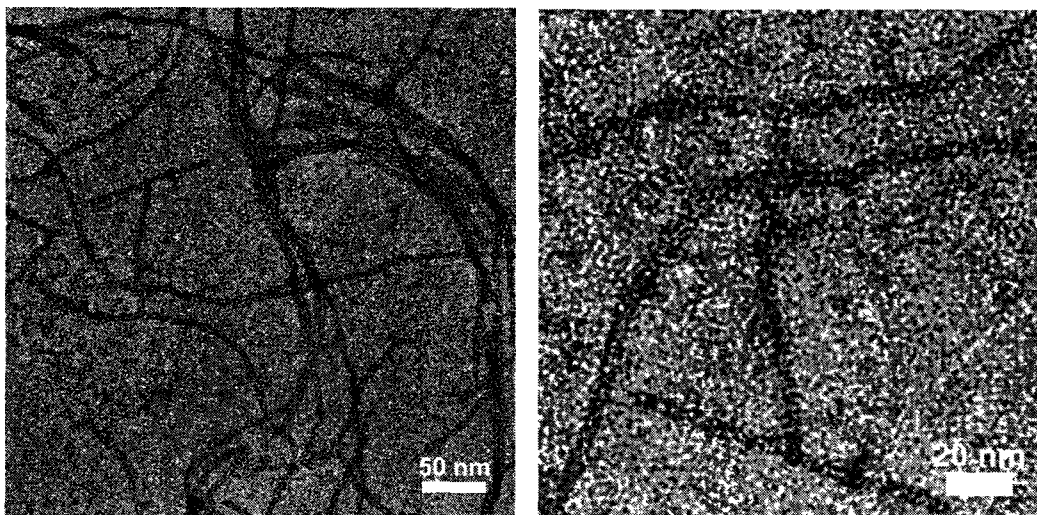


Figure 6.11: TEM images of TB-KSDGR in water

For AFM imaging, a stock solution of TB-KSDGR (0.5 mg/mL, 0.290 mM) was prepared in dH₂O and the solution was allowed to age for one month. An aliquot of the stock solution was diluted to 0.1 mg/mL (0.058 mM) with dH₂O. One drop of the diluted RNT solution was deposited onto a freshly cleaved mica substrate and the excess solution was removed by spin coating. The AFM images¹⁹ obtained confirmed the presence of the RNTs as in this case too, structures of high aspect ratio were revealed (Figure 6.12). The height measurements in the AFM images gave an average height of 3.9 ± 0.2 nm, which was lower but in agreement with the TEM measurements given the tendency of deformation of soft materials due to interaction with the probe.²⁰

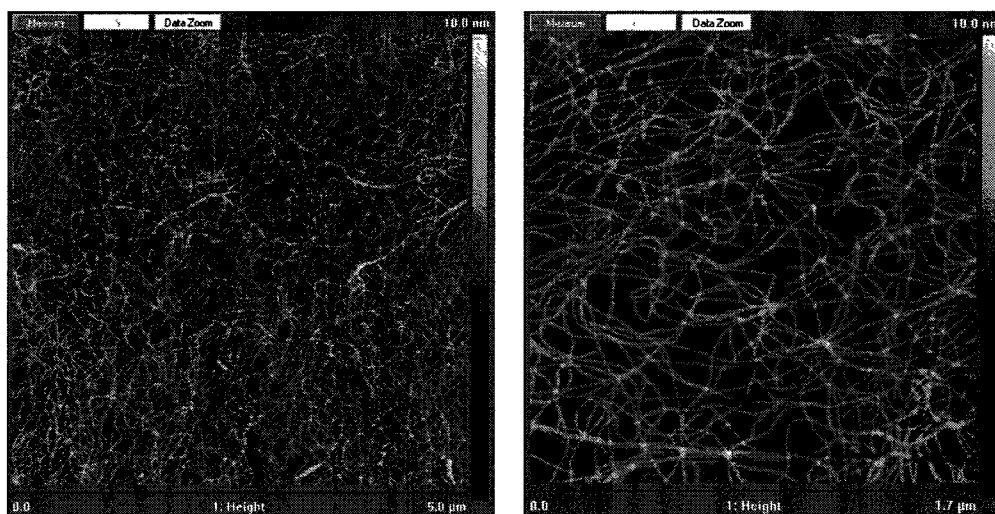


Figure 6.12: AFM images of TB-KSDGR in water

6.7. Biological applications of TB-KRSR and TB-KSDGR

The preliminary cell adhesion studies done at Brown University in collaboration with the Webster group revealed that TB-KRSR had excellent cytocompatibility. The TB-KRSR RNTs were coated on titanium and the relative cell adhesion on the surface was measured and compared to other RNTs and uncoated titanium. It was found that TB-KRSR enhanced very high osteoblast densities compared to untreated titanium. In addition, it was found that TB-KRSR selectively improved osteoblast adhesion relative to fibroblast (soft-tissue forming cell) and endothelial cell adhesions.²¹ These properties make TB-KRSR a good candidate for probing its use as an implant-coating material.²² As for TB-KSDGR, the potential applications are currently being tested by a number of our collaborators.

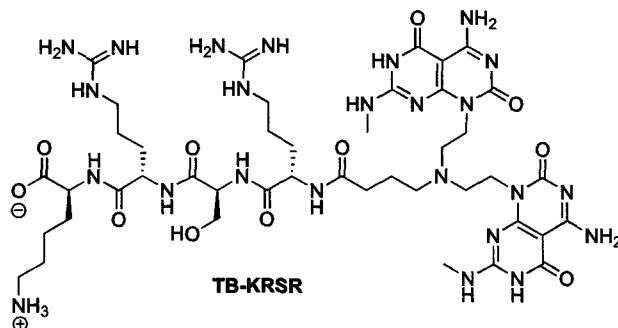
6.8. Conclusion

In this chapter, two new self-assembling molecules (TB-KRSR and TB-KSDGR) were synthesized by SPPS, which allowed easy access to these derivatives. These twin GAC compounds were functionalized with the tetrapeptide lysine-arginine-serine-arginine and pentapeptide lysine-serine-aspartic acid-glycine-arginine, respectively. These compounds can self-assemble readily under physiological conditions to give abundant, long and well-dispersed RNTs. Collaborative work showed that surface modification of titanium using RNTs revealed improved bone

forming cell adhesion. The preliminary cell adhesion studies look prospective for the application of TB-KRSR as an improved implant coating material. Though further studies is clearly required, the ease of chemical modification make RNTs a promising material, geared towards orthopedic applications. Future work involves making a library of bioactive RNTs for similar applications.

6.9. Experimental section

6.9.1. Synthesis of TB-KRSR



DMF (5 mL) was added to 12 mL disposable plastic syringe containing Wang resin (0.650 mmol/g, 0.500 g, 0.325 mmol) and was shaken for 20 min. The solvent DMF was then drained. A solution of Fmoc-Lys(Boc)-OH (0.610 g, 1.30 mmol) and DMAP (0.033 g, 0.325 mmol) in DMF (8 mL) was then poured into the syringe containing the resin. After activating the resin for 20 min, DIC (205 μ L, 1.31 mmol) was added to the syringe and the reaction mixture was shaken for 6h. The resin was then filtered under vacuum, washed with (3 x 10 ml) DCM, MeOH, DMF and then treated with 50:50 acetic anhydride/pyridine (5 ml, 1 x 10 min and 2 x 20 min) to cap the unreactive hydroxyl groups. The resin was then filtered and washed with (3 x 10 ml) with DMF, DCM and MeOH and dried under vacuum. The substitution degree was determined by spectroscopic quantification of the fulvene-piperidine adduct at 301 nm, which was done by recording the UV-vis spectra of three resin samples. The samples of mass 5.3 mg, 9.8 mg and 10.7 mg gave absorbance intensities of 0.207, 0.380 and 0.413 respectively. Using the expression below, a substitution degree of 0.502 mmol/g was obtained, which corresponded to a yield of 77%.

$$\text{Substitution degree} = \frac{101 \times \text{Absorbance}}{7.8 \times \text{mass of resin (mg)}}$$

The Fmoc protecting group from the Wang supported lysine derivative was removed by incubation of the resin in a 20% piperidine solution in DMF (5 ml, 1

x 5 min, 1 x 30 min). The resulting peptidyl resin was washed with (4 x 10 ml) DCM, MeOH and DMF prior to the coupling with the second amino acid. A mixture of Fmoc-Arg(Pbf)-OH (0.649 g, 1.00 mmol), HBTU (0.350 g, 0.951 mmol) and DIEA (310 μ L, 2.00 mmol) in DMF (8 mL) was then poured to the peptidyl resin and was shaken for 4 h. The reaction solution was drained and the resin was washed with (4 x 10 ml) DCM, MeOH and DMF. The absence of free amino groups was indicated by a yellow colour by Kaiser test.

The Fmoc protecting group from the Wang supported dipeptide was removed by incubation of the resin in a 20% piperidine solution in DMF (5 ml, 1 x 5 min, 1 x 30 min). The resin was then washed with (4 x 10 ml) DCM, MeOH and DMF prior to the coupling with the third amino acid. A mixture of Fmoc-Ser(^tOBu)-OH (0.385 g, 1.00 mmol), HBTU (0.350 g, 0.951 mmol) and DIEA (310 μ L, 2.00 mmol) in DMF (8 mL) was then poured to the resin and was shaken for 4 h. The resulting peptidyl resin was washed with (4 x 10 ml) DCM, MeOH and DMF and a Kaiser test confirmed the completion of the amide coupling by displaying a yellow colour.

The Fmoc group from the tripeptide was removed by shaking the resin in a 20% piperidine solution in DMF (5 ml, 1 x 5 min, 1 x 30 min). The resin was then washed with (4 x 10 ml) DCM, MeOH and DMF prior to the coupling with the arginine derivative. A mixture of Fmoc-Arg(Pbf)-OH (0.649 g, 1.00 mmol), HBTU (0.350 g, 0.951 mmol) and DIEA (310 μ L, 2.00 mmol) in DMF (8 mL) was then poured to the peptidyl resin and was shaken for 4 h. The reaction solution was drained and the residual resin was washed with (4 x 10 ml) DCM, MeOH and DMF. The absence of free amino groups was indicated by a yellow colour by Kaiser test.

The Fmoc protecting group from the Wang supported tetrapeptide was removed by incubation of the resin in a 20% piperidine solution in DMF (5 ml, 1 x 5 min, 1 x 30 min). The resin was then washed with (4 x 10 ml) DCM, MeOH and DMF

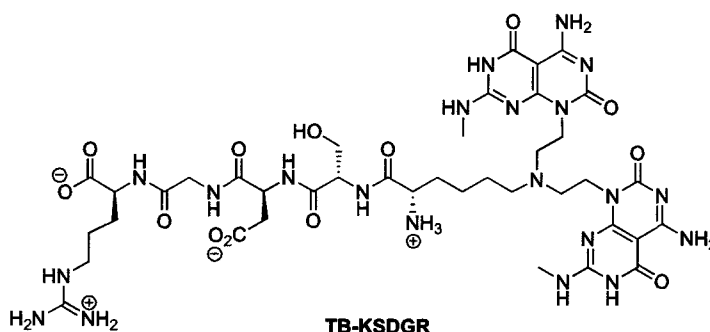
prior to the coupling with a linker. Fmoc- γ -Abu-OH (0.330 g, 1.00 mmol), HBTU (0.350 g, 0.951 mmol) and DIEA (310 μ L, 2.00 mmol) in DMF (8 mL) were then poured into the syringe containing the resin and the resulting mixture was shaken for 4 h. The resin was then washed with (4 x 10 ml) DMF, DCM and MeOH and was dried under vacuum.

The Wang resin supported Lys-Arg-Ser-Arg-Abu (0.200 g, 0.100 mmol) was transferred to a 5 mL disposable plastic syringe and treated with 20% piperidine solution in DMF (5 ml, 1 x 5 min, 1 x 30 min) for the Fmoc group removal. The resin was then filtered and washed with (3 x 10 ml) with DMF, MeOH and DCM and dried. GAC aldehyde **2.13** (0.256 g, 0.400 mmol) and 1,2-DCE (5 ml) were then added to the resin and the mixture was shaken for 4 h. Sodium triacetoxy borohydride (0.042 g, 0.200 mmol) and DIEA (70 μ L, 0.400 mmol) were then added and the mixture was shaken for 36 h. A second round of sodium triacetoxy borohydride (0.042 g, 0.200 mmol) and DIEA (70 μ L, 0.400 mmol) were added and the mixture was shaken for an additional 36 h. The reaction liquor was drained and the resulting resin was washed with (4 x 10 ml) DCM, MeOH and DMF, and dried under vacuum. Cleavage from the resin and deprotection was achieved by the treatment with 95% TFA/H₂O for 2 h. The beads were filtered out over celite and the resulting filtrate was concentrated to a viscous solution by rotary evaporation. Cold Et₂O was then added to precipitate crude product. The precipitate was centrifuged, and the supernatant liquid was removed by decantation. The residual solid was resuspended in Et₂O (2 times), sonicated and centrifuged down. The precipitate was dried to yield the desired product as an off-white powder.

¹H NMR (600 MHz, d₆-DMSO): δ = 12.34 (bs, 2H), 9.24 (bs, 2H), 9.06 (bs, 2H), 8.97 (m, 1H), 8.26 (m, 2H), 8.13 (m, 2H), 8.08-7.98 (m, 2H), 7.65 (bs, 3H), 7.54-7.50 (m, 2H), 7.39-7.16 (bs, 4H), 7.10-6.65 (bs, 4H), 4.43 (m, 4H), 4.35-4.27 (m, 3H), 4.12 (m, 1H), 3.62 (m, 1H), 3.59-3.47 (m, 4H), 3.33 (m, 1H), 3.08 (bs, 5H), 2.91 (d, J = 4.2 Hz, 6H), 2.74 (m, 4H), 2.34-2.23 (m, 2H), 1.90-1.86 (m, 2H),

1.77-1.64 (m, 2H), 1.60-1.43 (m, 8H), 1.34-1.27 (m, 2H); ^{13}C NMR (150 MHz, d_6 -DMSO): δ = 174.9, 174.1, 173.7, 172.0, 171.9, 170.4, 169.8, 162.6, 161.7, 160.3, 157.2, 156.7, 156.0, 148.6, 128.9, 128.7, 83.0, 82.2, 62.2, 55.4, 52.6, 52.5, 52.2, 52.0, 49.5, 40.9, 39.2, 39.1, 31.0, 30.7, 29.8, 29.5, 28.3, 27.1, 27.0, 25.4, 25.3, 22.9; HRMS calcd for $\text{C}_{43}\text{H}_{71}\text{N}_{24}\text{O}_{11}$ $[\text{M}+\text{H}]^+$ 1099.5729, found 1099.5727; elemental analysis calcd (%) for $(\text{C}_{43}\text{H}_{70}\text{N}_{24}\text{O}_{11})(\text{TFA})_5(\text{H}_2\text{O})_3(\text{H}_2\text{SO}_4)_{1.5}(\text{Et}_2\text{O})$ C, 35.22, H, 4.82, N, 17.30, S, 2.47; found: C, 35.21, H, 4.87, N, 17.29, S, 2.47.

6.9.2. Synthesis of TB-KSDGR



DMF (5 mL) was added to 12 mL disposable plastic syringe containing Wang resin (0.65 mmol/g, 0.600 g, 0.390 mmol) and was shaken for 20 min. The solvent DMF was then drained and a solution of Fmoc-Arg(Pbf)-OH (1.01 g, 1.56 mmol) and DMAP (0.048 g, 0.39 mmol) in DMF (8 mL) was added to the resin. After shaking the resin for 20 min, DIC (205 μL , 1.31 mmol) was added to the syringe and the reaction mixture was shaken overnight. The resin was then filtered under vacuum, washed with (3 x 10 ml) DCM, MeOH and DMF. The resin was treated with a 50% acetic anhydride solution in pyridine (5 ml, 1 x 10 min and 2 x 20 min) to cap the unreactive hydroxyl groups. The resin was then filtered and washed with (3 x 10 ml) with DMF, DCM and MeOH and dried under vacuum. The substitution degree was determined by spectroscopic quantification of the fulvene-piperidine adduct at 301 nm. The samples of mass 7.9 mg, 9.6 mg and 10.1 mg gave absorbance intensities of 0.159, 0.192 and 0.241 respectively. A substitution degree of 0.278 mmol/g was obtained, which corresponded to a yield of 43%.

The Fmoc protecting group from the Wang supported arginine analogue was removed by treatment of the resin in a 20% piperidine solution in DMF (5 ml, 1 x 5 min, 1 x 30 min). The resulting resin was washed with (4 x 10 ml) DCM, MeOH and DMF. A mixture of Fmoc-Gly-OH (0.128 g, 0.430 mmol), HBTU (0.163 g, 0.430 mmol) and DIEA (150 μ L, 0.860 mmol) in DMF (8 mL) was then poured to the peptidyl resin and was shaken for 4 h. The reaction solution was drained and the resin was washed with (4 x 10 ml) DCM, MeOH and DMF. The absence of free amino groups was confirmed by a yellow colour through Kaiser test.

The Wang resin supported dipeptide was incubated in a 20% piperidine solution in DMF (5 ml, 1 x 5 min, 1 x 30 min) for the Fmoc group removal. The resin was washed with (4 x 10 ml) DCM, MeOH and DMF prior to the next coupling. A mixture of Fmoc-Asp(^tOBu)-OH (0.177 g, 0.430 mmol), HBTU (0.163 g, 0.430 mmol) and DIEA (150 μ L, 0.860 mmol) in DMF (8 mL) was then added to the resin and was shaken for 4 h. The resulting peptidyl resin was washed with (4 x 10 ml) DCM, MeOH and DMF and a Kaiser test confirmed the completion of the amide coupling by displaying a yellow colour.

The Fmoc group from the tripeptide was removed by shaking the resin in a 20% piperidine solution in DMF (5 ml, 1 x 5 min, 1 x 30 min). The resin was then washed with (4 x 10 ml) DCM, MeOH and DMF prior to the next coupling. A mixture of Fmoc-Ser(^tOBu)-OH (0.165 g, 0.430 mmol), HBTU (0.163 g, 0.430 mmol) and DIEA (150 μ L, 0.860 mmol) in DMF (8 mL) was then added to resin and was shaken for 4 h. The solution was drained and the resin was washed with (4 x 10 ml) DCM, MeOH and DMF. The absence of free amino groups was indicated by a yellow colour by Kaiser test.

The Wang resin supported tetrapeptide was treated with a 20% piperidine solution in DMF (5 ml, 1 x 5 min, 1 x 30 min) for the Fmoc group removal. The resin was

then washed with (4 x 10 ml) DCM, MeOH and DMF prior to the coupling with the lysine derivative. Fmoc-Lys(Boc)-OH (0.202 g, 0.430 mmol), HBTU (0.163 g, 0.430 mmol) and DIEA (150 μ L, 0.860 mmol) in DMF (8 mL) were then added to the resin and the resulting mixture was shaken for 4 h. The resin was then washed with (4 x 10 ml) DMF, DCM and MeOH and was dried under vacuum.

The Wang resin supported Arg-Gly-Asp-Ser-Lys (0.226 g, 0.147 mmol) was transferred to a 5 mL disposable plastic syringe and was shaken with 20% piperidine solution in DMF (5 ml, 1 x 5 min, 1 x 30 min) to remove Fmoc protecting group from the terminal amine functionality. The resin was then filtered and washed with (3 x 10 ml) with DMF, MeOH and DCM and dried. G^AC aldehyde **2.13** (0.256 g, 0.400 mmol) and 1,2-DCE (5 ml) were added for coupling with the free amine on the resin by shaking for 4 h. Sodium triacetoxy borohydride (0.026 g, 0.123 mmol) and DIEA (20 μ L, 0.123 mmol) were then added and the mixture was shaken for 36 h. A second round of sodium triacetoxy borohydride (0.026 g, 0.123 mmol) and DIEA (20 μ L, 0.123 mmol) were added and the mixture was shaken for an additional 36 h. The reaction liquor was drained and the resulting resin was washed with (4 x 10 ml) DCM, MeOH and DMF, and dried under vacuum. Cleavage from the resin and deprotection was achieved by the treatment with 95% TFA/H₂O for 2 h. The resin beads were filtered out over celite and the resulting filtrate was evaporated to give a viscous solution. Cold Et₂O was then added to the resulting solution and a precipitate was formed. The latter was centrifuged, and the supernatant liquid was removed by decantation. The residual solid was resuspended in Et₂O (2 times), sonicated and centrifuged down. The precipitate was dried to yield the desired product as an off-white powder.

¹H NMR (600 MHz, d₆-DMSO): δ = 12.39 (bs, 2H), 9.23 (bs, 2H), 9.16 (bs, 2H), 8.61 (d, J = 7.2 Hz, 1H), 8.43 (d, J = 8.2 Hz, 1H), 8.34 (app. d, J = 4.7 Hz, 2H), 8.13 (bs, 3H), 8.07 (d, J = 8.2 Hz, 1H), 7.94 (t, J = 5.6 Hz, 1H), 7.55 (t, J = 5.9 Hz, 2H), 7.39-7.16 (bs, 4H), 7.40-6.70 (bs, 4H), 4.57 (m, 1H), 4.41 (m, 4H), 4.17

(m, 1H), 3.86 (m, 1H), 3.75-3.56 (m, 4H), 3.52 (m, 4H), 3.32 (m, 2H), 3.06 (m, 2H), 2.90 (d, $J = 4.8$ Hz, 6H), 2.68 (m, 2H), 2.53 (m, 2H), 1.78-1.63 (m, 4H), 1.61-1.51 (m, 1H), 1.50-1.41 (m, 2H), 1.40-1.30 (m, 1H); ^{13}C NMR (150 MHz, $\text{d}_6\text{-DMSO}$): $\delta = 173.6, 172.3, 171.2, 170.1, 169.0, 168.9, 161.7, 160.3, 159.6, 157.2, 157.2, 156.0, 83.0, 62.3, 55.3, 52.7, 52.4, 52.7, 52.4, 51.9, 50.0, 49.4, 42.2, 40.7, 40.5, 31.2, 28.7, 28.3, 25.5, 21.8$; HRMS calcd for $\text{C}_{39}\text{H}_{60}\text{N}_{21}\text{O}_{13} [\text{M}+\text{H}]^+$ 1030.4674, found 1030.4671; elemental analysis calcd (%) for $(\text{C}_{39}\text{H}_{59}\text{N}_{21}\text{O}_{13})(\text{TFA})_{4.5}(\text{H}_2\text{O})_3(\text{H}_2\text{SO}_4)_{0.75}(\text{Et}_2\text{O})_{0.75}$: C, 35.48, H, 4.58, N, 17.04, S, 1.39; found: C, 35.79, H, 4.39, N, 17.11, S, 1.44.

6.10. References

1. Taylor, D.; Hazenberg, J. G.; Lee, T. C. *Nature Mater.* **2007**, *6*, 263-268.
2. American Academy of Orthopedic Surgeons (AAOS), online: <http://www.aaos.org/Research/stats/patientstats.asp>.
3. Khademhosseini, A.; Borenstein, J.; Toner, M.; Takayama, S. *Micro and nanoengineering of the cell microenvironment: technologies and applications*. Norwood Artech House, **2008**, 431-460.
4. Chun, A. L.; Moralez, J. G.; Fenniri, H.; Webster, T. J. *Nanotechnology* **2004**, *15*, S234-239.
5. (a) Fenniri, H.; Deng, B. L.; Ribbe, A. E.; Hallenga, K.; Jacob, J.; Thiyagarajan, P. *Proc. Natl. Acad. Sci.* **2002**, *99*, 6487-6492. (b) Fenniri, H.; Mathivanan, P.; Vidale, K. L.; Sherman, D. M.; Hallenga, K.; Wood, K. V.; Stowell, J. G. *J. Am. Chem. Soc.* **2001**, *123*, 3854-3855. (c) Fenniri, H.; Deng, B. L.; Ribbe, A. E. *J. Am. Chem. Soc.* **2002**, *124*, 11064-11072.
6. Chun, A. L. *Helical rosette nanotubes: an investigation towards its application in orthopedics* (Ph.D. thesis), Weldon School of Biomedical Engineering, Purdue University, West Lafayette, IN, **2006**.
7. Zhang, L.; Rodriguez, J.; Raez, J.; Myles, A. J.; Fenniri, H.; Webster, T. J. *Nanotechnology* **2009**, *20*, 17510.
8. Zhang, L.; Chen, Y.; Rodriguez, J.; Fenniri, H.; Webster, T. J. *Int. J. Nanomed.* **2008**, *3*, 323-333.
9. Journeay, W. S.; Suri, S. S.; Moralez, J. G.; Fenniri, H.; Singh, B. *Int. J. Nanomed.* **2008**, *3*, 373-383.
10. Zhang, L.; Ramsaywack, S.; Fenniri, H.; Webster, T. J. *Tissue Eng.* **2008**, *14*, 1353-1364.
11. Zhang, L.; Rakotondradany, F.; Myles, A. J.; Fenniri, H.; Webster, T. J. *Biomaterials* **2009**, *30*, 1309-1320 and references therein.
12. Dee, K. C.; Andersen, T. T.; Bizios, R. *J. Biomed. Mater. Res.* **1998**, *40*, 371-377.
13. Moralez, J. G.; Raez, J.; Motkuri, R. K.; Yamazaki, T.; Kovalenko A.; Fenniri, H. *J. Am. Chem. Soc.* **2005**, *127*, 8307-8309.

14. Hemraz, U.; Fenniri, H. *Mater. Res. Soc. Symp. Proc.* **2008**, 1057-II05-37.
15. Carpino, L. A.; Han, G. Y. *J. Org. Chem.* **1972**, *37*, 3404-3409.
16. Atherton, E.; Fox, H.; Harkiss, D.; Logan, C. J.; Sheppard, R. C.; Williams, B. *J. J. Chem. Soc., Chem. Commun.* **1978**, 537-539.
17. Merrifield, R. B. *J. Am. Chem. Soc.* **1963**, *85*, 2149-2154.
18. Kaiser, E.; Colescott, R. L.; Bossinger, C. D.; Cook, P. I. *Anal. Biochem.* **1970**, *24*, 595-598.
19. AFM and TEM images were taken by Dr Jae-Young Cho.
20. (a) Muir, T.; Morales, E.; Root, J.; Kumar, I.; Garcia, B.; Vellandi, C. Jenigian, D.; Marsh, T.; Henderson, E.; Vesenska, J. *J. Vac. Sci. Technol. A* **1998**, *16*, 1172-1177. (b) DeRose, J. A.; Revel, J. P. *Thin Solid Films* **1998**, *331*, 194-202. (c) Kasumov, A. Y., Klinov, D. V.; Roche, P. E.; Gueron, S.; Bouchiat, H. *Appl. Phys. Lett.* **2004**, *84*, 1007-1009.
21. Zhang, L.; Hemraz, U. D.; Fenniri, H.; Webster, T. J. *Mater. Res. Soc. Symp. Proc.* **2009**, 1209-YY01-05.
22. (a) Zhang, L.; Hemraz, U. D.; Fenniri, H.; Webster, T. *J. Biomed. Mater. Res. A, Osteogenic peptide modified rosette nanotubes for improved orthopedic applications*, **2010**, *95A*, 550-563. (b) Fenniri, H.; Hemraz, U. D.; Webster, T. J. Zhang, L. *Methods and Materials for Tuning Bone Cells Adhesion Behavior on Titanium Implants*, U.S. Provisional patent application, Serial number 61/314,243.

Significance of this thesis work and outlook

Nanomaterials have been the subject of enormous interest for the past two decades because of their potential applications in the industrial, electronic and biomedical fields. As such, the quest for new strategies has led to the emergence of a number of novel functional materials, including self-assembled supramolecules such as Rosette Nanotubes (RNTs). Large architectures made of covalent bonds, though structurally more stable, are difficult to functionalize and adapt to biological systems. Superstructures originating from noncovalent interactions on the other hand, can be easily functionalized using the bottom up approach. In biological systems, which have the great potential to disrupt the noncovalent forces, the stability of these architectures is paramount. RNTs - a nanomaterial with unique surface chemistry and biomimetic features is made up of a self-complementary DNA base hybrid molecule and has been shown to have low toxicity in vitro and in vivo. As a result, this novel material was tested and studied for a number of biological applications. While the structural design of the RNTs made chemical modification of both the single and twin G \wedge C-based RNTs a relatively easy task, the latter had a higher stability. As such, in an attempt to fully exploit these organic materials for biomedical and other materials applications, in-depth studies of the physical properties of the twin RNTs were necessary.

Part of the initial goal of this thesis work was to design twin G \wedge C-based self-assembling modules with different functional groups, core modification and steric bulk and test their RNT forming ability under different conditions including solvent systems, charge density and counterions. The length distribution of the RNTs and their relative stability (Chapter 2) was investigated and it was found that polarity, hydrophobicity and charge density could be tuned to generate longer RNTs. Along the same lines, the self-assembly behaviour of certain single G \wedge C-based modules was studied (Chapter 4). Single G \wedge C-based modules, which did not self-assemble in aqueous and/or methanolic media, underwent higher order

aggregation at higher pH and in presence of hydrogen-bond acceptor solvents. Results from these studies can be extrapolated to other RNTs or self-assembling systems in an attempt to optimize their self-assembly behaviour under various physical conditions.

While in the earlier chapters, the versatility and stability of the twin G \wedge C-based RNTs was evident, the design of an even stable system was our next challenge. As such, a new self-assembling molecule (G \wedge C-4) having two twin G \wedge C units was designed (Chapter 5). Based on our imaging and modeling studies, this class of new modules formed quad-rosettes in solution, which then stacked into stable nanotubes. Future work related to this new system involves side-chain functionalization, which would allow bulkier substituents to be expressed on the periphery of the nanotubes, and further tuning of the length and nature of the spacer between the interconnected twin G \wedge C units.

We are surrounded by systems, made of chiral building blocks (including proteins, sugars, amino acids, lipids). Though the advantages of living in a chiral world over an achiral one are not clearly understood, a number of processes proceed by favouring one of the two possible chiralities. The most significant work from this thesis is the discovery of a unique CD activity exhibited by a class of achiral twin G \wedge C-based RNTs (Chapter 3), which had not been previously reported. We have demonstrated that true supramolecular chirality emerged when the achiral RNT samples were subjected to mechanically-induced symmetry breaking on a macroscopic scale. In a field, which is highly dominated by chiroptical properties and where the quest for the origin of homochirality is always lurking, creation of chirality without the contribution of molecular chirality is definitely a significant advance. We anticipate that the impact of this work would be greater when such vortex-induced supramolecular chirality could be successfully transferred from RNTs to neighbouring achiral molecular systems. Using our system, we can generate RNTs of reversible chirality by stirring in opposite fashion. Successful transfer of chirality will imply that any of the two

enantiomers can be selected using one type of RNTs, unlike current catalysis protocols that necessitate catalyst of a specific chirality for the generation of enantiopure components.

The main motivation behind the sixth chapter of this thesis was to address a challenging problem. Each year millions of people suffer from various bone diseases often resulting in costly orthopedic implant surgeries, whereby the injured bones are replaced by artificial metal implants. The limited lifetime of these metal implants is due to insufficient bonding between the implant material and juxtaposed bone. It was envisaged that biologically inspired coatings could turn the metal surfaces into biomimetic nanostructured interfaces, hence increasing the implant lifetime by enhancing the affinity between the bone cells and implant. It was earlier shown that titanium coated with lysine functionalized RNTs promoted bone cell deposition. As such, the design of RNTs functionalized with peptides known to promote bone cell adhesion, seemed a logical step. In fact, KRSR functionalized RNTs selectively improved osteoblast adhesion relative to fibroblast and endothelial cell adhesion. While, this invention is in process of being patented and licensed, research is still ongoing. Future work involves making a library of bioactive RNTs for similar applications, based on peptides from the bone morphogenetic proteins.

Finally, this thesis work demonstrates extensive research on the complex relationship between molecular structure and self-assembly of G \wedge C systems. It has also unraveled some novel properties of these self-assembling systems.